EXPERIMENTAL INVESTIGATIONS IN FRICTION STIR WELDING OF NON-FERROUS DISSIMILAR MATERIALS

A Thesis Submitted
In Partial Fulfillment of the Requirement
for the Degree of

DOCTOR OF PHILOSOPHY

by

PRADEEP KUMAR MOURIA
(2K17/Ph.D/ME/34)

Under the Supervision of

Dr. Ranganath M. Singari
Professor Mechanical Engineering
Delhi Technological University

Dr. Reeta Wattal
Professor Mechanical Engineering
Delhi Technological University

To the
Department of Mechanical Engineering
DELHI TECHNOLOGICAL UNIVERSITY
(Formerly Delhi College of Engineering)
Shahabad Daulatpur, Main Bawana Road, Delhi- 110042, India

December, 2024

DELHI TECHNOLOGICAL UNIVERSITY

(Formerly Delhi College of Engineering)

Shahbad Daulatpur, Main Bawana Road, Delhi-110042, India

CANDIDATE'S DECLARATION

I hereby certify that the work is being presented in this thesis entitled, **"Experimental Investigations in Friction Stir Welding of Non-Ferrous Dissimilar Materials"** is an original and authentic work carried out by me under the supervision of Dr. Ranganath M. Singari, Professor, Department of Mechanical Engineering, and Dr. Reeta Wattal, Professor, Department of Mechanical Engineering, Delhi Technological University, Delhi. This thesis has been prepared in conformity with the rules and regulations of the Delhi Technological University, Delhi. The research work reported and the results presented in the thesis have not been submitted either in part or full to any other university or institute for the award of any other degree or diploma. As per my understanding, this thesis is free from any plagiarized content.

Mr. Pradeep Kumar Mouria
2K17/Ph.D./ME/34
Research Scholar
Department of Mechanical Engineering
Delhi Technological University

Date:
Place: Delhi

DELHI TECHNOLOGICAL UNIVERSITY

(Formerly Delhi College of Engineering)

Shahbad Daulatpur, Main Bawana Road, Delhi-110042, India

SUPERVISOR'S CERTIFICATE

This is to certify that the Ph.D. thesis entitled *"***Experimental Investigations in Friction Stir Welding of Non-Ferrous Dissimilar Materials***"* being submitted by Mr. Pradeep Kumar Mouria, Roll No. 2K17/Ph.D./ME/34 for the award of the degree of Doctor of Philosophy in Mechanical Engineering, to Delhi Technological University, Delhi, India, is a bonafide record of the original research work carried out by him under our guidance and supervision. The work presented in this thesis has not been submitted to any other university or institution for the award of any degree or diploma.

Prof. Ranganath M. Singari
Department of Mechanical Engineering,
Delhi Technological University,
Delhi, India

Prof. Reeta Wattal
Department of Mechanical Engineering,
Delhi Technological University,
Delhi, India

ACKNOWLEDGEMENT

The successful culmination of this research work is indebted to the unwavering support and guidance of numerous individuals. I extend my sincere gratitude to all those who have contributed to this endeavor. First and foremost, I express my heartfelt gratitude to the Almighty God for blessing me with the fortitude, wisdom, and guidance to complete this research work. The strength and inspiration derived from these blessings have been fundamental throughout this journey.

I am profoundly thankful to my supervisors for their invaluable support, guidance, and encouragement. Their expertise, continuous assistance, and constructive feedback significantly shaped the outcome of this research. I feel great pleasure that I have reached at his stage of time when I would like express my deep gratitude and special thankfulness foremost to supervisors Prof. Ranganath M. Singari and Prof. Reeta Wattal who have always been like a search light in dark night for me. Their continuous help, encouragement and supervision went a long way in the journey of this thesis work. Their scientific inputs, personal helps, caring and friendly nature has always made me feel at ease with them and I could always look back on them for any support during my research of Ph.D. They have always been there for me with their supporting hands whenever I needed it the most.

I extend my heartfelt gratitude to Prof. B.B. Arora, Head of the Mechanical Engineering Department, Prof. B. D Pathak, Prof. Suresh Kumar Garg, Prof. Atul Kumar Agarwal, Prof. R.C Singh and Prof. S.G. Warkar for providing me with all the essential facilities needed to complete my work. I am also thankful to all the faculty members of the department for their timely advice, support and help on various occasions along with non-teaching staff of Mechanical Engineering Department who have helped me directly or indirectly in completion of the Ph.D. work.

I feel proud for special mention of thanks to Prof. Sujata Nayak, Dr. Prashant Bhardwaj, Dr. Husain Mehdi, Dr. Shadab Ahmad, Dr. J.P Sharma, Dr. Ajit , Mr Mandeep Bhadana, Dr. Piyush Mahendru, Dr. Smriti, Dr. Gianender Kajal, Dr. Smriti Mr. Nazish, who help me at different stage of my life and motivate me and made it possible for me to see this day.

My heart-felt regards goes to my parents Sh. Ramesh Chand and Smt. Bimla Devi and Brother Mr. Praveen Mouria who motivate me at difficult time and always provide me good suggestions. I owe my deepest gratitude towards my better half, my

wife Ms. Shikha for her eternal support and for understanding my goals and aspirations. Her infallible love and support has always been my strength. Her patience and sacrifice will remain my inspiration throughout my life. I am thankful to my son Jiyansh Mouria for giving me happiness during my studies. His love is source of my spirit at every difficult moments of my life.

I am always grateful and thankful to ALMIGHTY GOD in providing me good health, energy and patience in every best and worst situation. An encouragement with a sense for being in stable behavior for every victory and failure is given by THY GRACE.

Mr. Pradeep Kumar Mouria
2K17/Ph.D./ME/34
Research Scholar
Department of Mechanical Engineering
Delhi Technological University

Delhi

Dec, 2024

ABSTRACT

Friction Stir Welding (FSW) has emerged as a revolutionary solid-state welding technique, exhibiting exceptional promise for joining non-ferrous materials with dissimilar compositions. This research aims to advance the understanding and application of FSW in the context of dissimilar non-ferrous materials. The study involves a systematic experimental investigation, encompassing a diverse range of non-ferrous alloys. The primary objectives include unraveling the intricate dynamics of the FSW process when applied to dissimilar materials, optimizing key welding parameters, and evaluating the resulting microstructural evolution. The research also delves into the mechanical properties of the welded joints, with a specific focus on the influence of dissimilarity between materials on the overall weld quality.

The influence of three different pin profiles (square, triangular, and threaded circular pin profile) on the metallurgical characterization of the friction stir welded joints of AZ91D and AA2024 was analyzed. Among the different pin profiles, the square pin profile revealed the most favorable joint properties in terms of both mechanical and metallurgical behavior. Conversely, the joint fabricated with the triangular pin profile exhibited the lowest tensile properties. The intermetallic compounds (IMCs) tended to migrate toward the weld surface adjacent to the AZ91D plate, potentially resulting in constitutional liquation during solidification. To minimize the effect of these IMCs, different types of tool pin were used and observed that the square pin profile results in defect-free joints. The optimal welding parameters for achieving a sound weld were determined to be a traverse speed (TS) of 35mm/min and an RTS of 700 r/min. The presence of two specific intermetallic phases, Al_3Mg_2 and $Al_{12}Mg_{17}$, was observed in all joints, with $Al_{12}Mg_{17}$ showing a tendency to migrate toward the weld surface adjacent to the AZ91D plate, possibly resulting in constitutional liquation during solidification. The results revealed that the morphological characteristics and input heat significantly influenced the formation of IMCs. The anticipated outcomes of this study are expected to contribute significantly to the body of knowledge surrounding FSW of non-ferrous dissimilar materials. The insights gained will optimize FSW processes for better joint integrity in diverse industries. This research aims to bridge gaps in FSW knowledge, advancing the welding of dissimilar non-ferrous materials and expanding its industrial use.

TABLE OF CONTENTS

LIST OF TABLES

LIST OF FIGURES

NOMENCLATURE

Friction stir welding	FSW
Tool Rotational Speed	TRS
Tungsten Inert Gas welding,	TIG
Standard Deviation	SD
Standard Error	SE
Confidence Interval	CI
Tool Tilt Angle	TTA
Metal Inert Gas welding	MIG
Ultimate Tensile Strength	UTS
Stir Zone	SZ
Thermo-Mechanically Affected zone	TMAZ
Traverse Speed	TS
Dynamic Recrystallization	DRX
The discontinuous DRX	DDRX
Scanning Electron Microscope	SEM
Advancing Side	AS
Retreating side	RS
Severe plastic deformation	SPD
Gas Tungsten Arc Welding	GTAW
Gas Metal Arc Welding	GMAW
Signal to Noice Ratio	SNR

CHAPTER 1

1. Introduction

1.1 Overview

Welding is a globally recognized method used for joining two metal pieces through the application of pressure and heat to create a permanent joint that behaves as a single entity. This process is critical in producing joints that can achieve superior structural strength properties, often surpassing those of the individual components being joined [1, 2]. The primary motivation behind welding is to create robust and durable joints. Employing suitable welding techniques will achieve joints with exceptional tensile properties, ensuring the longevity and reliability of the structures. Welding has become a pivotal process in various industries due to its material efficiency and relatively low production costs. Welding is a fundamental process that has evolved significantly to meet the demands of modern industry. The focus on aluminum and the progress of advanced welding techniques, i.e., FSW, have revolutionized the field, enabling the production of high-strength, durable, and efficient joints. As industries continue to seek improvements in material efficiency and production costs, welding remains a critical technology driving innovation and growth [3].

Welding aluminum and Mg-Alloys is a critical process in modern manufacturing, where the exceptional properties of these materials—such as high strength-to-weight ratios and good electrical, thermal, and corrosion resistance —are highly valued. Despite their desirable characteristics, both aluminum and magnesium present unique properties in welding due to their physical properties and chemical composition. Aluminum, for instance, has a high thermal conductivity and a low melting point, which can lead to issues like warping and excessive heat input during welding. It also forms a tenacious oxide layer that must be meticulously cleaned prior to welding to avoid defects. Common welding methods for aluminum include TIG welding and MIG welding, both of which require careful control of heat input and shielding gas to prevent contamination and ensure weld integrity [4, 5].

Mg-Alloys, on the other hand, are even lighter than aluminum, making them ideal for weight-sensitive applications. However, magnesium is highly reactive and has a lower

melting point, which makes it prone to burn-through and other welding defects. It also forms a brittle oxide layer that complicates the welding process. Techniques such as TIG and MIG are commonly employed for welding magnesium, but they require special considerations like pre-weld cleaning and the use of flux or inert gases to protect the weld bead from a corrosive atmosphere. Additionally, solid-state welding processes, such as FSW, are increasingly being utilized for both aluminum and Mg-Alloys due to their excellent metallurgical properties of the welded joints. FSW, in particular, generates frictional heat to soften the materials without melting them, resulting in superior mechanical properties and reduced residual stresses [6].

Another significant challenge in welding these alloys is their susceptibility to cracking and porosity. Light metal alloys are disposed to hot cracking due to their wide solidification temperature range, while Mg-Alloys can suffer from both solidification and liquation cracking [7]. To mitigate these issues, careful selection of filler materials and welding parameters is essential. For instance, using fillers can help to reduce thermal stresses and minimize cracking.

In addition to traditional and solid-state welding methods, advanced techniques like laser welding and hybrid welding processes are also being explored to improve the weld quality of aluminum and Mg-Alloys. These methods control heat input and can achieve high TS, making them suitable for high-volume production environments [8]. The ongoing development of these technologies aims to address the challenges associated with welding aluminum and magnesium, enabling the production of lighter, stronger, and more durable components. In summary, welding aluminum and Mg-Alloys is a complex yet essential process that requires specialized techniques and meticulous control to overcome the inherent challenges and leverage the full potential of these alloys in advanced engineering applications.

1.2 Friction stir welding (FSW)

FSW is a solid-state joining process that utilizes a non-consumable tool to generate frictional heat and plastic deformation at the joint line. The primary components involved in FSW are the rotating tool, consisting of a shoulder and a pin, and the workpieces to be joined. The FSW tool, with a specially designed pin, is inserted into the material at the joint line. The tool then begins to rotate at a controlled speed. As the tool rotates and traverses along the joint, frictional heat is generated between the

tool and the workpiece demonstrated in Fig. 1.1. This heat softens the material without melting it. The softened material undergoes plastic deformation due to the mechanical stirring action of the rotating tool. The tool's pin stirs the material from the front of the tool to the back, creating a mix of materials from both workpieces. The tool traverses along the length of the joint line, continuously generating heat and causing plastic deformation [9]. The shoulder of the tool applies downward force, consolidating the stirred material and forging the joint. As the tool moves forward, the material behind the tool cools and solidifies, forming a solid-phase bond between the workpieces. The weld nugget, or stir zone (SZ), is characterized by a fine-grained microstructure due to dynamic recrystallization. After the tool has passed, the material continues to cool, solidifying the joint with a refined microstructure. The resulting weld is strong and free from defects[10]. FSW is highly effective for joining materials with different properties and is widely used in industries requiring high-strength, defect-free joints. Process parameters, such as TRS, TS, and axial force, are critical to achieving the desired weld quality [11].

One of the primary advantages of FSW over traditional fusion welding techniques is its ability to join materials that are otherwise considered unweldable due to their propensity for cracking and porosity when melted, such as aluminum and Mg alloys. FSW not only enhances mechanical properties by producing a fine-grained microstructure in the weld zone but also minimizes distortion and residual stresses, leading to improved fatigue performance. The absence of a melting phase in FSW reduces the risk of defects, which is common in conventional welding methods. Additionally, the process parameters, including tool design, TRS, and TS, can be precisely controlled to tailor the weld characteristics. As research and development in FSW technology continue to advance, its application scope is broadening, with ongoing innovations aimed at improving tool materials, process monitoring, and real-time quality control [12]. In summary, FSW stands out as a transformative technique for the efficient and reliable joining of aluminum and Mg alloys, offering significant advantages in terms of mechanical performance, environmental impact, and industrial scalability. Magnesium alloys, like AZ31, AZ91D, and WE43, are prized in the aerospace and automotive sectors for high strength-to-weight ratio. With a density of approximately 1.8 g/cm^3, they are significantly lighter than aluminum alloys. AZ91D (9% aluminum, 1% zinc) and WE43 (4% yttrium, 3% rare earth elements) are common types [13]. Their physical properties include good machinability, corrosion

resistance, and high thermal conductivity. FSW enhances these properties by creating strong, defect-free joints without melting, preserving the alloys' inherent strengths and minimizing distortion [14, 15].

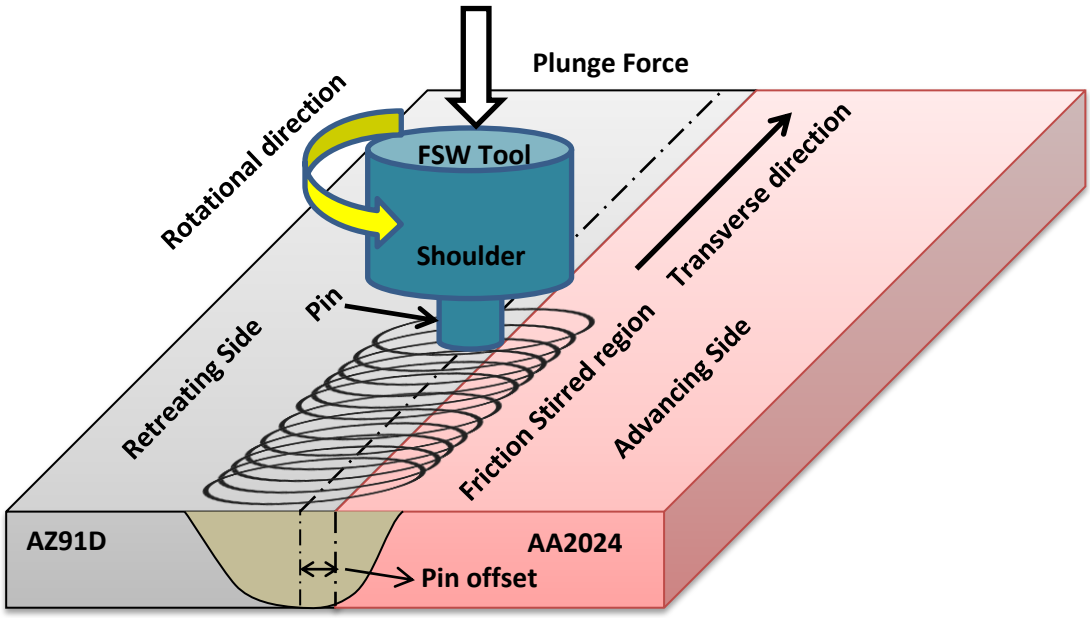

Figure 1.1: Process principle of FSW

Mg and Al materials have good thermal and electrical conductivity and are helpful for thermal and electrical applications. Some typical applications are condenser foil windings, heat exchanger tubes, Electrical connectors, transformers, capacitors, refrigeration tubes, tube sheets, etc [16, 17]. Butt joints and lap joints are two types of joints used in metalworking and welding. Both joints are used to connect two pieces of metal, but they differ in their design and application [18]. A butt joint is a joint where the two pieces of metal are placed end-to-end and welded or bolted together. This type of joint is commonly used for joining thin sheets of metal that are of similar thickness. However, it can also be used to join thicker materials, although additional reinforcement may be required. A lap joint, where the two pieces of metal overlap each other and are welded or bolted together. This type of joint is commonly used for joining thicker materials or when additional strength is required. Lap joints can also be used to join materials of varying thicknesses, as the overlap can be adjusted to accommodate different thicknesses [18-21]. When it comes to joining materials of various thicknesses, both butt and lap joints can be used. However, a lap joint is

generally preferred as it provides greater strength and can better accommodate the differences in thickness.

Additionally, lap joints can be designed to distribute the load across the joint, reducing stress and preventing failure. Overall, the choice of joint and method of joining will depend on the specific application and the materials being used. The rotational motion of the tool softens the material, making it pliable enough to join [22-27]. The probe then moves through the joint, pushing and mixing the softened material from both workpieces together. Fig. 1.2 illustrates the fundamental working concept of the dissimilar FSW technology. As the tool is removed, the material behind it cools and solidifies, forming a strong joint. There are four basic steps in FSW.

1.2.1 Plunging

The plunging phase in FSW is a crucial initial step where the rotating tool is inserted into the base plates to generate the necessary frictional heat. This process begins with the precise alignment and positioning of the tool at the weld joint. As the tool starts rotating, it is gradually lowered until the pin makes contact with the material's surface, generating localized heating and softening the material. The tool continues to penetrate till the shoulder engages with the plate surface, significantly increasing the heat generation and plasticizing the material around the pin. The tool is then momentarily held in place to stabilize the temperature and ensure uniform heat distribution before it begins to traverse along the joint line. Throughout this phase, careful control of parameters, i.e., TRS, plunge rate, and axial force, is essential to optimize material flow and heat generation, setting the stage for a high-quality, defect-free weld.

1.2.2 Dwelling

The dwelling phase in FSW is a critical step that follows the plunging phase, where the rotating tool, fully engaged with the material, is held stationary for a brief period. This phase ensures the material adequately softened and plasticized by maintaining consistent frictional heat generation. During dwelling, the tool remains at a constant depth, allowing heat to evenly distribute through the material, eliminating temperature

gradients that could lead to weld defects. This uniform heating enhances the material's plasticity, ensuring a stable and continuous weld formation when the tool begins to move along the welding line. The dwelling phase is essential for achieving optimal weld quality, as it helps in homogenizing the material, reducing internal stresses, and minimizing defects. Good control of the dwelling duration and tool parameters during this phase is crucial for ensuring a strong, defect-free weld with desirable mechanical properties.

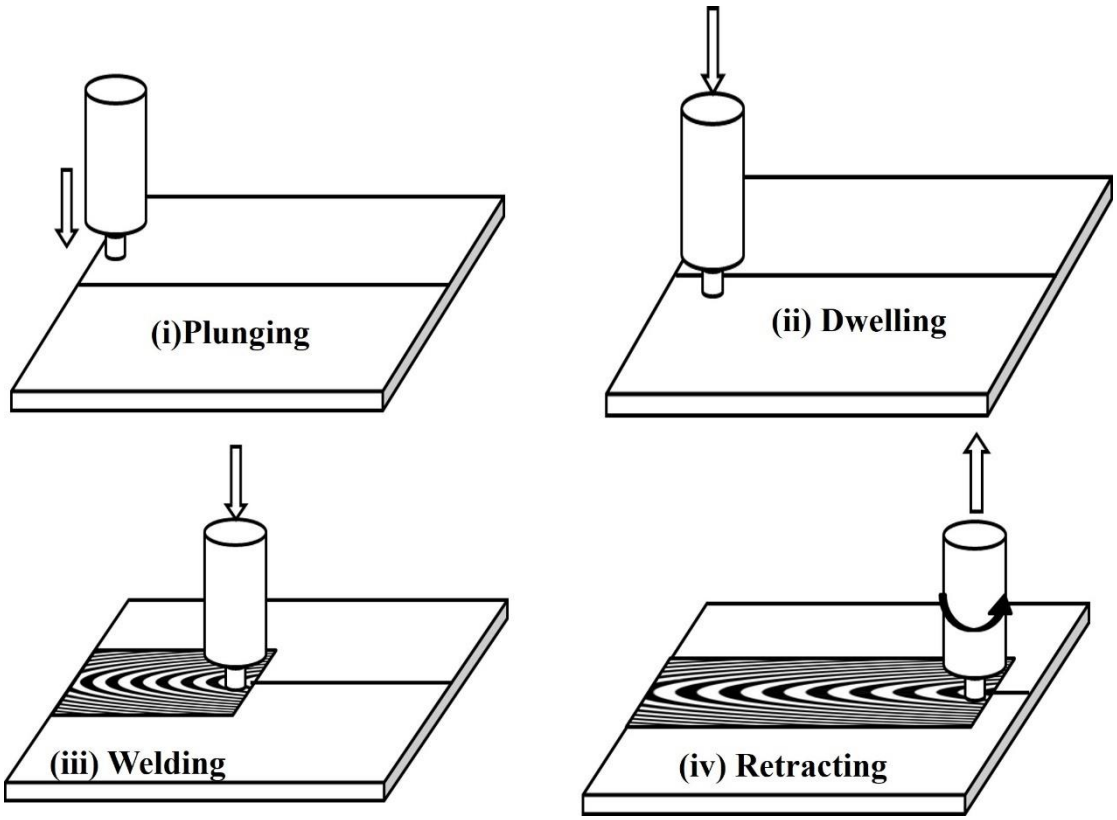

Figure 1.2: Different steps involve in FSW

1.2.3 Welding process

After the dwelling phase in FSW, the tool transitions into the welding stage, where it moves along the welding line. During this phase, the rotating tool moves along the path previously prepared by the plunging and dwelling stages. The primary objective is to forge and consolidate the softened material within the weld zone. As the tool travels, the shoulder of the tool applies pressure to the plasticized material, creating a bond between the workpieces. The rotational motion of the FSW tool helps in mixing the base materials across the joint, promoting metallurgic bonding below the melting point. This solid-state joining method results in an equiaxed and refined grain

structure in the weld zone, which typically exhibits superior mechanical properties than traditional fusion welding methods. The controlled input heat and mechanical action of FSW contribute to reduced distortion and minimized residual stresses in the welded material. Throughout the welding phase, precise control of parameters to maintain weld integrity and achieve consistent quality. The post-dwelling and welding phases in FSW collectively ensure a robust and defect-free weld, making this technique particularly advantageous for joining aluminum, magnesium, and other challenging materials in various industrial applications.

1.2.4 Retracting

The retracting phase in FSW occurs after the tool completes the welding pass. This phase involves the withdrawal of the rotating tool from the welded material. Retracting is a critical step to disengage the tool from the workpieces while minimizing any potential defects or damage to the newly formed weld. During retracting, the TRS of the tool is typically reduced to a lower level compared to the welding phase. This reduction helps in gradually disengaging the tool from the welded material without abruptly disrupting the metallurgical bond or causing excessive mechanical stress. The retracting speed is controlled to ensure a smooth and uniform withdrawal of the tool.

As the tool is retracted, any excess material displaced during the welding process is typically smoothed out and consolidated behind the tool's shoulder. This consolidation helps in refining the microstructure of the weld and ensuring uniformity across the joint. Additionally, the controlled retraction phase allows the welded area to cool gradually, which contributes to reducing residual stresses and enhancing the metallurgical characteristics of the weldments.

Proper execution of the retracting phase in FSW is essential for achieving a high-quality weld with optimal strength, durability, and integrity. It complements the preceding phases of plunging, dwelling, and welding by ensuring that the entire welding process concludes smoothly and efficiently, meeting the stringent requirements of various industrial applications where FSW is utilized.

1.3 FSW tool materials

The rotating tool used in FSW is able to endure high temperatures and pressures, as well as provide the necessary frictional force to stir the materials being welded. Therefore, the material selection for FSW tools is critical to confirm the durability and quality of the welded joints. The most general materials used for FSW tools are:

1.3.1 Tool steel H13

H13 tool steel is commonly used in FSW due to its advantageous combination of properties that make it suitable for light metal alloys. H13 offers high toughness, hardness, and thermal conductivity, which are essential for withstanding the abrasive wear and high temperatures encountered during FSW. Its toughness helps in resisting mechanical stresses and impacts during the welding process, while its high hardness ensures prolonged tool life by minimizing wear. The good thermal conductivity of H13 aids in efficiently dissipating heat away from the welded zone, contributing to temperature control. Moreover, H13 is relatively cost-effective compared to other tool materials, making it a practical choice for industrial applications.

1.3.2 Tungsten Carbide (WC) tool

WC tools are widely preferred for FSW due to several key advantageous properties that cater specifically to the demands of this advanced welding technique. Firstly, WC is renowned for its exceptional hardness, ranking among the hardest materials available. This hardness enables WC tools to withstand the severe abrasion and wear encountered during FSW, particularly when welding high-strength alloys and composite materials. The durability of WC tools translates into extended tool life, reducing downtime for tool changes and maintenance, which is crucial for industrial applications requiring continuous operation and high productivity.

Moreover, Tungsten Carbide exhibits high thermal conductivity, aiding in effective heat dissipation from the weld zone. This property helps to control temperatures during welding, minimizing thermal distortion and ensuring consistent weld quality. The combination of high hardness and thermal conductivity makes WC tools well-

suited for handling the intense frictional heat generated during FSW without compromising on performance or durability.

Additionally, WC tools typically possess low coefficients of friction, facilitating smooth material flow and enhancing the joint efficiency. This attribute contributes to the fabrication of defect free welded joints with high tensile strength.

Furthermore, WC tools are capable of maintaining dimensional stability under high temperatures, ensuring precise control of the welding parameters and achieving consistent weld quality. While Tungsten Carbide tools offer numerous benefits for FSW, including durability, thermal management, and performance reliability, their use requires careful consideration of operational parameters to optimize performance and mitigate potential challenges. Overall, the unique combination of hardness, thermal conductivity, and frictional characteristics makes Tungsten Carbide an ideal choice for attaining high-quality welds in challenging materials and demanding industrial environments.

1.3.3 Polycrystalline cubic Boron Nitride (PCBN) tool

PCBN tools are selected for FSW primarily due to their exceptional thermal stability, hardness, and wear resistance, which are crucial for effectively processing high-strength materials and achieving high-quality welds. PCBN is one of the hardest materials known, second only to diamond, making it highly resistant to abrasive wear and deformation during the intense frictional and mechanical forces experienced in FSW. This inherent hardness enables PCBN tools to maintain sharp cutting edges and withstand prolonged use without significant wear, thereby ensuring extended tool life and reducing downtime for tool changes in industrial applications. PCBN tools exhibit excellent thermal conductivity, which plays a critical role in FSW by efficiently dissipating heat away from the weld zone. This property helps in controlling temperatures during welding, minimizing thermal distortion of the workpieces, and ensuring consistent weld quality. The combination of high hardness and thermal stability allows PCBN tools to operate effectively at high temperatures, maintaining dimensional accuracy and achieving precise control over the welding parameters. PCBN tools offer low coefficients of friction, facilitating smooth heat transfer flow and minimizing the welding defect. This attribute contributes to the production of high-integrity welds with superior mechanical properties, including enhanced strength

and fatigue resistance. PCBN tools are also known for their chemical inertness and resistance to corrosion, which further enhances their suitability for welding of light metal alloys. While PCBN tools offer significant advantages in terms of hardness, thermal conductivity, and wear resistance for FSW, their use requires careful consideration of operating parameters to optimize performance and ensure consistent weld quality. Overall, the exceptional properties of PCBN make it a preferred choice for achieving reliable and high-performance welds in challenging materials and demanding industrial applications.

1.3.4 Composite tool

Composite tools used in FSW integrate multiple materials to capitalize on their individual strengths, enhancing the tool's overall performance and longevity. These tools typically feature a base material, often steel or other high-strength alloys, embedded with hard particles such as tungsten carbide (WC), ceramics like alumina, or other reinforcing agents. The combination of materials in composite tools provides several advantages crucial for FSW applications. Firstly, embedded hard particles significantly bolster wear resistance, crucial for withstanding the abrasive forces and high temperatures generated during FSW. This extends tool lifespan and minimizes the need for frequent replacements, thereby optimizing operational efficiency and reducing costs. Secondly, the tailored thermal conductivity of composite tools helps manage heat distribution during welding, ensuring uniform material flow and reducing thermal distortion in the welded components. Additionally, composite tools can be customized to meet specific welding requirements, adapting to different material compositions and operational conditions with precision. Despite potentially higher initial costs, composite tools deliver substantial long-term benefits through enhanced durability, versatility, and performance consistency in achieving high-quality welds across diverse industrial sectors such as aerospace, automotive, and marine engineering.

1.4 FSW tools design

The design of the tools used in FSW is essential for defect-free joints. The primary components of the tool include the shoulder and the pin (or probe). The shoulder

produces frictional heat and contains the softened material, while the pin facilitates the stirring and mixing of the materials being welded. The pin geometry is very crucial in determining the weld quality, with many profiles, i.e., triangular, square, circular, and threaded circular, each offering distinct advantages. Cylindrical pins are known for their simplicity and ease of fabrication, providing a good balance of heat generation and material flow. Triangular pins enhance mechanical interlocking and material mixing due to their sharp corners, resulting in superior joint strength. Rectangular pins, on the other hand, increase the surface area for frictional heat generation, leading to improved plastic deformation. The choice of pin profile, along with other factors like tool material and TRS, must be wisely measured to optimize the welding parameters for different material combinations and thicknesses.

1.4.1 Design of FSW tool's Shoulder

The shoulder design in FSW tools is critical to the process's success, influencing material flow, heat generation, and overall joint quality. Typically, FSW tool shoulders are crafted with a flat or slightly concave surface that interacts directly with the workpieces during welding. This design serves several essential functions: it facilitates the generation of frictional heat, effectively softening the material without melting it. The shoulder also applies pressure to the plasticized material, promoting its consolidation and ensuring uniformity across the weld zone. The shape and size of the shoulder govern the total heat generated and the pressure exerted on the material, directly impacting the weld's integrity and strength. Advanced designs may incorporate features such as cooling channels within the shoulder to manage temperatures and prevent overheating, which is crucial for maintaining consistent weld quality in different materials. In essence, the shoulder design of an FSW tool is pivotal in controlling the welding parameters to achieve reliable, high-quality welds across various materials and operational conditions.

1.4.1.1 Concave shoulder

This shoulder design influences the joint efficiency. Among various shoulder designs, the concave shoulder stands out for its unique advantages. A concave shoulder features a recessed surface that helps to consolidate and trap the plasticized material

more effectively during FSW. This design enhances the downward forging action, ensuring better connection between the base plate and rotating tool, which results in improved material flow and distribution. The concave profile also aids in directing the material flow towards the pin, reducing the surface defects and enhancing the joint efficiency. Additionally, the concave shoulder can contribute to lower welding forces, making it easier to maintain the stability of the welding process. This design is particularly beneficial when welding materials with high thermal conductivity or when working with thinner sheets, as it provides better control over the process parameters to achieve the high-quality joints.

1.4.1.2 Convex Shoulder

In FSW, the design of the convex shoulder is a pivotal element that greatly affects the weld quality. The convex shoulder, characterized by its outwardly curved surface, offers distinct benefits in specific welding scenarios. Unlike concave shoulders, convex shoulders exert higher forging pressure on the workpiece, which can enhance the consolidation of the plasticized material and ensure deeper penetration of the pin into the workpieces. This results in a more homogeneous mixing of the materials being welded. The elevated pressure also helps in minimizing voids and defects, leading to stronger and more reliable welds. Convex shoulders are particularly advantageous when welding thicker materials, as they can handle higher loads and generate more heat through increased contact area. Additionally, the convex profile assists in directing the plasticized material downward and away from the tool, reducing the occurrence of surface flash and ensuring a cleaner weld surface. This design is essential for achieving high-quality welds in challenging conditions, making it a versatile choice in the FSW tool design arsenal.

1.4.1.3 Pin Design

The pin, or probe, design is a fundamental characteristic that significantly influences the welding process and the quality of the final weld. The pin, which extends from the shoulder into the workpiece, is responsible for generating heat through friction and mechanically stirring the materials to create a solid-state joint. Several pin profiles offer distinct advantages and are chosen based on the specific welding requirements.

Cylindrical pins are the simplest in design and are known for their ease of fabrication and balanced performance, providing adequate heat generation and material flow. Triangular pins, with their sharp edges, enhance mechanical interlocking and improve the stirring action, leading to superior joint strength and material mixing. Rectangular pins, with their increased surface area, generate more frictional heat and facilitate better plastic deformation, which is particularly useful for welding thicker materials. The pin's length, diameter, and thread design are also critical factors that affect the weld quality, influencing parameters and the formation of defects. Proper pin design is essential for optimizing the welding process, ensuring efficient material mixing, and achieving high-quality welds across different material combinations and thicknesses.

1.4.1.4 Round bottom cylindrical pin (RBCP)

RBCP is a specialized tool design that plays a crucial role in achieving high-quality welds across a variety of materials and thicknesses. This pin design features a smooth, rounded bottom that facilitates uniform heat dissemination during the FSW. The round bottom shape reduces the likelihood of material entrapment and promotes consistent plastic deformation, ensuring a homogenous mixing of the materials being welded. One of the key advantages of the round bottom cylindrical pin is its ability to generate sufficient frictional heat while maintaining a stable welding process. This promotes the softening and plasticizing the base materials, facilitating easy movement and effective joining without causing excessive stirring or material expulsion. The smooth curvature of the pin also contributes to reducing the surface defects, resulting in cleaner welds with improved aesthetic appearance. Additionally, the round bottom cylindrical pin is particularly effective in welding thin materials or when working with alloys that are sensitive to heat input. Its design allows for precise control over welding parameters, ensuring consistent weld quality and mechanical characteristics across the joint. Overall, the round bottom cylindrical pin exemplifies an important tool design choice in FSW, offering versatility and reliability in achieving strong, defect-free welds in diverse welding applications.

Figure 1.3: Design of RBCP [18]

1.4.1.5 Flat bottom cylindrical pin (FBCP)

FBCP represents a specialized tool design for achieving precise and controlled welds across a wide range of materials and thicknesses. Unlike other pin designs, the flat bottom cylindrical pin features a flat, smooth surface at its bottom. This design minimizes material displacement and ensures consistent plastic deformation, leading to strong and reliable weld joints. One of the primary advantages of the FBCP is its ability to maintain stable welding conditions while providing effective heat generation. The flat surface promotes even pressure distribution and adequate contact with the base plate, enhancing the consolidation of the softened material around the pin. This results in improved joint strength and reduced porosity, contributing to superior joint efficiency. The design of the flat bottom cylindrical pin is particularly beneficial in applications where precise control over welding parameters is essential. It allows for optimized material flow, thereby minimizing the defects risk. Additionally, this pin design is well-suited for welding materials with varying thermal conductivity or thickness, offering versatility and reliability in achieving consistent weld quality. Overall, the flat bottom cylindrical pin stands as a critical component in FSW tool design, providing engineers and welders with a reliable solution to produce high joint efficiency and performance across diverse industrial applications.

Figure 1.4: Design of flat bottom cylindrical pin [18]

1.4.1.6 Truncated cone pin

The truncated cone pin represents a sophisticated tool design renowned for its ability to achieve precise and efficient welds across a spectrum of materials and thicknesses. This pin design features a conical shape with a flattened or truncated end, combining the advantages of both cylindrical and conical pins.

Figure 1.5: Design of truncated cone pin [18]

The tapered profile of the truncated cone pin facilitates enhanced material mixing and flow, promoting uniform heat distribution during the FSW. One of the distinctive advantages of the truncated cone pin lies in its capability to effectively manage heat generation and material displacement. The conical taper allows for gradual plasticization of the material as the pin moves through the workpiece, ensuring thorough mixing without excessive stirring or disruption. This results in weld joints with improved mechanical properties and reduced welding defects. The design versatility of the truncated cone pin makes it particularly suitable for welding applications where varying material thicknesses or compositions are involved.

Additionally, the tapered geometry of the pin facilitates smoother entry and exit from the workpiece, minimizing tool wear and extending tool life. In essence, the truncated cone pin stands as a pivotal innovation in FSW tool design, embodying precision, efficiency, and reliability in achieving high-quality welds across diverse industrial applications. Its unique profile underscores its importance as a key component for engineers and welders seeking superior performance and consistency in friction stir welding operations.

1.4.1.7 Thread less pin

Threadless pins in Friction Stir Welding (FSW) represent an innovative approach to tool design that enhances the efficiency and reliability of the welding process. Unlike threaded pins, which feature helical grooves designed to channel and mix materials during welding, threadless pins are characterized by a smooth surface without any external threading. This design simplifies the fabrication process and eliminates potential complications associated with thread wear or damage during prolonged use. The absence of threads on threadless pins contributes to several advantages in FSW operations. This results in cleaner weld surfaces and improved aesthetic appearance of the joints. Secondly, the smooth surface of threadless pins facilitates easier removal from the completed weld, minimizing the risk of tool marks or damage to the workpiece. Moreover, threadless pins offer enhanced versatility in welding various materials and thicknesses. Their uniform surface ensures consistent heat distribution and plastic deformation, which are crucial for achieving strong and durable weld joints.

Figure 1.6: Design of thread less pin [18]

1.5 Effect of Processing parameter of FSW

The FSW process, widely recognized for its effectiveness in joining lightweight materials, is significantly influenced by various process parameters (i.e. TRS, TS, TTA, and axial force). Adjustments in these parameters can lead to substantial variations in grain size, UTS, micro hardness, and overall joint integrity. The effect of process parameters on FSW is essential for optimizing welding conditions and achieving superior weld quality, particularly in challenging materials like aluminum and magnesium alloys. This study aims to explore these relationships, providing insights into the optimization of FSW parameters to enhance weld performance.

1.5.1 Rotational tool speed

The TRS of the tool in FSW significantly influences the characteristics and weld quality. TRS determines the heat input and the mechanical agitation applied to the workpieces during welding, which in turn affects the metallurgical properties, and defect formation in the weld joints.

At lower TRS, a low frictional heat generated, this can lead to insufficient plasticization of the material, potentially resulting in inadequate bonding between the workpieces and a weaker weld joint. Conversely, excessively high TRS can cause excessive frictional heat, leading to material overheating and potential defects such as burn-through or excessive tool wear. Optimal TRS selection is crucial for achieving

desirable weld characteristics. It promotes effective material plasticization and mixing without causing thermal degradation or excessive wear on the tool. Properly chosen TRS enhance the formation of a homogeneous microstructure in the welded zone, contributing to improved mechanical properties.

Moreover, the TRS influences the flow dynamics of the material around the tool, affecting the uniformity and smoothness of the weld bead. A controlled TRS helps maintain consistent material flow and ensures uniform distribution of alloying elements within the weld, minimizing the formation of welding and lack of fusion.

1.5.2 Tool TS

The TS in FSW significantly impacts the quality and characteristics of weld joints, supported by empirical data across various studies. Research indicates that lower TS generally led to higher heat input and longer dwell times in the weld zone. For instance, studies have shown that reducing TS from higher to lower values can increase the heat input by up to 30%, resulting in enhanced material flow and better consolidation of the weld material. This extended exposure to frictional heat allows for more thorough mixing of the alloying elements, contributing to a refined microstructure with improved mechanical properties. While higher TS reduce the input heat and dwell time, which can lead to less effective material plasticization and mixing. This reduction in heat input and dwell time may result in shallower penetration depths and potentially weaker bonding between the workpieces. For example, data from experimental studies have demonstrated that increasing TS beyond optimal ranges can lead to decreased joint strength. Overall, optimizing TS is crucial in FSW to achieve weld joints with desirable properties. This involves balancing heat input, material flow dynamics, and mechanical requirements to ensure consistent and high-quality welds across different materials and applications. Statically supported findings underscore the importance of precise control over TS in maximizing weld quality and performance in industrial settings.

1.5.3 Tool Tilt Angle (TTA)

The TTA in FSW exerts a profound influence on weld joint characteristics, backed by empirical data illustrating its impact on weld quality and mechanical properties.

Studies have shown that variations in TTA significantly alter material flow dynamics and heat distribution during FSW. For instance, increasing the tilt angle from 0° to optimal values (typically between 1° to 3°) enhances material consolidation and promotes more uniform plasticized material distribution around the tool. This results in a refined microstructure within the welded area, leading to improved UTS and fatigue resistance of the joints. Conversely, excessive tilt angles can disrupt material flow patterns, leading to irregular mixing and potential defects in the weld. Data from experimental studies highlight that deviations from optimal tilt angles can lead to reduced joint strength and increased susceptibility to defects. For example, research has shown that deviations beyond recommended ranges can significantly impact joint integrity, with even small variations in tilt angle affecting weld quality.

Overall, optimizing the TTA is critical in FSW to achieve consistent and high-quality welds across various materials and applications. The numerical data underscores the importance of precise tilt angle control in enhancing weld performance and reliability, emphasizing the need for careful adjustment to maximize the benefits of this parameter in industrial welding processes.

1.5.4 Effect of Tool pin profile

The role of pin profile in the FSW determining the characteristics and weld quality, supported by empirical data highlighting its influence on weld properties. The different shapes of pin profile protruding part of the FSW tool that interacts directly with the workpiece material during welding.

Research has shown that variations in pin profile, including diameter, shoulder angle, and thread configuration, significantly impact the plasticization during FSW. For instance, studies have demonstrated that increasing the pin diameter can lead to deeper penetration into the material, enhancing bond strength and improving mechanical properties such as joint UTS. Numerical data often shows that smaller pin diameters, which exert less plastic deformation, tend to produce welds with lower UTS and reduced elongation compared to larger pin profiles.

Moreover, the pin shape affects the stirring action and heat generation within the weld zone. For example, pins with tapered profiles or threaded designs can facilitate better material mixing and expulsion of trapped gases, resulting in more uniform welds with fewer defects. Empirical studies have illustrated that optimizing pin profile

parameters can lead to significant improvements in weld quality and performance across a range of materials, including Al-alloys, steels, and titanium alloys.

Table 1.1: Influence of input parameters in FSW

S. No	Parameters	Effect	Ref
1	TRS	FSW's high tool rotation speed results in good UTS of the weldment, oxide layer breaking, frictional heat, stirring, and good mixing of material.	[26]
2	TS	Increasing the TS, decreased frictional heat and hence produced to inferior input heat input.	[27]
3	TA	The tool TTA may affect the material flow and heat generation during the weld; the friction generates the plastic dissipation and heat occur in FSW.	[28]

1.5.5 Axial force

The axial force, refers to the force applied in the direction perpendicular to the welding surface during FSW. The axial force applied during FSW affects the heat generation in the welding zone. It helps to maintain contact between the base plate and the rotating tool and the workpiece, ensuring effective frictional heating. It promotes plastic deformation and assists in the mixing of material between the AS and RS of the weldments. The applied force helps in breaking down the metal's crystalline structure, facilitating grain refinement and producing a sound weld.

1.5.6 Tool geometry

The tool geometry, including its shape, dimensions, and features is very important in FSW. The diameter of the shoulder affects the material flows and heat transfers during welding. A higher heat and better material mixing is generated in larger shoulder diameter. The thread profile of the pin determines the material stirring and mixing characteristics. Different pin geometries may influence the heat distribution, and defect formation. For example, tapered or threaded pins may enhance material mixing compared to cylindrical pins. The choice of tool material affects the

durability, heat transfer, and frictional properties during welding. Tool materials with good wear resistance and thermal conductivity are typically preferred.

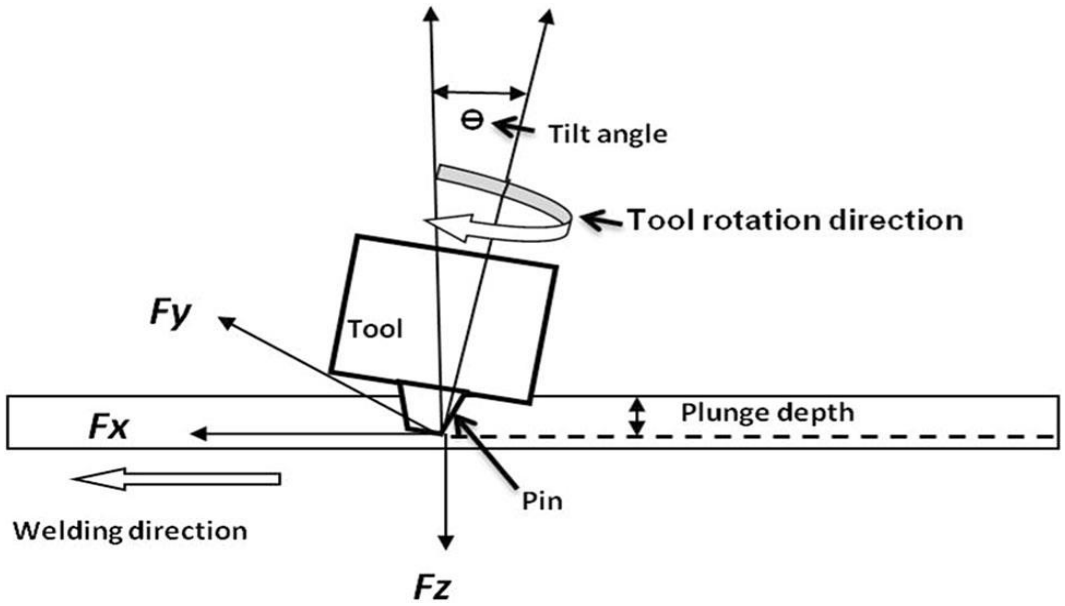

Figure 1.7: Schematic diagram for main process parameters of FSW

1.5.7 Plunge Depth

The plunge depth in FSW affect the weld quality and joint efficiency. It refers to the depth to which the tool pin penetrates the workpiece, typically ranging between 80-95% of the workpiece thickness demonstrated in Fig. 1.7. For example, in welding a 5 mm thick aluminum plate, the plunge depth would typically be between 4 and 4.75 mm. This depth ensures sufficient material deformation and heat generation, which are critical for achieving a defect-free weld. If the plunge depth is too shallow, it may lead to incomplete joint penetration and weak bonding. It can cause excessive heat input, resulting in defects like flash formation and tool wear. Precise control of plunge depth is essential for optimizing the welding process, ensuring adequate material mixing, and achieving the desired mechanical properties in the welded joint. This study examines the optimal parameters for superior weld quality.

1.6 Different types of FSW zones

FSW creates distinct zones within the welded joint, each characterized by unique microstructural and mechanical properties. The SZ, located at the center of the weld,

experiences the highest degree of plastic deformation and heat, resulting in a fine, equiaxed grain structure due to DRX. Surrounding the SZ is the TMAZ, where the material undergoes both thermal and mechanical influences but to a lesser extent than the SZ, leading to elongated grains [29]. Adjacent to the TMAZ is the HAZ, which is exposed to elevated temperatures but does not experience plastic deformation, causing changes in the material properties without significant grain deformation. Finally, the base metal remains unaffected by the welding process and retains its original microstructure and properties. Understanding these zones is critical for optimizing FSW parameters to achieve desired weld quality and performance. This study focuses on analyzing the characteristics of these zones, providing insights into their formation and the resulting mechanical properties of the weld [30].

1.6.1 Stir zone (SZ)

The SZ in FSW is the central region of the weld joint where the FSW tool interacts directly with the workpieces. This zone is characterized by intense mechanical stirring and frictional heat generation caused by the rotating FSW tool. When the tool travels along the welding path, it plunges into the base plate, creating severe plastic deformation. This deformation leads to DRX, where the original grain structure of the material is broken down and reformed into a refined, equiaxed grain structure within the SZ. The SZ typically exhibits a fine-grained microstructure that is smaller and more uniform than the parents' metals [31]. This microstructural refinement enhances the tensile properties of the weld joint, including increased UTS, microhardness, and fatigue resistance. The mixing of material from both workpieces without melting, resulting in a homogenized bond between the surfaces being joined. As a result, the SZ in FSW offers advantages in producing high-strength, defect-free welds suitable for applications in aerospace, automotive, marine, and other industries where superior joint integrity and performance are critical.

1.6.2 Thermo-mechanically affected zone (TMAZ)

TMAZ is the adjacent zone of SZ and is characterized by significant but less intense mechanical and thermal effects compared to the SZ. In the TMAZ, the material undergoes mechanical deformation and thermal cycles due to the heat and pressure

exerted by the FSW tool. While the TMAZ temperature is lower than the SZ, it still experiences heating close to or below the material's melting point, leading to softening, grain growth, and grain structure changes [32]. Different types of FSWed zone are demonstrated in Fig. 1.8.

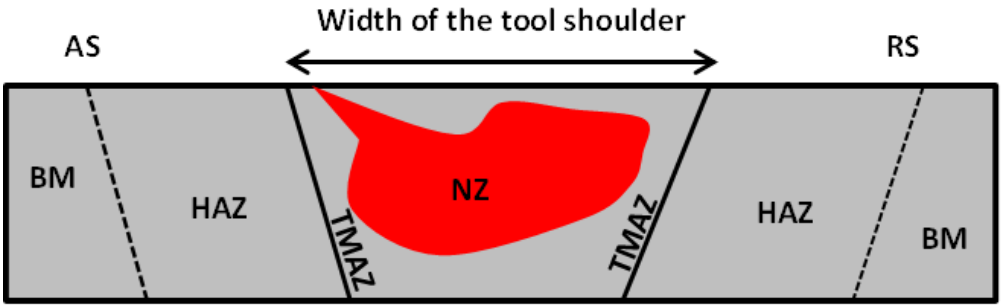

Figure 1.8: Different zones in FSW

The mechanical deformation in the TMAZ results in localized plasticity and strain hardening effects, which alter the material's properties than the parents' material. Depending on the FSW parameters and the specific alloy composition, the TMAZ may exhibit varying degrees of grain refinement or coarsening, as well as changes in hardness and residual stresses. These microstructural alterations can affect the overall mechanical performance and joint efficiency [33]. The width and characteristics of the TMAZ are influenced by factors such as the TRS, TS, and the material properties of the workpieces. By carefully managing the thermal and mechanical effects in the TMAZ, engineers and manufacturers can ensure consistent and reliable performance of friction stir welded components in sectors ranging from aerospace and automotive to shipbuilding and structural engineering [34].

1.6.3 Heat affected zone (HAZ)

The HAZ in FSW is a critical area that undergoes significant thermal exposure but remains free from the plastic deformation experienced in other regions of the weld. The HAZ, adjacent to the TMAZ and SZ, significantly influences the mechanical properties of the welded joint, with changes primarily due to the thermal cycle rather than the severe plastic deformation and DRX seen in the SZ [35].

In the HAZ, the material is exposed to elevated temperatures sufficient to alter its microstructure, yet insufficient to cause plastic deformation or recrystallization. As a result, the grains within the HAZ often become coarser compared to the base metal. This coarse grain structure is a direct consequence of the thermal exposure, which facilitates grain growth but does not induce the mechanical stirring and deformation seen in the SZ. The extent of this grain growth and the resultant mechanical properties depend on the peak temperatures reached and the duration of thermal exposure [36]. The presence of coarse grains in the HAZ can lead to a decrease in joints efficiency, making it a potential site for the initiation of failure under mechanical loads. Additionally, the microstructural changes in the HAZ can affect its corrosion resistance, which is particularly important for light meta materials used in aerospace and automotive industries. Understanding the transformations within the HAZ is essential for optimizing FSW parameters to minimize adverse effects and enhance the performance of the welded joint [37].

The HAZ is also distinct from the TMAZ, where the material experiences both thermal exposure and plastic deformation. In the TMAZ, the grains are typically elongated due to the plastic deformation associated with the FSW tool's movement, resulting in a distinct elongated grain structure. This zone, subjected to both thermal and mechanical effects, bridges the properties between the highly deformed SZ and the thermally influenced HAZ [39]. Managing the characteristics of the HAZ involves careful control of welding parameters. These parameters influence the heat input and distribution during welding, thereby affecting the size and properties of the HAZ. Optimizing these parameters can help in achieving a balance where the adverse effects of grain coarsening are minimized, and the integrity of the welded joint is maintained.

In conclusion, the HAZ in FSW is a crucial zone that, while free from plastic deformation, undergoes significant thermal changes leading to a coarse grain structure. The understanding and management of this zone are essential for optimizing weld quality and ensuring the mechanical reliability of the welded joint. This study aims to investigate the microstructural and mechanical changes within the HAZ, providing insights for enhancing the performance of FSW joints.

1.7 Advantages of FSW

FSW presents a host of advantages that make it a superior choice for many welding applications. Its ability to produce high-quality welds with enhancement in joint efficiency, reduced environmental impact, and economic benefits positions it as a key technology in modern manufacturing. These advantages are driving the adoption of FSW across various industries, paving the way for innovative and sustainable joining solutions. Some other advantages are discussed below:

- **Improved Mechanical Properties** The welds produced by FSW typically exhibit superior joint efficiency, higher UTS, better toughness and fatigue resistance. This is due to the refined microstructure and the absence of defects like voids and inclusions often found in fusion welds.
- **Reduced Distortion and Residual Stresses** FSW generates less heat compared to conventional welding processes, resulting in lower thermal distortion and residual stresses. This is particularly beneficial for applications requiring high dimensional accuracy and minimal post-weld machining.
- **No Filler required** FSW does not require the use of filler materials or shielding gases, reducing costs and simplifying the welding setup. This also eliminates the risk of contamination from external sources, leading to cleaner and more consistent welds.
- **Environmental Benefits** At fumes absence, gases, and spatter makes FSW an naturally friendly process. There is also reduced energy consumption compared to fusion welding, contributing to lower overall environmental impact.
- **Versatility in Material Joining** FSW can join a wide range of materials, including Al, Cu, Mg, and even dissimilar material combinations. This versatility makes it applicable in diverse industries, from aerospace and automotive to shipbuilding and railways.
- **Automation and Reproducibility** FSW is well-suited for automation, allowing for high reproducibility and consistent weld quality. Automated FSW systems can be integrated into manufacturing lines, enhancing productivity and reducing costs.
- **Minimal Preparation and Post-Weld Processing** FSW requires minimal surface preparation before welding and generally results in a smooth, clean weld

surface. This reduces the need for extensive post-weld processing, such as grinding or polishing, saving time and costs.

- **Enhanced Safety** The absence of high-temperature arcs, spatter, and fumes makes FSW a safer process for operators. The reduced risk of burns and inhalation of harmful substances contributes to a safer working environment.
- **Economic Efficiency** The cumulative benefits of reduced material costs, lower energy consumption, minimal post-weld processing, and the potential for automation lead to significant economic efficiency. FSW can offer cost savings in both production and maintenance phases.

1.8 Disadvantages of FSW

Despite its many advantages, FSW also has some disadvantages and limitations. Understanding these is important for making informed decisions about its use in various applications. Here are the main disadvantages of FSW in detail:

- Initial Equipment Cost The equipment for FSW, including specially designed welding machines and tools, can be significantly more expensive than fusion welding equipment.
- Limited to Linear Joints FSW is most effective for linear or slightly curved joints. Welding complex, three-dimensional shapes or intricate geometries can be challenging and may require advanced and costly equipment or customized tooling.
- Thickness Limitations While FSW is effective for a range of material thicknesses, it is generally more suited to relatively thin to medium-thickness materials. Welding very thick sections requires larger, more powerful equipment and specialized tools, which can be more expensive and difficult to handle

1.9 Application of FSW

FSW has been adopted across various industries due to its numerous advantages, such as improved mechanical properties and reduced defects. Here are detailed applications of FSW in specific sectors:

1.9.1 Aerospace Industry

- **Aircraft Structures**: FSW is used to join Al-alloys in the manufacturing of fuselage panels, wing skins, and fuel tanks. The high-strength, defect-free welds enhance the structural integrity and performance of aircraft.
- **Cryogenic Fuel Tanks**: For space applications, FSW is utilized to construct cryogenic fuel tanks for rockets and spacecraft due to its ability to produce leak-proof, high-strength joints in lightweight aluminum-lithium alloys.
- **Propellant Tanks**: Used in launch vehicles, the tanks require strong, reliable welds to ensure safety and performance during missions.

1.9.2 Railway Sector

- **Train Carriages**: FSW is employed to weld aluminum panels for train carriages, resulting in lightweight, durable structures that improve fuel efficiency and reduce operating costs.
- **Bogies and Under frames**: The use of FSW in manufacturing bogies and under frames contributes to enhanced strength and durability, ensuring safety and longevity of railway vehicles.

1.9.3 Automobile Sector

- **Chassis and Body Panels**: FSW is used to join lightweight aluminum components in car bodies and chassis, contributing to weight reduction, improved fuel efficiency, and enhanced crashworthiness.
- **Electric Vehicle Battery Housings**: The robust and leak-proof joints produced by FSW are ideal for battery housings in electric vehicles, ensuring safety and reliability.
- **Heat Exchangers**: FSW is used in the production of heat exchangers due to its ability to create high-integrity joints that withstand thermal cycling and pressure variations.

1.9.4 Ship and Marine Industry

- **Ship Hulls and Decks**: FSW is used to weld aluminum panels in the construction of ship hulls and decks, providing high-strength, corrosion-resistant joints that enhance the vessel's durability and performance.
- **Offshore Platforms**: The technology is applied in fabricating structures for offshore platforms, ensuring strong, reliable welds that can withstand harsh marine environments.

1.9.5 Other Applications

- **Pipe and Tube Fabrication**: FSW is used to join pipes and tubes, particularly in the oil and gas industry, where leak-proof and high-strength welds are critical for safe operations.
- **Heat Sinks and Electronic Housings**: In electronics, FSW is employed to manufacture heat sinks and housings, providing efficient thermal management and reliable protection for electronic components.
- **Industrial Machinery**: The technology is used to join components in industrial machinery, such as frames and supports, where robust and durable welds are essential for operational reliability.
- **Consumer Goods**: FSW is applied in the production of bicycles, ladders, and other consumer products, enhancing strength, reducing weight, and improving overall product quality.
- **Aerospace Tooling and Fixtures**: FSW is used to produce tooling and fixtures for aerospace manufacturing, ensuring precision and durability in the production process.

1.10 Challenges in FSW of Dissimilar Non-Ferrous materials

FSW of AZ91D and aluminum presents several unique challenges. These challenges arise from the differing physical and chemical properties of the two materials, and the inherent difficulties in welding Mg-Alloys and aluminum. Here are the detailed challenges:

- **Dissimilar Material Properties** FSW of dissimilar non-ferrous materials like AZ91D magnesium and AA2024 aluminum faces challenges including uneven heat distribution, brittle intermetallic compound formation, and differing material properties leading to defects. Residual stresses, galvanic corrosion, and tool design complexities further complicate the process, requiring precise parameter control and advanced techniques for optimal weld quality.
- **Formation of IMCs:** The IMCs formation in AA2024 aluminum and AZ91D magnesium welded joints is a significant challenge in FSW. These IMCs are typically brittle and can severely undermine the tensile strength of the joint. During the FSW process, the intense heat and plastic deformation cause aluminum and magnesium atoms to diffuse and react, forming various intermetallic phases such as Al_3Mg_2 and $Al_{12}Mg_{17}$. These compounds, while bonding the two dissimilar metals, often exhibit poor ductility and can become points of weakness, leading to reduced tensile strength and increased susceptibility to fracture. Controlling the formation and distribution of IMCs requires careful optimization of welding parameters.
- **Oxide Layers** Both magnesium and aluminum form oxide layers on their surfaces, which are difficult to break up during welding. These oxide layers can prevent proper bonding between the materials, leading to weak welds with poor mechanical properties. Proper surface preparation and control of the welding environment are necessary to mitigate this issue.
- **Tool Wear and Selection** The tool material must be carefully chosen to withstand the abrasiveness and reactivity of both magnesium and aluminum. The high temperatures and friction involved in FSW can lead to significant tool wear, especially when welding dissimilar materials. Tool design and material selection are critical to ensure longevity and effectiveness.

1.11 Types of Aluminum Alloy

Al alloys are metallic materials composed primarily of Al, along with other elements i.e. Fe, Mn, Zn, Si, Mg, and Cu. These alloys are used in an extensive range of applications, including automotive, construction, aerospace and consumer products. One of the key advantages of Al alloys is their low density, which make them

lightweight where weight is a critical factor. Additionally, Al alloys have good corrosion resistance and can be easily formed, welded, and machined. There are many types of Al alloys, each with its own unique properties and characteristics. Some common Al alloys include: 6061-T6: A popular general-purpose alloy with good strength, weldability, and machinability. 7075-T6: A high-strength alloy commonly used in aerospace applications. 2024-T3: An alloy with good fatigue resistance, often used in aircraft structures. 5052-H32: A corrosion-resistant alloy used in marine and automotive applications. 6063-T5: A popular extrusion alloy with good surface finish and corrosion resistance. Al alloys can be further strengthened through heat treatment and other processes to improve their mechanical properties [40, 41].

1.11.1 Types of Al-alloys

Aluminum alloys are highly valued in various industries for their exceptional properties, including lightweight, high strength, and excellent corrosion resistance. These alloys, which are classified into series such as the 2000, 5000, 6000, and 7000 series, are engineered to meet specific requirements. For example, the 2000 series, like AA2024, is known for its high strength and fatigue resistance, making it ideal for aerospace applications. The 5000 series, such as AA5083, is prized for its corrosion resistance and is commonly used in marine environments. The 6000 series, including AA6061, offers a good balance of strength, corrosion resistance, and weldability, making it suitable for structural and automotive applications. The 7000 series, exemplified by AA7075, provides exceptional strength and is often used in high-stress components like aircraft frames. These alloys achieve their unique properties through careful control of their chemical composition and processing techniques, enabling them to meet the diverse and demanding needs of modern engineering and manufacturing [42].

1.11.2 1xxx series

The 1xxx series of Al-alloys consists predominantly of pure aluminum, typically with over 99% aluminum content and minor traces of impurities such as iron and silicon. Known for their high purity, these alloys exhibit excellent electrical conductivity, making them ideal for applications in the electrical industry, including overhead

transmission lines and transformer windings. They also offer good corrosion resistance in neutral environments, which suits them for use in food and beverage containers where contact with foodstuffs requires inert materials. Additionally, their high thermal conductivity makes them suitable for heat exchangers and other heat transfer applications. However, the 1xxx series alloys are relatively soft and ductile, limiting their use in structural applications requiring higher mechanical strength. Their versatility extends to decorative and architectural applications, where their appearance and corrosion resistance are valued. Overall, the 1xxx series of Al-alloys plays a critical role in various industries.

1.11.3 2xxx series

The 2xxx series of Al-alloys is characterized by its primary alloying element, copper (Cu), which typically ranges from 2% to 10%. This series is prominent for its excellent strength-to-weight ratio and good machinability, making it particularly well-suited for demanding applications in various industries. The addition of copper enhances the alloy's strength significantly, making 2xxx series alloys some of the strongest Al-alloys available. This strength, combined with relatively good machinability, allows for the precise fabrication of complex components needed in aerospace structures, including aircraft fuselage skins, wings, and landing gear. The alloys also exhibit excellent fatigue resistance, making them suitable for components subjected to cyclic loading conditions. However, their corrosion resistance is lower compared to other Al-alloys, particularly in marine environments, necessitating protective coatings or anodizing processes for extended durability. Overall, the 2xxx series alloys excel where strength, lightweight properties, and machinability are paramount, contributing to their widespread use in aerospace, military applications, and high-performance sports equipment.

1.11.4 3xxx series

The 3xxx series of Al-alloys consists primarily of Al-alloyed with manganese (Mn), typically ranging from 1.0% to 1.5%. This alloy series is widely recognized for its excellent corrosion resistance, moderate strength, and good formability, making it versatile for various applications across different industries. The addition of

manganese enhances the alloy's ability to resist corrosion, particularly in marine environments and acidic conditions, which is advantageous for applications requiring long-term durability and reliability. These alloys are known for their moderate strength, suitable for structural components in automotive manufacturing, where corrosion resistance and formability are crucial. They are commonly used in the production of automotive body panels, trim components, and structural parts. Additionally, the 3xxx series alloys are favored in architectural applications for roofing, siding, and window frames due to their corrosion resistance and aesthetic appeal. Another significant advantage of the 3xxx series is its excellent formability and weldability, allowing for the production of complex shapes and assemblies without compromising structural integrity.

1.11.5 4xxx series

The 4xxx series of Al-alloys primarily consists of Al-alloyed with silicon (Si), typically in concentrations ranging from 4.5% to 13%. These alloys are notable for being non-heat treatable, deriving their strength primarily from solid solution strengthening rather than precipitation hardening processes. This characteristic makes them advantageous in applications where heat treatment may not be practical or cost-effective, simplifying manufacturing processes and reducing production time and costs. One of the key advantages of the 4xxx series is their excellent weldability. They exhibit superior weldability compared to many other Al-alloys, with minimal risk of cracking or distortion during welding. This property makes them highly suitable for applications requiring intricate welded structures, such as automotive components (e.g., fuel tanks, body panels) and shipbuilding.

While the 4xxx series alloys offer moderate strength, they are not as strong as some heat-treatable Al-alloys. However, their combination of good weldability and sufficient strength makes them preferred in industries where ease of fabrication and welding are critical considerations. They are also utilized in brazing applications, particularly in manufacturing heat exchangers and similar components where corrosion resistance and ease of joining through brazing processes are essential.

1.11.6 5xxx series

The 5xxx series of Al-alloys is characterized by its predominant alloying element, magnesium (Mg), typically ranging from 2% to 6%. This series is renowned for its excellent corrosion resistance. The addition of magnesium enhances the alloys' natural resistance to corrosion, making them well-suited for marine environments and industrial settings where exposure to moisture and harsh chemicals is common.
These alloys also boast good weldability, allowing for efficient joining processes without compromising structural integrity. This feature makes them highly suitable for applications requiring intricate designs and complex assemblies, such as automotive components, marine structures, and architectural panels. Moreover, the 5xxx series alloys offer moderate to high strength depending on the specific alloy composition and heat treatment, providing a balance between strength and formability. In industries ranging from transportation to construction, the 5xxx series plays a crucial role due to its combination of weldability, corrosion resistance, and mechanical properties. It is particularly valued in applications where durability, aesthetics, and ease of fabrication are essential considerations. Overall, the 5xxx series of Al-alloys continues to be a preferred choice for manufacturers seeking reliable materials capable of withstanding diverse environmental challenges while maintaining performance and longevity.

1.11.7 6xxx series

The 6xxx series is distinguished by its composition primarily consisting of magnesium (Mg) and silicon (Si), typically with magnesium content ranging from 0.5% to 1.5% and silicon content from 0.6% to 1.5%. This alloy series is renowned for its versatility and widespread application across diverse industries. Compared to other Al-alloys, the 6xxx series offers a balanced combination of strength, formability, and corrosion resistance. It can achieve varying levels of strength through heat treatment processes followed by artificial aging (T6 temper), making it suitable various applications. The alloys in the 6xxx series are highly formable, allowing for efficient shaping through processes like extrusion and rolling.

1.11.8 7xxx series

The 7xxx series is distinguished by its composition primarily consisting of Zn as the major element, typically ranging from 5% to 12%, along with magnesium (Mg) and copper (Cu) to enhance specific mechanical properties. This alloy series is renowned for its exceptional strength, toughness, and resistance to fatigue, making it highly suitable for demanding applications in aerospace, military, and high-performance industries.

These alloys achieve their high strength through a process known as precipitation hardening, where the material is heat-treated to form fine precipitates that strengthen the matrix. This characteristic ideal for structural components1, such as aircraft structural parts, military vehicle armor, and high-performance sporting equipment. In addition to their strength, the 7xxx series alloys exhibit remarkable toughness and resistance to fatigue, ensuring reliability under rigorous operational conditions. Despite their high strength, they retain good machinability, allowing for precise machining and fabrication of complex components required in aerospace and defense applications [43]. While the 7xxx series alloys offer impressive mechanical properties, their corrosion resistance is typically lower than that of other Al-alloys like the 5xxx series. However, this can be mitigated through appropriate surface treatments and coatings to enhance durability in harsh environments.

1.12 Types of Magnesium alloy

Mg-Alloys are a group of materials primarily composed of Mg as the main metallic component, often alloyed with other elements i.e. Al, Zn, Mn, and rare earth metals. These alloys are prized for their exceptional lightweight properties, being among the lightest structural metals available. With a density about one-third that of steel and roughly two-thirds that of aluminum, Mg-Alloys offer significant weight savings in various applications. Beyond their lightweight nature, Mg-Alloys possess favorable mechanical properties. In terms of fabrication, Mg-Alloys are generally machinable and can be cast, forged, extruded, and welded with relative ease compared to other metals. They also feature good thermal and electrical conductivity, which adds to their versatility in applications requiring heat dissipation or electrical conduction. Different types of Mg-Alloys are as follow.

1.12.1 AZ series

The AZ Series Mg-Alloys are characterized by their composition primarily consisting of Mg-Alloyed with aluminum (Al), typically ranging from 8% to 12% aluminum content. These alloys are well-regarded for their excellent metallurgical properties making them highly desirable materials across various industrial sectors.

Additionally, the addition of aluminum enhances the corrosion resistance of these alloys, making them resilient in environments prone to moisture and chemicals. This property ensures durability and longevity, supporting their use in outdoor and industrial applications where protection against corrosion is essential.

AZ Series Mg-Alloys also exhibit good weldability and formability, allowing for ease of fabrication into complex shapes and structures. They are utilized extensively in automotive components like transmission cases and engine parts, as well as in aerospace for aircraft components and in consumer electronics for lightweight housings and structural components.

In manufacturing, AZ Series alloys are favored for die casting applications due to their ability to maintain dimensional stability and achieve intricate designs with high precision. This versatility in fabrication methods further enhances their appeal in industries requiring intricate and lightweight solutions.

1.12.2 AZ91 series

The AZ91 series Mg-Alloys are renowned for their composition primarily consisting of magnesium (Mg), aluminum (Al), and zinc (Zn). These alloys typically contain around 9% aluminum and 1% zinc, providing a balance of lightweight properties, moderate strength, and good corrosion resistance. With a density approximately 29% less than that of Al and one-quarter that of steel, AZ91 alloys are exceptionally lightweight, making them ideal for applications where weight reduction is critical without compromising structural integrity.

In terms of mechanical properties, AZ91 alloys offer good strength relative to their weight, though they are not as strong as some other Mg-Alloys like those in the AM or AE series. They excel in die casting applications due to their exceptional castability, allowing for the manufacture of intricate components with high dimensional accuracy and surface finish.

While AZ91 alloys exhibit moderate corrosion resistance, particularly in dry environments, they may require protective coatings or surface treatments to enhance their performance in more corrosive conditions. Common applications of AZ91 alloys include automotive parts, such as engine components, housings, and structural elements, as well as in aerospace for lightweight structural components. Overall, the AZ91 series Mg-Alloys represent a versatile choice for industries seeking lightweight materials with adequate strength and corrosion resistance properties.

1.13 Aluminum Magnesium phase diagram

The aluminum-magnesium (Al-Mg) phase diagram is a crucial tool for understanding the behavior of Al-Mg alloys under various temperature and composition conditions shown in Fig. 1.9. This diagram maps the phases present in these alloys as a function of Mg content and temperature, providing insights into the solidification process, metallurgical properties of the alloys. The horizontal axis of the diagram represents the composition, ranging from pure aluminum (0% Mg) to pure magnesium (100% Mg), while the vertical axis denotes the temperature, extending from atmospheric temperature to above the melting points of Al and Mg.

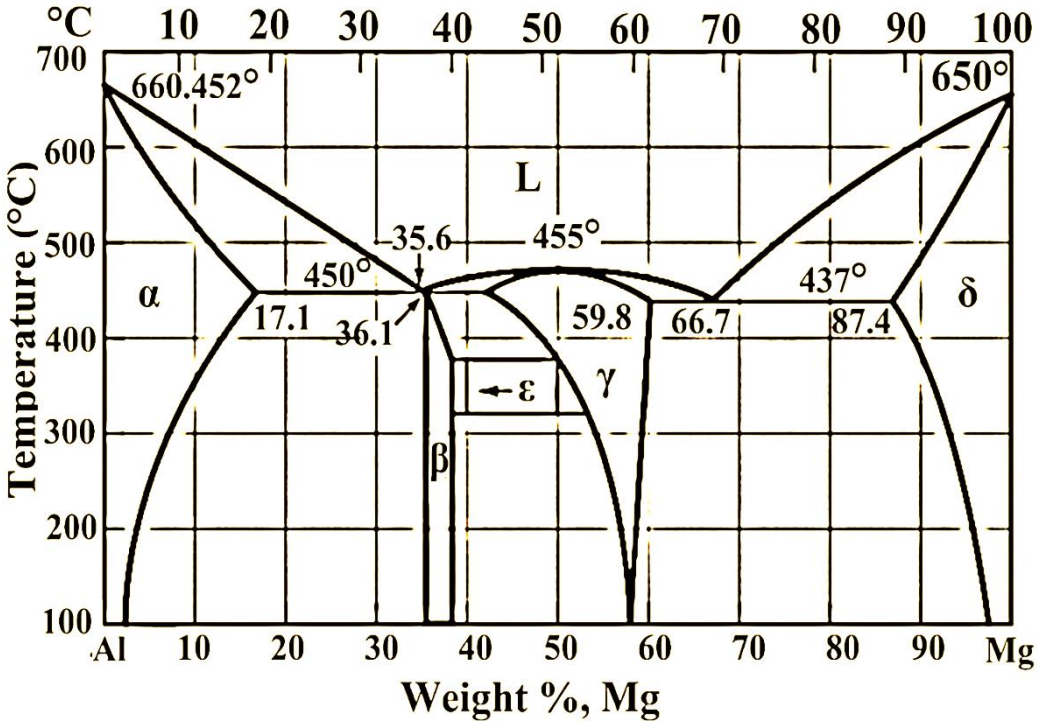

Figure 1.9: Phase diagram of Al/Mg [44]

At the heart of the Al-Mg phase diagram are several key lines and regions that define the phase boundaries. The Liquidus Line is one of the primary features, representing the temperature above which the alloy is entirely liquid. As the alloy cools down, it crosses this line, and solidification begins. For compositions with low magnesium content, the Liquidus Line slopes downwards, indicating a decrease in melting temperature with increasing magnesium content. Conversely, for higher magnesium compositions, the line continues to slope but at a reduced gradient. Below the Liquidus Line is the Solidus Line, which marks the temperature below which the alloy is completely solid. Between the Liquidus and Solidus lines lies a region where liquid and solid phases coexist [45, 46].

This two-phase region is critical for understanding the solidification behavior of Al-Mg alloys, as it dictates the temperature range over which solidification occurs and the resulting microstructures. The intersection of the Liquidus and Solidus lines occurs at the eutectic point, a significant feature of the diagram. The eutectic point is characterized by a specific composition (around 33% Mg) and a temperature (approximately 450°C). At this point, the liquid phase transforms directly into a mixture of solid α (aluminum-rich) and β (magnesium-rich) phases upon cooling. This eutectic reaction is vital in determining the final microstructure of the alloy, particularly for compositions near the eutectic composition. The microstructure resulting from eutectic solidification typically consists of fine, alternating layers or lamellae of α and β phases, contributing to the alloy's unique mechanical properties [47, 48]. In addition to the Liquidus and Solidus lines, the phase diagram also includes the Solvus Line, which indicates the limits of solubility of magnesium in aluminum and vice versa at different temperatures. Beyond this line, second-phase particles precipitate out of the solid solution, affecting the alloy's mechanical properties through precipitation hardening. For example, in aluminum-rich compositions, the α phase can dissolve a certain amount of magnesium at elevated temperatures. As the temperature decreases, excess magnesium precipitates out, forming secondary phases that enhance the alloy's strength [49, 50].

For heat treatment, the diagram guides the optimization of processes like solution treatment and aging, which rely on controlling the solubility and precipitation of alloying elements. In welding, understanding the phase diagram is essential for controlling the solidification process, minimizing defects like hot cracking, and ensuring sound welds.

1.14 Organization of Thesis

Chapter-1: Introduction

This chapter provides an in-depth explanation of the FSW process, detailing its operation, applications, and the challenges involved in welding nonferrous dissimilar materials. Furthermore, it presents an overview of the subsequent chapters of the thesis.

Chapter-2: Literature Review

This chapter offers a comprehensive review of the literature on dissimilar FSW, with a particular focus on the welding of aluminum to magnesium. This chapter summarizes the effects of various FSW process parameters on joint quality based on available literature. Key parameters include welding speed, rotational speed, FSW tool design and configuration, base material (BM) thickness and joint configuration, plunging force, tilt angle, pin offset, and BM positioning. Additionally, this chapter references newly published studies on tool geometry optimization, process optimization, and material flow. The chapter concludes by highlighting the objectives of the study and identifying gaps in the existing literature.

Chapter-3: Materials and Methods

This chapter provides a detailed description of the properties of the workpiece materials and the specifications of the friction stir welding tool. It also outlines the selection of friction stir process parameters, including their ranges and levels.

Chapter-4: Experimentation

This chapter describes the preparation of plates for FSW, the selection of tool pin profiles, the fabrication of FSWed joints, and the preparation of tensile specimens and microstructural analysis.

Chapter-5: Results and Discussion

This chapter examines the effects of pin profile and tool rotational speed on the mechanical properties of the weldments, including ultimate tensile strength and microhardness. It also discusses the impact of nanoparticles on the FSWed joints. Taguchi's technique is used to determine the optimal combination of FSW parameters

for achieving maximum temperature and residual stress responses, while analysis of variance (ANOVA) identifies the significant parameters for each response.

Chapter-6: Conclusion & Future Work

This chapter presents the key findings from the research and suggests potential directions for future studies in the field.

CHAPTER-2

2. LITERATURE REVIEW

The growing use of Mg and Al in automotive, shipbuilding, and aerospace is due to their low density and high specific strength [51, 52]. Effective joining of Mg alloys with Al is essential for design flexibility. However, traditional fusion welding methods are unsuitable for Mg and Al due to brittle IMC formation [53–56]. Thus, developing reliable methods for joining these dissimilar alloys is a significant technical challenge.

Fusion welding of Al/Mg alloys poses challenges due to significant metallurgical and physical differences. This process often leads to the formation of brittle IMCs and microvoids, compromising joint quality. Issues stem from IMC dispersion caused by high strain rate, severe plastic deformation, and low processing temperatures in fusion welding. As a result, producing high-quality Al/Mg joints with conventional fusion welding methods is complex and time-consuming. FSW is an effective alternative for joining Mg and Al alloys, such as AZ31 and AA1050 [57]. This solid-state process reduces the generation of brittle IMCs by operating at lower temperatures and causing less severe plastic deformation than fusion welding. FSW retains the desirable mechanical and physical properties of light metal alloys, making it highly suitable for use in the automotive, aerospace, and shipbuilding industries.

The adoption of FSW for the Mg and Al alloys presents a promising solution to the challenges posed by fusion welding processes. By avoiding the materialization of brittle IMCs. FSW enables the creation of high-quality, reliable joints essential for advancing the use of these materials in various industrial applications.

In the automotive industry, coated metal matrix is frequently utilized to improve corrosion resistance. However, the coating layers can negatively impact material flow during FSW, resulting in the generation of both macro and micro defects that can diminish the joint efficiency [58]. A considerable body of research has been dedicated to the exploration of different alloy combinations using FSW techniques [59, 60].

The selection of process parameters is very significant for determining the joint efficiency of Mg/Al alloys. For instance, placing AZ31 magnesium alloy on the AS and AA2024 aluminum alloy on the RS has been shown to enhance the joint

efficiency of Al/Mg welds [61]. For FSW between AA6064 and AZ31 alloys, positioning the AZ31 on the advancing side (AS) is crucial for optimizing joint efficiency. Misalignment of the rotating tool, particularly if perpendicular to the weld center, can lead to cracks and defects [62, 63]. Proper positioning ensures better weld quality and reduces the risk of structural weaknesses in the joint.

During FSW, high pressure causes rough base metal surfaces to bond despite some oxide layers remaining [64]. Studies on Al/Mg alloy FSW reveal that brittle IMCs form in the weld region, leading to increased hardness and residual stress in the welded area [65–70]. Additionally, the complexity of the weld interface in Mg-Al alloys has been documented, with some studies noting a tortuous shape that can enhance joint efficiency by 15 to 45% under various conditions [71]. This complexity in weld morphology not only affects mechanical performance but also offers insights into optimizing welding parameters for improved results.

During FSW of light metal alloys promote brittle IMCs Al_3Mg_2 and $Al_{12}Mg_{17}$ in the SZ at high temperature. Al3Mg2 precipitates are usually found in the lower and middle SZ regions, where magnesium atoms migrate to grain boundaries due to severe plastic deformation [72]. Substantial heat, strain, and pressure during FSW enhance atom diffusion, forming a supersaturated solid solution at the Al/Mg interface. When this solid solution reaches certain temperature thresholds, it transforms into IMCs. The diffusion rate, temperature, and local composition in the weld zone critically influence IMC formation and growth. By comprehending the formation and behavior of IMCs and other phases during FSW, researchers can fine-tune the welding process to enhance joint strength, durability, and overall performance. This knowledge helps ensure that the welded joints meet the necessary mechanical requirements for various industrial applications [73].

The impact of tool travel speed on FSWed AZ31 and AA6061 has been extensively studied, highlighting their mechanical, microstructural, and corrosion behaviors. Electrochemical techniques, including potentiodynamic polarization tests and electrochemical impedance spectroscopy, were conducted at pH levels 2 to 12 [74]. Studies on different FSW parameters reveal complex flow patterns in the stir zone due to brittle IMCs and non-uniform intermixing, affecting the mechanical properties of AZ31 and AA6061 [75, 76].

The unique combination of AZ91D and AA7075 with FSW presents challenges due to differing melting temperatures and mechanical properties. However, FSW enhances

joint strength compared to traditional methods, effectively addressing the disparities in their metallurgical properties. Researchers evaluated the ballistic performance of AA5083 base metal and underwater FSW (UWFSW) plates with 18.5 mm armor-piercing projectiles at a velocity of 200 m/s. The UWFSW joints were produced with a TRS of 1200 rpm, TS of 40 mm/min, tilt angle of 1°, and a straight hexagonal pin, resulting in defect-free welds with enhanced tensile and impact properties [77]. Additional optimization using Grey Relational Analysis (GRA) has been reported, further improving the performance of UWFSW joints [78]. Different probe profiles, such as straight cylindrical and hexagonal, were used to join AA5083 Al-alloy plates. The straight hexagonal (SH) probe significantly enhanced the joint efficiency of the UWFSW joints [79, 80].

FSW enhances microstructure by reducing porosity and ensuring a more uniform dissemination of alloying elements, resulting in better tensile strength, and corrosion resistance. Unlike fusion welding, FSW avoids issues like porosity, cracking, and unwanted phase transformations. Welding AZ91D and AA2024 alloys presents both challenges and opportunities, making it a crucial area for materials joining and fabrication. Successful FSW of these alloys supports lightweight structures in aerospace, automotive, and marine industries, with ongoing research improving techniques and expanding applications.

Understanding and managing the formation of IMCs is essential, as they can influence the joint's properties in both beneficial and detrimental ways. Effective control of IMC formation ensures that the welded joints achieve the desired mechanical characteristics, enhancing overall performance and reliability [81, 82].

2.1 Consequence of FSW parameters on Mg/Al weldments

Welding parameters are significant for achieving high joint efficiency. Certain parameters significantly enhance weld quality, while others have minimal impact on the FSWed joints of Al and Mg alloys. According to Yazdipour et al., these parameters also contribute to weld defect phenomena [83]. Understanding the influence of these parameters is essential for producing superior quality weld joints during FSW [84]. Key welding parameters that greatly affect the FSW process include TRS, travel speed, tilt angle, and tool design. These parameters are discussed

in detail below to highlight their importance in optimizing the welding process and ensuring the desired mechanical properties and integrity of the weldments.

2.1.1 Consequence of TS and TRS on the welded joints

TRS directly affects heat input, with higher speeds increasing it, while higher travel speeds reduce heat input. Since heat input is directly proportional to TRS and inversely proportional to TS, optimizing these parameters is essential for achieving high-quality welds. Proper adjustment ensures optimal heat distribution and material flow, leading to improved weld quality and performance [85].

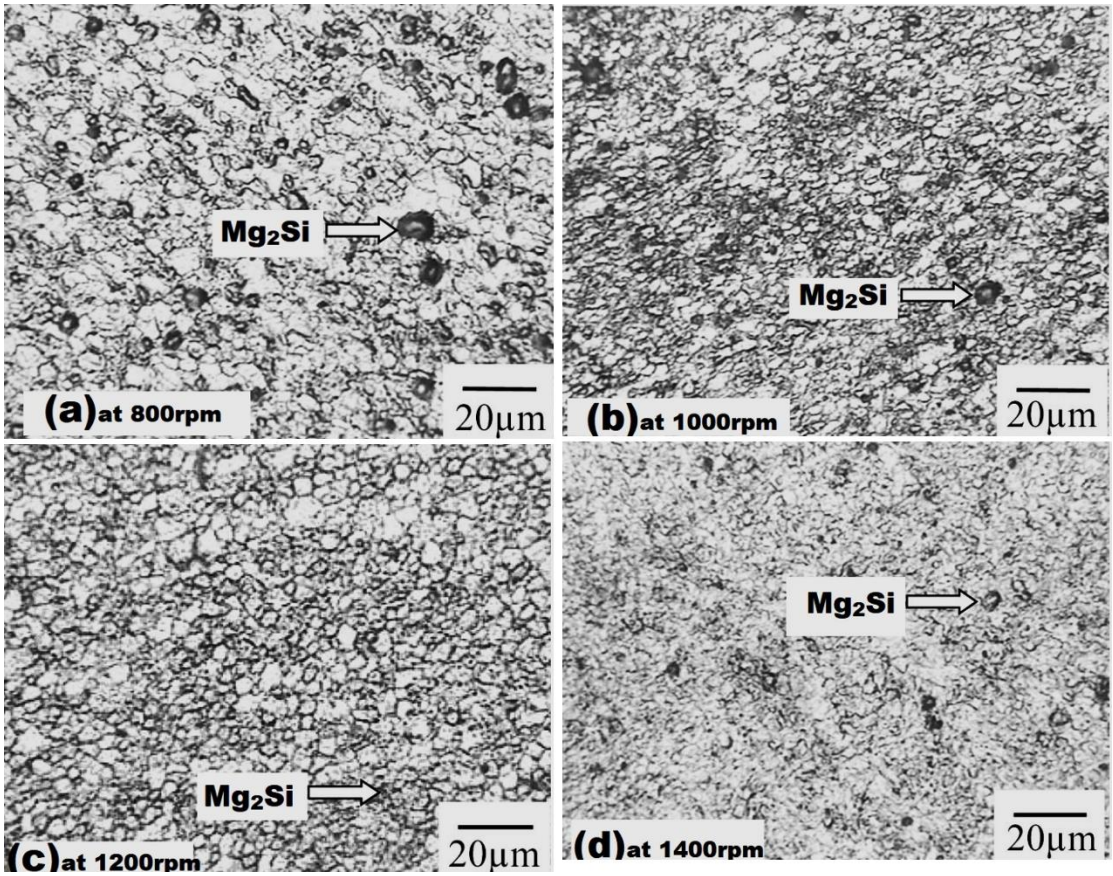

Figure 2.10: Influence of TRS on grain structure of the FSWed joints of Al/Mg alloys [87]

The TRS influences the fracture position of the weld, affecting strain distribution by shifting the area of greatest strain from the RS to the AS [86, 87]. The ratio of TS to TRS (υ/ω), is crucial for weld quality [88-90]. A higher pitch indicates faster, cooler welding with lower temperatures and poor material flow, while a lower pitch results

in slower, hotter welding, which can cause excessive liquation and IMC formation, deteriorating weld quality [91, 92].

Low TRS generates low temperatures in the SZ, increasing the particle strengthening, as shown in Fig. 2.1(a) and 2.1(b). Conversely, high TRS cause particle separation in the TMAZ, as depicted in Fig .2.1(c) and 2.1(d) [87]. These results revealed the importance of balancing TRS and TS to optimize heat input and material flow, ensuring weld strength and integrity.

Optimizing FSW parameters is not only for preventing weld defects but also for improving the joint efficiency. A thorough understanding of how these parameters interact, and can lead to significant improvements in the reliability of welds in dissimilar materials, such as aluminum and Mg-Alloys. Proper control and adjustment of TRS and TS can mitigate issues related to material flow and input heat, thereby reducing defects and improving the performance of the welded joint in various industrial applications.

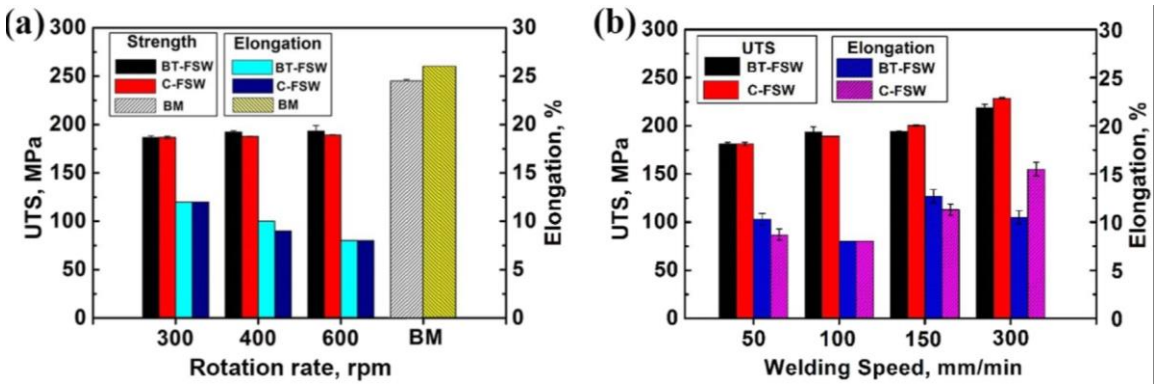

Figure 2.2: Variation of UTS at different welding and TRS [93]

Fig. 2.2a reveals that joint's UTS remains nearly constant across different rotation rates, with minimal variation for both Bobbin tool FSW (BTFSW) and Conventional FSW (CFSW) joints. Specifically, the UTS of CFSW welded joints ranges from 185-188 MPa, while BTFSW joints exhibit a range of 185 to 199 MPa. The highest tensile strength, 198 MPa, was achieved with the BT-600-100 parameter, representing 82% of the BM's strength. It indicates that BTFSW joints have comparable or slightly higher strength than CFSW joints at the same rotation rates [93]. The variation of UTS and TS in Fig. 2.2b demonstrates that tensile strength increases with TS within the same process, correlating well with the hardness profile. No significant differences were observed between the two processes' joints at the same TS. For BT-

FSW joints, the UTS varies from 182 to 223 MPa at different TS, while for C-FSW joints, it ranges from 182-228 MPa. The maximum UTS of 228 MPa was perceived with the C-600-300 parameter, representing 92.5% of the base metal's strength. Generally, BT-FSW joints exhibit lower strength compared to C-FSW joints, with strength efficiencies of about 89% for conventional FSW and 83% for bobbin tool welding. This reduction is due to the increased heat input from the two shoulders, which causes more severe softening. Despite this, softening in the HAZ did not significantly impact fracture behavior in this study. The UTS and hardness results are consistent with existing theories, showing that increased density and slight coarsening of precipitates at BT-600-100 contributed to higher strength [93]. Higher tool rotation speeds and lower travel speeds generally enhance frictional heat and result in greater plastic deformation in the SZ. Fig. 2.3 illustrates the temperature variations at different rotation and travel speeds, highlighting several key points.

- All parameters produced peak temperatures exceeding 450°C.
- The top layer (Al) experienced significantly higher temperatures than the bottom layer (Mg), indicating that the shoulder, rather than the tool pin, was the primary source of heat generation.
- Higher TRS and lower TS led to higher temperatures.

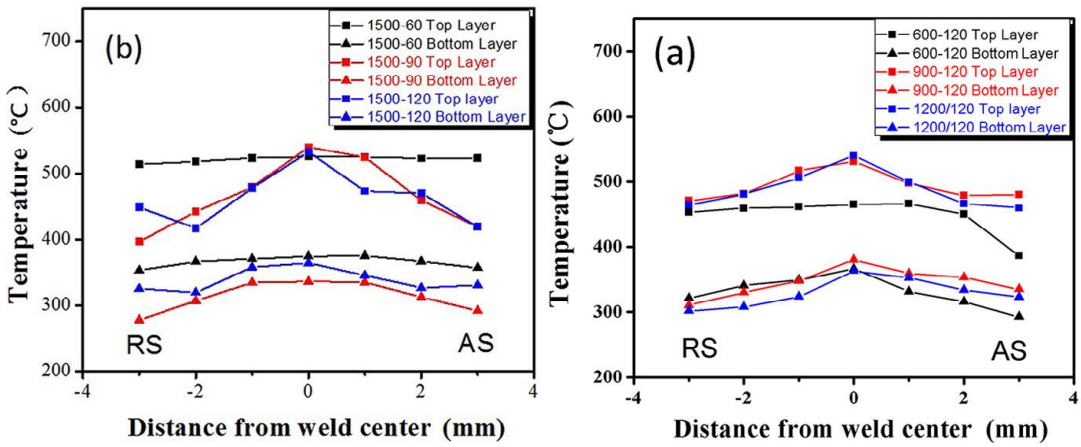

Figure 2.3: Temperature variation of FSWed joints, (a) at constant TRS of 1500 rev/min, (b) Constant TS of 120 mm/min [94]

Fig. 2.4 displays the transverse macrostructure of welded region at a TS of 130 mm/min and TRS of 500 to 1200 rev/min. These sections clearly show significant material flow and intermixing between the Mg and Al alloys due to the tool pin's

penetration into the lower sheet. Material flow during FSW primarily occurs beneath the tool shoulder in the SZ and beside the rotating pin, influenced by the TRS. The FSWed joints are asymmetrical about the weld center, with more severe mixing on the AS and RS [94]. As shown in the temperature data, reducing the TRS decreases the heat generated, resulting in inadequate material mixing and a smaller SZ. It is evident when the TRS was 600 rev/min, and the TS was 120 mm/min, where micro-voids form due to inadequate input heat.

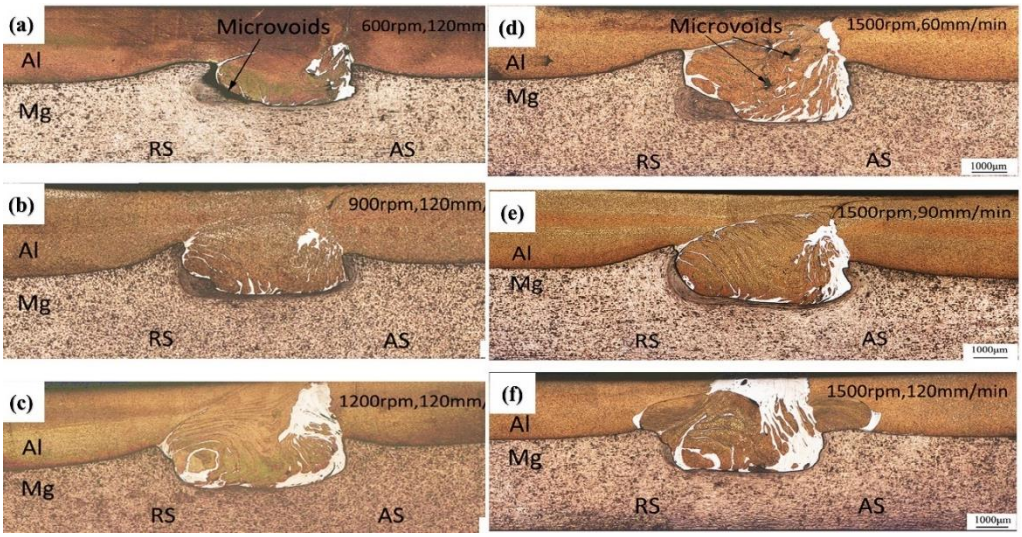

Figure 2.4: Macrostructure of the FSWed joints of NZ30K and AA6061, (a) 600 rev/min, (b) 900 rev/min, (c) 1200 rev/min, (d) 60 mm/min, (e) 90 mm/min, (f) 120 mm/min [94]

Micro-voids are visible at a TS of 60 mm/min due to excessive heat, leading to material expulsion and abnormal flow. When the TS increases to 90 to 120 mm/min, the micro-voids disappear. An optimal travel speed reduces heat input and minimizes or eliminates micro-voids, which are perceived with too low frictional heat. Microstructural analyses were performed on joints prepared at Ts of 120 mm/min and 900 rev/min to investigate the impact of different process parameters. These studies provided insights into how varying rotational and travel speeds influence the weld microstructure and overall joint quality [94].

Fig. 2.5a–c presents the microstructures of the Mg side nugget at increasing TRS. The side SZ shows fully recrystallized grains, with the Mg structure having a larger grain size compared to parent materials. Notably, the average grain size in AZ31B welds increases with higher TRS, resulting in significant grain coarsening compared to the

base material. At all tested speeds, the grain size exceeded that of the parent metals, which has an average grain size of 3.7 μm. This grain coarsening phenomenon is consistent with observations reported in previous studies on AZ31B Mg alloy FSW. Increased TRS generates more heat, leading to enhanced thermal exposure and promoting grain growth. The observed grain coarsening can impact the mechanical properties of the welds. These results emphasize the significance of optimizing TRS to balance heat input and grain size in FSW, ensuring weld quality and performance. Such insights are crucial for refining welding parameters and improving the overall effectiveness of the FSW process [95].

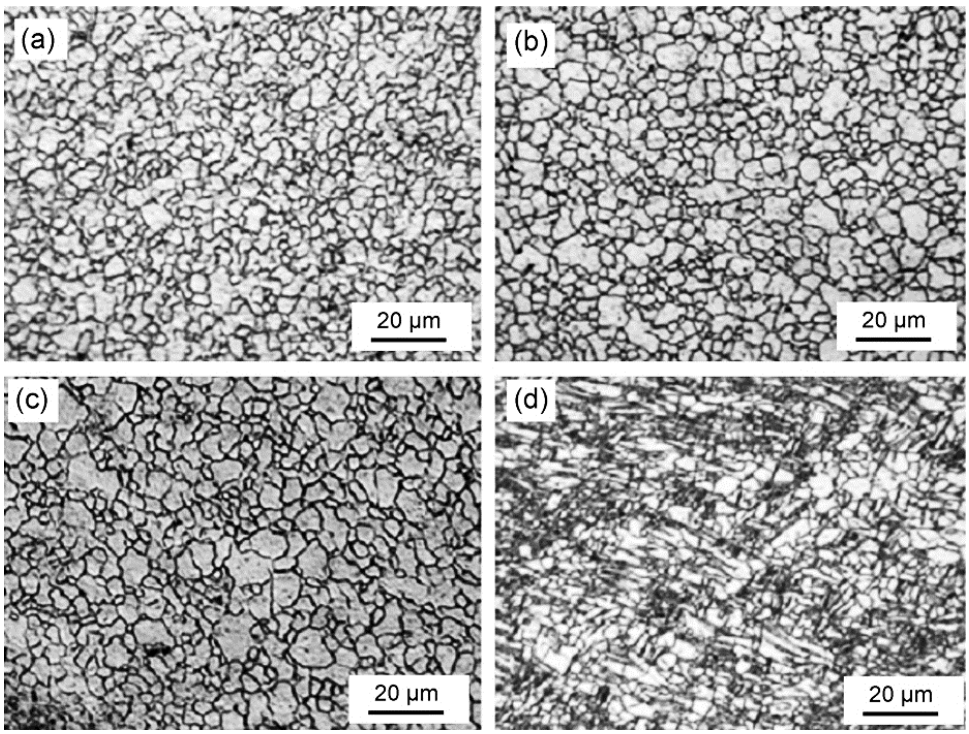

Figure 2.5: FSWed joint of Mg/Al alloys at SZ: (a) 900 rev/min, (b) 1120 rev/min, (c) 1680 rev/min, (d) AZ31B base [95]

In AZ31B friction stir welds, grain coarsening occurs due to the annealing effect of welding heat. At TS up to 15 mm/s, grain size in AZ31B alloy remains slightly smaller than the base metal at higher speeds. Grain refinement was observed in 2 mm thick AZ31B Mg sheets with a 10 mm shoulder diameter, but coarsening occurred with a 13 mm shoulder diameter under similar conditions. Although grain refinement and coarsening in AZ31B welds have been reported [96], the precise mechanisms remain unclear. Data indicates that these phenomena are influenced by welding

temperature and the initial grain size of the base metal. Temperatures exceeding 673 K at the probe likely contribute to grain coarsening, compounded by the absence of second-phase particles in AZ31B to inhibit grain growth.

2.1.2 Influence of reinforcement particles on the joint strength

FSW with reinforcement particles has emerged as a frontrunner in creating high-performance Metal Matrix Composite (MMC) welded joints. This technique integrates nanoparticle reinforcement during FSW, leading to significant improvements in properties like microhardness, corrosion resistance, and UTS [97, 98]. Pioneering Studies with Nanoparticles: Sun and Fujii (2012) observed a substantial increase in the microhardness of FSWed copper joints when reinforced with silicon carbide nanoparticles [97].

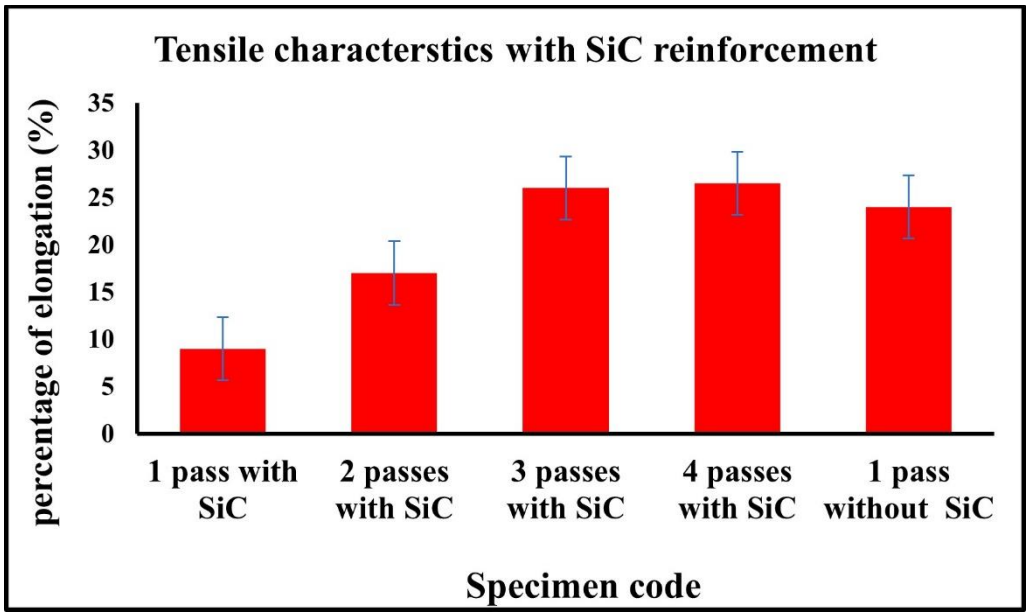

Figure 2.6: Variation of % elongation to the SiC nanoparticles with number of passes [99]

Saeidi et al. (2014) reported enhanced corrosion resistance and mechanical properties in dissimilar aluminum 5xxx series joints reinforced with Al_2O_3 reinforcement particles. These enhancements were attributed to rapid DRX and hindered grain growth within the joint [98]. Optimizing Welding Parameters: Beyond the nanoparticle type, optimizing welding parameters is crucial. For instance, Kang et al.

(2016) revealed that increasing the FSP passes for SiC-reinforced AA5086 welds improved joint efficiency and reduced grain size compared to single-pass welds without reinforcement [99].

Similar improvements were observed with other nanoparticles. Mirjavadi et al. (2015) reported positive results in AA5083 welds reinforced with titanium dioxide (TiO_2) nanoparticles [99, 100]. Researchers have investigated various nanoparticle reinforcements. Studies by Bahrami et al. (2016-2018) explored the impact of SiC nanoparticles on AA7075-O, reporting significant enhancements in joint toughness, fatigue life, and UTS [101-103]. Karthikeyan and Mahadevan (2015) attributed the improved tensile characteristics of FSWed AA6351 alloy with SiC reinforcement to the pinning action of SiC particles that prevents grain boundary expansion [104]. Beyond SiC, researchers are exploring other possibilities, such as B_4C, Al_2O_3, and metal powder nanoparticles [105, 106]. The reinforcement particle size also plays a key role. Nosko et al. (2017) examined the effect of Al-nanoparticle in FSW. They discovered that a decrease in particle size led to improved UTS and hardness [107]. Similarly, Tebyani et al. (2014) observed enhancements in microhardness and UTS of welds when reinforced with finer SiC nanoparticles (25nm) compared to larger particles [108]. Conventional welding is unsuitable for light metal alloys due to the formation of micro-defect and brittle IMCs. FSW overcomes these challenges, producing high-quality Mg-Al joints by dispersing IMCs under high strain rates and SPD at comparatively low temperatures. The successful joining of dissimilar pure aluminum and AZ31 has resulted in outstanding metallurgical [109].

The 7xxx and 6xxx Al-alloys can also be effectively joined to Mg alloys by FSW [110]. However, the formation of $Al_{12}Mg_{17}$ and Al_3Mg_2 IMCs may result in micro-cracks in AZ31 and AA1060 joints due to intercalation lamellae and complex vortex patterns [111]. The UTS of Al/Mg alloys is inversely correlated to the IMC layer's thickness, with thinner IMC layers improving UTS [112]. Key processing parameters affect the joint efficiency of Al/Mg. During the FSW of AA2024 and AZ31, the Al alloy on the AS and Mg alloy on the RS were for optimum welds [113]. In FSW joints of Mg/Al alloys, the TRS and TS are critical, with Al on the RS and tool offset towards Mg [114, 115]. Studies consistently observe the formation of Al_3Mg_2 and $Al_{12}Mg_{17}$ intermetallic phases during the welding of Al/Mg alloys by FSW [116, 117]. Controlling heat input, influenced by FSW passes, TS, and tool offset, is crucial to limiting these IMCs. Lower input heat reduces the interface between parents' material,

thus restricting IMC formation. TRS and TS suggestively affect the consequences in Mg-Al welding. The Bottom Interface zone (BIZ) shows insufficient Al-Mg mixing, and BSZ contains several brittle IMCs. Brittle fractures typically occur in the BSZ. Enhancing the strength of these specific areas, particularly the BSZ, is vital for creating more durable joints of Mg/Al FSW [118].

Studies have analyzed the metallurgical characteristics of AZ31 and AA2024 welded joints by different plate positions. Placing AA2024 on the RS and AZ31 on the AS improves joint efficiency [119]. However, in the case of AZ31 and AA6064 FSW, optimal joint efficiency was observed by placing AA6064 on the RS to prevent welding cracks during 0° TTA [120-123]. The FSW process promotes metallic bond formation through the convergence of jagged base metal edges under high pressure, effectively eliminating oxygen. Tool geometry significantly impacts joint efficiency, with improvements ranging from 15 to 45% [124]. A study on 12 mm-thick AZ31 and AA5083 plates showed superior welds when AZ31 was placed on the RS. This positioning, along with tool offset towards AZ31, enhanced the flow characteristics of the softer AZ31 magnesium during the retreating phase [125]. The analysis revealed that welding AA1050 and AZ31 at 2450 rpm and 90 mm/min TS produced a eutectic microstructure with higher hardness (~200 HV) compared to AA5083 (25 HV) and AZ31 (50 HV) [126]. FSW of AA2024 and AZ91D enables the creation of complex, high-strength, low-weight structures essential for the aerospace and automotive industries. Experiments showed that 6.35 mm thick AZ91C and AA6061 joints achieved 242 MPa strength at tool speeds below 1100 rev/min [127]. Optimal FSW conditions at 1200 rev/min for AZ80A and AA6061 alloys induced grain transition, resulting in a tensile strength of the joint 225.1 MPa, achieving 73.14% of AA6061'sAA6061's UTS and 77.79% of AZ80A'sAZ80A's UTS [128].

Optimal FSW at 1200 rev/min for AZ80A and AA6061 induced grain transition, achieving a UTS of 225.1 MPa, 73.14% of AA6061'sAA6061's UTS, and 77.79% of AZ80A'sAZ80A's UTS [129]. The corrosion performance of FSPMg/Al alloys was studied, revealing that TRS (800-1400 rev/min) and TS (50-200 mm/min) influence metallurgical characteristics. Grain refinement (~1 μm) increased corrosion rates, with the highest observed at 200 mm/min and 800 rev/min, reaching 0.018 mm/year [130].

Investigations into FSW of AA6082 and AZ31 joints revealed varying IMC adhesion qualities and thickness. UTS from 155 MPa to 173 MPa, with corresponding microhardness, elucidated by fractography to determine fracture modes [131]. FSW of

AA6061 and AZ91D innovatively creates defect-free joints in dissimilar materials, reducing distortion and eliminating melting-related defects. This method enhances mechanical properties over conventional welding, which is crucial for lightweight, robust structures in the aerospace and automotive sectors. These alloys excel in corrosion resistance, high strength-to-weight ratios, and recyclability, supporting fuel efficiency and environmental sustainability through reduced material waste and post-welding treatments.

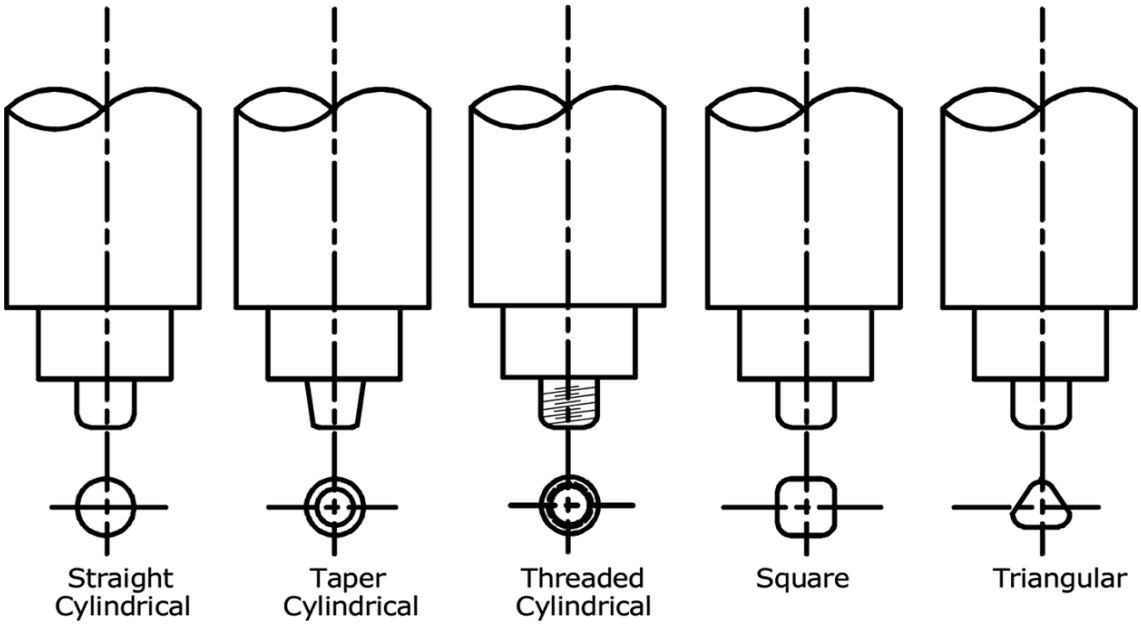

Figure 2.7: Five different tool profile [133]

The FSW pin profile may affect the metallurgical characteristics of the weldment. Due to precipitation hardening of the base metal, the UTS of the FSW joints increases. The ductility and UTS of flaw free FSWed joint is depends on the parent material's thermal properties. Various pin profiles are employed in FSW i.e., flat and cylindrical surface, square shapes, triangular shapes, octagonal, etc. Triangular and square faces are related by eccentricity.

it was observed that when same nature plates (specimen 4 and 2) were positioned in a certain way as shown in table 2, they exhibited better yield and UTS and percentage elongation compared to when the plates position was reversed. This improvement in properties may be due to rapid solidification. Furthermore, it appears that the straight cylinder pin profile observed higher UTS compared to the other profiles tested, possibly due to its sharp edge. Overall, these findings suggest that the UTS of Al

alloys might pretentious by factors such as sample composition, plate positioning, and pin profile, and that careful consideration of these factors can lead to improved mechanical performance in certain applications.

There were five FSW tool pin profiles, i.e., tapered, triangular, cylindrical, square, and threaded cylindrical used to join the base plate with various rotational speed (800 r/min to 1600 r/min) and perceived that square pin profile with TRS of 1200 r/min revealed enhanced UTS compared to other profiles [132].

Table 2.1: Tensile characteristics of the FSW joints of AA7075 and AA6061 [133]

Pin profile	Specimen	Base plate position	YS (Mpa)	UTS (MPa)	(%) Strain
Straight Cylinder	1	R.S-AA6061 A.S-AA7075	124.53	140.21	3.2
	2	R.S-AA7075 A.S-AA6061	174.13	196.96	8.8
Straight square	3	R.S-AA6061 A.S-AA7075	151.6	168.03	4.4
	4	R.S-AA7075 A.S-AA6061	163.76	181.2	9.2
Tapered Hexagon	5	R.S-AA6061 A.S-AA7075	164.15	184.5	6
	6	R.S-AA7075 A.S-AA6061	152.11	171.4	6.4

2.1.3 Micro-hardness

it was found that the tool pin profiles have a momentous impact on the micro-hardness of FSW weldments. The researchers investigated five different pin profiles, including a square, straight cylindrical, triangular with flat faces, triangular with concave faces, and threaded profile. The maximum microhardness values of 86 HV was perceived in joints welded with a square pin profile, while the minimum hardness (60 HV) was found in joints welded with a straight cylindrical profile revealed in fig. 2.8. The eccentricity, which is associated with triangular and square profiles, was also

found to have an impact on the micro-hardness of the weldment. In particular, the study observed that welded joints with a threaded profile demonstrated the maximum microhardness due to the occurrence of very refine equiaxed grain size in joints. The study also observed that the material is placed differently in the RS and AS of the weldment, with the RS containing material in the lower part of the weldment and the AS containing material in the upper part of the weldment. Overall, the study highlights the importance of considering the profile in FSW and its impact on the micro-hardness of the weldment [132].

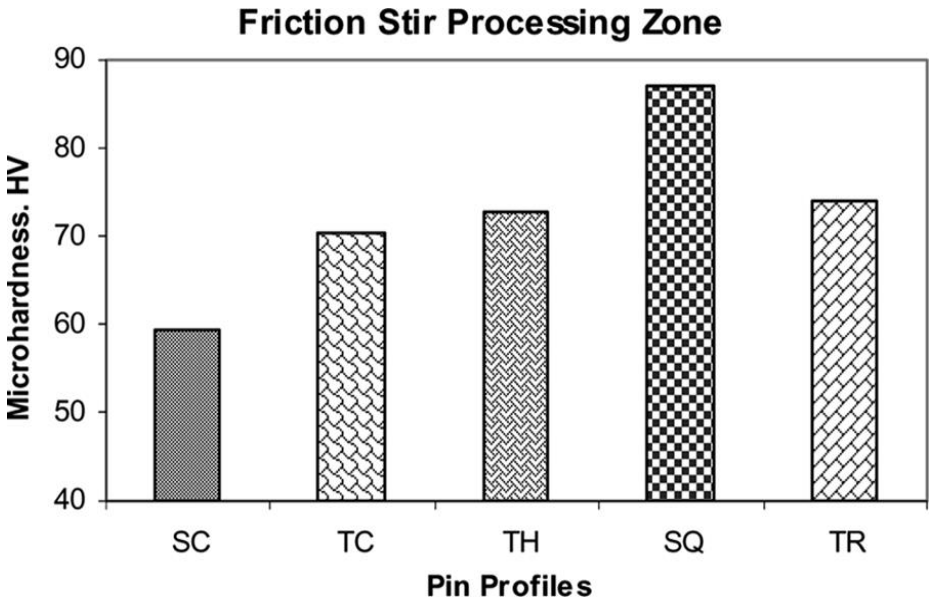

Figure 2.8: Influence of pin profiles on hardness at TRS of 1180 rev/min [132]

X.L Shi et al. [134] focused on the UTS of weldments of Al alloys produced using FSW with different parameters. The results exhibited which the ductility of the FSW joint improved to 11.7%, but there was a loss in yield strength, with values decreasing from 632 to 564 Mpa compared to the parent material. The study also observed that during the welding, DRX occurred, resulting in the materialization of refine grain structures in the weldment. DRX is a process that occurs during deformation where new grains are formed within a material due to the breakdown of existing grains. This can lead to improved mechanical properties, such as increased ductility, but may also result in a loss of strength.

Dawood et al. [135], it was observed that pin profiles used in FSW of AA-6061 Al alloy have a momentous effect on the metallurgical characterization of the weldment. In their investigation, they used various profiles, i.e. square, cylindrical, threaded

cylindrical, and triangular and compared their effects on the weldment. Their analysis showed that the triangular profile resulted in the best microstructural properties among the different pin profiles used. The use of a triangular pin profile led to a more refined and homogeneous microstructure with fewer defects such as voids and porosity. Additionally, the weldment produced using the triangular profile exhibited maximum strength and ductility associated to those welded using other pin profiles. In contrast, the UTS and microhardness were observed with the square pin profile. The fractured surface shows that the square and threaded tapered cylindrical specimens break with brittle fractured due to excess heat generation during FSW. In contrast, ductile fractured was observed in the triangular pin profile.

R.S Mishra et al., [136] concluded that at high temperature ranges from 490º to 530º for one hour for AA7075, the refine grain structures were perceived stable. At this temperature ranges, the strain rate range was found from $1x10^{-3}$ to $1x10^{-1}$. At 480° C, with strain rate ranges from $3x10^{-3}$ to $3x10^{-2}$, the superplastic elongation of 1250% was observed. In contrast, maximum ductility (1042%) was found at 498°C.

T. Srinivasa Rao et al. [137] investigate the FSW of thick plates (10mm and 16mm) of AA7075 Al alloy. The researchers were able to achieve full penetration and defect-free weld by carefully selecting the process parameters. It was perceived that the microhardness in the HAZ decreased for the 10mm thick plate due to the higher input heat used through FSW. The UTS of the FSWed joint for the 10mm thick plate was found to be higher compared to the 16mm thick plate. The efficiency of the joints for the 16mm thick plate was observed to be 53%, while a joint efficiency of 70% was achieved for the 10mm thick plate. Previous research has reported joint efficiencies of 82-92% for 2-5 mm thick plates of the similar metal.

Nilesh Kumar, R.S Mishra., [138], analyzed that FSP was employed to enhanced the microstructure and UTS of the base plate. The FSPed plate was observed equiaxed and ultrafine grain structure compared to base plate by changing the input prosess parameters. The Al-alloy Al-Mg-Sc was processed with three different tools rotational speed (325, 400, and 800 rev/min). Depending on the process parameters, the grain size of the weldment varied from 0.39 to 0.89 μm. When the Zener-Hollman parameter is increased, the reduction of grain size was observed. It was found that under current deformation and microstructural conditions, DRX may not be possible during FSP.

ZY Ma, [139] examined the multipass FSP (MPFSP) on the Al-alloys od A356 and found that the strength of TMAZ and HAZ was decreases when the distance from the 5^{th} pass increases, and the UTS and ductility of single pass and fifth pass welded plate are almost. MPFSP did not influence the dissemination of Si particles, aspect ratio, and grain size of the welded plate. The silicon particles were uniformly distributed during the single or multiple-pass processing.

Z.Y. Ma, et al., [140], analysed that the influence of double passes on the metallurgical characterization of FSP of AA7075. Almost similar grain sizes ranging from 5.3 to 5.8 μm were found in single and double pass FSP. The higher temperature was observed in a double pass FSP. Double pass FSP found an improvement in superplastic strain as compared to single-pass FSP Al-7075. At 480°C, the maximum elongation of 1220% was found in the 2^{nd} pass FSP on AA7075.

Jianqing Su, Jiye Wang et al., [141], analysed the FSP on a 2mm thick plate of Ti-6Al-4V by different parameters, i.e., TS (1-4 IPM), TRS (800 rev/min, 1000 rev/min). The higher TS and lower TRS resulted in α colony and refine β grains size, giving higher UTS. The higher UTS and YS was observed 1156 MPa and 1067 MPa, respectively, without losses of ductility at TRS of 900 rev/min with a TS of 4 IPM.

F. Khodabakhshi et al. [142] analyze the potential of FSP for the fabrication of AMC with nano and micro particles. The researchers found that FSP has greater mechanical properties compared to the other fusion welding process. he researchers found that FSP could effectively incorporate nanoparticles into the Al matrix to form hybrid micro and nanocomposites. The tensile properties of the fabricated AMCs were perceived to be significantly improved compared to the base Al alloys. The researchers attributed this improvement to the refined microstructure, increased grain boundary area, and improved distribution of the nanoparticles in the MMC.

Sun YF et al. [143] investigate the consequence of MPFSP (FSP) on the uniform spreading of nanoparticles in copper plates. In the study, nanoparticles were incorporated into 2mm thick copper plates, and FSW was performed for one and two passes. It was found that the second pass FSPed plate showed a more uniform dissemination of the nanoparticles associated to the first pass. The MPFSP reduced the cluster size and led to a fall in grain size, resulting in a uniform dissemination of reinforcement particles. The researchers observed that the dissemination of reinforcement in the copper matrix was influenced by the FSP parameters, such as the TRS, TS and FSP passes.

Gibson BT et al. [144] suggested that the FSW/FSP have an extensive range of applications in the aerospace and automobile industries due to its ability to produce high-quality, defect-free welds with enhanced UTS, hardness, and wear properties. omechanical properties. The first implementation of FSW/FSP was initiated by NASA in 1998 for manufacture space shuttle tanks. In the automobile industry, FSW/FSP has been used for the fabrication of body structures, frames, and engine components. The technique has also been used to join dissimilar metals i.e. Al to steel, which is difficult to achieve using conventional welding methods. The U.S. Navy has also used FSW/FSP for marine applications, such as welding of 7xxx, 6xxx, and 5xxx series Al alloys for shipbuilding.

Azimzadegan T et al. [145] investigated the metallurgical characterization of FSWed joints of AA7075. The researchers found that the precipitation hardening of the joint was depending on the dissemination of strengthening precipitates in terms of their size, shape, and volume. They observed that the tiny grains size in the SZ resulted in a higher microhardness compared to the HAZ and TMAZ. However, they also found that the microstructure in the HAZ and TMAZ regions experienced a decreasing trend due to the dissolution and coarsening of the segments. The researchers also perceived that the UTS of the welded joints was influenced by the microstructure of the joint, with the joints exhibiting a higher strength when the microstructure was more homogeneous.

Deore HA et al. [146] analyzed the influence of MPFSP with SiC filler on the metallurgical characterization of AA7075. The researchers found that the microhardness value increased due to the improvement of grain modification of the multipass FSP region. They observed that during multipass FSP with SiC nanoparticles, the heat generation and plastic strain occur due to the rotating tool. This leads to the materialization of fine grains through DRX.

Rathee S. al., [147], analyzed that the location of the fracture was observed with in the HAZ in all MPFSP. To improve the metallurgical characterization of multipass FSP, the fracture analysis of the FSP is significant. The fraction location of multipass FSP sample was changed as revolutionary pitch change. When increasing the revolutionary pitch led to a shift in the fractured location of the FSWed joints from the TMAZ towards the weld centerline. This was attributed to the fact that increasing the revolutionary pitch results in a decrease in the input heat and a decrease in the amount of material that is stirred during the welding process, leading to a reduced

strain hardening in the TMAZ. The consequence of the revolutionary pitch on the fracture location and UTS of FSW joints of magnesium alloy. The researchers found that increasing the revolutionary pitch resulted in a shift in the fracture location towards the weld centerline and an improvement in the UTS of the joint due to the decrease in the heat input and the reduction of flaws in the joint. Overall, the revolutionary pitch effect on the fracture location in FSW joints is dependent on several factors, including the material being welded, the welding parameters, and the tool geometry.

O. Lorrain et al. [148] conducted experimentations on unthreaded tool profiles with and without flat faces. The purpose of their study was to examine the material flow in the weld using longitudinal and transverse sections. Their results indicated that the material flow using unthreaded pin profiles with flat faces was similar to that of classical threaded tools.

Harish Suthar et al. [149] analyzed the failure behavior of the FSWed joint of AA7075 and AA6061, and they observed that the welded region was softened at HAZ in AA6061. The microhardness was perceived to be low in the HAZ region. The fractography analysis has revealed that there is inadequate fusion of the material at the SZ-TMAZ interface. This means that the material did not properly fuse together in that region, which could be due to a variety of factors such as improper welding technique or incorrect welding parameters.

Jerry wong et al., [150], observed better weld joint with no defect at higher TS and intermediate TRS, and the SZ observed refine grain's structure due to DRX. The UTS was also enhanced on these parameters which confirm above results.

Noor zaman et al., [151], investigated the FSWed joints' fracture surfaces, hardness, microstructure and mechanical properties of AA7475 and AA2219, and observed that, due to dynamic recrystallization generated by significant plastic deformation, grain refinement is exhibited near the SZ. The dissimilar joint has the lowest strength due to the non-homogeneous movement of parent metal caused by variances in physical and mechanical properties. Due to thermal softening, the TMAZ retreating side of all joints had the lowest hardness. Similar joint fractured surfaces demonstrated more ductile fracture than dissimilar joint fractured surfaces, resulting in lesser elongation of the dissimilar joints.

Rodriguez et al. (2015) [152], the microstructural characterisation of the AA6061 and AA7050 Al-alloys was examined by The remaining variables are maintained

constant, except for the rotating speeds. The microstructure displays bands of mixed and unmixed components indicating the degree of material mixing when the RTS was changed. The intermixing of the materials and joint strength are improved by an increase in RTS. According to scanning electron microscopy, incorrect material intermixing causes failure in the SZ at low RTS.

Jianqing Su, Jiye Wang, [153] examined the FSP on a 2mm thick Ti-6Al-4V plate using various process parameters, including feed rate (1-4 IPM), rotational speed, and temperature (800 rev/m- 1000 rev/m). In the SZ of the FSP samples, a basketweave lamellar structure indicates an altered microstructure. Higher UTS was produced due to the colony and fine grain sizes produced by the higher TS and lower RTS. At a RTS of 900 rev/m and a TS of 4 IPM, the higher tensile and yield strengths of 1156 MPa and 1067 MPa were recorded without ductility losses.

Gibson BT et al., [154], studied how widely the aerospace and automotive sectors employed the FSW/FSP approach. NASA used the FSW/FSP process to create the first space shuttle external tanks in 1998, marking the start of the first FSW/processing application. The US Navy used FSW of the 5xxx and 6xxx families of aluminium alloys for maritime operations.

B.B. Verma et al., [155], among high-strength aerospace-grade aluminum alloys, AA 7475 provides a better mix of strength and fracture toughness. It is used in a variety of aviation parts that require a mix of desired qualities. It has also been noted that the aluminum alloy AA7475 exhibits outstanding corrosion fatigue behavior.

M. Esmaily et al. 2010 [156] to investigate the heat distribution in the welding process. Their research focused on the welding of an Al-alloy and high-carbon steel. They employed the finite element approach and the Arbitrary Lagrangian-Eulerian (ALE) formulation to analyze this process. By enhancing the meshing intervals and optimizing mesh transfers, they effectively minimized excessive element deformation, thereby increasing the accuracy and reliability of the results obtained. These measurements were used to construct a temperature diagram based on thermocouple readings, providing valuable insights into the temperature profiles during welding. This research contributed to understanding the heat distribution in welding and demonstrated the importance of precise numerical simulations and experimental data in evaluating welding processes involving dissimilar materials.

Nilesh Kumar, R.S Mishra., [157], analysed that FSP was used to improve the UTS of the base plate. The FSPed plate was observed equiaxed and ultrafine grain structure

compared to base plate by changing the input process parameters. Three separate tools with varying rotational speeds were used to produce the aluminium alloy Al-Mg-Sc (325, 400, and 800 rev/m). The grain size of the FSWed joint varied from 0.39 to 0.89 m depending on the procedure conditions. The reduction of grain size was noticed when the Zener-Hollman parameter was raised.

Kalemba Rec et al. (2018) [158] studied the impact of FSW parameters on the tensile characterisation and microstructures of dissimilar weldments made of the alloys AA5083 and AA7075 was examined. Various factors are considered. In the configuration, the RS has the AA7075-T651 alloy, and the AS has the AA5083-H111 alloy. Furthermore, increased rotational speeds result in a more significant mixing of the two materials. Despite this, other flaws, such as porosity, wormholes, voids, and porosity, were discovered in the weldment's SZ. Regardless of arrangement or pin design, an increase in RTS causes a reduction in mechanical characteristics. Higher weld efficiency and UTS are achieved when a triflate pin is used.

R.S Mishra et al., [159] concluded that at high temperature ranges from 490º to 530º for one hour for AA7075. At this temperature ranges, the strain rate range was found from $1x10^{-3}$ to $1x10^{-1}$. At 480° C, with strain rate ranges from $3x10^{-3}$ to $3x10^{-2}$, the superplastic elongation of 1250% was observed. In contrast, maximum ductility (1042%) was found at 500°C with a strain rate $3x10^{-3}s^{-1}$.

Mehta et al. (2016) [160] evaluated the impact of TTA on electrolytic tough pitch copper and aluminium 6061-T651's different FSW's microstructural and mechanical properties. The tool TTA in this experiment ranges from 0 to 4 degrees with a regular 1-degree interval. In addition, constant values are maintained for several parameters, including TS, workpiece material position, tool pin offset, and RTS. Weld joint qualities are investigated using a variety of tests, including SEM, XRD, EDX, hardness and tensile test. Numerous testings reveals that the weld at the TTAs of 2°, 3°, and 4° is flawless. At 4° in the SZ, the greatest UTS and macro hardness are attained. The TMAZ confirmed the weakest zone on the copper side.

Bozkurt and Duman (2011) [161], studied the mechanical property variations of FSWed joints of AA3003 and AA2124 at RTS of 850 rev/m and TS of 130 mm/min. It was also observed the greater UTS is about 182 MPa. Moreover, the microhardness through the SZ varies, and the least value occurred on the R.S of the HAZ.

Harish Suthar [162] analyzed the failure characteristics of the friction-stir-welded (FSW) joint of AA7075 and AA6061 alloys. Their observations revealed a notable

softening of the welded region, particularly in the HAZ of the AA6061 component. Significantly, a decrease in hardness values was documented within the HAZ region, indicating alterations in the material's mechanical properties in this zone. Fractography analysis unveiled essential insights into the failure mechanism, indicating insufficient fusion of the materials at the SZ and TMAZ interface. This insufficient fusion resulted in a lower density of tiny dimples on the fracture surface, implying lower strain during the fracture process. Additionally, the presence of facets further corroborated the fracture pattern, shedding light on the mechanisms at play during the failure of the FSW joint in this specific alloy combination.

Wang et al. [163] conducted the mechanical assessment of as-extruded welded joints, focusing on the impact of various Friction Stir Welding (FSW) process parameters. Their analysis revealed a notable enhancement in the ductility of the FSWed joints, which improved to 11.8% compared to the parent material. Although there was a slight reduction in the tensile properties—from 632 to 564—this trade-off demonstrated the increased ductility achieved through the FSW process. One of the critical observations during FSW was the development of a fine and equiaxed grain structure, which was attributed to dynamic recrystallization. This structural transformation indicates the favorable changes in the material microstructure during the FSW process, contributing to the improved ductility of the welded joints.

Pourali et al. (2017) [164] examined how process variables affected an aluminium and steel FSWed joint. At the FSWed joint, thick intermetallic compounds occur due to the significant differences between steel and aluminium. The difference in the material thickness is assumed to be 2mm, and FSW lap welded AA1100 and mild steel. The process parameters were RTS of 315 rpm and 400 rpm and TS of 50 mm/min and 63 mm/min. The EDX analysis reveals that a thick layer of Fe-rich intermetallic compound was produced in welded joints surface up to 93 µm since it has no impact on the strength of the FSWed joints. Additionally, defects in the welded zone may cause harm, which affects the welded joints' strength. High heat input was observed with high TRS, which ensures good metallurgical and mechanical mixing. Lower TS leads to good mechanical properties.

Raghu Babu et al., (2008) [165] investigated the influence of the process parameters on mechanical properties and microstructural of AA6082-T6. They identified that the UTS of the parent metal is greater than the FSWed joint. The tunnel defects were also

observed at the intersection of TMAZ and SZ due to high RTS and TS, and the hardness was decreases in the weld region.

Ratnam et al. (2018) [166] optimise and enhance the tensile characteristics of two 6mm FSW alloys, AA2024 and AA6061. The levels TS, RTS, and TTA, are selected. L27, the orthogonal array, calculates the findings using Taguchi's ANOVA. TS is the most critical aspect of RTS and the least important in UTS. The best UTS is obtained at TS of 11mm/min, RTS of 1340 rev/m, and TTA of 2°. RTS and TS are the most significant and least essential elements in hardness, respectively. With a TTA of 3° and a TS of 11 mm/min, RTS 2000 rev/m.

Hassan et al. (2003) [167], Investigated the effect of FSW parameters on the metallurgical characterstics of the welded joints of AA7010, and it was revealed that the optimum TS and TRS which gives the excellent mechanical properties in the stir zone. As the TS rises, it was required to increase the TRS to retain the optimum condition. Variation in the grain size and the microhardness was found from the top to bottom of the welded joints for a given TS.

Lorrain (2010) [168] aimed at the mechanical assessment of FSW joints in 4 mm thick plates of AA7020-T6 alloy. Their investigation involved using two distinct pin profiles, one with threads and the other without, featuring flat faces. They discovered that the material flow patterns observed when using the conventional threaded tools closely resembled those observed when employing the unthreaded tools, thus indicating a high degree of similarity in material deformation characteristics. This comparative analysis of different pin profiles offered valuable insights into the mechanical properties of FSW joints and the influence of pin profile variations, shedding light on the potential advantages and disadvantages associated with each.

V. Saravanan in 2015 [169], an examination was undertaken to assess the tensile properties and microstructure of AA2014 and AA7075 alloys. The investigation revealed that the highest UTS, reaching 346 MPa, was achieved at a RTS of 1200 revolutions per minute (rev/m) and a TS of 20 mm/min, with an axial load of 8 kN applied. Conversely, the lowest microhardness values were observed within the As-Welded (A.S) region of the HAZ. In contrast, the most excellent hardness level, measuring 146 HV, was identified within the SZ. This observation indicated the distinct mechanical characteristics present in different zones of the FSW joints. Moreover, the SZ exhibited a fine recrystallized microstructure, contributing to the superior tensile properties and increased hardness of the FSW joints.

Jerry wong et al., [170], observed better weld joint with no defect at higher TS and intermediate RTS, and the SZ observed fine and equiaxed grains structure due to recrystallization. The UTS was also enhanced on these parameters which confirm above results.

Daood et al. [171] delved into the impact of pin profiles on the mechanical properties of FSWed joints in AA6061. Their investigation involved the utilization of various pin profiles, specifically triangular, square, and threaded tapered cylindrical shapes. Their findings unveiled a distinct trend: the best mechanical properties were achieved when using the triangular pin profile, surpassing the outcomes of the other pin profiles. The threaded tapered and square pin profiles led to brittle failures attributed to excessive heat generation during welding. The triangular pin profile resulted in a ductile failure mode, signifying a more favorable and robust performance. This study highlights the critical role of pin profiles in influencing the mechanical characteristics of friction stir-welded joints, underscoring the significance of their selection in optimizing welding outcomes.

Sachin Kumar et al. (2021) [172], successfully fabricated FSWed joints of AZ31B and AZ31B and AA6061 alloys with and without ultrasonic vibrations. Ultrasonic assistance significantly enhanced material flow and intermixing in the SZ of Al and Mg layers, forming homogeneous intercalated lamellae. Symmetric weld morphology and Mechanical interlocking were improved due to acoustic turbulence. The Al-SZ exhibited higher hardness than the Mg-SZ due to the IMCs phase, though the ultrasonic joint's maximum microhardness was 16.5 HV lower than the conventional joint. Both traditional and ultrasonic joints displayed dual IMCs, but XRD analysis revealed reduced peak heights and IMC distribution in ultrasonic joints. Fracture samples failed in regions with high IMC accumulation, with acoustically treated samples showing swallow and deep dimples, indicating a mixed fracture pattern. This research highlights the advantages of ultrasonic vibrations in enhancing the joint efficiency of the Mg/Al FSW joints.

Sachin Kumar et al. (2020) [173] positively achieved ultrasonic-assisted FSW (UVaFSW) on AZ31B and A6061. They observed significant improvements in the joint properties. The IMCs thickness at the butt interface was reduced by up to 57.90%, from 9.4, 5.0, and 2.8 microns to 4.4, 2.1, and 1.4 microns, respectively, with ultrasonic assistance. This reduction enhanced joint strength to 161 MPa and joint

efficiency to 70.3%, compared to 58.4% without ultrasonic assistance. Improved material flow and reduced defects were also noted.

Chunliang Yang et al. (2020) [174] established a mathematical model to analyze aluminum-magnesium FSW, focusing on dissimilar materials. Simulations showed that Mg-Alloy properties dominate near the FSW tool, while aluminum properties dominate farther away. A variable volume fraction index, n(r), provided results closer to experimental measurements compared to a constant n=1. This approach enhances the understanding and application of dissimilar material welding.

Huachen Liu et al. (2020) [175] investigated the study on the effects of tool offset in Al/Mg dissimilar alloy FSW and found that optimal microstructures and mechanical properties were achieved with Mg on the advancing side (AS) and an offset towards Mg. However, a 2.5 mm offset caused defects due to insufficient stirring. $Al_{12}Mg$ and Al_3Mg_2 and IMCs could not be eliminated, but their distribution improved with a specific offset. The UTS increased with offset, peaking at 1.5 mm with 108 MPa, while the maximum hardness value in the SZ decreased as offset increased.

Bandi et al. (2020) [176] investigated the lap FSWed joints of a 3 mm thick plate of AZ31 and AA6061 with the AA6061 on top. Trials varied pin length (3 to 4.5 mm) and TRS (600 to 1000 rev/min). Eutectic mixtures Mg17Al12 were perceived on both sides. Failure modes included interface failure and sheet failure, with Mode 1 showing the highest strength (149 ± 5 N/mm) for 3.2 to 3.8 mm pins at 700 rev/min. The maximum lap shear strength (214 ± 4 N/mm) was observed with a 4.5 mm pin at 650 rev/min, attributed to Mode 2 failure.

Sameer MD (2019) [177] concluded that FSWed joints of AZ91 and AA6082 alloy placing AZ91 Mg on the AS resulted in higher aluminum content in the SZ than putting it on the RS, affecting mechanical properties. The highest UTS (173.2 MPa) was achieved with Mg on AS, and a lower UTS (157.65 MPa) with Mg on RS. A thin IMC was observed in the D1 specimen (Mg on AS), while a thicker layer with poor adhesion was seen in the D2 specimen. Fractography showed brittle failure due to IMCs. Hardness was 86 HV with Mg on AS and 89 HV with Mg on RS.

Abdollahzadeh et al. (2018) [178] successfully fabricated FSWed joints of AZ31 and AA6061 with SiC nanoparticles. Optimal conditions were 35 mm/min travel speed and TRS of 650 rev/min. The reinforced sample's UTS was 28% higher, and elongation improved threefold compared to the non-reinforced sample. SiC nanoparticles significantly refined the nugget's grain structure, reducing the Mg side's

mean grain size (12 to 3 µm). The reinforced sample's stirred zone exhibited higher microhardness due to SiC's hardness and grain boundary stabilization. Low hardness fluctuations confirmed homogeneous nanoparticle dispersion. All samples fractured along the banded structure on the AS; non-reinforced samples showed brittle fractures, while reinforced samples exhibited ductile, zigzag-shaped fractures, enhancing ductility.

Zhao Y et al., (2016) [179] successfully joined the FSWed joints of AZ31 and AA6013 with underwater and conventional processes and observed that at a TRS of 1,200 rpm and a TS of 80 mm/min, water-cooled welding improved joint strength to 152 MPa, compared to 131 MPa in air. The air-welded joint had a higher microhardness due to more vigorous stirring. Both joints exhibited brittle fracture.

Banglong Fu et al. (2015) [180] achieved defect-free FSWed joints of Mg/Al with excellent metallurgical properties using an intermediate rotation rate (600–800 rev/min) and low TS (35-65 mm/min), with Magnesium on the AS and a 0.28 mm tool offset towards Mg. UTS got up to 72% of the Mg, with distinct zones in the nugget area: severe intercalated zones, shoulder-affected, and banded with Al-Mg intercalated structures. Intermetallic such as Al_3Mg and $Al_{12}Mg_{17}$ formed, along with a eutectic structure. Heat input, intended from spindle torque, increased when Al was on the AS and decreased with higher rotation rates and TS. Effective intermixing and intermediate heat input significantly enhanced weld properties.

Yong Zhao et al., (2015) [181] successfully fabricated AZ31 and AA6013 welded joints underwater. They observed that the optimal welding with a TS of 80 mm/min and a TRS of 1200 rev/min resulted in sound welds with good tensile properties. The underwater FSWed joints achieved a UTS of 153 MPa, 64% of AZ31 strength, but exhibited low ductility due to IMCs. XRD analysis identified Al_3Mg_2 and $Mg_{17}Al_{12}$ in the fracture surface. EPMA images revealed that Al and Mg elements formed a mixed structure in the SZ, with EDS analysis showing lamellar shear bands of DRX at the SZ. A thin IMC was observed compared to air-welded specimens. Microhardness tests showed the highest microhardness value of 143HV at the SZ, slightly more significant than the AA6013.

Kwang-Jin Lee et al. (2014) [182], investigated the metallurgical characterization of the welded joints of AZ31 and AA6061. The welds were produced with the tool plunge position shifted toward AZ31. Optimal TRS and TS were determined through preliminary experiments. EBSD was used to analyze the texture in the SZ, revealing a

fine-grained microstructure. AA6061-T6 exhibited randomized plane orientations, while AZ31 had rotated basal plane orientations. The average grain size was 2.5−4.5 μm. No welding defects were found, and the interface showed lamellar-like shear bands, indicating intense material flow.

Liang, Z. et al. (2013) [183] achieved joints with high UTS of 164 MPa and a significant % strain of approx.—6% of FSWed joints of Al-Mg alloys. The bottom interface (BI) zone, resulting from inadequate diffusion and material mixing, and the banded structure (BS) zone, containing IMCs, while the softened Al alloy to the retreating side (SAA-RS) zone, due to precipitate coarsening and dissolution. By optimizing TRS and offset, the strengths of these zones were balanced, enhancing ductility and maintaining high strength.

P. Venkateswaran et al. (2012) [184] exhibited the Al–Mg dissimilar FSWed joints at lower TRS, while higher speeds (>850 rev/min) produce interpenetrating features and curved interfaces, promoting micro void amalgamation on fracture surfaces due to the mechanical interlinking. UTS increases with microvoid coalescence area fraction, interpenetrating, and interface length feature thickness but decreases with thicker IMCs. The increased strength is due to mechanical interlocking, creating a longer fracture path. Optimal parameters include a TS of 1.8 to 3.5 mm/s and a TRS of 850–1700 rpm. Microhardness distribution is influenced by grain size and IMCs. $Al_{12}Mg_{17}$ and Al_3Mg_2 IMCs inevitably form, with tensile failure occurring through IMCs and aluminum in IPF regions. Maximum tensile strength in Al-Mg FSWed joints is achieved through complex weld interfaces promoting mechanical interlocking.

Jing Shang et al., (2012) [185], successfully fabricated Mg and Al dissimilar metals by CMT process by copper wire. The optimized process parameters of TS of 0.65 m/min, wire feed rate of 5.8 mm/s, a voltage of 12.0 V, and welding current of 129 A were observed. Various IMCs, such as AlCu and Cu9Al, formed in the Al fusion zone, while a Cu-based solid solution appeared in the welded region. The Mg fusion zone contained Cu4Mg and a ternary eutectic structure. The joint's bonding strength was 34.7 MPa, with brittle fracture occurring at the highest micro-hardness point in the Mg fusion zone due to continuous Cu-Mg IMCs. It revealed the feasibility of CMT welding for joining Mg and Al with pure copper filler metal.

Woong-Seong Chang et al. (2011) [186] enhanced the strength of dissimilar joints. They investigated the IMC improvement using a third material foil in FSWed and hybrid welded joints of AZ31 and AA6061. The metallurgical properties of FSWed

joints and hybrid weldments were compared. Hybrid butt welding with filler wire of Ni foil and defect-free laser-FSW hybrid joining by 2 kW laser power was successful. The transverse UTS of the hybrid welded joint reached 66% of the Mg parent material UTS due to fewer IMCs. Joint strengths were 66% for hybrid welding, 45% for FSW with Ni foil, and 38% without Ni foil.

Yan Yong et al. (2010) [187], successfully investigated the joining of AZ31 and AA5052 alloy by FSW having a thickness of 6 mm at TS of 35 mm/min and TRS of 600 rpm. The SZ exhibited a refined microstructure with intercalation lamellae, differing significantly from the base materials. Microhardness measurements showed uneven distribution due to the weld's complex microstructure, with the SZ reaching twice the maximum hardness of the base materials. The fracture occurred 2.7 mm from the weld center on the AA5052 side, where microhardness decreased sharply. This process produced a sound weld, transforming the base metal microstructure into equiaxed grains in the SZ, with a distinct onion-ring structure at the bottom.

Somasekharan et al. (2004) [188], successfully joined AZ91D and AZ31B, and 6061-T6 alloys using friction-stir welding, demonstrating DRX and fine-grained structures. Elemental analysis revealed distinct bands of Mg and Al. Vickers microhardness showed stable properties, with spikes up to three times the base hardness, indicating the technique's effectiveness for creating solid and high-quality welds in dissimilar materials.

Table 2.2: Literature review of some similar and dissimilar alloys

Author & year	**Material Used**	**Processing Parameter**	**Conclusion**
C. Hamilton et al [2009] [189]	Al-Zn-Cu-Mg	TRS: 225 to 400 rpm TS: 2.1 mm/s	The model accurately predicts the maximum welding temperatures and their distributions across the investigated energy range.

C. Hamilton et al [2008] [190]	AA6061	TRS: 50-550 rpm with constant TS of 50 mm/min	A thermal model of FSW, incorporating a new slip factor based on energy per unit weld length, was developed. It effectively predicts maximum welding temperatures across diverse energy levels, demonstrating its robustness and accuracy in thermal analysis for various welding conditions.
S. Hwan et al. [2003] [191]	SS304	TRS: 1400 rpm TS: 1.3 mm/s TTA: 3.5°	Microstructural observation revealed the formation of sigma phase with numerous stacking faults at the advancing side of the stir zone, highlighting localized microstructural changes induced by the FSW.
G. Buffa et al [2011] [192]	A 3D FE model.	TRS: 500 rpm TS:100 to 325 mm/min	A new numerical FEM procedure was used for predicting residual stresses in FSW, revealing how grain refinement and heat treatment affect the corrosion behavior of Mg-Y-RE alloy through various testing methods.

G.R. Argade at al [2012] [193]	Mg Alloy	TRS: 800 rpm TS: 25 mm/min	The findings highlighted significant insights into how the welding conditions influence grain refinement, residual stress distribution, and overall mechanical performance.
Y.S. Sato et al [2004] [194]	AA1100	TRS: 500 rpm TS 1.2 mm/sec	FSW was applied to accumulative roll-bonded (ARBed) AA1100, resulting in the reproduction of fine grains in the SZ and slight growth of ultrafine grains just outside the SZ. This demonstrates FSW's effectiveness in refining grain structures in ARBed materials.
S. Mironov et al [2011] [195]	S31254 steel	TRS: 400 rpm TS: 30 mm/min	The structural response of low stacking fault energy material S31254 to FSW has been examined. The final SZ microstructure formation is primarily influenced by DDRX occurring during the FSW cooling cycle.

L. Fratini et al [2010] [196]	AA7075	TRS: 700 to 1500 rpm TS: 105, and 214 mm/min	The effects of in-process cooling on the material characteristics and joint performance of AA7075-T6 were examined. The study highlights how cooling during processing influences the alloy's properties and the overall quality of the welded joint, providing valuable insights for optimizing welding conditions to improve joint performance.
S.Mironov et al [2009] [197]	Pure Titanium	TRS: 200 rpm TS: 65 mm/min	The microstructure evolution during FSW of commercial titanium was investigated. Material flow resembled simple-shear deformation, primarily arising from prism slip. The grain structure evolution was found to be a complex, multi-stage process, highlighting the intricate nature of microstructural changes during FSW.
L.Commin et al [2009] [198]	AZ31	TRS: 1000, 1300, and 1400 rpm TS: 200, 300, and 700 mm/min.	Higher stress levels were observed on the retreating side, with grain growth increasing alongside

			processing parameters that generate more heat. FSW resulted in reduced UTS for the hot-rolled base metal alloy.
R.Nandan et al [2007] [199]	Mild Steel	TRS: 450 rpm TS: 0.42 mm/s Pin length: 6.22 mm Pin radius: 3.95 mm	3D plastic and temperature flow fields during FSW of mild steel were calculated using conservation equations for mass, momentum, and energy. The non-Newtonian viscosity, varying spatially, was derived from computed strain rate values, providing insights into the material behavior under welding conditions.
N.Kamp et al [2006] [200]	AA7449	The interfacial energy of the different rates and phases were considered.	This model based on Kampmann and Wagner Numerical (KWN) effectively forecasts the changes in precipitate behavior, enhancing the understanding of alloy microstructure development under various processing conditions.

S.R Ren et al [2007] [201]	AA 061	TRS: 400 to 1600 rpm TS: 100 to 400 mm/min	The study found that traverse speed significantly influences the tensile properties and fracture modes of FSW AA6061 joints. Welds made at 400 mm/min exhibited higher strength and a 45° shear fracture, while those welded at 100 mm/min showed lower tensile strength with nearly vertical fractures.
Omar.S. Salih et al [2015] [202]	Al composite	TRS: 600 to 1000 rpm TS: 40 and 80 mm/min	Welding parameters, including TRS, TS, and axial force, significantly impact heat generation and the strength of FSW joints. Microstructural evaluation revealed tunnel defects caused by improper flow of plasticized metal due to suboptimal welding conditions.
Z.Y. Ma et al [2010] [203]	Al-4Mg-1Zr alloy	TRS: 600 rpm TS: 25 mm/min	Exceptional superplasticity exceeding 1200% was observed at high strain rates (10^{-2} to -$1x10^{-1}$ s^{-1}) and low temperatures (300-350°C). Even at 425°C, superplasticity reached

			1400% at a high strain rate of 1 s^{-1}, demonstrating the alloy's remarkable deformation capabilities.
Jianqing Su et al [2013] [204]	Ti–6Al–4V alloy	TRS: 800 to 1000 rpm TS: 1 to 4 IPM	A sample processed at 900 rpm and 4 IPM achieved high yield and ultimate tensile strengths of 1067 MPa and 1156 MPa, respectively, without losing ductility. This was attributed to the smallest prior β grain size of approximately 12 μm.
Z.Y.Ma et al [2003] [205]	A356	TRS: 300 to 1100 rpm TS: 2 to 8 IPM.	The strength of FSP A356 alloy increased with higher tool rotation rates. The maximum strength was achieved at a tool rotation rate of 900 rpm using the standard pin.
Z.Y.Ma et al [2009] [206]	AA7075	TRS: 600 rpm TS: 102 mm/min	In two-pass FSP 7075Al, an optimum temperature shift was observed. The maximum superplastic elongation of 1220% was achieved at 480°C and an initial strain rate of 10^{-2} s^{-1} in the center region of the second pass.

Z.Y.Ma et al [2004] [207]	A356	TRS: 700 rpm TS: 203 mm/min Plate thickness: 6.35 mm	The flow stress of FSP A356 was significantly lower than that of cast A356. A maximum superplasticity of 650% was achieved at 530°C with an initial strain rate of $1x10^{-3}$ s^{-1} in FSP A356.
N. Kumar et al [2012] [208]	Al-Sc-Mg alloy	TRS: 323, 400, and 800 rpm	Grain size varied from 0.4 to 0.8µm based on processing and the initial thermo-mechanical condition of the alloy. An increase in the Zener-Holloman parameter correlated with grain size reduction.
Jian-Qing Su et al [2011] [209]	Pure Cu	TRS: 800 rpm TS: 120 mm/min TTA: 2.5°	Material flow in a thin layer around the pin tool caused severe strain heterogeneity, resulting in concentrated microplastic deformation within this layer. Consequently, a high density of microband structures was formed.
S.R Sharma [2004] [210]	A356 Alloy	TRS: 700 to 900 rpm Constant TS: 200 mm/min	Fatigue life improved due to significant microstructure refinement, homogenization, and

			porosity elimination. FSP led to the substantial breakup and uniform distribution of Si particles within the aluminum matrix, as well as the removal of porosity.
Z.Y.Ma et al [2003] [211]	AA7075	TRS: 350, and 400 rpm TS: 4, and 6 IPM	The density, size, and volume fraction of cavities decreased with lower initial strain rates from $1x10^{-1}$ to $1x10^{-2}$ s^{-1} at a constant temperature of 480°C. Additionally, cavity density decreased with increasing temperature from 450°C to 510°C at a constant initial strain rate of $1x10^{-2}$ s^{-1}.
Z.Y.Ma et al [2005] [212]	Al-Mg-Zr	TRS: 350 rev/min TS: 4 IPM	Maximum superplastic ductility of 1280% was achieved at 525°C and a strain rate of $1x10^{-1}$ s^{-1}. The strain rate sensitivity of both as-extruded and FSP Al-4Mg-1Zr alloys increased steadily with strain rates from $1x10^{-3}$ s^{-1} to 1 s^{-1}.
S. Jana et al [2010] [213]	Al–Si–Mg alloy	TRS: 2236 rpm TS: 2.33 mm/s	FSP improved fatigue life fivefold in a hypoeutectic Al–Si–Mg cast alloy. The cast fatigue specimen had a

			life of 45,500 cycles. Cracks, originating from porosity, were observed after the first 5,000 cycles, indicating a crack initiation period of 10% or less.
S. Jana et al [2007] [214]	F357 Al alloy	TRS: 2236 rev/m TS: .367, 2.33, 0.98, and 0.42 mm/s.	Multiple passes did not refine Si particles beyond a certain limit. However, the second configuration of multiple passes indicated that abnormal grain growth (AGG) can be reduced if the material undergoes FSP multiple times.
R.S Mishra et al [2003] [215]	Composite Al-SiC	TS: 25.4, and 101.6 mm/min Tool depth: 2.28, 2.03, 1.78 mm.	A target depth of 2.03 mm successfully incorporated SiC particles into the aluminum matrix, while depths of 2.28 mm and 1.78 mm were ineffective.
Z.Y.Ma et al [2003] [216]	Al-Mg-Zr Alloy	TS: 3 mm/s Temperature ranges: 400 to 550 °C	FSP produced a fine microstructure with a grain size of 1.5 µm and a uniform distribution of fine Al3Zr dispersoids in the Al-Mg-Zr alloy.
Z.Y.Ma et al [2002] [217]	AA7075	TRS: 350, and 400 rev/min TS: 4, and 6 IPM	Grain size decreases between 420-530°C and strain rates of 1x10^-3 to 10^{-1} s^{-1}. The 3.8 µm 7075Al alloy achieved 1250% superplastic elongation at

			480°C with strain rates of $3x10^{-3}$ to $3x10^{-2}$ s^{-1}. The 7.5 µm 7075Al alloy showed 1042% ductility at 500°C and $3x10^{-3}$ s^{-1}.
Z.Y.Ma et al [2006] [218]	A356	TRS: 300 to 900 rev/min TS: 51 to 203 mm/min	A higher TRS results in a more homogeneous microstructure. However, the varied distribution, size, and volume fraction of Si particles in different locations within the FSP zone indicate inhomogeneous material flow.
S.Jana, et al [2009] [219]	Al–Si–Mg alloy	TRS: 2236 rev/min TS: 2.33 mm/s Pin height: 1.9 mm Pin diameter: 4 mm Plate thickness: 2 mm	FSP significantly enhanced the fatigue life of cast Al–7Si–0.6 Mg alloy by a factor of 15. This improvement was observed when specimens were tested under the same stress level with a stress ratio of R = 0. The process led to a more fine & homogeneous microstructure, which contributed to the increased fatigue resistance. The uniform distribution of Si particles and the reduction in porosity played crucial roles in this enhancement.

J-Q-Su et al [2002] [220]	AA7050	TS: 15 mm/min TRS: 350 rev/min	During FSW, the strengthening precipitates coarsened significantly, and the precipitate-free zone along the grain boundaries expanded fivefold compared to the parent material. The original base metal grains were entirely replaced by a fine equiaxed grain structure in the DXZ.
Jiye Wang et al [2014] [221]	Ti–6Al–4V	TRS: 1000 rev/min TS: 25 mm/min	The CY16 tool experienced fracture failure, while the WC411 tool showed micro-cracking with improved fracture toughness, inhibiting crack propagation. The W-La tool exhibited degradation due to plastic deformation, which can be mitigated by increasing the pin diameter.
Y.Wang et al [2007] [222]	Al–4.0Y–4.0Ni–0.9Co Alloy	TS: 51 mm/min TRS: 1000 to 1200 rpm TTA: 0°	FSW of UFG Al–4.0Y–4.0Ni–0.9Co alloy significantly improved ductility with a slight decrease in strength. The process homogenized the microstructure and altered the shape of intermetallic particles.

Table 2.3: Summarized table of Literature Reivew

Author's	Work material	Tool material	Tool shape and size	Operating parameters
I. Dinaharan et. al. 2018 [223]	Aluminium AA6061 and Mg Alloy AZ1 Copper (pure)	HCHCr H13	SD:18mm; PD:6mm, PH:5.8mm; Thickness: 6 mm;	Rev/min=1600; WS=60mm/min; Force= 10 KN
			SD:15,18,21mm; PD:6mm, PH:5.7mm; Thickness: 6 mm;	rev/min=1200; WS=40mm/min; Force= 10 KN
			SD:15,18,21mm; PD:6mm, PH:5.7mm; Thickness: 6 mm;	Rev/min=1000; WS=40mm/min; Force= 10 KN
N. Sun et. al. 2009 [224]	AZ31 Mg	H13 Steel	SD:10mm; PD:4mm; PH:1.8mm Thickness:1.5mm	Rev/min =1000,3000; WS=150mm/min; Dwell time=1,4 sec;
G. Padmanaban et. al. 2009 [225]	AZ31B Mg alloy	Armour steel, stainless steel, Mild Steel	SD:15,18,21mm; PD:6mm, PH:5.7mm; Thickness: 6 mm;	RPM=1600 WS=21; 40 mm /min; tilt angle =0;
D. Bakavos et. al.2008 [226]	AZ31 Mg-Alloy	HCHCr	SS: SD:18 mm; PD: 6mm PH:5.7 mm; Thickness:3mm;	RPM=500,1000; WS=150;200;250; Butt joint
Y. HU et. al. [227]	AA6082T6 Aluminium	Steel Alloys	SS: concave SD:10mm; Thickness : 3mm;	RPM=715,1500;WS= 100,200mm/min;
R. Beygi et. al. [228]	Aluminium and copper laminated composite	H13 Steel	SS:flat SD:12mm; PD:2.9mm; PH:2.6mm;	RPM=600,1200; WS=50mm/min; Butt joint; Rake angle=2.5º
R. Beygi et. al. [229]	Aluminium and copper bilayer sheet	Tool Steel	SS:SD:12 mm; PD: 2.8mm; PH:2.6mm;	RPM=800; WS=50mm/min;Butt joint;

T. K. Bhattacharya [230]	Aluminium AA6063 and copper - HCP(C-10300)	Chromium Alloy Steel	SS: SD:18mm; PD:6mm; PH:5.9mm;	RPM=3000; WS=69 mm/min; Tilt angle= 2º;Lap joint;
A. O. Al-Roubaiy et. al. [231]	AA5086-H116 and Cu-99.972%	Chromium Alloy Steel	SS: Concave SD:18mm; PD:6mm; PH:5.9mm; Thickness: 6.3mm;	RPM=560, 710; WS=69 mm/min; Tilt angle= 2º; Force = 67 KN; Butt joint;
A. Paoletti et. al. [232]	Thermoplastic Polymer	Low Carbon Steel AISI1010	SS: SD:11mm; PD:5mm; PH:4.3mm; Thickness:3mm;	RPM=900,1260,1500; WS=34mm/min
E. T. Akinlabi et. al. [233]	Aluminium AL5754 and CU(C11000)	H13 Tool Steel	SS: SD:15mm,18mm,25mm; PD:5mm PH:5 mm Thickness3.175 mm	RPM=600,950,1200; WS=50,150,300; mm/min; Lap joint;
M. E. Aalami et. al. [234]	Aluminium AL1050-H16 and Pure CU	H13 Tool Steel	SS: SD:14.5, 17.8 mm; PD:4.5mm; PH:6.1mm Thickness:3mm;	RPM=1000; WS=40 mm/min; Lap joint;
E. Akinlabi et. al. [235]	Aluminium AL5754 and CU(C11000)	H13 Tool Steel	SS: Concave SD:15,18,21mm; PD:6mm, PH:5.7mm; Thickness: 3.175 mm;	RPM= 600,950,1200; WS=50,150,300mm/min Tilt angle=2º; Butt joint;
I. Galvao et. al. [236]	Aluminium AA6082 & Cu-DHP, R240)	H13 Tool Steel	SD:16mm; PD:5mm, PH:2.9mm;	RPM=1000; WS=200mm/min;

2.1.4 Effect of Process parameters on UTS and microstructure

A thorough understanding of FSW and its mechanical properties is essential for aerospace applications, necessitating detailed research. While FSW can join various

materials, it has primarily focused on aluminum alloys. Defect-free welds with good mechanical properties have been achieved in aluminum alloys of thicknesses from 1 mm to over 35 mm. FSW can be performed in any position [188, 205-210]. The ultimate tensile strength and hardness of bimetallic weld joints increase with pre-stress, while ductility decreases with higher thermal loading. To prevent brittle failure in carbon steel, pre-stress and thermal stress should be minimized. The optimum strain rate for maximum elongation at 525°C was 1x10^-1 s^-1, indicating that high strain superplasticity can be achieved in Al-4Mg-1Zr alloy through FSP.

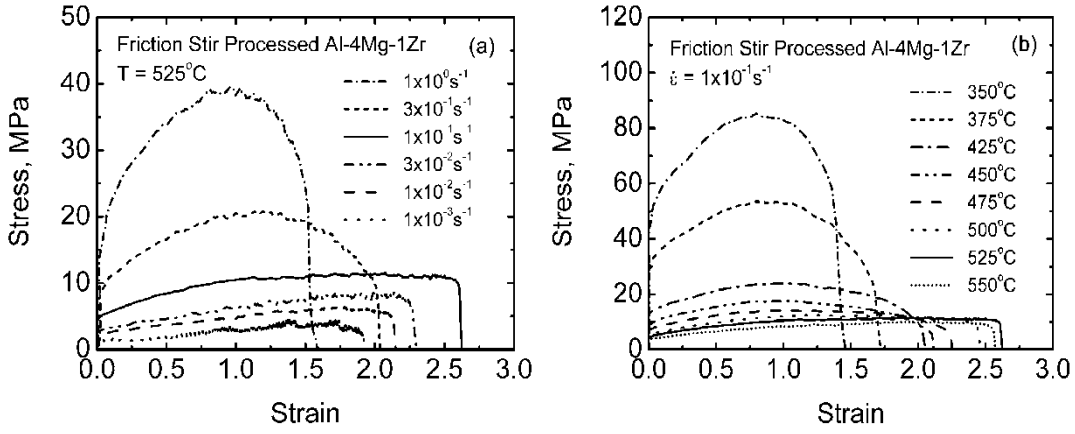

(a) *(b)*

Figure 2.9: Stress strain diagram of FSP of Al-Mg-Zr alloy at various processing conditions [216]

The superplastic deformation behavior of FSP Al-Mg-Zr alloy was investigated across a strain rate range of 1x10^-3 to 1 s^-1 and a temperature range of 350°C to 550°C, compared to the as-rolled alloy. Maximum elongation of 1280% was achieved at 525°C. FSP significantly decreased the flow stress in Al-4Mg-1Zr alloy. Specimens deformed to failure at 525°C for different strain rates and at 1x10^-1 s^-1 for different temperatures, showing neck-free elongation indicative of superplastic flow. The strain rate sensitivity (m value) of FSP Al-Mg-Zr increased from 0.12 to 0.55 at 450°C and from 0.15 to 0.53 at 525°C as initial strain rates increased from 10^-3 to 10^-1 s^-1 [216]. Tensile properties of as-extruded and welded materials with different FSW parameters are shown in Fig. 2.9. Weld 1 showed improved ductility to 11.6% with a slight strength decrease, while Weld 2 showed enhanced ductility to 14.7% with a

yield strength reduction from 633 MPa to 568 MPa, likely due to microstructure coarsening.

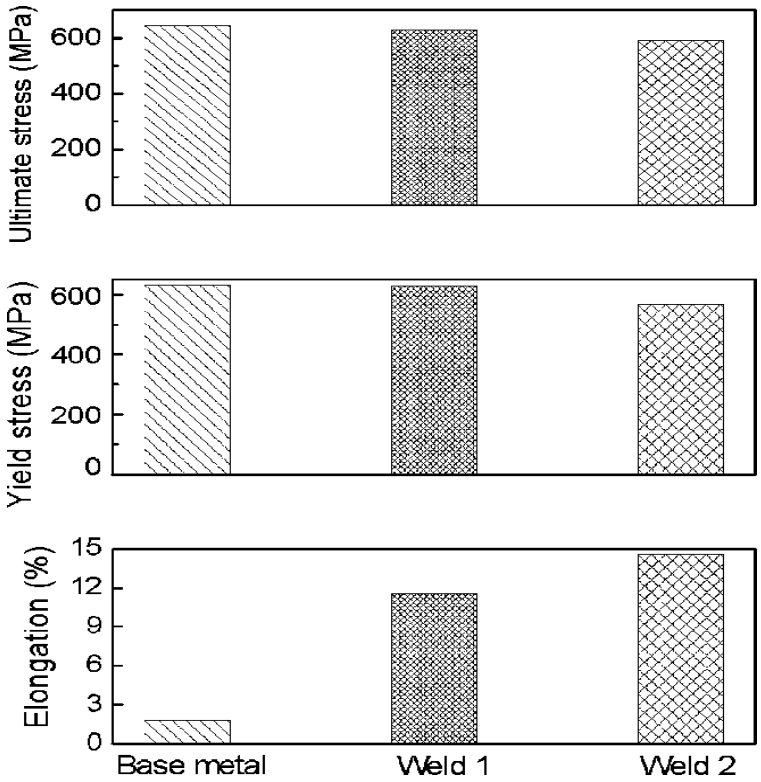

Figure 2.10: Mechanical properties of the welded joints at room temperature [216]

AA7475 was used during these experiments, where single pass and six pass, joint welding was applied to a 2.5 mm thick lap joint. Substantial plastic stirring during FSW was evident from the material flow inside the nugget. The average grain size of the parent material was 10 µm, while the microstructures of one-pass and six-pass nuggets were finer, with average sizes of 2.2 µm and 3.2 µm, respectively. The parent material exhibited yield strength of 398 MPa, ultimate tensile strength of 511 MPa, and ductility of 21.8%. For the single-pass nugget, these values were 402 MPa, 541 MPa, and 31.4%, and for the six-pass nugget, they were 334 MPa, 451 MPa, and 31.8%. The weld HAZ maintained a stable microstructure and superplastic properties, with a high-strength weld nugget due to increased flow stress at 783K compared to the parent metal. Additionally, the FSW of Cu with carbon nanotubes enhanced the microstructure, hardness, and tensile properties of the composite material through single, double, and triple passes. Brinell hardness increased with more passes due to a more compact microstructure.

Friction between the tool and workpiece generates localized heating, softening, and plasticizing the material. This process results in significant grain refinement as the material moves from the front to the back of the pin [119, 120].

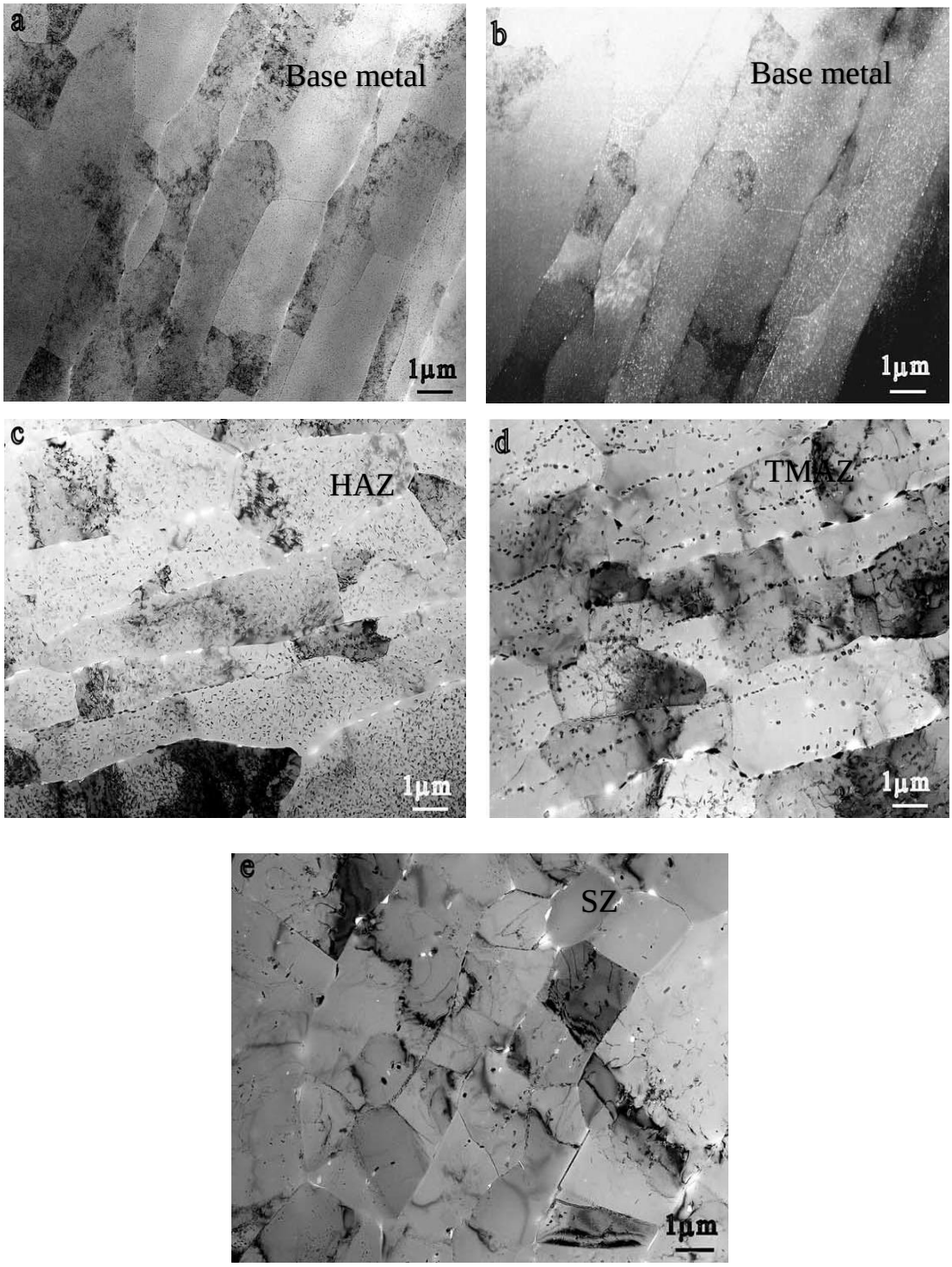

Figure 2.11:TEM images of weldments at different welded regionons: (a) base metal, (b) dark field image of region (a), (c) HAZ, (d) TMAZ I, (e) TMAZ [237]

Fine-grained microstructure is essential for superplasticity, making FSP a promising technique for producing superplastic aluminum alloys. However, superplasticity in FSP parts is limited at elevated temperatures due to coarse-grained microstructure evolution [108, 109]. FSP effectively fabricates surface metal matrix composites with well-distributed particles and strong bonding, offering advantages over laser processing, high-energy electron beam irradiation, and casting sinter.

The grain structures in the base metal and weldment are shown in low magnification TEM images in Figure 2.11(c). The parent alloy microstructure displays partially recrystallized pancake-shaped grains with sub-grains about 1-5 μm in size (Fig. 2.11a). Minimal diffraction contrast between neighboring grains in the dark field image indicates dominance of low-angle boundaries (Fig. 2.11b). The HAZ region, mechanically undisturbed by FSW, resembles the base metal's grain structure, with low dislocation density (Fig. 2.11c). The TMAZ, between the parent metal and DXZ, shows a highly deformed structure with elongated grains preserved (Fig. 2.11d) [26].

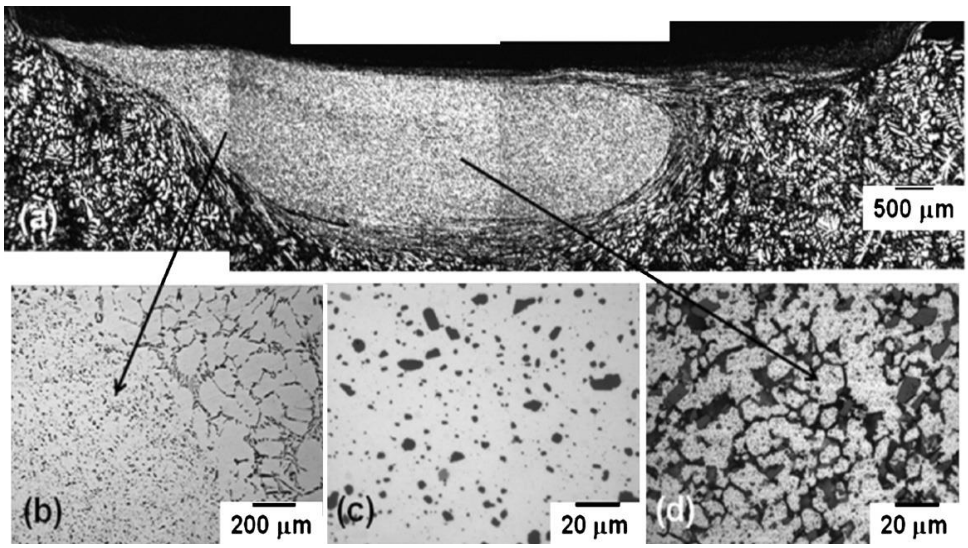

Figure 2.12: Optical images of different welded region [237]

The study evaluated the impact of process parameters and FSP run configurations on nugget microstructure stability at elevated temperatures. Single-pass runs exhibited abnormal grain growth (AGG), whereas multi-pass runs were more resistant to AGG. Using cast Al-Alloy F357, a hypoeutectic Al-Si alloy, the AGG increased when tool rotation was reduced from 2236 rpm to 1500 rpm. The research highlighted that multiple passes did not refine Si particles beyond a certain limit but reduced AGG.

Figure 2.12a shows a single-pass nugget with a basin shape, while Figures 2.12b and 2.12c illustrate highly refined eutectic Si particles. Figure 2.12d depicts mostly equiaxed grains in the FSPed nugget, with occasional alignment parallel to the advancing or retreating side [237]. Tool wear in FSW is a critical issue, particularly for aluminum matrix composites. The primary wear mechanisms include plastic deformation, abrasion, diffusion, and environmental reactions with the tool material [128]. While FSW of soft metals like aluminum and magnesium shows minimal tool wear, the issue becomes more pronounced when welding hard metals or metal matrix composites (MMCs). This wear is characterized by deformation and reduction in the pin diameter.

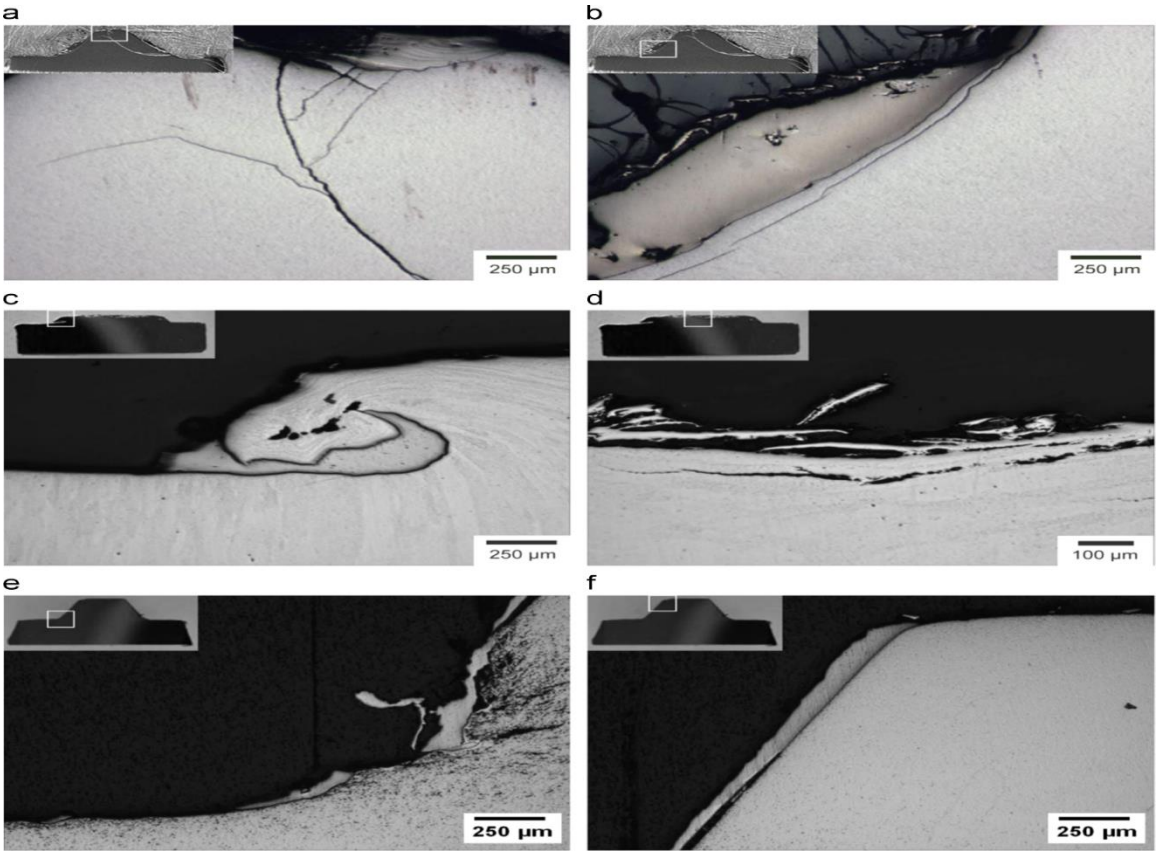

Figure 2.13: OM images of welded joints at different tool materials [214]

Fig. 2.13 presents optical microscopy images of cross-sections for CY16, W-La, and WC411 tools. In the CY16 tool (Fig. 2.13a), cracks initiated at the shoulder corner and propagated through the pin, leading to rapid fracture and chipping. Cracks commonly started at the shoulder edge and shoulder-pin corner due to stress concentrations. Adhesion between Ti-6Al-4V and CY16 was noted (Fig. 2.13b), with

cracking under the adhesion layer indicating stress concentration. The W-La tool (Fig. 2.13c) showed plastic deformation and stress-induced cracks at the pin tip, though no Ti-6Al-4V adhesion was observed. In the WC411 tool, voids nucleated at the shoulder and coalesced due to localized strain, with Ti-6Al-4V adhesion present on the surface (Fig. 2.13e) [214].

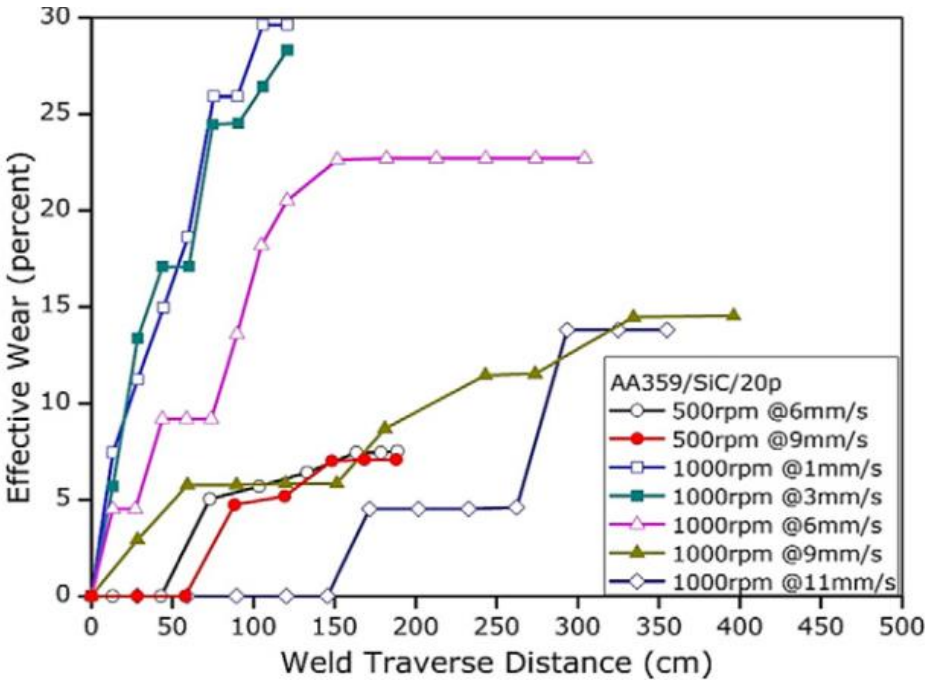

Figure 2.14: variation of wear to the traverse distance [220]

There was a linear correlation between wear rate and tool rotation speed in FSW. Initially, tool wear was delayed by reducing rotation speed and increasing transverse speed, but the wear rate eventually stabilized (Fig. 2.14). This suggests self-optimization of the tool shape due to the base material's solid-state flow during welding, with a worm pin achieving a more homogeneous structure [220]. FSP significantly enhanced the fatigue life of Al-7Si-0.6Mg alloy by eliminating porosity and refining Si particles. Crack growth rates were lower in the FSP condition, with oscillatory crack growth ceasing at 180 μm in FSP samples versus 450 μm in cast samples【132】. FSP-treated alloy showed improved fatigue life and a stress threshold greater than 80% in the stir zone, attributed to a finer microstructure and reduced crack growth rates. Overall, FSW successfully improves aluminum alloy properties, often surpassing those of the base material, although high strain amplitudes can reduce hardness and fatigue life.

2.2 Summary of Literature review

The different processes of FSW, process parameters and weld material combinations, the mechanical and micro structural study of FSW stated by numerous researchers are discussed. The core inferences of this study are:

- Welding of two dissimilar metals by FSW in butt configuration, the softer metal should be on retarding side and harder metal should be on AS.
- When the two different metals are to be weld in lap joint, the softer metal should be on topper side and harder metal should be on bottom side.
- On other hand, the cylindrical tool pin profile was observed to be suitable, by which defect free dissimilar joints can be obtained.
- The shoulder diameter and tilt angle significantly influence the plunge load value in FSW. Increasing both the shoulder diameter and tilt angle results in a higher plunge load.
- With an increase TRS, the mechanical properties decrease.

2.3 Research Gap

1. **1.** Very few experimental investigations have been made on Friction Stir Welding of Non Ferrous dissimilar Materials.
2. **2.** It has been observed that very few studies have been made on tool material and tool geometry on FSW of similar material but the research with non-ferrous dissimilar Materials is still to be done in detail.
3. **3.** Parametric study of FSW on non-ferrous dissimilar material is again a major research gap.
4. **4.** Simultaneous effect of various parameters is to be studied for various industrial applications.

2.4 Objectives

1. To Study the effect of various process parameters of FSW process.
2. To Study different tool geometry used for FSW.
3. To Select optimization technique depending on the input and output parameters for welding of dissimilar metals using FSW.

4. To study metallographic characterization of weld joint using optical and SEM microscope.
5. To study mechanical properties of welded metals such as micro-hardness, tensile behavior and residual stress.

CHAPTER 3

3. Materials and Methods

This research focuses on the FSW of AZ91D and AA2024 by three different tool pin profiles: triangular, circular, and rectangular. The methodology involves a systematic approach to comprehend the impact of these pin profiles on the weldments, and metallurgical properties of the weldments. The initial phase involves the preparation of the base materials, AA2024 and AZ91D. The plates are cut into specific dimensions suitable for welding and then meticulously cleaned to remove any surface oxides or contaminants. This step ensures optimal contact between the workpieces and the tool, which is critical for high-quality welds.

Following material preparation, three distinct FSW tools with circular, triangular, and rectangular pin profiles are designed and made of tool steel (H13). The design of the pin profiles is aimed at exploring how different geometries influence the stirring action and material flow during the FSW. Each tool is also equipped with a shoulder designed to provide adequate input heat and facilitate the plastic deformation required for welding.

To establish the optimal FSW process parameters, preliminary trials are conducted. These trials involve varying TRS, TS, and axial forces to identify the best combination for each pin profile. The parameters are carefully documented to ensure that the welding conditions remain consistent across all experiments. This step is crucial for ensuring that any differences observed in the weld quality are attributable to the pin profile rather than variations in the welding process.

Once the optimal parameters are determined, the actual welding process is carried out. Each tool pin profile is used to weld a series of samples under identical conditions. This consistency allows for a fair comparison of the consequences of the different pin profiles on the joint efficiency.

Post-welding, a comprehensive metallographic analysis is conducted. This involves preparing cross-sectional samples of the welds, which are then polished and etched to observed the microstructure. Optical and SEM microscopy were employed to study the grain structure, phase distribution, and any defects present in the weld zones.

Special attention is given to identifying differences in grain size and morphology that may be affected by the pin profile.

Mechanical properties of the weldments are evaluated through a series of tests. Tensile testing is performed to measure the UTS and ductility of the joints. Microhardness analysis was taken across the weld zones to assess the distribution of hardness and identify any regions of weakness.

The results are expected to show how different pin geometries affect the joint efficiency of the FSW joints, ultimately providing valuable insights for optimizing FSW processes for these specific materials. This comprehensive approach aims to establish a clear correlation between tool pin profiles and weld characteristics, contributing to the advancement of FSW technology for AZ91D and AA2024. The flow chart of the experimental is shown in Fig. 3.1.

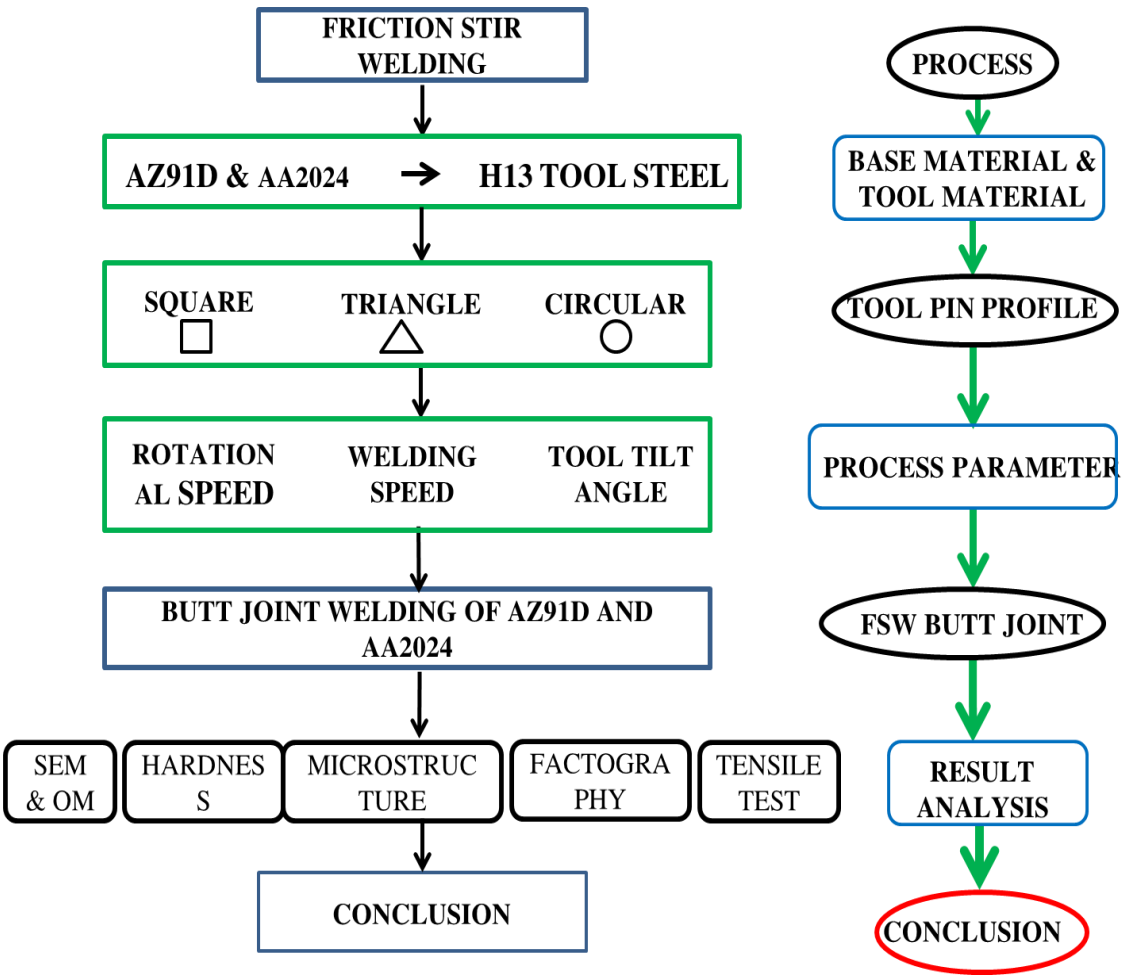

Figure 3.1: Flow chart for experimentation

3.1 Chemical composition of base metals

FSW of AA2024 and AZ91D has significant industrial applications and superior mechanical properties. In the aerospace industry, AA2024 is extensively used for wing skins, aircraft fuselage panels, and other structural components. In the automotive sector, AZ91D is favored for lightweight components such as engine blocks, transmission cases, and steering wheels, where FSW improves the strength and integrity of the weldments, improving vehicle performance and fuel efficiency.

The chemical composition of AA2024 typically includes 4.21% Cu, 1.45% Mg, 0.36% Mn, and small amounts of Fe, Si, Zn, and Ti, with the remainder being aluminum. AZ91D consists of 9.18% Al, 0.35% Zn, 0.29% Mn, and traces of Si, Cu, Ni, and Fe, with the remainder being magnesium. The chemical composition of the base metals and H13 tool steel is revealed in Table 3.1 and 3.2.

Table 3.1: Chemical composition of AZ91D and AA2024

Material	Al	Si	Mn	Zn	Cu	Fe	Ti	Mg
AZ91D	8.95	0.059	0.36	0.54	0.02	0.01	0.03	Balance
AA2024	Bal	0.58	0.29	0.35	4.37	0.31	0.08	1.19

Table 3.2: Chemical composition of H13 tool steel

Material	Cr	Mo	Si	V	C	Ni	Cu	Mn	P	S
AZ91D	4.96	1.56	0.94	1.12	0.38	0.21	0.19	0.36	0.025	0.026

H13 tool steel is commonly used for FSW tools due to its excellent combination of properties suited for the demanding conditions of FSW. It has high temperature resistance, maintaining its strength and hardness at elevated temperatures, which is crucial given the significant heat generated during the process. Additionally, H13 tool steel offers high wear resistance, ensuring durability and a longer tool life, even when welding abrasive materials.

CHAPTER 4

4. Experimentation

The experimental procedure for FSW of AZ91D and AA2024 involves two primary phases. The first phase aims to analyzed the consequences of three pin profile on the joint efficiency, while the second phase focuses on examining the influence of TRS using the best-performing tool pin profile identified in the first phase. In the initial phase, three distinct tool pin profiles—circular, triangular, and rectangular—are tested to investigate their influence on the resultant joint properties. The chosen materials, AZ91D and AA2024, present unique challenges due to their differing properties, making the welding process complex yet promising for creating high-strength, lightweight joints. Plates of both alloys, each measuring 150 mm x 50 mm x 6 mm, are prepared with machined edges to ensure smooth and clean surfaces suitable for welding. H13 tool steel is selected for the FSW tools due to its excellent high-temperature strength, and hardness, which are essential for withstanding the intense conditions of the FSW process. Each tool features a different pin profile: circular, triangular, or rectangular, while maintaining constant shoulder diameter and pin length to ensure that the variations in welding outcomes are attributable solely to the differences in pin profiles.

During the welding trials, the AZ91D and AA2024 plates are clamped onto a backing plate to prevent movement and ensure proper heat dissipation. Initial welding process parameters, including TRS, TS, and axial force, are based on literature values and preliminary trials to achieve sound welds. The welding trials are conducted with each tool pin profile, and the welded joints are subjected to a series of tests to evaluate their quality, including visual inspection, metallographic examination, hardness testing, and tensile testing. Visual inspection identifies surface defects, such as flash formation, voids, and incomplete fusion, indicating the suitability of a particular pin profile. Metallographic examination involves cutting cross-sections of the welded joints, mounting, polishing, and etching them to reveal the microstructure, providing insights into grain refinement, the presence of IMCs, and the homogeneity of the weld zone. Hardness testing assesses the distribution of mechanical properties across the weld cross-section, while tensile testing determines the tensile strength and % strain of the joints, offering a comprehensive understanding of the joint performance. Based on the

results from the first phase, the tool pin profile producing the highest quality welds is identified, considering minimal surface defects, fine and homogeneous microstructure, uniform hardness distribution, and high UTS. In the 2nd phase, the effect of TRS on weld quality was examined by the best-performing tool pin profile from the first phase. The rationale is to optimize the TRS, which significantly influences heat generation, material flow, and overall welding dynamics. A range of TRS is selected, covering lower, medium, and higher speeds, to comprehensively understand their impact. The same welding setup is used, with AZ91D and AA2024 plates prepared as before, and the best-performing tool pin profile is employed while keeping TS and axial force constant to isolate the effect of TRS. Welding trials at different TRS are conducted, and the welded joints are subjected to the same series of tests as in the first phase, including visual inspection, metallographic examination, hardness testing, and tensile testing. Additionally, thermal cycles experienced by the welds are monitored using thermocouples to correlate heat input with observed microstructural and mechanical properties. The consequences reveal the optimal TRS that, in combination with the best tool pin profile, produces the highest quality FSW joints between AZ91D and AA2024. Optimal parameters are determined based on achieving minimal defects, a refined and homogeneous microstructure, uniform hardness distribution, and superior tensile properties. This two-phase experimental procedure systematically optimizes the FSW process for AZ91D and AA2024 alloys, contributing valuable insights for developing robust welding parameters that ensure high-quality, reliable joints for various industrial applications requiring strong and lightweight structures.

4.1 Preparation of base plate

The preparation of base plates before FSW is critical for reaching high-quality welds. The process begins with the selection and inspection of AZ91D and AA2024 plates, each typically measuring 150 mm x 50 mm x 6 mm revealed in Fig. 4.1. The plates are inspected for surface defects such as cracks, dents, or corrosion, ensuring they are free from mechanical damage that could compromise the weld quality. The plate's edges to be welded are then machined to ensure they are smooth, clean, and free of burrs, providing an ideal surface for welding. After machining, the plates are thoroughly cleaned to remove by acetone any contaminants such as oil, grease, dirt, or

oxide layers. Once cleaned, the plates are carefully aligned to ensure proper joint configuration. Accurate alignment is crucial to avoid defects such as misalignment or lack of fusion during welding.

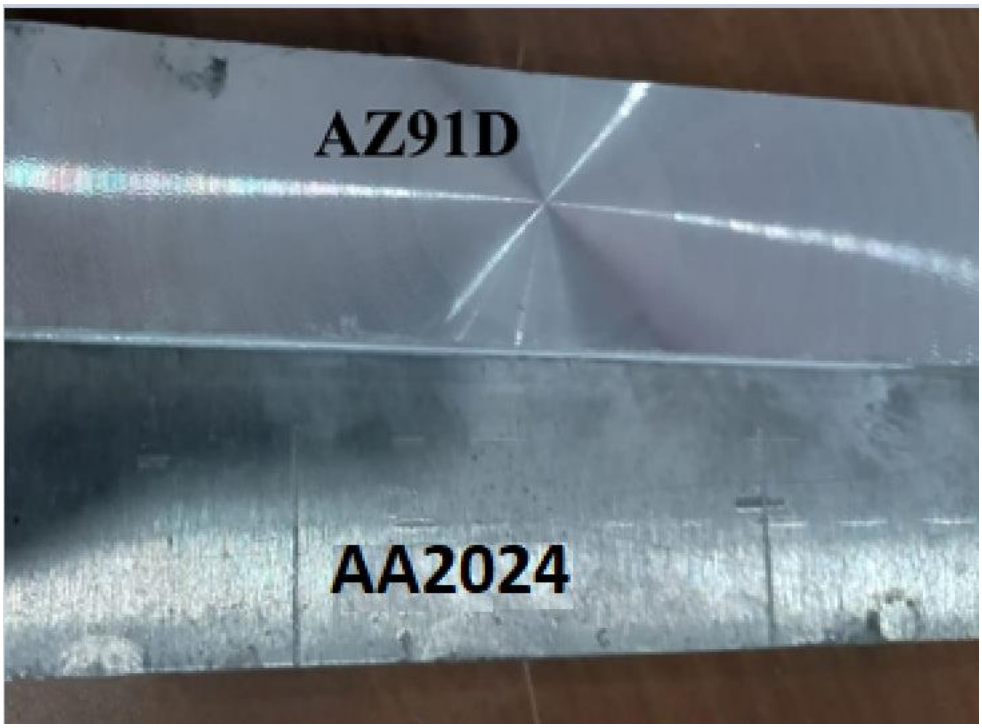

Figure 4.1: Base plate AZ91D and AA2024 before welding

The aligned plates are then securely clamped onto a backing plate to prevent movement and ensure stability during the FSW process. The backing plate also helps in dissipating heat and supporting the material during welding. Special attention is given to ensuring that the clamping does not introduce any distortions or stresses in the plates, which could affect the weld quality. This thorough preparation process ensures that the base plates are in optimal condition for the FSW operation, facilitating the production of good welded joints.

4.2 Tool pin profile selection

The pin profile selection—whether circular, triangular, or square—in FSW is crucial as it directly effects the welding process and the quality of the resulting joints shown in Fig. 4.2, 4.3. Each profile offers unique characteristics that cater to specific welding needs and material properties.

4.2.1 Circular Pin Profile

The circular pin profile is a versatile choice in FSW due to its ability to facilitate uniform material flow around the pin during welding. This profile generates lower peak forces and heat compared to other profiles, making it suitable for softer materials or applications where minimizing distortion and thermal effects is critical. The circular profile promotes steady material mixing and plastic deformation, which can contribute to achieving homogeneous welds with minimal defects. It is commonly used in general-purpose welding scenarios across a broad range of materials, including Al-alloys and Mg-Alloys.

4.2.2 Triangular Pin Profile

A triangular pin profile features sharper edges compared to a circular profile, which enhances its ability to break down oxide layers and promote thorough material mixing during welding. This profile is particularly effective for materials prone to oxide formation, such as Al-alloys. The triangular shape facilitates more aggressive material displacement and stirring action, leading to improved metallurgical bonding and potentially enhancing joint strength. It is often chosen when a more aggressive material flow and enhanced intermetallic bonding are desired, making it suitable for applications requiring high-strength and reliable joints.

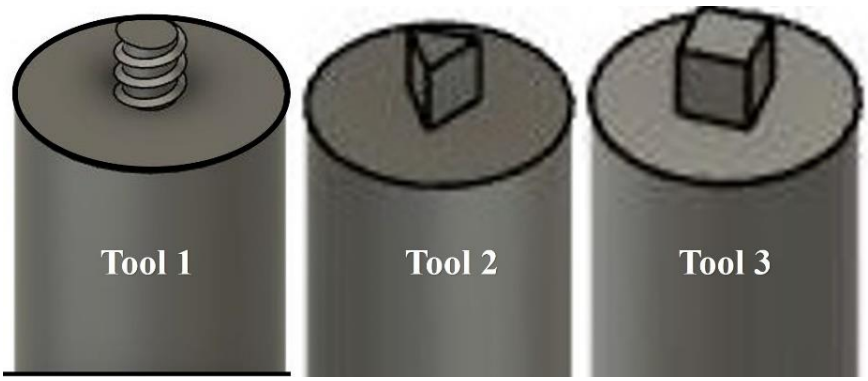

Figure 4.2: 3D images of tool pin profile

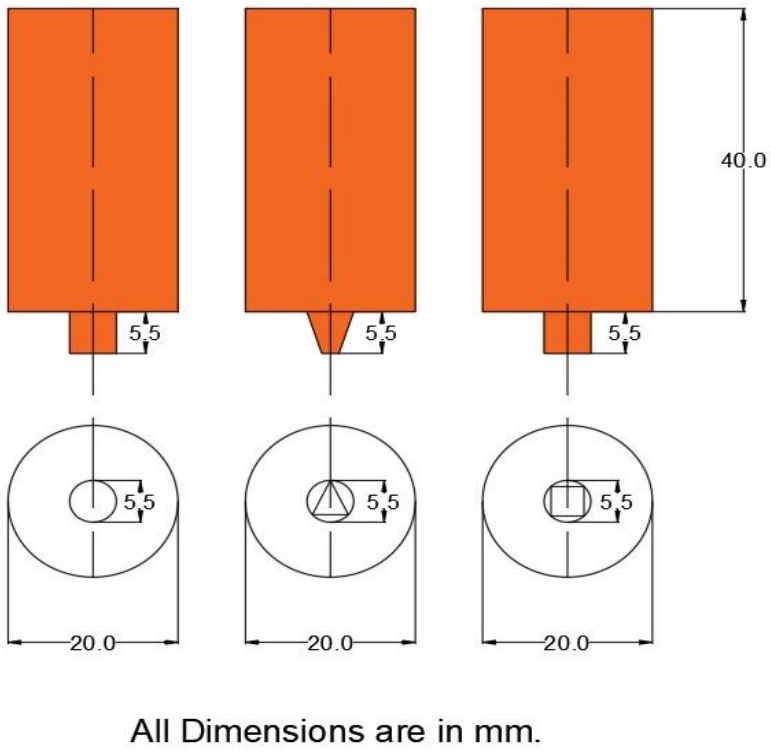

Figure 4.3: Line diagram with dimension of tool pin profiles

4.2.3 Square Pin Profile

The square pin profile offers distinct advantages in specific welding applications where precise material displacement and control over heat generation are essential. This profile provides a larger contact area compared to circular and triangular profiles, distributing heat and forces more evenly during welding. It is favored in applications where stability and control over welding parameters are critical, such as welding thicker materials or achieving specific joint configurations. The square profile can facilitate deformation and efficient material mixing, contributing to consistent weld quality and mechanical properties.

4.3 Fabrication of FSWed joints

After preparation of base plates, once inspected, the plates undergo edge preparation where edges are machined to achieve smooth surfaces free of burrs, crucial for establishing proper contact during welding. Subsequently, the plates are thoroughly cleaned to remove any residual oils, greases, dirt, or oxide layers that could impair the welding process. Simultaneously, the FSW tool is chosen or fabricated using

materials like H13 tool steel, renowned for its resilience to high temperatures and wear. The tool design incorporates a specific pin profile—circular, triangular, or rectangular—and dimensions tailored to the material thickness and welding requirements.

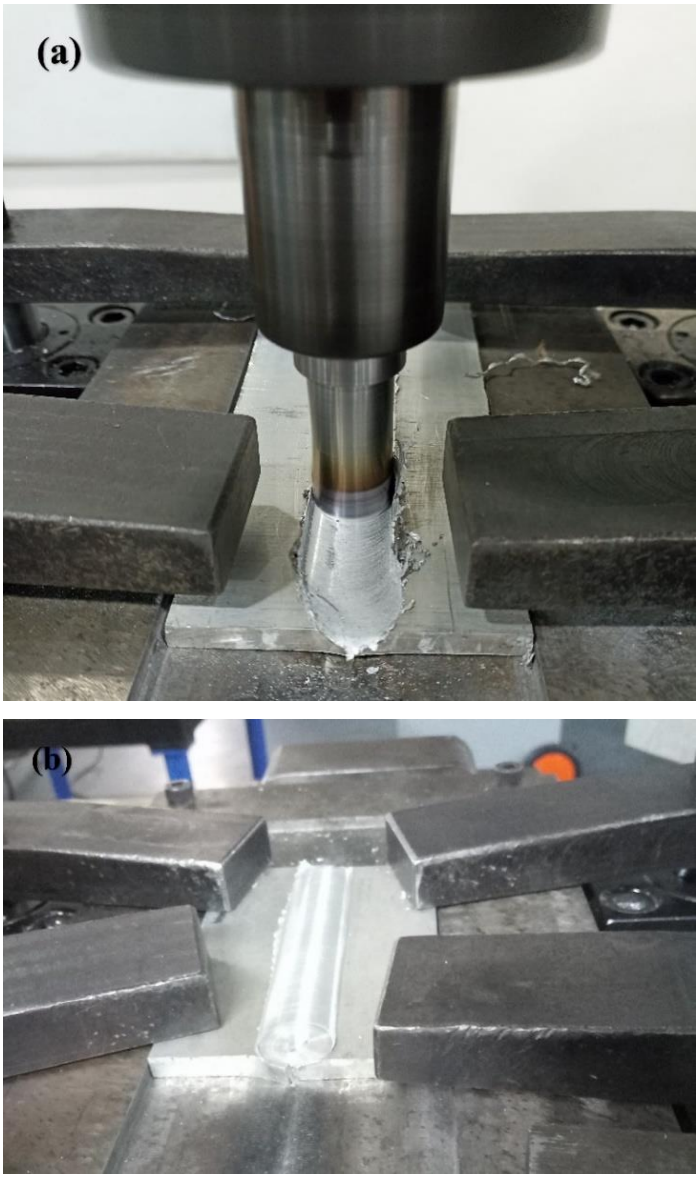

Figure 4.4: (a, b) Fabrication process of FSWed joints

During setup, the prepared plates are aligned precisely, typically on a backing plate, to ensure accurate joint configuration and to prevent misalignment, which could compromise weld integrity. Clamping securely holds the plates in place during welding, preventing movement and ensuring stability throughout the process. The

backing plate aids in heat dissipation and provides support to the workpieces, enhancing the overall stability of the welding.

The FSW involves plunging the tool into the joint line, where it generates mechanical pressure and frictional heat. This causes the materials to soften and mix together without melting, ensuring a solid, defect-free weld. This results in a solid-state bond characterized by refined microstructures and minimized distortion compared to conventional welding methods. Fabrication process of FSW and fabricated plate is shown in Fig. 4.4, 4.5.

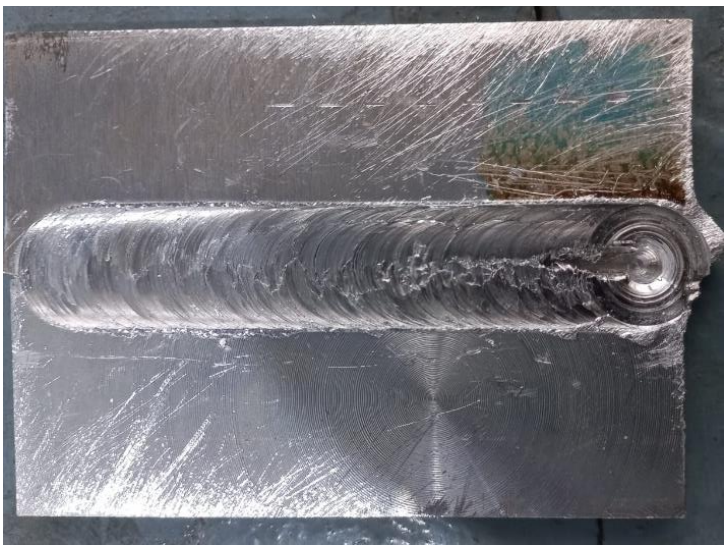

Figure 4.5: Fabricated plate after FSW

4.4 Preparation of tensile specimens

Preparing tensile specimens of FSW joints of AA2024 and AZ91D according to ASTM E8 standard involves specific considerations to ensure accurate mechanical testing. First, after welding, the FSW joints are sectioned to obtain specimens that represent the welded region. The fabrication process and dimension of tensile test specimen is demonstrated in Fig. 4.6, 4.7 respectively.

Figure 4.6: Finishing of welded plates

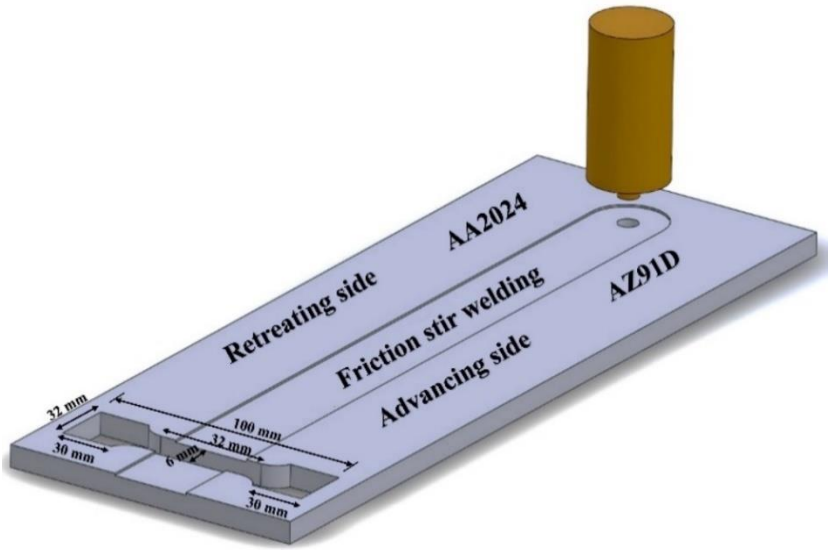

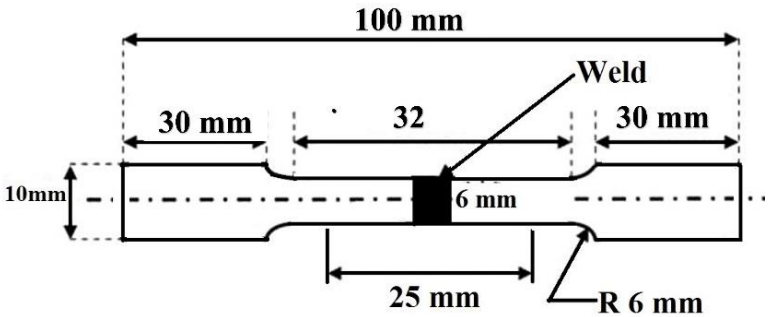

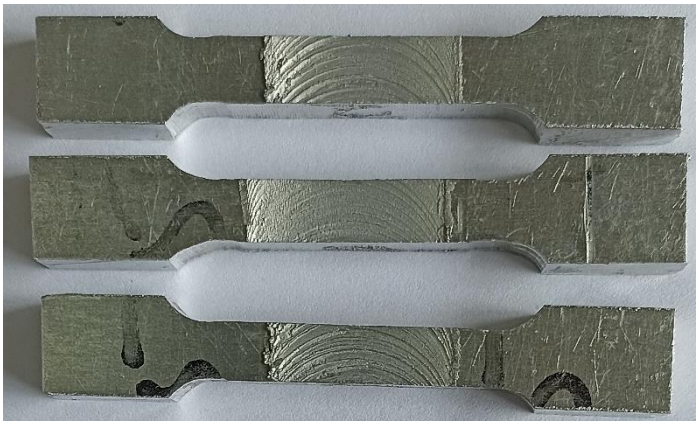

Figure 4.7: Dimension of tensile sub test specimen according to ASTM standard

Careful machining follows to create specimens with precise dimensions, as per ASTM E8 specifications for length, width, and thickness. Machining ensures all surfaces are smooth, free of defects, and parallel to the weld axis to minimize variability in test results. Once machined, the ends of the specimens are prepared by milling to ensure they are flat and square within tight tolerances, crucial for proper alignment during tensile testing.

4.5 Tensile testing

The computer-operated tensile testing of the AA2024 and AZ91D weldments involves several meticulous steps to ensure accurate and reliable results. First, the welded specimens are fabricated according to ASTM E8, ensuring uniform dimensions and surface finish. The specimens are then securely mounted in the grips of a UTM, which is interfaced with a computer system for precise control and data acquisition.

Before initiating the test, the machine is calibrated, and the test parameters such as the crosshead speed, load range, and gauge length are set according to the material specifications and desired testing conditions. The computer software is configured to monitor and record real-time data including applied load, displacement, and strain. As the test begins, the machine applies a steadily increasing tensile force to the specimen, elongating it until failure occurs. Throughout the process, the computer system captures detailed data on the specimen's response to the applied stress, generating a stress-strain curve that provides insights into the UTS, YS, and % elongation at break. Upon completion of the test, the software analyzes the data and generates comprehensive reports, which include graphical representations and numerical values

of the mechanical properties revealed in Fig. 4.8. This automated approach ensures high accuracy, repeatability, and detailed documentation of the tensile testing process.

Figure 4.8: Computer operated universal testing machine

4.6 Microhardness testing

The hardness analysis of the FSWed joint between AA2024 and AZ91D alloys involves a detailed and systematic procedure to accurately measure hardness variations across the weld shown in Fig. 4.9. Initially, the specimen is meticulously prepared by sectioning it perpendicular to the weld direction and polishing the surface to a mirror finish using progressively finer abrasives. This preparation ensures that the indentations are precise and the measurements are not affected by surface irregularities. The test begins by placing the specimen under the microscope of the testing machine.

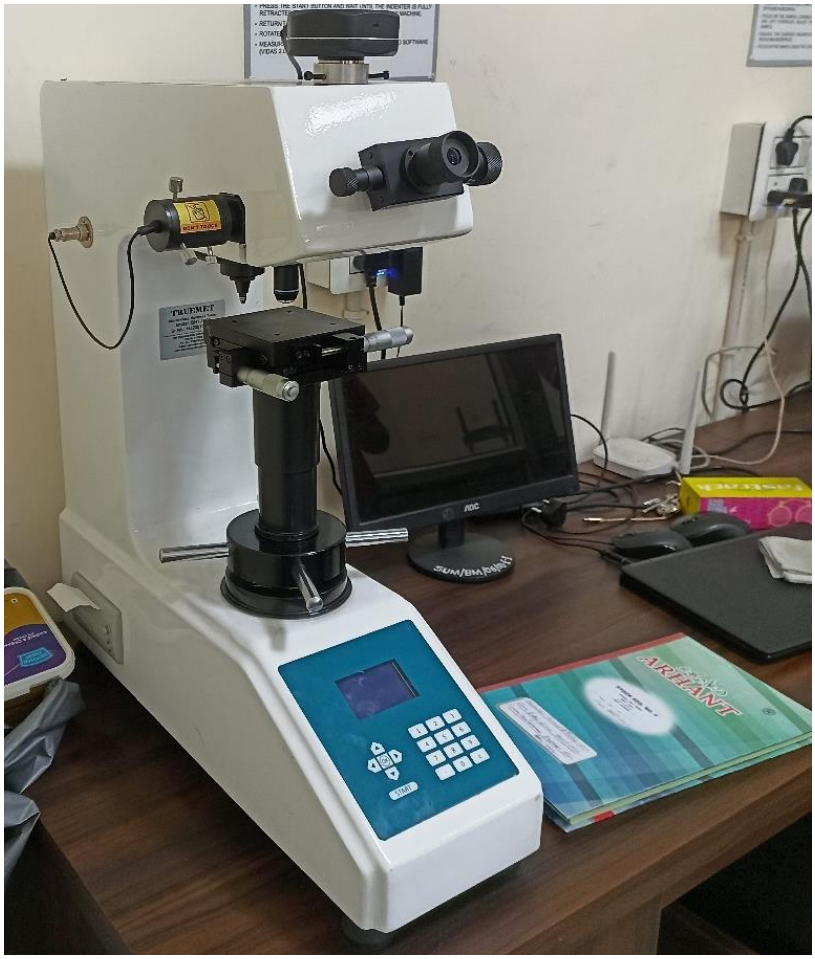

Figure 4.9: Microhardness testing machine

The machine is calibrated, and the test parameters, such as the load and dwell time, are set according to the standard testing protocols. Starting from the AZ91D side of the weld, indentations are made at regular intervals along the transverse cross-section of the joint, progressing toward the AA2024 side. A total of 41 indentations are made, with careful attention to maintaining consistent spacing between them to capture the microhardness profile across different zones of the welded joints, including the SZ, TMAZ, and HAZ. After each indentation, the microscope is used to measure the diagonal lengths of the indentations, which are then converted to hardness values using the appropriate formula. 3The collected data provides a comprehensive hardness profile from the AZ91D to the AA2024 side, highlighting variations in hardness due to modifications in material properties and the effects of the welding process. This detailed analysis is crucial for understanding the mechanical integrity and performance of the welded joint.

4.7 Microstructural analysis

4.7.1 Sample preparation

The samples preparation for microstructure analysis of a welded joint on a disc polishing machine involves a series of meticulous steps to ensure a high-quality polished surface suitable for microscopic examination. Initially, the specimen is cut to 10×10 mm size to expose the weld cross-section, typically perpendicular to the weld direction. This ensures that all relevant zones, such as SZ, TMAZ, and HAZ are included. The cut specimen is then mounted in a mounting medium, such as epoxy resin, to provide a stable and easy-to-handle sample during the grinding and polishing process. Once the resin is cured, the mounted specimen is ready for grinding.

Grinding begins with coarser grit emery papers, starting from 400 grit, and progressively moving to finer grits up to 3000 grit. Each stage of grinding is performed on a rotating disc polishing machine. The specimen is held firmly against the rotating disc, ensuring consistent pressure and movement to achieve a flat and scratch-free surface. During this process, the specimen is frequently rinsed with water to remove debris and prevent overheating.

After grinding, the specimen undergoes a polishing process to attain a mirror-like polishing demonstrated in Fig. 4.10. This involves using a polishing cloth on the disc machine impregnated with Al_2O_3 powder. Polishing is conducted with progressively finer grades of Al_2O_3, ensuring that all previous scratches are removed, and a smooth, reflective surface is obtained.

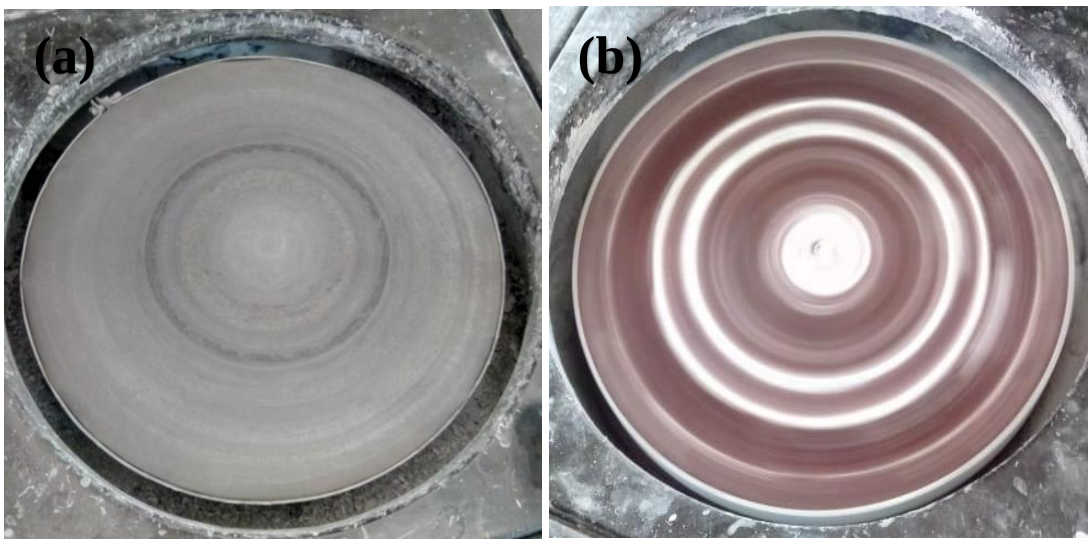

Figure 4.10: (a, b) polishing on emery paper and emery cloth, (c) making etching solution

Following the polishing process, the specimen is cleaned thoroughly to remove any remaining polishing compound. It is then ready for etching to reveal the microstructure. Keller's etchant, a solution typically composed of nitric acid, hydrochloric acid, hydrofluoric acid, and water, is used for this purpose. The samples are carefully immersed in or swabbed with the etchant for a specific duration, usually 15-20 secs to minutes.

After etching, the specimen is rinsed with alcohol, and dried. The etched surface reveals the grain boundaries, phase distribution, and weld zones, which can be observed and analyzed under an optical and SEM machine for detailed examination. This thorough preparation ensures that the microstructural characteristics of the AZ91D and AA2024 welded joint are accurately represented and analyzed.

4.7.2 Optical microscopy testing

After polishing and etching the welded joints, the specimens are prepared for optical microscopy and SEM analysis following a detailed procedure shown in Fig. 4.11 and

4.12. First, ensure the specimens are thoroughly cleaned to remove any debris or residual etchant. This involves rinsing with distilled water and then with alcohol, followed by gentle drying using compressed air or a lint-free cloth to avoid contamination.

Figure 4.11: Optical Microscopy machine

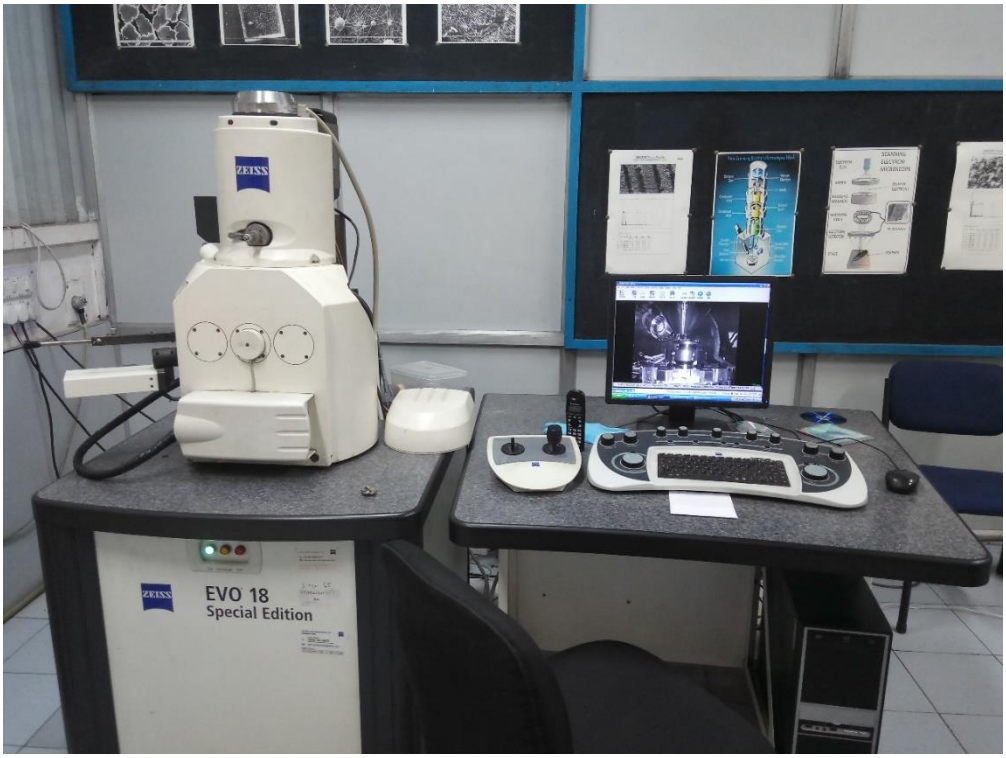

Figure 4.12: Scanning Electron Microscope Machine

For optical microscopy, the specimen is mounted on a microscope slide or stage using a suitable mounting medium to secure it in place. The polished and etched surface is then examined under a light microscope equipped with suitable magnification and lighting conditions. Observations focus on features such as grain structure, weld bead morphology, and any microstructural changes induced by the welding process. Photomicrographs may be captured to document key findings.

For SEM analysis, the specimen is mounted on a SEM stub using a conductive carbon tape to ensure electrical conductivity. The SEM is operated at appropriate voltage and magnification settings to investigate the microstructure at higher resolutions. This includes observing details like grain boundaries, second-phase particles, fracture surfaces, and any defects within the welded joint. Elemental analysis using EDS may also be performed to identify chemical compositions across different regions of interest. Both optical microscopy and SEM provide complementary insights into the metallurgical properties of the welded joints, offering a comprehensive understanding essential for evaluating the weld quality and performance. Detailed documentation of observations and analysis is crucial for subsequent interpretation and comparison with theoretical models or standards.

CHAPTER 5

5. Results and Discussion

5.1 Effect of pin profile on the mechanical properties of the weldments

5.1.1 Microstructure analysis

The study of the macrostructure of FSWed joints created using triangular, square, and circular pin profiles reveal significant understandings into weld quality and defect formation. Fig. 5.1 illustrates these macrostructures, showing that when triangular and circular threaded pin profiles were employed at a TS of 30 mm/min and TRS of 600 rpm, and a tunnel like defects appeared at the weld bottom. While, using a square pin profile resulted in a sound, defect-free weld.

The results indicate that the square pin profile is more effective in generating sufficient frictional heat to soften both AA2024 and AZ91D at the specified TS and TRS. The area near the rotating tool undergoes significant temperature gradients and plastic deformation, leading to pronounced deformation on the AS [238]. The varying thermal cycles experienced by the two edges result in different precipitate distributions and distinct material properties within the welded zones. In these regions, plastic deformation is often accompanied by DRX. Macrostructure analysis of the weldments reveals that specimens made with triangular and threaded circular pin profiles exhibited tunnel defects in the surface roots of the SZ, while the square pin profile fabricates defect-free welds. The absence of defects in the SZ with the square pin profile indicates effective material flow around the tool pin, showcasing its superiority in creating high-quality welds compared to the other profiles. This effective material flow and heat transfer are crucial for achieving sound welds without defects [239]. The findings suggest that optimizing pin profile design, particularly using a square pin profile, can significantly enhance the welding quality of dissimilar materials like AZ91D and AA2024.

Defects in the SZ result from inadequate material flow, especially with threaded and triangular pin profiles, due to excessive heat input promoting turbulent flow and cavity formation. The vortex flow pattern created during welding AZ91D and

AA2024 leads to chaotic mixing and lamellae of different phases [240]. Cracks or voids in the SZ reducing strength. On the AA2024 side, the TMAZ shows coarse grains, while the AZ91D side displays partial CDRX with refined grains. Fortunately, this does not negatively impact joint efficiency. The square pin profile effectively achieves defect-free welds and enhances the quality of the joints by promoting better material flow and heat transfer.

Pin profile	
Threaded circular	
Triangular	
Square	

Figure 5.1: Macrostructure of the welded region of AA2024 and AZ91D, (a) Circular threaded, (b) triangular, (c) square pin

The effectiveness of different tool pin profiles in FSW thoroughly examined. The macrostructure of joints created by different pin profile observed distinct differences in weld quality. At a TRS of 600 rpm and a TS 30 mm/min, tunnel defects were consistently present in welds produced using triangular and circular threaded pin profiles. Conversely, welds made with a square pin profile were free from such defects, indicating superior weld quality [241]. This suggests that the square pin profile is more efficient in facilitating adequate heat transfer and material flow, thereby preventing defects commonly associated with excessive heat input and insufficient material flow in other profiles.

A detailed investigation into the tool offset effects on the welded joints of AZ91D and AA2024 highlighted several key findings. When a zero-tool offset was applied, the resulting welds had a smoother surface with minimal flash formation, indicating improved surface quality and fewer defects. This optimal condition enhances material flow and mixing, resulting in a uniform and defect-free weld zone. The microstructural analysis of the FSWed zone revealed complex interactions of vortex and lamellae structures, leading to momentous fluctuations in hardness across all pin profiles shown in Fig. 5.2. These values were measured using specific techniques to assess the band of lamellae [242]. Irregular hardness spikes result from severely deformed DRX regions mixed with dislocation-free zones due to the DDRX mechanism, creating non-equilibrium grain boundaries with high dislocation densities.

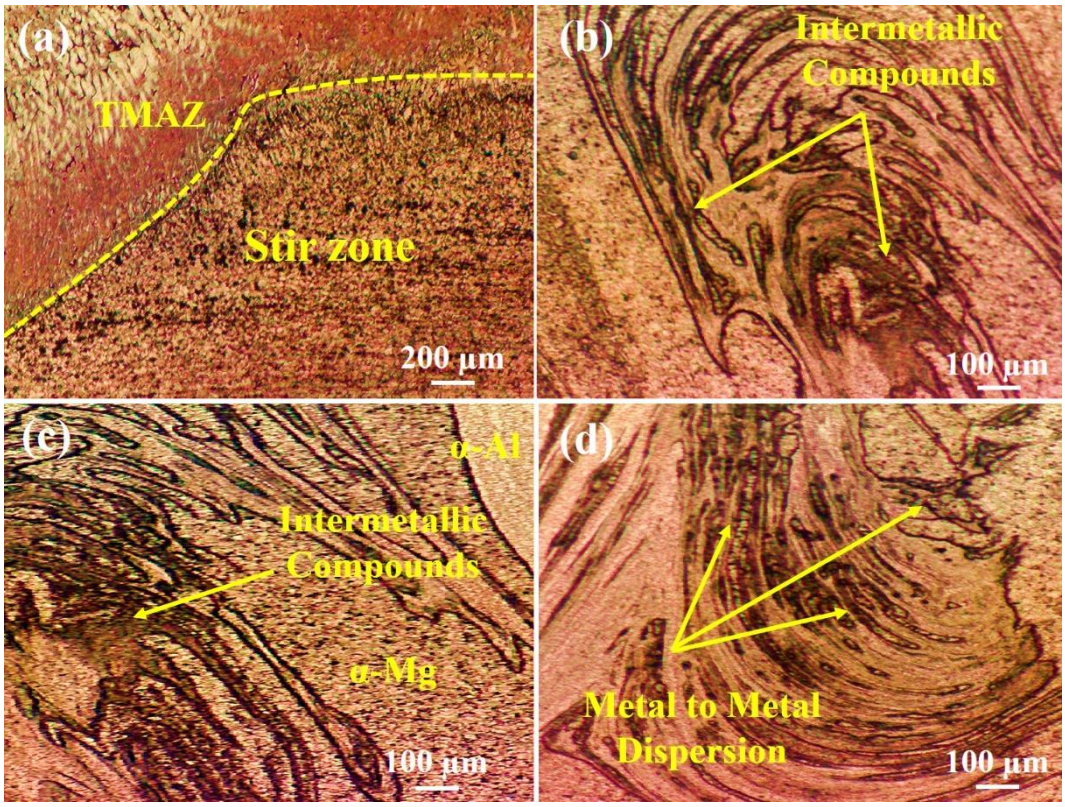

Figure 5.2: Microstructure images of AZ91D and AA2024 weldments (a) different zones, (b) square pin, (c) triangular pin, (d) circular threaded pin

The optimal tool offset condition promotes mixing and superior material flow, resulting in enhanced intermixing of base metals. This interplay is critical for attaining high mechanical properties in the weldments. The microstructural

examination also revealed that the formation of IMCs and the distribution of 2nd phase particles are vital in determining the UTS and microhardness of the weld zone. The presence of deformed DRX, alongside dislocation free regions, suggests a complex recrystallization process affected by the thermal cycle and tool offset experienced during welding [243]. The DDRX mechanism significantly impacts the microstructural characteristics of the weldments. It leads to the generation of non-equilibrium grain boundaries with high dislocation densities, unevenly distributed within the grain boundaries and interiors. This results in significant variations in microhardness values, reflecting the intense plastic deformation and dynamic recovery processes during welding. The rotational tool speed in FSWed joints dramatically impacts the microstructure on the AZ91D side. It was found that the triangular pin generated insufficient heat, resulting in void defects and poor intermixing. EDX analysis of samples welded with the square pin profile shows that tool offset can fragment hard particles, enhancing strength. However, excessive offsets cause significant particle fragmentation, leading to voids and reduced UTS in the joint [244].

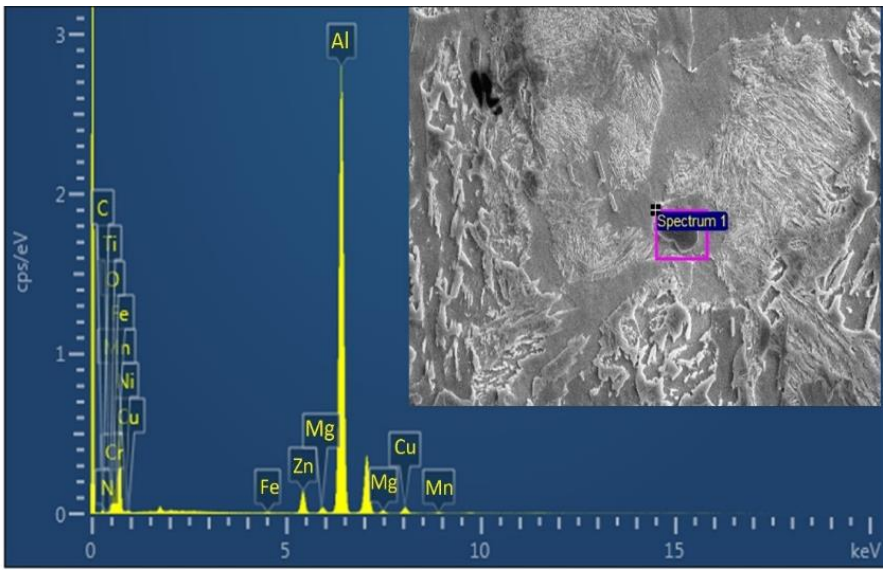

Figure 5.3: EDX image of welded joints of AA2024 and AZ91D of square pin.

The EDX results reveal that the IMC layers on the AZ91D side contain 42.4 wt% Al and 53.7 wt% Mg, while the AA2024 side has 64.1 wt% Al and 32.9 wt% Mg shown in Fig. 5.3. These findings emphasize balancing particle distribution and fragmentation, enhancing joint strength, and minimizing void formation. Fine-tuning

FSW parameters, particularly tool offset, is crucial for achieving effective intermixing and preventing voids. The SEM images of friction stir weldments of between AZ91D and AA2024, by circular, triangular, and square pin, were revealed in Fig. 5.4a-c. There was a notable improvement in intermixing at the interface between AZ91D and AA2024 in square pin profile. The acoustic during welding further enhanced disrupted the oxide layer and mixing, leading to a robust metal-to-metal bond. This enhancement signifies the development of strong interfacial bonds in the weldments of these two alloys. DRX in the SZ leads to the materialization of very fine grains, which significantly improve tensile strength of the weldments [245].

During welding, the SZ grains undergo significant deformation due to the tool shoulder's extrusion action.

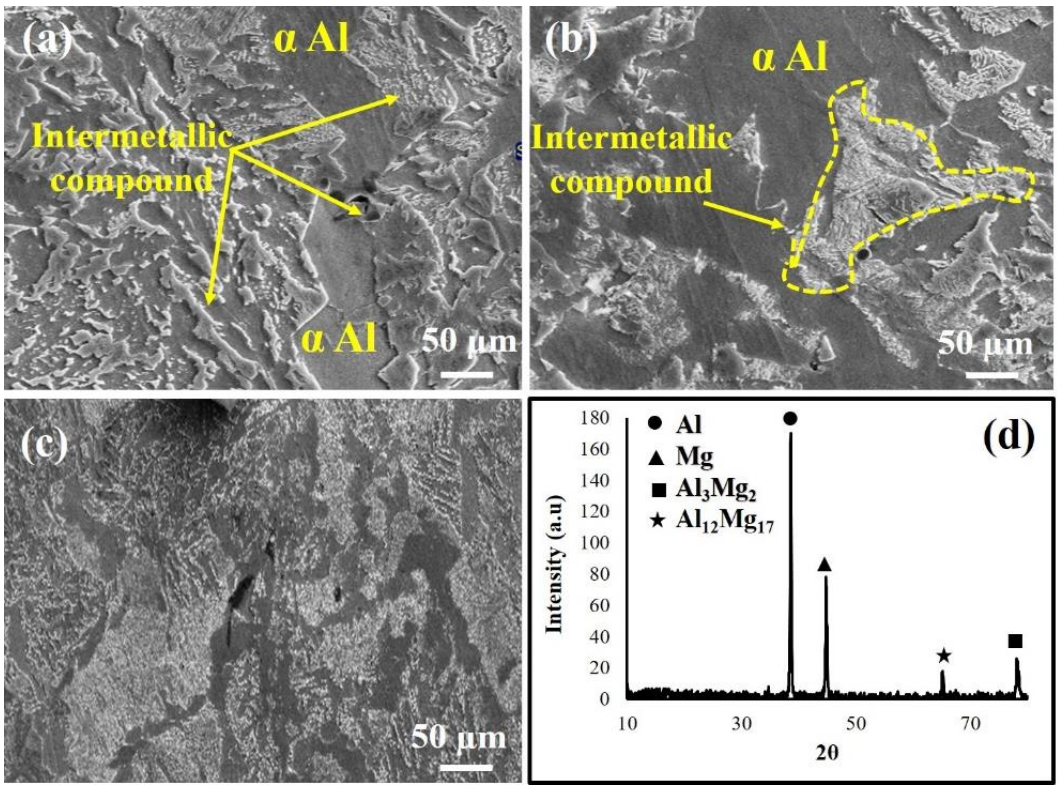

Figure 5.4: High magnification SEM image of FSWed joints, (a) circular threaded, (b) triangular (c) Square (d) XRD image for square pin profile

The top surface of the FSWed joints experiences high temperatures and strain gradients, causing numerous irregular grains. Dense sub-grain boundaries contribute to these irregularities. Al_3Mg_2 and $Al_{12}Mg_{17}$ IMCs form due to Mg and Al atom dispersion, with $Al_{12}Mg_{17}$ migrating towards the AZ91D plate side, potentially

causing liquation and eutectic microstructures. Different tool pin profiles were evaluated to minimize the effects of IMCs, with the square pin profile producing defect-free joints [246]. Refined grains result from stirring action and the rotation of the tool. Significant microstructural differences were observed between the pin profiles. The HAZ experiences a moderate strain rate, resulting in a microstructure characterized by larger grains.

In contrast, the SZ exhibits equiaxed grains due to a combination of moderate plastic strain and lower temperature compared to the TMAZ and HAZ. In the welding process, the DRX and grain refinement mechanisms are paramount. The SZ sees a combination of high strain and DRX, promoting the development of refined, equiaxed grains. It is due to the DRX processes triggered by severe plastic deformation and heat generated by the tool's rotation and traverse movements [247-249]. The role of the tool's shoulder and pin in material flow and heat generation is critical. The square pin profile, with its unique geometry, enhances material mixing and heat generation, resulting in defect-free welds. The absence of tunnel defects, commonly seen in joints made with triangular and circular pin profiles, underscores the efficiency of the square pin profile in achieving optimal material flow and consolidation. The distinct microstructural zones—SZ, TMAZ, and HAZ—each exhibit unique characteristics due to varying thermal and mechanical conditions during FSW. The SZ, subjected to the highest temperatures and strains, shows fine, equiaxed grains due to DRX [250]. The TMAZ, located adjacent to the SZ, experiences a combination of deformation and partial recrystallization, resulting in a mixture of refined and coarser grains. The HAZ, farthest from the weld center, undergoes thermal cycles that lead to grain growth without significant plastic deformation. Tool geometry significantly influences the mechanical properties of FSW joints. The square pin profile's ability to generate sufficient frictional heat and facilitate material flow results in superior joint strength and ductility.

The presence of IMCs, i.e., Al_3Mg_2 and $Al_{12}Mg_{17}$, in determining the joint's mechanical performance. These IMCs form due to the reaction between aluminum and magnesium at elevated temperatures. The formation of IMCs can be beneficial or detrimental, depending on their distribution and morphology. Proper control of welding parameters can minimize the formation of brittle IMCs, ensuring improved joint properties. Thermal cycles during FSW play a crucial role in the materialization of metallurgical properties. The welding temperature influences grain growth,

recrystallization, and the formation of IMCs. Optimizing the TRS and TS is essential to control the heat input and achieve the desired microstructural characteristics. Higher TRS increases the heat input, promoting grain refinement and DRX in the SZ. Conversely, higher TS reduces the heat input, leading to a more pronounced HAZ with coarser grains.

The FSW process also affects the residual stress dissemination in the FSWed joints. The thermal and mechanical cycles during welding induce residual stresses, which can impact the joint's mechanical properties and service performance. Proper optimization of welding parameters and tool design can minimize residual stresses and improve the joint's efficiency. The consequence of pin profiles on the FSW process extends beyond the microstructural characteristics. The tool geometry and welding parameters directly influence the mechanical properties of the welded joints. The square pin profile, with its ability to enhance material flow and heat generation, results in superior mechanical properties compared to other pin profiles. The formation of defect-free welds with the square pin profile is attributed to its efficient material mixing and heat distribution. The absence of tunnel defects and voids in the SZ ensures optimal mechanical performance. The refined grain structure, uniform distribution of alloying elements, and controlled formation of IMCs contribute to the joint's enhanced strength and ductility. DRX promotes the formation of new, smaller grains during deformation at high temperatures. In the SZ, high temperature and plastic deformation facilitate the nucleation and growth of new grains, resulting to a refined grain structure. The stirring action of the rotating tool further breaks and redistributes grains [251], enhancing this refinement. Smaller grain sizes improve strength and mechanical properties, thus enhancing the UTS and overall performance and structural integrity of the FSWed joint.

Additionally, the study highlights the optimizing tool offset to achieve superior weld quality in FSW of AA2024 and AZ91D. A zero-tool offset not only improves the surface appearance and reduces defects but also enhances the tensile properties of the weldments by promoting uniform material flow and adequate mixing. The intricate microstructural features observed in the weld zone, including the interplay of vortex and lamellae structures, DRX regimes, and dislocation densities, underscore the complexity of the welding process and its impact on the resultant weld properties. The findings emphasize that the pin profile is crucial in achieving optimal weld quality in FSW of dissimilar materials. Proper selection and fine-tuning of these parameters can

lead to improved mechanical properties, higher joint strength, and reduced defects, making FSW a viable method for joining dissimilar materials in various industrial applications.

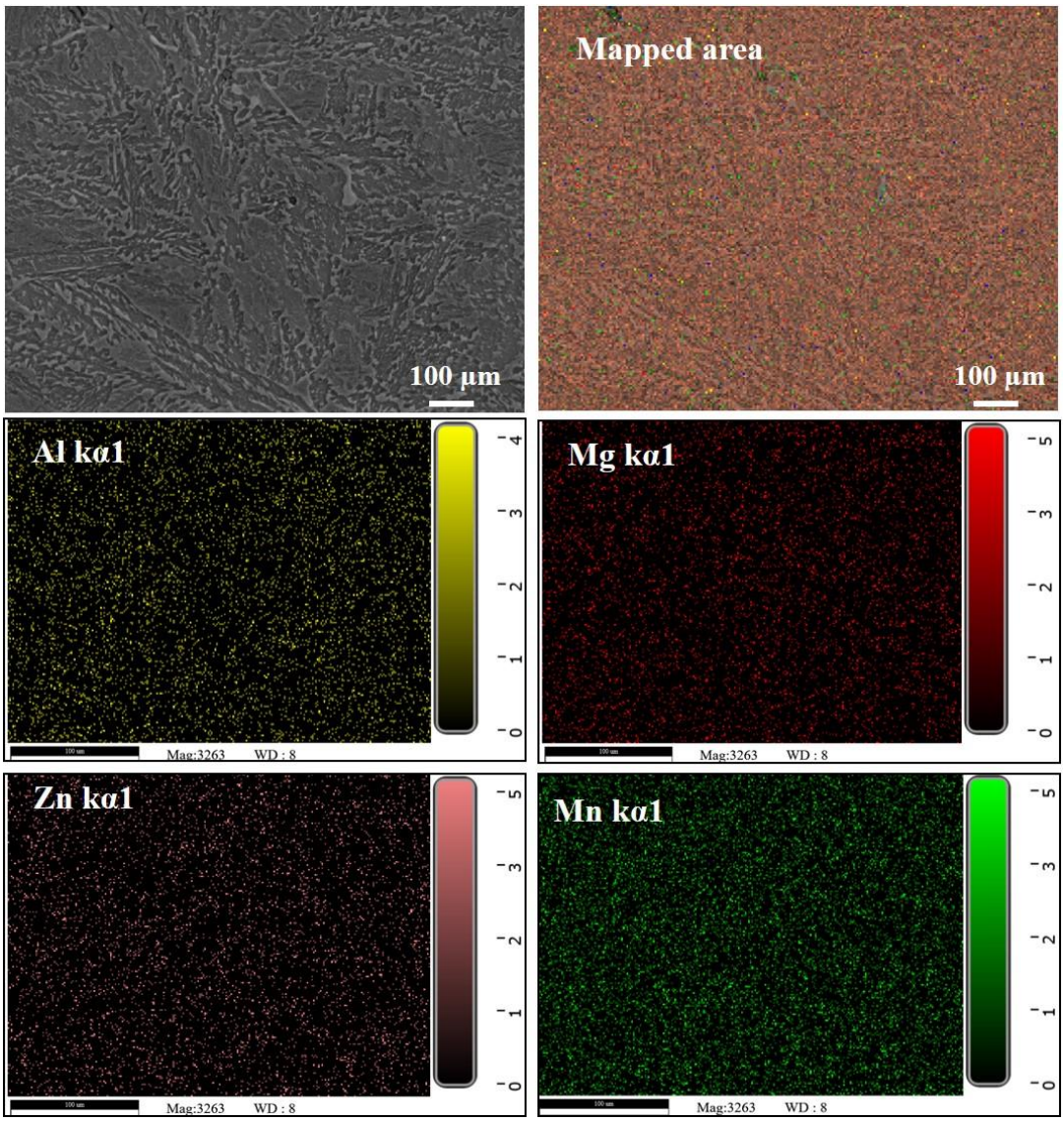

Figure 5.5: Elemental mapping of FSWed joint for square pin.

Fig. 5.5 illustrates the elemental mapping of the SZ in FSWed joints, highlighting the dissemination of key elements, i.e., Mn, Al, Zn, Mg, and Si. The mapping reveals a uniform distribution of these elements throughout the SZ, which signifies the presence of distinct flow patterns during the welding process. The mapping shows Mg in green and Al in red, indicating the formation of Al and Mg-rich phases or IMCs. The use of a square pin profile, combined with acoustic assistance, significantly enhances the mixing and bonding of the materials, resulting in a strong joint. The microstructure is

characterized by refined grains and uniform distribution of elements, contributing to enhanced joint efficiency [252]. This observation underscores the importance of choosing the appropriate tool pin profiles and optimizing welding parameters to produce defect-free joints with superior mechanical performance. Understanding these factors allows for tailoring the welding process to enhance the strength and durability of dissimilar metal joints, such as those between AZ91D and AA2024. Elemental mapping reveals that Al and Mg content is lower at grain boundaries compared to within the grains, confirming the presence of shear bands in the SZ. Shear bands are regions of localized deformation with intense shear forces, resulting in the preferential alignment and distribution of elements along the boundaries. This finding highlights the impact of shear forces on the microstructure and elemental distribution within the welded joint, contributing to its overall mechanical properties.

The flow behaviors and mixing during the FSW process indicate complex patterns. High temperatures in the SZ promote recrystallization in some grains while others undergo nucleation. The stirring action of the rotating tool breaks down grains and redistributes them into smaller, uniformly distributed ones, refining the grain structure. This high energy input can induce both continuous and discontinuous DRX. Continuous DRX typically occurs at lower strain rates and higher temperatures, while discontinuous DRX involves abrupt nucleation and growth under higher strain rates and lower temperatures. Understanding these mechanisms is crucial for optimizing the FSW process to achieve the desired microstructural and mechanical properties.

5.1.2 Effect of pin profile on UTS

The microhardness and tensile properties in the SZ for different pin profiles are detailed in Tables 5.1-5.3. The UTS of the base AA2024 and AZ91D alloys were 412.68 MPa and 216.27 MPa, respectively. The UTS of the welded joints varied based on the tool pin profile used. The highest UTS value of 153.7 MPa was achieved with the square pin profile, while the lowest UTS value of 123.84 MPa was observed with the triangular pin profile. The reduced UTS in the triangular pin profile is attributed to the formation of a brittle β-phase layer, which negatively impacts the joint's mechanical properties, leading to decreased strength. Most welded joints were free from cracks and defects, except for those produced with the triangular tool pin profile. In these instances, cavity defects formed due to insufficient heat input and

improper tool-to-material contact conditions [253]. The square pin profile proved to be more effective in generating sufficient frictional heat, facilitating better material mixing and flow around the tool, resulting in defect-free welds. The superior performance of the square pin profile can be attributed to its ability to produce a more homogeneous and refined grain structure in the SZ through DRX. The stirring action of the rotating tool, combined with appropriate thermal cycles, breaks down the grains and redistributes them, enhancing the joint's overall strength and structural integrity.

Table 5.1: UTS of FSWed joints of AZ91D and AA2024 at 95% CI

Parameter	UTS (MPa)			Mean UTS (MPa)	SD	SE	95% confidence Interval (CI)	
	Sp-1	Sp-2	Sp-3				Maximum	Minimum
Square Pin	154.76	152.44	152.85	153.35	1.24	0.71	151.95	154.75
Triangular Pin	123.77	125.95	124.56	124.76	1.10	0.64	123.51	126.01
Threaded circular pin	134.5	137.21	135.36	135.69	1.38	0.80	134.12	137.26

These findings underscore the importance of tool pin profile selection in optimizing the microstructural and mechanical properties of the FSWed joints. The strength of the weldments via FSW were notably lower than the base alloys. The tool pin profile significantly impacted microhardness and UTS, with the square pin profile showing improved tensile properties. In contrast, the triangular and threaded circular pin profiles caused poor material flow and increased liquation, reducing joint efficiency.

Table 5.2: % Elongation of the AZ91D and AA2024 welded joints at 95% CI

Parameter	% Elongation			Elongation (%)	SD	SE	95% CI	
	Sp-1	Sp-2	Sp-3				Maximum	Minimum
Square Pin	11.68	11.06	12.24	11.66	0.59	0.34	10.99	12.33
Triangular Pin	9.59	9.63	9.78	9.67	0.10	0.06	9.55	9.78
Threaded circular pin	9.52	9.15	8.89	9.19	0.32	0.18	8.83	9.54

The use of the triangular tool pin profile in FSW resulted in inadequate distribution of IMCs and poor distribution of IMCs, which led to reduced joint strength. Factors such as interlocking, material flow, IMCs, and input heat between dissimilar alloys are

crucial when selecting a tool pin profile to enhance joint strength [254, 255]. The triangular pin profile's suboptimal performance highlights the need to address these variables to enhance the joint efficiency. The spinning action of the tool plays a vital role in breaking and redistributing the grains within the SZ, leading to a refined microstructure. Smaller grains resulting from this process are associated with enhanced microhardness [256]. The grain refinement within the SZ attributes to the structural integrity and performance of the FSWed joint. To achieve optimal results in FSW, particularly when welding dissimilar metals like AZ91D and AA2024, it is essential to select an appropriate tool pin profile and control welding parameters meticulously. It includes balancing heat input, ensuring adequate material flow, and achieving a desirable distribution of IMCs. Properly optimized parameters will enhance joint strength and improve the joint strength. The circular threaded pin design impacts plastic deformation and heat input, influencing the elongation of FSWed joints. On the other hand, the triangular pin profile, with its three sides, facilitates more efficient material mixing and deformation during welding, enhancing plastic flow and leading to better grain refinement, which can improve elongation. The square pin profile, with its four sides, also affects material flow and heat distribution uniquely. The square pin profile enhances material mixing and deformation, leading to a refined microstructure and higher elongation in welded joints. Elongation values for threaded circular, triangular, and square pin profiles were 9.2%, 9.7%, and 11.7%, respectively. Elongation is affected by the pin profile, process parameters, and alloy compositions. Optimizing these factors is essential for achieving improved elongation and weld quality in FSW of AA2024 and AZ91D.

Table 5.3: Microhardness value of the weldments of AA2024 and AZ91D at 95% confidence interval

Parameter	Microhardness (HV)			Mean Hardness (HV)	SD	SE	95% CI	
	Sp-1	Sp-2	Sp-3				Maximum	Minimum
Square Pin	85.88	84.46	86.21	85.52	0.93	0.54	84.46	86.57
Triangular Pin	94.25	90.26	92.72	92.41	2.01	1.16	90.13	94.69
Threaded circular pin	90.23	87.74	88.59	88.85	1.27	0.73	87.42	90.29

5.1.3 Effect of pin profile on the microhardness

The microhardness of FSWed joints of AZ91D and AA2024 and AZ91D using various tool pin profiles are summarized in Table 5.3. These measurements are crucial for evaluating the joint strength and hardness value of the weldments. The DRX significantly impacts the hardness of the weldments. For joints made with a square pin, DRX leads to the generation of a fine microstructure in the SZ, contributes to increased hardness values. DRX involves the generation of new, and refined grains due to plastic deformation and high temperatures, enhancing the microhardness in the SZ [256]. The influence of dislocations and grain boundaries also affects the microhardness. The highest microhardness recorded was 92.14 HV with the triangular pin profile, while the minimum was 85.52 HV with the square pin.

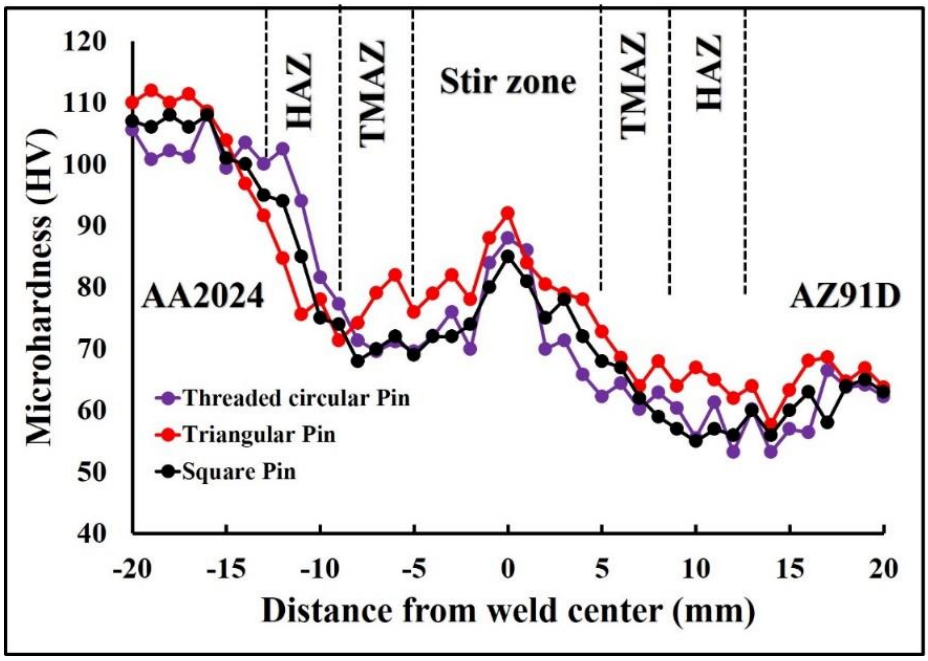

Figure 5.6: Microhardness dissemination of FSWed joints of AA2024 and AZ91D

These differences are attributed to the formation of complex structures, with lamellae and vortex patterns, during FSW, which affect hardness. The presence of lamellae bands in the SZ contributes to maximum hardness than the neighbor zones. The HAZ shows reduced microhardness relative to the base materials due to input heat and localized softening [257]. This reduction is due to heat-induced changes in the material structure, resulting in lower microhardness in the HAZ. The microhardness

dissemination across the welded joints reflects the thermal gradient and microstructure of the weldments. The SZ generally exhibits higher microhardness than the adjacent zones due to the presence of dislocations and grain boundaries. The middle and lower sections of the SZ, where IMCs form, typically show the highest hardness values [258].

Fig. 5.6 shows the microhardness dissemination along the transverse axis of the welded joints, with uneven distribution in the HAZ and TMAZ. The triangular pin profile achieved the highest hardness of 92.42 HV. The SZ hardness exceeded that of AZ91D but was lower than AA2024, highlighting the consequence of pin profiles and processing conditions on weld quality.

The development of IMCs is crucial to determining the hardness of FSWed joints. Grain size, phase precipitation and dislocation density influence the hardness in the SZ [259]. Smaller grain sizes and high dislocation densities generally enhance hardness. However, excessive heat, as seen with the square pin, can lead to grain growth and reduced hardness due to softening. AZ91D, are particularly sensitive to temperatures exceeding 215°C, which can adversely affect weld strength. Therefore, precise control of heat input and maintenance of optimal welding temperatures are essential to achieve desired microhardness in the SZ.

5.1.4 Fractography

Figure 5.7a-d displays SEM images of fractured specimens from the welded joints of AA2024 and AZ91D by variation of different pin profiles. The fractography reveals that joints made with circular and triangular pin profiles predominantly exhibit brittle fracture behavior. This brittleness is primarily attributed to the IMC layers present in these welds, which act as weak points that facilitate crack propagation [260]. For the triangular and threaded pin profiles, the presence of brittle IMC layers leads to fractures primarily within these zones. This results in cracks spreading through the brittle IMC areas rather than through the base material. The square pin profile demonstrates improved toughness, with fractures showing more signs of plastic deformation. When analyzing joints with high tensile strengths, necking is perceived, and the rupture surface exhibits a swirl-like pattern indicative of substantial plastic deformation before failure. SEM images confirm that areas with higher microhardness values are more susceptible to fracture initiation, leading to brittle failure

characterized by cleavage facets, as shown in Fig. 5.7b. These facets are indicative of fractures propagating through pre-existing cracks in a brittle fashion, which can be linked to the increased microhardness in the welded region. The occurrence of IMC layers at the welded region contributes significantly to brittle failure. These IMC layers serve as stress concentrators, initiating and propagating cracks. Although eliminating IMC layers is challenging, optimizing FSW parameters can help mitigate their adverse effects. Techniques aimed at reducing IMC formation and controlling their distribution can enhance joint quality and minimize brittleness [161, 162].

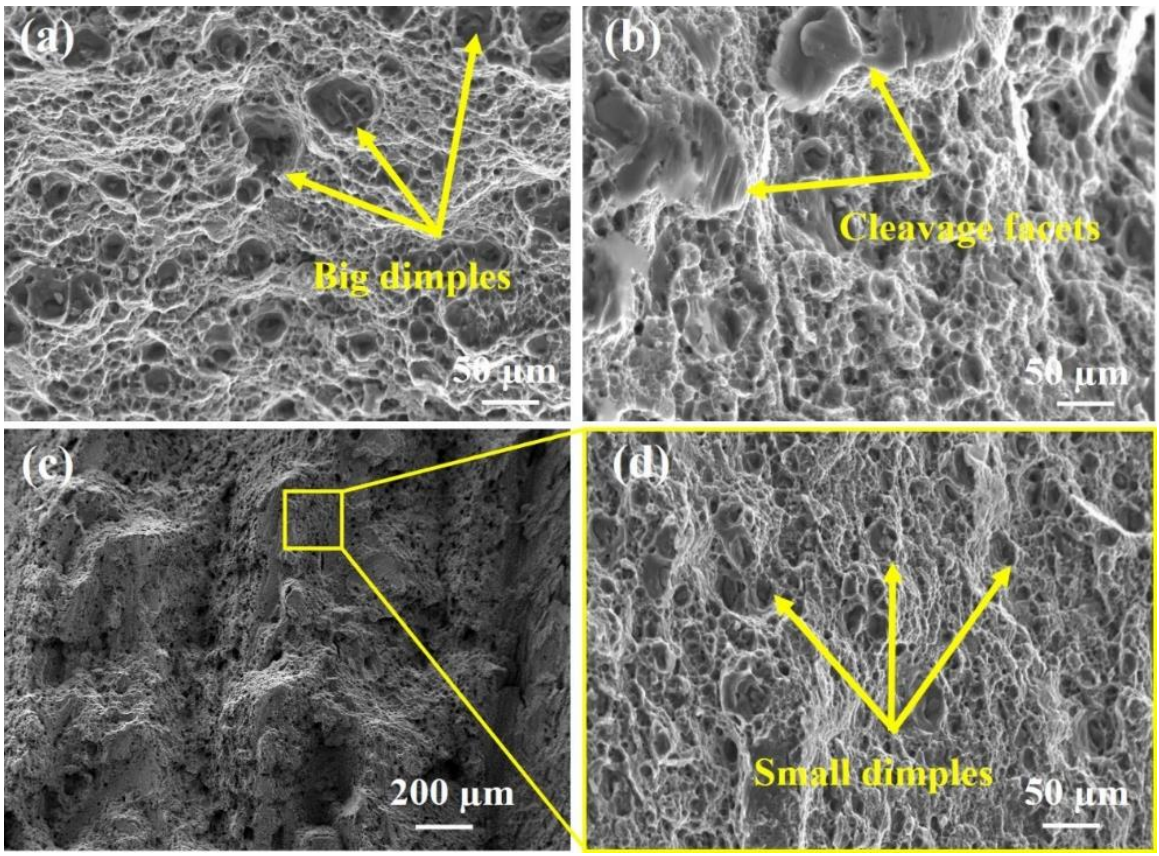

Figure 5.7: SEM images of tensile fractography of the FSWed joints at different pin profile (a) circular, (b) triangular, (c, d) Square pin

The choice of tool pin profile influences not only the microstructure but also the presence of IMCs and the joint's ability to resist cracking. For instance, the triangular pin profile, despite its potential to cause brittle failure, also shows areas of localized ductility. It suggests that variations in local mechanical behavior can impact the overall fracture path. In the case of the square pin profile, fractures generally exhibit improved ductility and less pronounced brittle failure. Micro void coalescence on

tensile fracture surfaces indicates localized deformation, with aluminum features expanding into mechanically locked configurations, leading to void formation. It highlights how joint microstructural features and heterogeneities influence failure mechanisms and overall mechanical behavior [263].

5.2 Effect of TRS on the welded joints

5.2.1 Phase diagram of Al-Mg

A phase diagram typically shows alloy composition on the x-axis and temperature on the y-axis, delineating different phase regions that are stable (Fig. 5.8). In FSW, Al12Mg17 and Al3Mg2 intermetallic compound can form, affecting the weld's tensile properties. The alloy composition, cooling rate and welding parameters significantly influence the formation and distribution of these IMCs. During FSW, the Al12Mg17 phase often forms near the β-Al12Mg17 phase, particularly at refined grain boundaries, restricting grain boundary mobility and impacting mechanical properties. The welding process alters eutectic phases within the alloy, breaking down coarse and elongated phases into finer particles. This breakdown is facilitated by DRX, where new grains nucleate and grow due to plastic deformation and high temperatures, influenced by the particle distribution within the alloy. Large, undissolved particles can accelerate DRX, while finely dispersed particles can impede it by preventing early grain growth. The Zener pinning effect, where dispersed particles hinder grain growth, can refine the microstructure and impact the tensile properties of the weldments. In FSW, the redistributes grains, and rotating tool's stirring action fractures, resulting in a finer grain structure. This refined grains and higher dislocation density, enhances microhardness and tensile properties. Intercalated microstructures, including vortex, and lamellae, contribute to microhardness variations. The thermal history of FSW affects hardness distribution. Heat input during welding can cause localized softening in the HAZ, leading to lower microhardness compared to base metals, while the SZ displays higher microhardness due to DRX and dislocations.

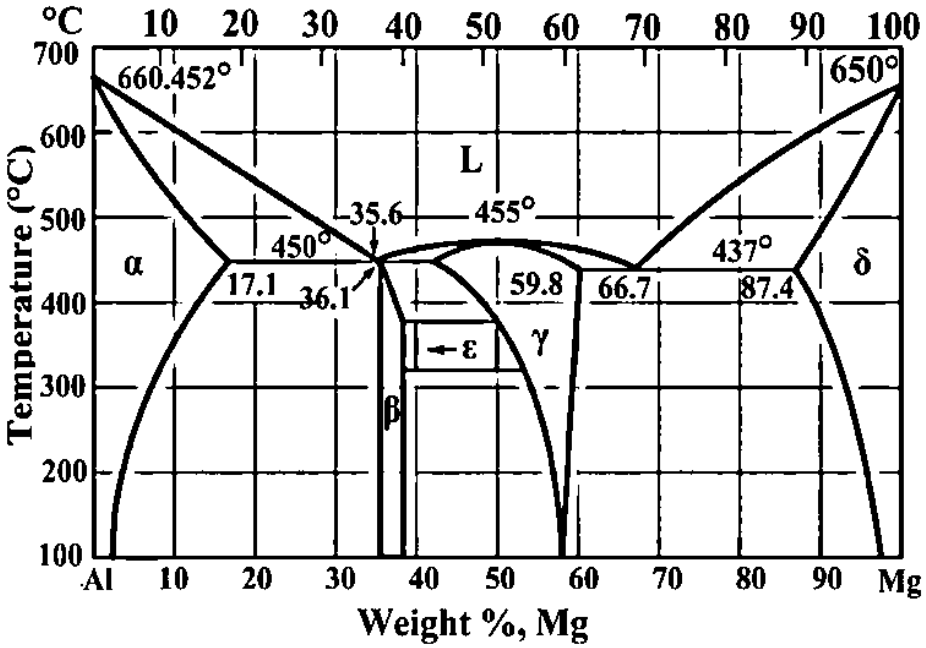

Figure 5.8: Al/Mg phase diagram [264]

5.2.2 Microstructure evaluation

Fig. 5.9 illustrates the microstructure of AZ91D and AA2024, while Fig. 5.10 shows the FSWed joint combining these alloys, displaying a multifaceted intercalated flow pattern. This pattern creates an intricate mesh, as seen in Fig. 5.10b, showcasing lamellar shear bands within the welded region. The interplay of vortexes and lamellae in this microstructure leads to significant variations and peaks in microhardness values across the FSWed zone. The rotating tool's stirring action fractures and redistributes grains, resulting in a finer grain structure. This refined structure, with smaller grains and higher dislocation density, enhances hardness and tensile properties. The thermal history of FSW affects hardness distribution: heat input during welding can cause localized softening in the HAZ, leading to lower microhardness compared to base metals, while the SZ displays higher microhardness due to DRX and dislocations. The interaction of AZ91D and AA2024 during FSW results in a complex, intercalated microstructure with improved mechanical properties.

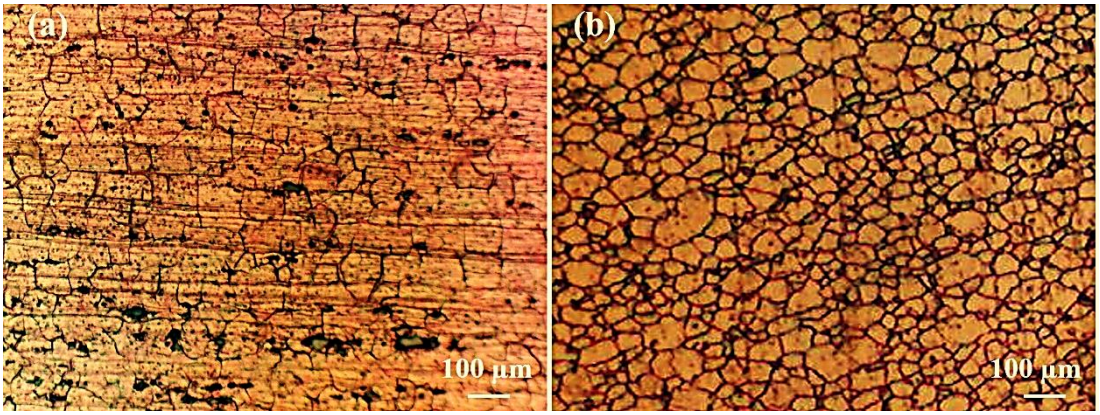

Figure 5.9: Microstructure of AZ91D and AA2024

Microhardness measurements, conducted along lamellae bands using specific methods, reveal irregular spikes indicating severely deformed DRX mixed with areas free of dislocations in the shear bands and intercalated DRX. The DDRX mechanism results in non-equilibrium grain boundaries characterized by a high density of dislocations both at the boundaries and within the grains themselves [265, 266].

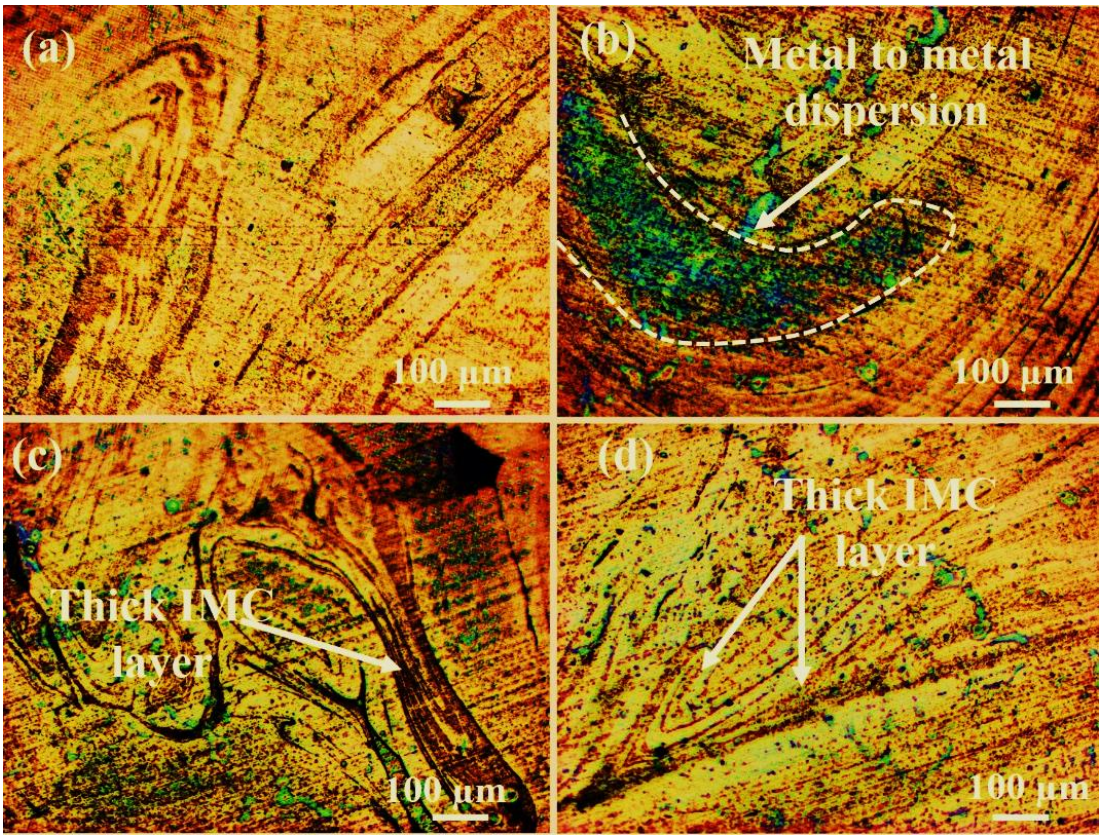

Figure 5.10: Microstructure of the welded joints at TRS of 800 rev/min and TS of 35 mm/min with at the SZ

These microstructural features and the distribution of dislocations and grain boundaries play crucial roles in determining the metallurgical characteristics of the weldments. They reflect the plastic deformation and thermal cycling experienced, influencing the hardness and overall structural integrity of the weldments. The microstructure of Mg-alloy was influenced by the TRS during FSW. Variations in TS can alter the DRX mechanism from CDRX to DDRX while maintaining a constant TRS. This phenomenon impacts the microstructural evolution of AZ91D, affecting grain size and distribution across the welded joint. Higher or lower TS alongside TRS may lead to distinct DRX behaviors, influencing the joint's property.

The IMC layers formation at the welded joints of AA2024 and AZ91D is crucial. Inadequate input heat, particularly at lower TRS, can result in insufficient intermixing between the alloys, potentially leading to void defects within the weld zone. The mixing behavior during FSW involves the rotational motion of the tool pin, generating a vortex flow pattern that facilitates chaotic mixing of aluminum and Mg-Alloys. This mixing process contributes to the development of lamellae structures comprising different phases, influencing the mechanical integrity of the weld.

Void and cracks in the SZ can serve as initiation points for crack propagation within the intermetallic material, significantly reducing the joint's overall strength compared to the base materials. The TMAZ exhibit distinct grain structures: coarse and elongated grains on the AA2024 side and equiaxed, smaller grains on the AZ91D side due to partial CDRX. Despite these variations, joint efficiency is generally maintained.

The influence of tool offset on weldments is significant, impacting the appearance and quality of the weld surface during FSW. A zero tool offset results in smoother welds with minimal flash, indicating better surface quality. EDX analysis shows varying offsets can enhance joint strength by effectively dispersing hard particles. However, excessive offset can lead to significant particle fragmentation, potentially creating voids that compromise the UTS of the bimetallic joint.

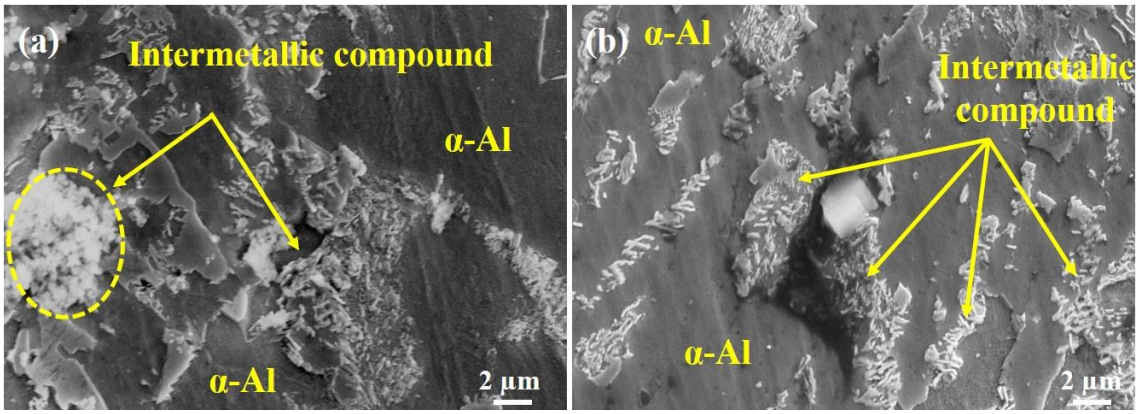

Figure 5.11: High Magnification Microstructure images of FSWed joints (a) 500 rpm, 20 mm/min, (b) 800 rpm, 20 mm/min.

Fig. 5.11a and 5b show high-magnification SEM images of weldments between AA2024 and AZ91D alloys. Increasing the rotational tool speed from 500 to 800 rev/min and using acoustic assistance enhanced intermixing, disrupted the oxide layer, and promoted strong metal-to-metal bonding, resulting in a robust joint [267]. Recrystallization phenomena were perceived in the SZ, leading to the formation of refined grains and contributing to enhanced joint strength—the higher TRS, coupled with DRX and plastic deformation, achieved these enhancements. The SZ exhibited irregular grain structures due to the strain gradients and high temperature experienced at the top surface of the joints [268, 269]. These conditions led to the development of dense sub-grain boundaries, which contributed to the uneven grain distribution observed.

EDS analysis provided insights into the composition of IMC (IMC) layers formed at the interface. On the Mg-alloys side, IMC layers consisted of 39.86 wt% Al and 55.47 wt% Mg, while on the AA2024 side, they contained 60.54 wt% Al and 35.57 wt% Mg, as depicted in Fig. 5.12. Higher TRS facilitated adequate intermixing between the base metals, promoted dispersion, and effectively suppressed the formation of voids within the joint. The occurrence of fined grains in the weldment is primarily attributed to stirring action and DRX exerted by the rotating tool during FSW. Understanding the distinct microstructural zones—SZ, HAZ, and TMAZ—is crucial for evaluating the material's properties. In the HAZ surrounding the SZ, the material undergoes significant thermal cycling during welding, leading to larger grains due to moderate strain rates. Conversely, the TMAZ displays equiaxed grains resulting from a combination of lower temperatures and plastic strain than the SZ. As welding

progressed from the SZ towards the parent materials, various levels of plastic strain were observed.

The SZ experiences intense plastic deformation and elevated temperatures due to the rotational tool's action. This combination triggers dynamic recrystallization, where new grains nucleate and grow within the SZ. DRX occurs as a response to elevated temperatures during plastic deformation, promoting the formation of smaller, refined grains [270]. The stirring action of the tool further enhances this process by redistributing and breaking grains, contributing significantly to microstructural refinement within the SZ.

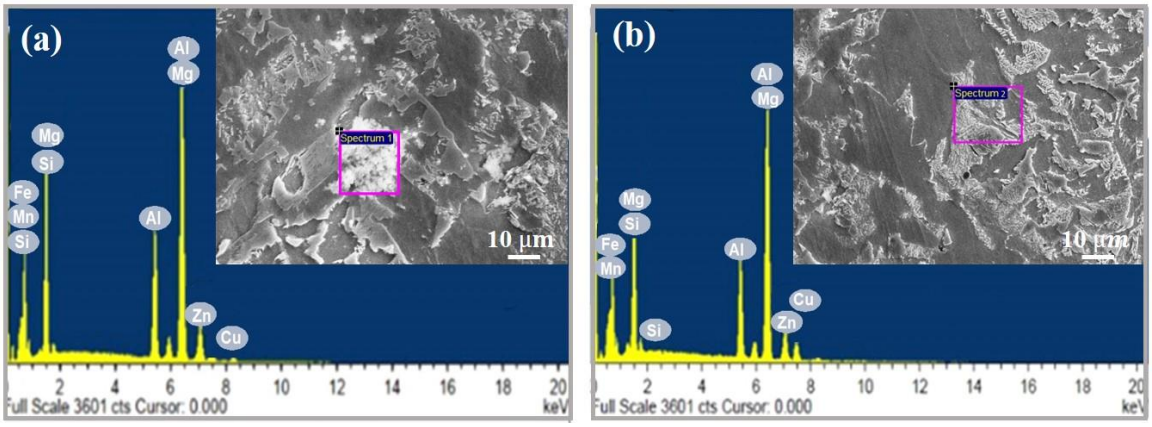

Figure 5.12: EDS analysis of welded joints at different process parameters (a) 700 rev/min, (b) 500 rev/min

The refined grain structure in the SZ significantly improves the UTS and overall mechanical properties of FSWed joints. Smaller grains enhance strength and performance, highlighting the need to optimize FSW parameters for desired microstructural and mechanical outcomes in industrial applications. During FSW, the SZ experiences intense heat produced by the frictional interaction between the base plates and the rotating tool. This heat promotes DRX in near grains while triggering nucleation further. Simultaneously, the rotating tool applies a stirring action that breaks down and redistributes grains, leading to an equiaxed microstructure within the SZ. This microstructural refinement is critical for enhancing joint efficiency. The high energy input during FSW induces DRX, which can occur in two forms: continuous and discontinuous. Continuous DRX involves the gradual formation of refined grains, whereas DDRX proceeds through sporadic growth and nucleation of new grains, depending on the base materials and welding conditions [271].

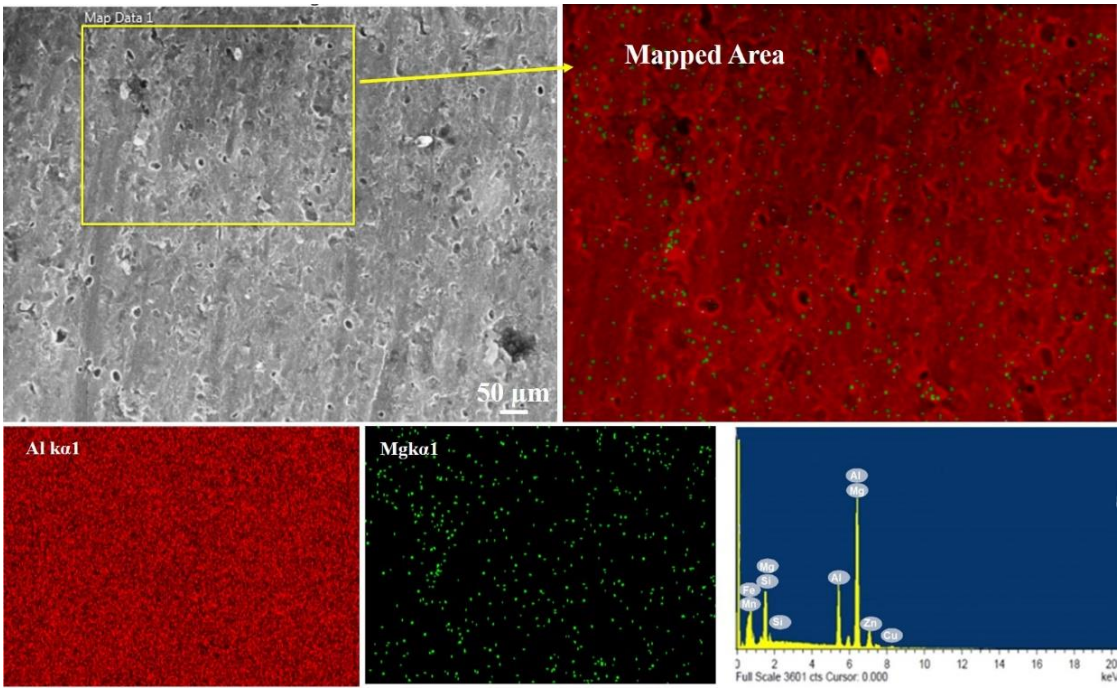

Figure 5.13: Elemental mapping of the FSWed joint at TRS of 700 rev/min.

Fig. 5.13 illustrates elemental mapping of the SZ, revealing a uniform dispersal of key elements such as Zn, Si, Mn, Cu, Mg, and Al. This uniform dispersion indicates complex flow patterns during FSW. Specifically, the mapping highlights regions minor in Mg (in green) and rich in Al (in red), suggesting the presence of Al and Mg-rich phases or IMCs. Notably, the Mg and Al content at grain boundaries is lower than within the grains themselves, confirming the existence of shear bands. Shear bands are localized regions where intense shear forces cause certain elements to align preferentially along boundaries, influencing the microstructural evolution.

Overall, the presence of shear bands and the uniform dissemination of elements underscore the intricate mixing behavior and flow dynamics inherent to the FSW process.

5.2.3 Tensile strength

In Fig. 5.14 and Table 5.4, the stress-strain curve and mechanical properties of FSWed joints of AZ91D and AA2024 alloys are presented, revealing significant differences from the individual alloys. The weldments exhibited lower strength and ductility than their respective base materials, influenced notably by the rotational tool speed (TRS) during welding. Individually, AZ91D and AA2024 demonstrated UTS of

216.27 MPa and 412.68 MPa, respectively. The UTS of the FSWed joint varied depending on the TS and TRS employed. The highest UTS of 147.26 MPa was achieved at a TRS of 700 rev/min, while the lowest UTS of 113.47 MPa was observed at 500 rev/min TRS with a TS of 35 mm/min, attributed to the formation of a brittle β phase layer, which adversely affected joint strength. Fig. 5.15 shows the maximum joint efficiency of 68.09% at a TS of 35 mm/min and TRS of 700 rev/min.

Table 5.4: Mechanical properties of AA2024 and AZ91D welded joints with different TRS

Sample No	TRS (rev/min)	WS (mm/min)	UTS (MPa)	Strain (%)	Joint efficiency (%)	Hardness at SZ (HV)
1	500	35	113.47	6.82	52.47	92
2	600		129.52	7.29	59.89	90
3	700		147.26	7.95	68.09	84
4	800		122.85	7.25	56.80	88

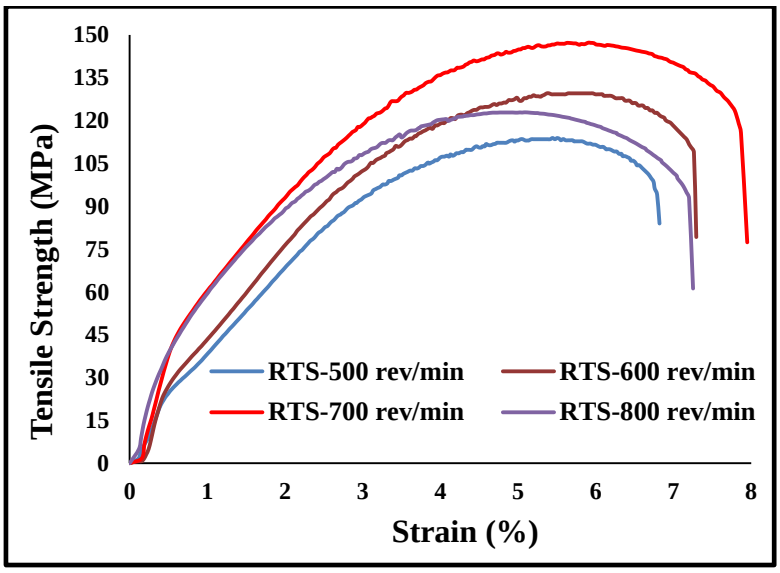

Figure 5.14: stress-strain curve of the FSWed joints of AA2024 and AZ91D at various TRS

Most joints were defect-free, except those made at low TRS and TS settings, which had cavity defects due to inadequate heat input and poor tool-to-material contact. Fracture analysis revealed brittle behavior in the elastic region of the FSWed joints. Tensile properties improved with higher TRS, while lower TS caused unfavorable

material flow and excessive heat, reducing joint efficiency. Inadequate dispersion of IMCs and poor distribution of intermetallic particles at lower TRS further weakened the joints. Optimizing welding parameters is crucial for achieving desired mechanical properties in dissimilar alloy joints. By carefully selecting and adjusting the TRS and TS, it is possible to minimize defects, enhance material flow, and ensure proper dispersion of intermetallic compounds, ultimately leading to stronger and more reliable welds.

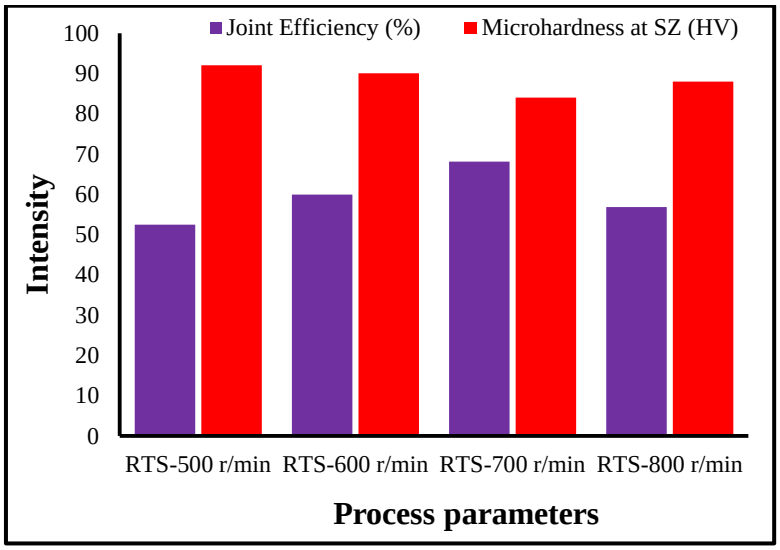

Figure 5.15: Variation of hardness value and joint efficiency at different parameters

5.2.4 Hardness distribution

Fig. 5.16 illustrates the dissemination of microhardness of the welded joints from the weld, highlighting variations influenced by microstructure changes and welding parameters. The hardness profile exhibited uneven distribution across the weldment, particularly in the TMAZ, SZ, and HAZ. In the SZ, which undergoes intense plastic deformation due to the tool rotation, the hardness was found to be lower than the AA2024 but higher than AZ91D due to the presence of intercalated microstructures such as lamellae and complex vortex patterns. These features contribute significantly to the observed hardness variations within the weldment. Specifically, the presence of lamellae bands in the SZ likely enhances its microhardness compared to adjacent zones [272]. The lower hardness values were observed at HAZ region compared to the base metals, primarily due to localized softening caused by heat input. This thermal effect leads to grain growth and reduced material hardness in the HAZ

relative to its parent metals. The microhardness distribution in the weldments is closely tied to the microstructural changes and thermal history of the FSW process. The SZ exhibited higher microhardness values than other zones due to DRX, where new grains nucleate and grow from plastic deformation and elevated temperatures. This refined grain structure significantly contributes to the increased hardness observed in the SZ [273].

Additionally, the presence of grain boundaries and dislocations further intensifies plastic deformation within the SZ, thereby influencing its hardness values. Dislocations act as strengthening elements in the crystal structure, while grain boundaries offer for dislocation interaction and accumulation, further enhancing material hardness. Within the SZ, variations in microhardness across different regions (lower, middle, and upper zones) may also be attributed to the generation of IMCs in specific areas [274].

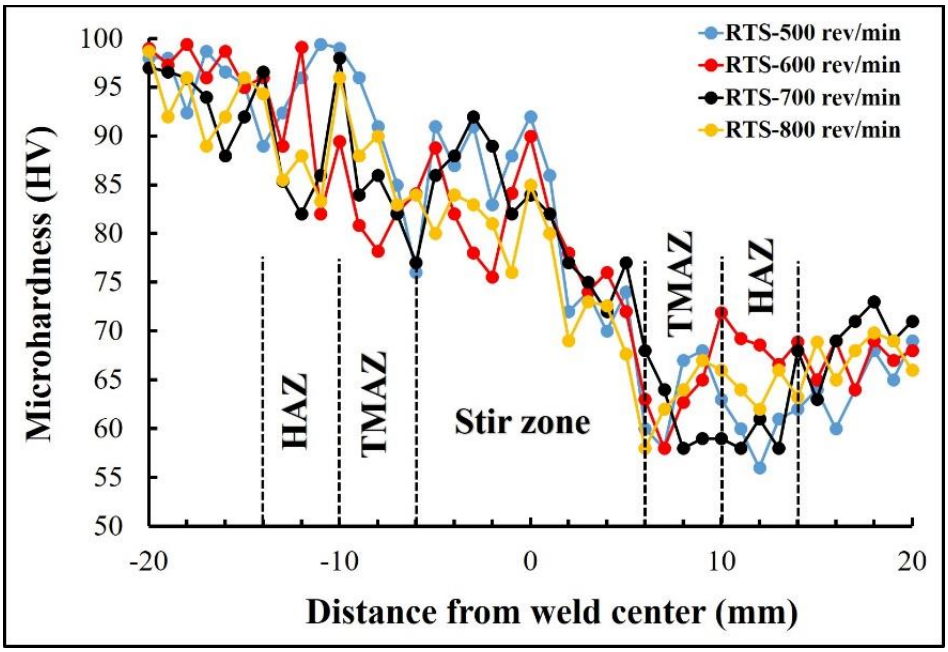

Figure 15.16: Distribution of hardness value of the AA2024 and AZ91D welded joints at various TRS

The hardness of the welded region was affected by precipitation of different phases, dislocation density, and grain size [275]. Higher dislocation density and smaller grains generally contribute to increased hardness, as they hinder dislocation movement, which strengthens the material. Additionally, the presence of precipitates can further enhance the material's strength through interactions with dislocations and

grain boundaries, providing additional barriers to deformation. This intricate interplay between grain size, dislocation density, and precipitates results in a microstructure that significantly contributes to the overall hardness. Therefore, understanding and controlling these factors is crucial for optimizing the performance and reliability of the welded joints [276]. Control of welding parameters, such as TRS and TS, is crucial for maintaining appropriate heat input during FSW. High TRS and low TS conditions can lead to excessive heat input, potentially causing grain growth, material degradation, and softening, particularly in Mg-Alloys like AZ91D, which are sensitive to temperatures above 210°C.The hardness distribution across the AZ91D and AA2024 welded joints reflects the intricate relationship between welding parameters, microstructure evolution, and resultant mechanical properties. The SZ, experiencing the most significant microstructural changes due to FSW tool action, typically exhibits maximum microhardness due to grain refinement and the occurrence of alloying elements and intermetallic phases from both base metals. Conversely, the HAZ undergoes recrystallization processes that can either increase or decrease hardness, depending on alloy composition and thermal cycles experienced.

5.2.5 Fractography

Fractography analysis using scanning electron microscopy (SEM), as depicted in Fig. 5.17, provides crucial insights into the failure mechanism and fracture behavior of the weldments between AA2024 and AZ91D alloys. The analysis revealed that regions with higher microhardness were more susceptible to fracture initiation, characterized by extensive brittle failure surfaces with cleavage facets. These IMC layers are known to form during welding and can adversely affect joint integrity by promoting crack initiation [277]. These layers not only initiated cracks but also influenced the path of crack propagation within the joint. The observation of brittle fracture surfaces suggests that the mechanical properties of the joint were compromised in regions containing these IMC layers.

In instances where the alloys exhibited higher tensile and yield strengths, necking was observed, indicating localized plastic deformation before eventual failure. This localized plasticity was evident in areas where significant energy absorption mechanisms, such as microvoid coalescence, were observed. Ductile materials like

AZ91D typically exhibit such dimpled fracture surfaces in SEM images, indicating substantial plastic deformation before fracture.

Conversely, regions with voids on the fracture surfaces were indicative of areas with porosity. Voids are irregular cavities or areas of darker contrast in SEM images, signifying weaknesses in the welded joint structure. These voids can arise due to inadequate welding parameters, poor process control, or contamination during welding, all of which can compromise the mechanical properties of the joint and contribute to premature failure under stress.

The presence of brittle areas in SEM images, characterized by smooth, flat surfaces without evidence of plastic deformation, underscores the role of IMCs or other factors in reducing ductility, especially in alloys like AA2024. Brittle fracture surfaces are typically associated with the presence of IMCs at weld interfaces or within the heat-affected zone (HAZ), where they can act as embrittling agents [278].

Mitigating the adverse effects of IMCs and optimizing welding parameters are crucial steps in enhancing the mechanical integrity of dissimilar alloy weldments. Techniques aimed at minimizing IMC formation and controlling their distribution within the joint can help mitigate the risk of brittle fracture. Adjusting TRS and other process parameters can influence microstructure evolution, IMC presence, and crack suppression, thereby improving the UTS and microhardness of the joints.

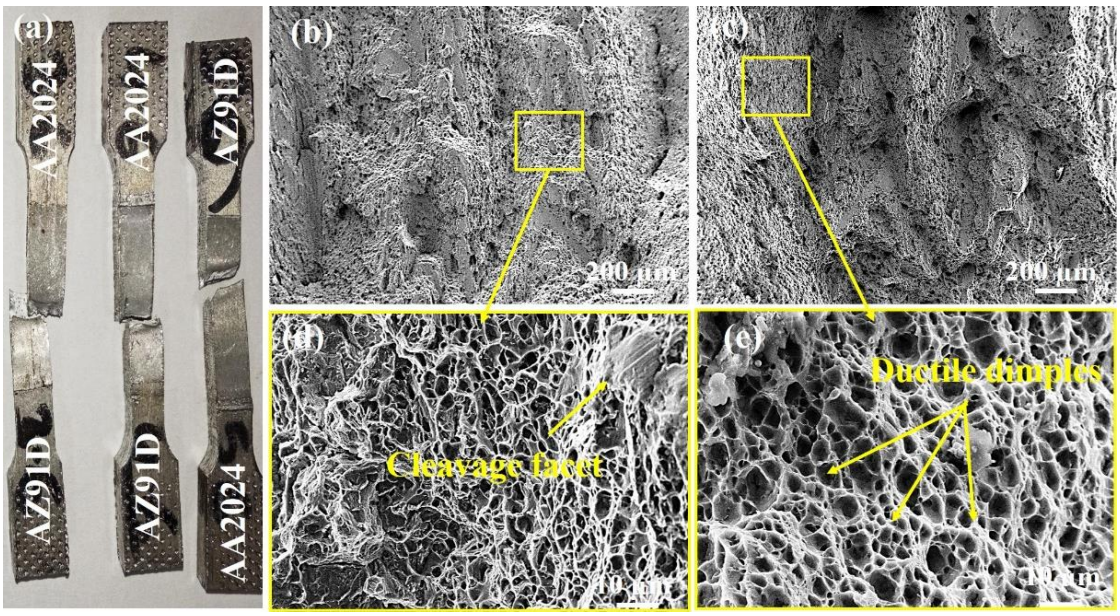

Figure 5.17: SEM images of fratography of the welded joints of AZ91D and AA2024, (a) TRS of 500 rev/min, (b) TRS of 700 rev/min

5.3 Effect of Nanoparticles on the FSWed joints of dissimilar alloys

This study utilized 150×50×6 mm AA2024 and AA7075 base plates reinforced with SiC and TiO2 nanoparticles, averaging 47±7 nm in size. These nanoparticles enhance the weld joint's efficiency and wear resistance by acting as reinforcement additives. They reduce defects and porosity, leading to more reliable and higher welds. The inclusion of SiC and TiO2 also improves thermal stability during welding, minimizing softening and enhancing joint strength. The chemical compositions of AA2024 and AA7075 were revealed in Table 5.5.

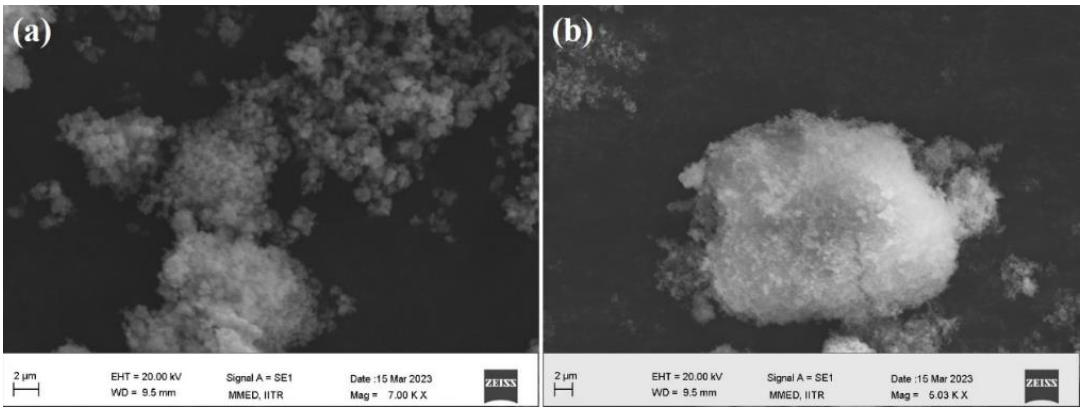

Figure 5.168: SiC and TiO2 Nanoparticles

Table 5.5. Chemical composition of AA2024 and AA7075

Metal	Mg	Si	Fe	Cu	Mn	Cr	Zn	Ti
AA2024	1.45	0.12	0.16	4.35	0.45	0.02	0.025	0.022
AA7075	2.35	0..29	0.319	1.315	0.02	0.17	5.32	0.129

TiO2 and SiC nanoparticles were chosen to enhance the metallurgical properties of the welded joints of AA2024 and AA7075. TiO2 nanoparticles enhance creep resistance, and high-temperature strength stability TiO2 nanoparticles, with their high melting point and exceptional thermal stability, offer remarkable reinforcement, and SiC particles provide excellent strengthening due to their dispersion and high hardness within the aluminum matrix, significantly improving hardness value, tensile properties and wear resistance. Fig. 5.18 reveals SEM images of TiO_2 and SiC nanoparticles, illustrating their morphology and distribution. The tool's traverse rate in FSW is governed by its shape, which is crucial for material flow. Fig. 5.19 depicts the

systematic geometry of the FSW tool, consisting of two parts: the pin and the shoulder. The tool design is tailored to the materials being welded and the desired joint configuration. The shoulder of the tool provides backing and support for the rotating pin, which should have a threaded shank to facilitate easy replacement. The tool's primary function is to localize heat and control material flow in the heating zone. Effective tool design ensures optimal heat generation and material mixing, leading to defect-free welds with enhanced mechanical properties.

Incorporating nanoparticles like TiO_2 and SiC into the FSW process not only improves the joint efficiency but also reduces defects such as porosity. These nanoparticles enhance the overall joint efficiency of the welded joints by promoting thermal stability and uniform dispersion, reducing the risk of softening, and enhancing weld integrity.

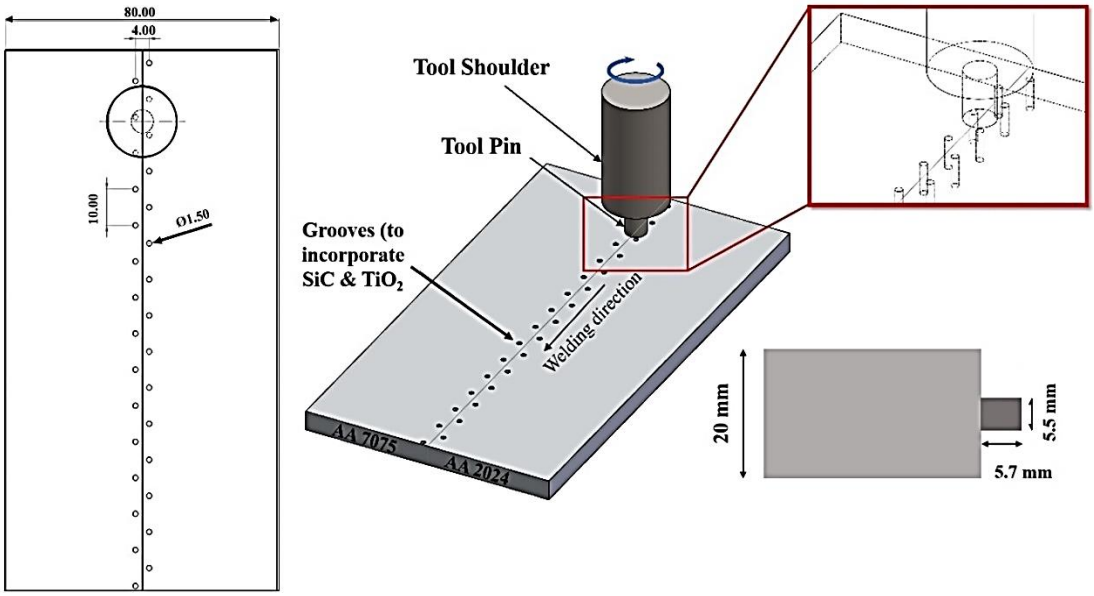

Figure 5.179: Schematic diagram of zig-zag pattern of holes

The tool material for this study was selected based on previous research and maintained consistent across all experiments [279-282]. The tool pin's geometry was cylindrical, with a shoulder diameter of 20 mm, a pin height of 5.7 mm, and a pin diameter of 5.5 mm of H13 steel with a hardness of 56 HRC, the circular shape of the tool pin significantly enhanced material mixing. This circular design minimized the risk of material expulsion, resulting in cleaner and defect-free welds, and it promoted more uniform heat distribution, thereby reducing the potential for distortion and

thermal damage in the workpieces. The versatility of the circular tool pin allowed for a broader range of joint designs, accommodating various material thicknesses and configurations.

For the incorporation of reinforcement materials into the AA2024 and AA7075 plates, grooves (depth of 4.5 mm, diameter of 1.5 mm) were drilled. These grooves were arranged in a zigzag pattern to ensure even distribution and optimal integration of the reinforcement particles during the welding process shown in Fig. 5.19.

This methodology ensured that the nanoparticles were effectively embedded within the aluminum matrix, enhancing the joint strength. The TiO_2 and SiC nanoparticles also contributed to reducing defects and porosity in the weldment, leading to higher quality and joint efficiency. A fixture was used to securely hold the base plate, ensuring stability and precision during the Multi-Pass Friction Stir Processing (MPFSP). This fixture prevented unintended misalignment or movement, which could compromise the joint's quality and structural integrity. Misalignment can lead to structural defects and poor joint quality. A zigzag pattern was used to uniformly distribute the reinforced material in the stir zone. Grooves were machined along the plate's length, 2 mm from the joining line, and filled with the reinforced material. After filling, a pinless tool compressed the material to prevent outpouring during welding [283]. Three experiments were conducted: two with reinforced materials and one without. The process parameters were identical for all three: TRS of 1000 rpm and TS of 30 mm/min. The study investigated the reinforced materials' effects on the weld joint's hardness, UTS, and microstructure. A double-pass welding technique ensured proper stirring of the material in the welded zone, with the second pass reversing the tool's rotation to optimize the welding process [284-287]. Comparing the weld nugget without reinforcement to the mixed alloys highlighted the grain refinement's benefits for optimal welding.

5.3.1 Characterization and Microstructural Analysis

SEM images in Fig. 5.20 (a-c) show the cross-section of FSW joints fabricated with TiO2, without reinforcement, and with SiC-reinforced material. In Fig. 5.20 (a), the joint between AA2024 and AA7075 with TiO_2 reinforcement appears sound, with no significant particle agglomeration. Literature indicates that a minimum of two passes are necessary for creating sound, defect-free joints [288, 289].

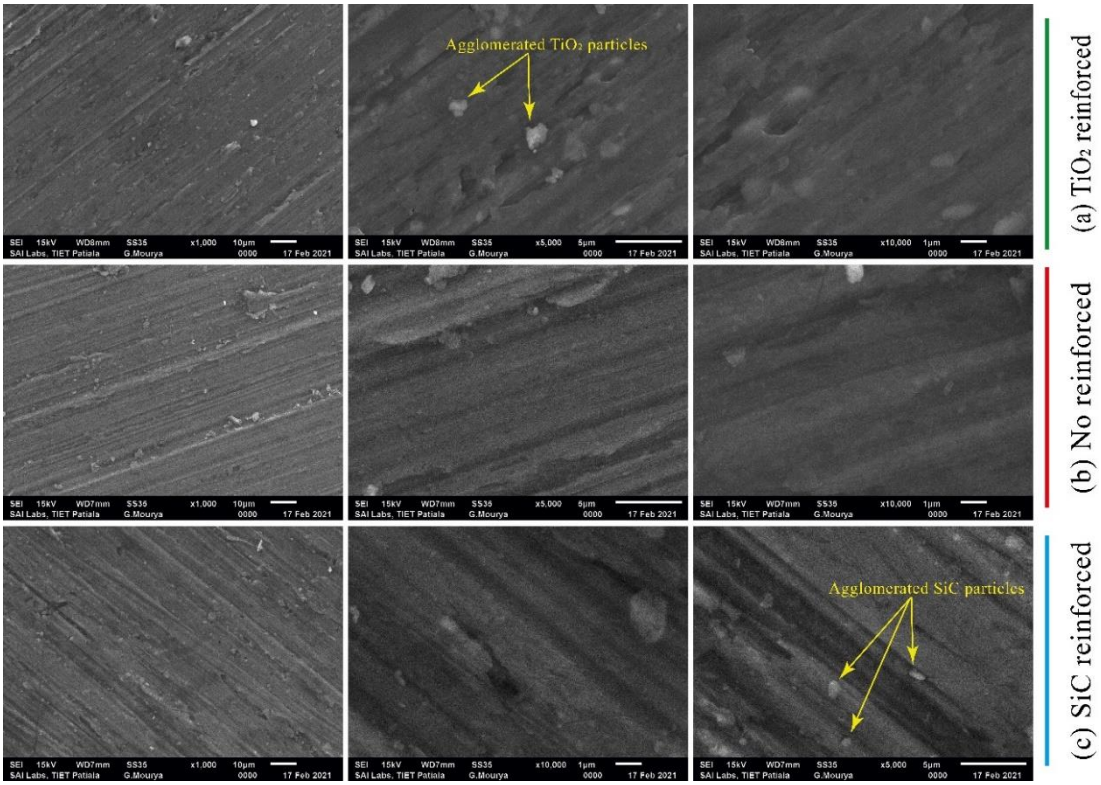

Figure 5.20: SEM images of welded joints of AA2024 and AA7075 with and without nanoparticles.

A double pass means the starting point of the 1st pass becomes the finishing point of the second pass, switching the RS of the first pass to the AS of the 2nd pass. This technique prevents the accumulation of reinforcement particles in a single pass [290]. Fig. 5.20 (b) and (c) show SEM images of FSW joints without reinforced material and with SiC material, respectively. The double-pass technique enhances the dispersion of reinforcement particles, resulting in a more uniform distribution. This is crucial for achieving the desired mechanical properties and microstructural integrity in the welded joints. Using a double-pass process mitigates the issues associated with single-pass welding, such as particle agglomeration and uneven distribution. The second pass helps redistribute the particles, promoting a more homogeneous mixture and improving the joint's overall quality. The incorporation of TiO_2 and SiC nanoparticles as reinforcement additives has been shown to enhance the weld joint's tensile strength, hardness, and wear resistance. These nanoparticles help reduce porosity and defects, leading to higher quality and more reliable joints. Their inclusion also contributes to improved thermal stability during the welding process, minimizing the risk of softening and enhancing weld stability [288]. EDX analysis was accomplished to

identify the elemental composition of the materials. Three spectrums were taken for each sample. The analysis revealed the presence of alloying elements from AA7075 and AA2024, which were adequately intermixed in the nugget area of the weld. Fig. 5.21 (a-c) presents the EDX analysis of the FSW joint with SiC-reinforced material, TiO2-reinforced material, and without reinforced material. This analysis confirms the effective integration of the alloying elements, indicating a well-mixed joint and the successful incorporation of reinforcement materials, enhancing the overall quality and properties of the welds.

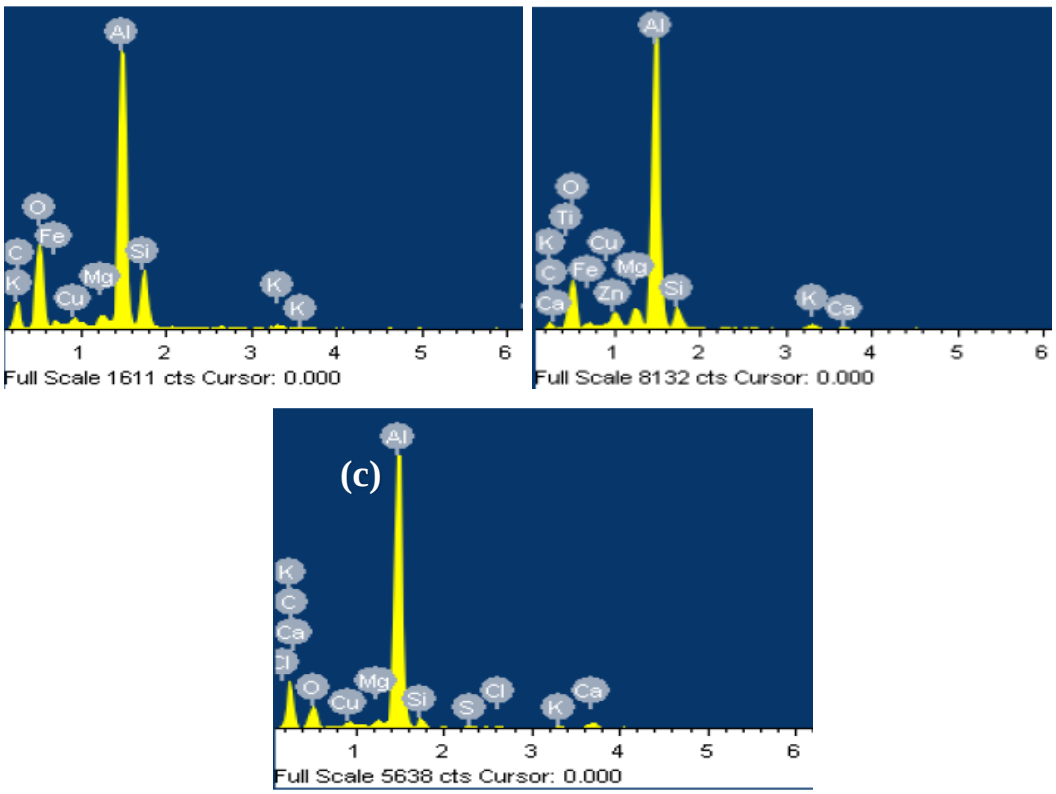

Figure 5.181: EDX images of the welded joints (a) using SiC, (b) using TiO2, (c) without nanoparticles

5.3.2 Microstructural Observation

The occurrence of SiC and TiO_2 nanoparticles significantly influences the recrystallization and grain growth processes during FSW. These nanoparticles act as nucleation sites for new grain formation or hinder grain growth, resulting in finer and more uniform grain structures in the weld zone. Understanding the distribution of SiC and TiO_2 nanoparticles within the weld microstructure is crucial. This meticulous

exploration involves a multifaceted analysis of structural, compositional, and mechanical aspects of an FSWed joint of AA7075 and AA2024, integrating these nanoparticles in the welding process. The grain size and structure dynamics are scrutinized to determine if nanoparticles function as nucleation catalysts, potentially leading to finer and more homogeneously distributed grains within the weld zone. Further investigations examine the dispersion pattern of nanoparticles, discerning whether their distribution is even across the weld matrix or if localized clusters emerge. An in-depth analysis of intermetallic compound formation is undertaken to ascertain the emergence of new compounds resulting from nanoparticle interactions with base metals, subsequently influencing mechanical and thermal properties.

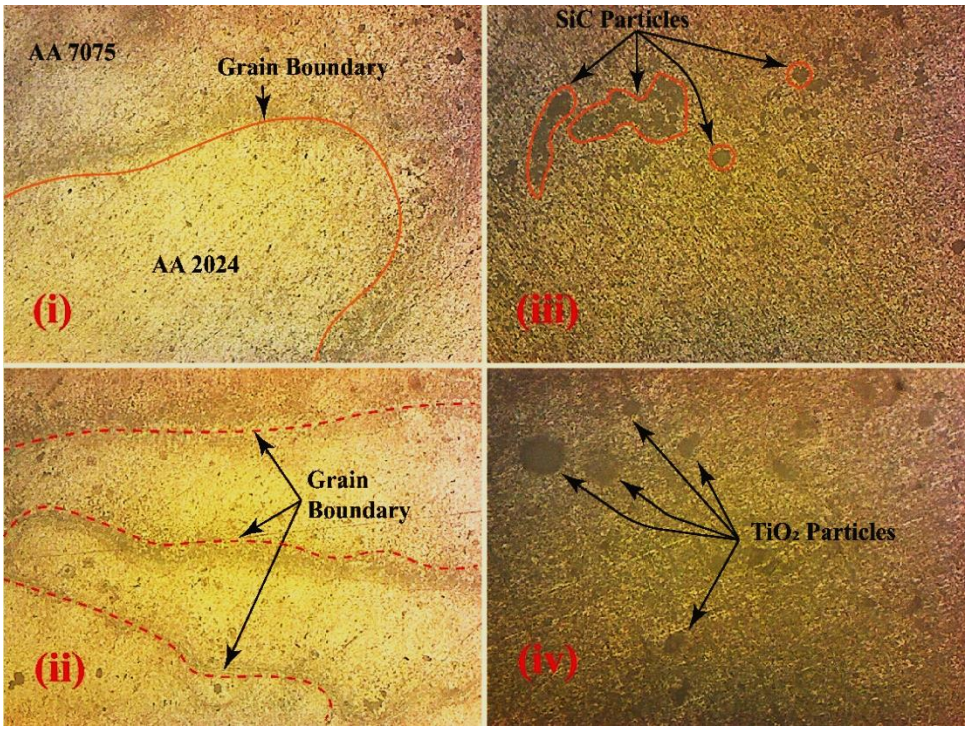

Figure 5.192: (a) FSW without reinforced, (b) grain boundary (c) FSW with SiC, (d) FSW with TiO_2

Additionally, alterations in dislocation density and defect mitigation are examined to understand whether nanoparticles impede or expedite dislocation movement and if they alleviate the formation of porosities, voids, or cracks within the microstructure. This comprehensive approach ensures a thorough understanding of how SiC and TiO_2 nanoparticles, providing insights that can lead to the optimization of welding processes and the enhancement of joint performance An assessment of hardness and

mechanical properties, focusing on how nanoparticles influence the joint efficiency of the welded joint. Heat distribution and Temperature gradients during welding are critically examined to understand how nanoparticles might alter the HAZ and the weld nugget. These analyses culminate in a comprehensive understanding of how SiC and TiO_2 nanoparticles intricately modulate the microstructure of the welded joints. Such insights have profound implications for optimizing welding parameters, enhancing joint performance in advanced materials joining. The microstructure evaluation of the weld was conducted after the specimens were polished and etched with a solution containing 80 ml H_2O, 10 ml HF, and 5 ml HNO_3, and etched for 15 seconds were used for microstructure tests. Microscopic studies revealed well-defined grain boundaries in Fig. 5.22a and b, showing proper material mixing near the boundaries, leading to grain refinement. No cracks or defects were observed in the SZ, and the reinforced particles were evenly distributed in the SZ. A high strain zone near the weld tool results in extreme frictional heating and plastic deformation, leading to a fine-grain microstructure in the SZ. The reduction in grain size, known as DRX, is depicted in Fig. 5.22(c). It was found that SiC and TiO2-reinforced materials were uniformly distributed in the SZ, with double passes ensuring superior distribution. Many researchers have observed defects like pinholes, cracks, and tunnel defects due to improper material flow. The tool generated significant heat at low traverse speeds, softening the material in the SZ. The optical microstructures of AA7075 and AA2024 friction stir welding with and without reinforced materials are shown in Fig. 5.22. Fig. 5.22(a) represents the grain boundary between the two materials, showing proper intermixing of SiC and TiO_2-reinforced materials in the welded zone [291].

5.3.3 XRD analysis

Fig. 5.23 depicts the XRD analysis conducted on the SZ of the cross-sectional view of the welded joints with TiO_2 and SiC particles. The identified peaks correspond to Al, TiO_2, SiC, $MgZn_2$, and Al_2Cu in all the joints, consistent with their composition in AA7075 and AA2024. The XRD analysis reveals the occurrence of two distinct intermetallic phases, namely $MgZn_2$ and Al_2Cu. The Al_2Cu intermetallic peaks are evident at $2\theta = 65.16°$ in samples lacking a compensation layer and those with a 1 mm compensation layer. The formation of MgZn2 intermetallic phases in samples

with a 1 mm compensation layer is indicated by Zn peaks at 2θ = 78.31°, owing to the higher Zn concentration in the AA7075 alloy than in Mg. Notably, an increase in the compensation interlayer width results in reduced peak height and increased peak width, reflecting a reduction in crystallite size. This reduction can be attributed to the extensive plastic deformation of metals during the FSW process, leading to grain size reduction. The occurrence of $MgZn_2$ and Al_2Cu IMCs significantly impacts the FSWed joint between AA2024 and AA7075. These compounds form during the welding process due to the intricate alloy compositions. Al_2Cu contributes to joint strength, varying based on alloy composition, particularly the copper content. $MgZn_2$, on the other hand, appears due to differing magnesium and zinc concentrations in the alloys. Their existence affects the joint's efficiency, potentially leading to variations in strength, hardness, and overall performance. Understanding their influence is crucial for optimizing the welding process and ensuring the desired joint quality in these aluminum alloy combinations.

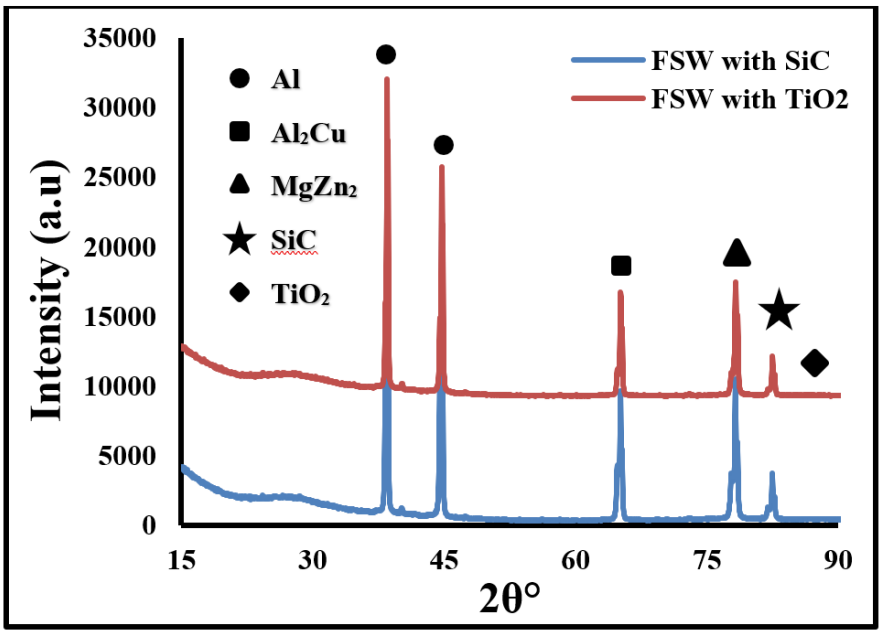

Figure 5.203: XRD diagram of welded joints in presence of TiO2 and SiC nanoparticles

5.3.4 Effect of TiO2 and SiC on UTS

The investigation into the effects of SiC and TiO_2 particles on the UTS of FSWed joints of AA7075 and AA2024 reveals significant improvements in mechanical

performance. The addition of these nanoparticles introduces complex interactions within the weld microstructure, enhancing tensile strength by promoting grain refinement and increasing dislocation density. These nanoparticles act as nucleation sites, which can impede or facilitate dislocation movement under applied stress, thereby influencing the joint's plastic deformation behaviour.

The tensile properties of the welded joints were evaluated with samples cut to a gauge length of 80 mm, width of 39.95 mm, and thickness of 6 mm. As shown in Table 5.6, the tensile strength of joints without reinforcement is 177 MPa, while those with TiO_2 and SiC reinforcement exhibit strengths of 199 MPa and 206 MPa, respectively. The incorporation of TiO_2 and SiC nanoparticles effectively refines the microstructure and prevents defect formation, leading to enhanced load-bearing capacity and overall joint strength. Fig. 5.24 illustrates the improved tensile strength due to nanoparticle reinforcement. The joint efficiency with SiC and TiO_2 nanoparticles was measured at 40.66% and 42.09% relative to AA7075 and 49.39% and 51.14% relative to AA2024. These results confirm that SiC and TiO_2 nanoparticles significantly enhance the mechanical performance and structural integrity of friction stir-welded joints, offering a promising approach for optimizing welding outcomes in Al alloy combinations.

Table 5.6: Mechanical properties of the FSWed joints of AA2024 and AA7075 with and without Nanoparticles

Materials	UTS (MPa)	Strain (%)	Hardness (HV)	Joint efficiency (%) compared to AA7075	Joint efficiency (%) compared to AA2024
AA7075	489.36	11.85	179	-	-
AA2024	402.85	20.27	142	-	-
FSW without Nanoparticles	177	14.69	155	36.17	43.94
FSW_SiC	199	8.36	165	40.66	49.39
FSW_TiO_2	206	14.67	180	42.09	51.14

The influence of both nanoparticles on the tensile strength of friction stir welded joints between dissimilar materials involves several complex interactions. These nanoparticles can modify stress and strain distribution during tensile loading, potentially creating stress concentration zones or redistributing stresses, which affects

fracture initiation and propagation. Additionally, they impact the precipitation kinetics of intermetallic phases during solidification and cooling, altering the distribution of strengthening phases such as θ' and θ".

Chemical interactions between nanoparticles and alloying elements may lead to the formation of new strengthening precipitates or modify the behavior of existing phases. This can directly affect the tensile strength of the joint. Nanoparticles also contribute to grain boundary pinning, which hinders grain boundary sliding and enhances cohesion, thus improving both ductility and strength.

The distribution of nanoparticles within the weld, particularly in the SZ and HAZ, can lead to localized variations in microstructure and mechanical properties. Understanding these distributions and any potential clustering effects is critical. Experimental validation through tensile testing is essential to confirm theoretical predictions and determine the net effect of nanoparticle integration on tensile strength. Overall, this research highlights how nanoparticles influence mechanical properties, providing valuable insights for optimizing friction stir welded joints for enhanced performance and reliability in engineering applications [291].

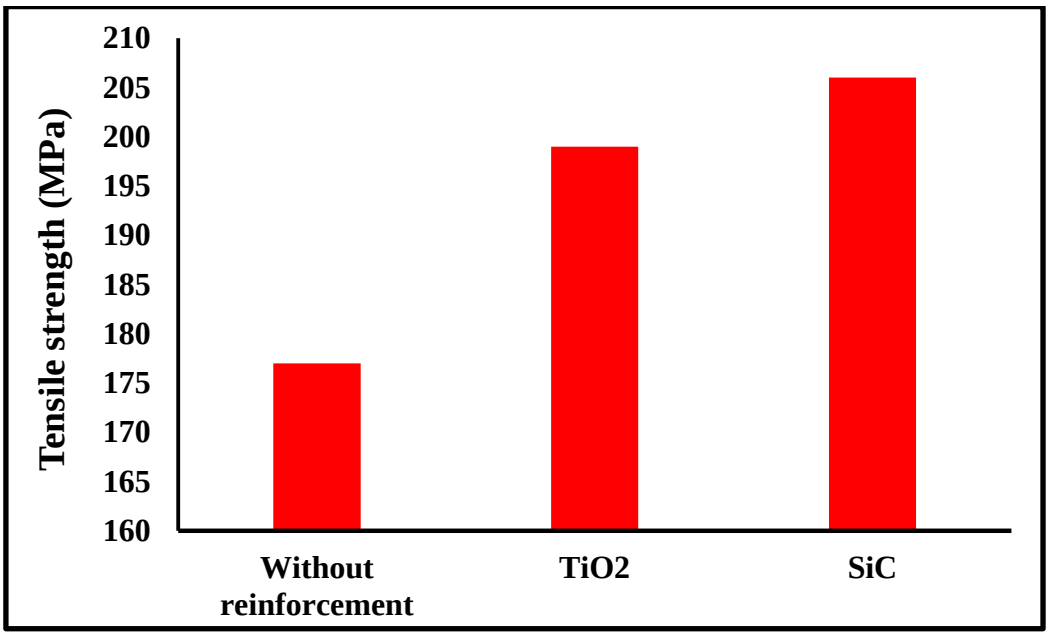

Figure 5.24: Comparison of the UTS of welded joints with and without nanoparticles

5.3.5 Influence of SiC and TiO_2 particles on microhardness

Fig. 5.25 shows the micro-hardness of the welded joints with TiO_2, SiC, and no

reinforcement. The introduction of TiO_2 significantly improves the microhardness of the weld SZ compared to SiC and unreinforced joints. Specifically, the hardness values are 180 HV for TiO_2, 165 HV for SiC, and 155 HV without reinforcement. This increase is attributed to the enhanced reinforcement provided by TiO_2, which leads to a finer microstructure and maximum microhardness in the SZ compared to using only AA7075. In the HAZ, hardness variations are observed due to the coarsening of reinforced materials through precipitation. The dispersion of these materials in the SZ contributes to the formation of hardness patterns, which can vary from higher to lower hardness values. The interaction of nanoparticles with the metal matrix creates nucleation sites for dislocations and modifies grain boundaries and phase interfaces. This can either hinder or facilitate dislocation movement under load, influencing plastic deformation and hardness distribution. A thorough examination of how TiO_2 and SiC nanoparticles impact the hardness distribution involves understanding their role in grain refinement and dislocation density variations. This comprehensive analysis highlights the complex interplay of microstructural changes and mechanical properties resulting from the inclusion of these nanoparticles [292].

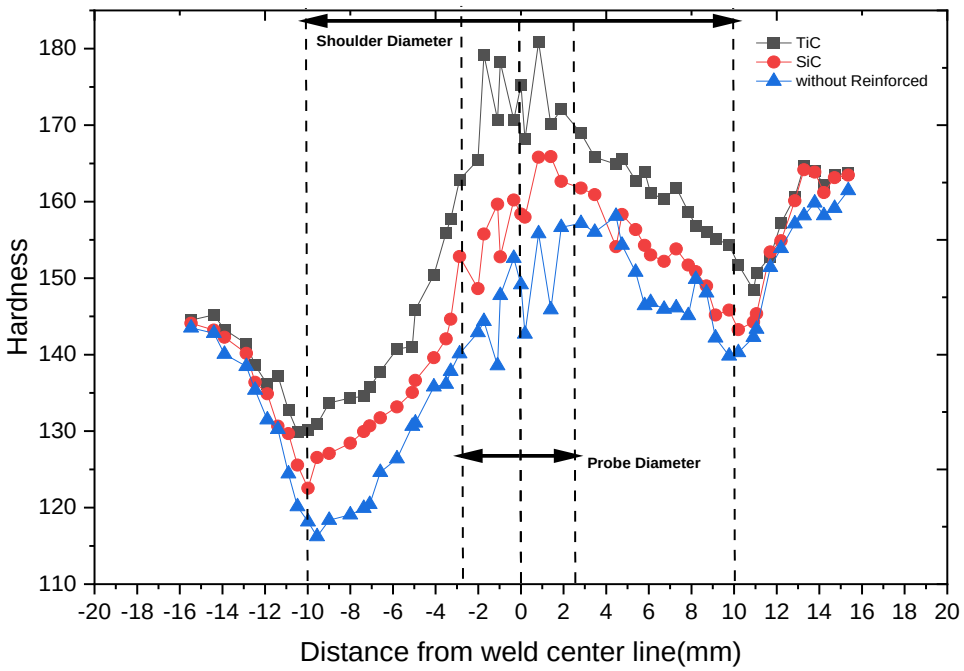

Figure 5.25: Hardness dissemination from the weld center of the welded joints with different reinforcement particles

The impact of both nanoparticles on hardness distribution in FSWed joints between

AA7075 and AA2024 is substantial. The nanoparticles interact with alloying elements to form new precipitates or modify existing phases, resulting in variations in hardness across different weld zones. Their spatial distribution, whether clustered or uniformly dispersed, influences the microhardness profile of the different region. Heat treatments further affect nanoparticle behavior and hardness distribution, making it essential to evaluate these effects through detailed microhardness testing. Advanced methods like micro indentation mapping can capture localized hardness variations induced by nanoparticles, offering insights into their influence on material properties. This comprehensive analysis highlights the complex interplay of microstructural, mechanical, and chemical factors, enhancing our understanding of how nanoparticles shape hardness profiles. Such knowledge is vital for optimizing friction stir welded joints to achieve precise hardness distributions

5.3.6 Fracture analysis

Fracture analysis of FSWed joints made from dissimilar aluminum alloys AA7075 and AA2024, both with and without TiO_2 and SiC nanoparticles, reveals significant insights into their mechanical behavior as illustrated in Fig. 5.26. Joints without nanoparticles predominantly display large, unevenly distributed dimples, indicating ductile fracture. This suggests that the FSW process itself enhances ductility, allowing for greater energy absorption and resistance to crack propagation, and the absence of cleavage facets confirms a lack of brittle fracture regions. In contrast, joints reinforced with TiO_2 and SiC nanoparticles exhibit smaller, more uniformly distributed dimples, reflecting improved ductility due to the nanoparticles' strengthening effects on the alloy matrix. However, these joints also show the presence of cleavage facets around the nanoparticles and their interfaces. This indicates that while the nanoparticles enhance strength and hardness, they can also induce localized brittle failure.

The key takeaway is that the incorporation of TiO_2 and SiC nanoparticles introduces a trade-off between increased strength and potential brittleness. Therefore, optimizing the dispersion of these nanoparticles and adjusting FSW parameters is critical to achieving an optimal balance between strength and ductility. This balance is particularly important in applications where both mechanical properties must be carefully managed to ensure the joint’s reliability and performance.

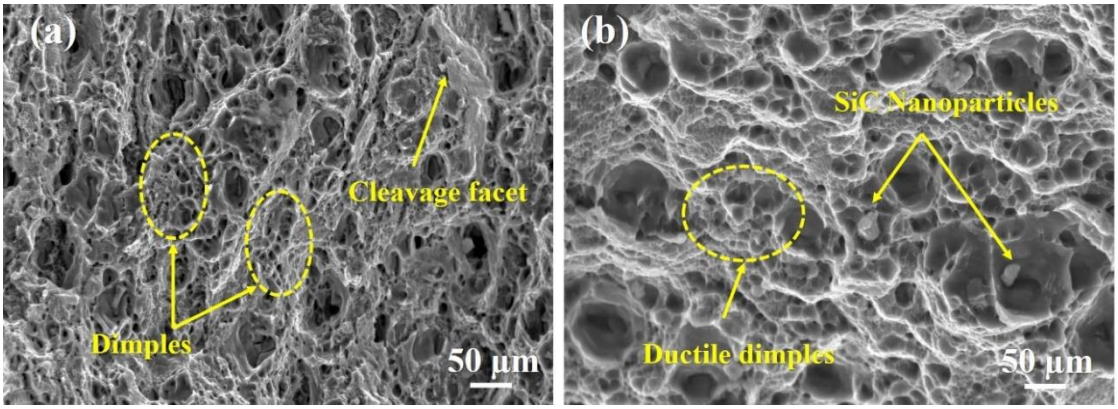

Figure 5.26: Fractured micro images of the specimens with and without Nanoparticles

5.4 Thermal Analysis of Dissimilar joints by Hyper Weld

In this work, AA2024, AA7075, and copper were selected for FSW to identify optimized process parameters for achieving high-quality welded joints. The study employed Altair's HyperWeld 2019 CAE software to simulate the FSW for these materials. The significance of this research lies in the extensive use of these aluminum alloys and pure copper in the automobile and aircraft industries due to their favorable properties. From the literature review, it is apparent that there have been limited investigations into the effects of process parameters and geometric parameters on peak temperatures during welding. This study aims to bridge that gap by exploring how these parameters influence the welding process and the resulting joint quality. The HyperWeld module was utilized to simulate and analyze these effects, providing valuable insights into optimizing welding conditions.

For the experiments, specimens were prepared with plate dimensions of 300mm× 100mm × 6mm. The mechanical properties of the selected materials and the welding tool were documented in Tables 5.7. These properties are critical for understanding the behavior of the materials during the welding process and for setting up accurate simulations in the HyperWeld software. The simulation results from HyperWeld highlighted the impact of various process parameters, such as TRS and TS and tool geometry, on the peak temperature and overall thermal distribution during the welding process. Understanding these effects is crucial for optimizing the welding parameters to achieve defect-free and high-strength joints.

Experimental validation was carried out to confirm the simulation results. The welded specimens were subjected to various tests to evaluate their mechanical properties, such as tensile strength, hardness, and microstructural analysis. These tests provided empirical data to support the simulation findings and helped in refining the process parameters for optimal welding conditions. The research found that the choice of process parameters significantly affects the peak temperature and thermal distribution, which in turn influences the metallurgical properties of the FSWed joints. For instance, an optimal combination of TRS, TS was identified to achieve a balanced heat input, resulting in a fine-grained microstructure and improved joint strength.

Additionally, the study emphasized the importance of tool geometry in the FSW process. The tool's shoulder diameter, pin profile, and pin length were found to play critical roles in material flow and heat generation during welding. Optimizing these geometric parameters helped in achieving uniform material mixing and reducing defects such as voids and cracks in the welded joint. The insights gained from this research are expected to benefit industries that rely heavily on aluminum alloys and copper by providing guidelines for selecting appropriate welding parameters and tool designs. This can lead to improved joint quality, enhanced mechanical properties, and increased reliability of welded structures in critical applications.

Table 5.7: Physical and mechanical properties of AA2024, AA7075, and Copper

Material	Copper	AA 7075	AA 2024
Conductivity ('K' in W/m-K)	198	173	193
Liquidus Temp (˚K)	927	908	911
Solidus Temp (˚K)	889	750	775
Young Modulus ('E' in N/m^2)	4×10^{10}	4×10^{10}	$4.\times10^{10}$
Co-efficient of Thermal Expansion (1/K)	1×10^{-5}	1×10^{-5}	1×10^{-5}
Poisson Ratio(μ)	0.35	0.35	0.35
Specific Heat ('Cp' in J/Kg-K)	900	960	827
Density ('ρ' in Kg/m^3)	2700	2810	2780

5.4.1 Selection of tool

In this study, an H-13 steel tool pin was utilized for welding the plates. The tool features a cylindrical geometry with a pin diameter of 5.5mm, pin height of 5.4mm, shoulder diameter of 18mm, and shoulder length of 70mm, as illustrated in Fig. 5.27 depicts the process of inputting the plate dimensions and tool specifications into the software. Numerous researchers have employed H-13 steel as a tool material in their investigations [293].

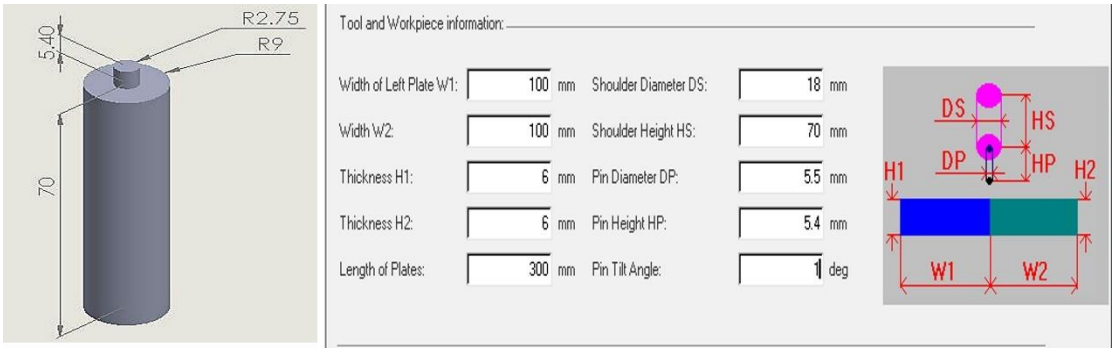

Figure 5.27: Tool geometry and workpiece data

Table 5.8: Physical and mechanical properties of H13 tool material

Tool Material	Density Kg/m^3)	Specific Heat J/Kg-K	Conductivity W/m-K	Young Modulus N/m^2	Poisson Ratio
H-13	7870	460	24.3	2.1×10^{11}	0.35

5.4.2 Design of experiments by Taguchi

In this work, a 6 mm thick plates of AA7075 and AA2024 were FSWed with pure copper using Altair's Hyper-Weld software. The investigation focused on three process parameters i.e. TRS, TS, and TTA, each with three levels. The specific values and symbols for these parameters are detailed in Table 5.9. This setup aimed to optimize the welding conditions and understand their effects on the properties of the weldments.

Table 5.9: Process parameters and levels of FSWed joints

Level	A	B	C
	TTA (°)	TS (mm/s)	TRS (r.p.m)
Level 1	1	0.1	500
Level 2	2	0.2	1000
Level 3	3	0.3	1500

In this study, TRS, TS, and TTA were selected at three levels each, forming an L9 orthogonal array for the design of experiments. The primary objective was to comprehend the effects of these parameters on maximum temperature and residual stresses during FSW, without considering the interactions between them.

Initially, Cu and AA2024 were welded with Cu positioned on the AS and AA2024 on RS. Nine virtual experiments were conducted to observe the variations in maximum temperature and residual stresses under different process parameter combinations. Subsequently, Cu and AA2024 were welded with AA2024 on the left side and copper on the right side. A similar approach was followed for welding AA7075 with copper. The virtual experiments utilized Altair's Hyper-Weld software, setting the initial plate temperature at 30˚C. The convection coefficients for the handle, top surface, and bench were set at , 15, 210 W/m²-C, respectively, as depicted in Fig. 5.28. These parameters were crucial in simulating the thermal and mechanical behavior of the materials during the FSW process [294].

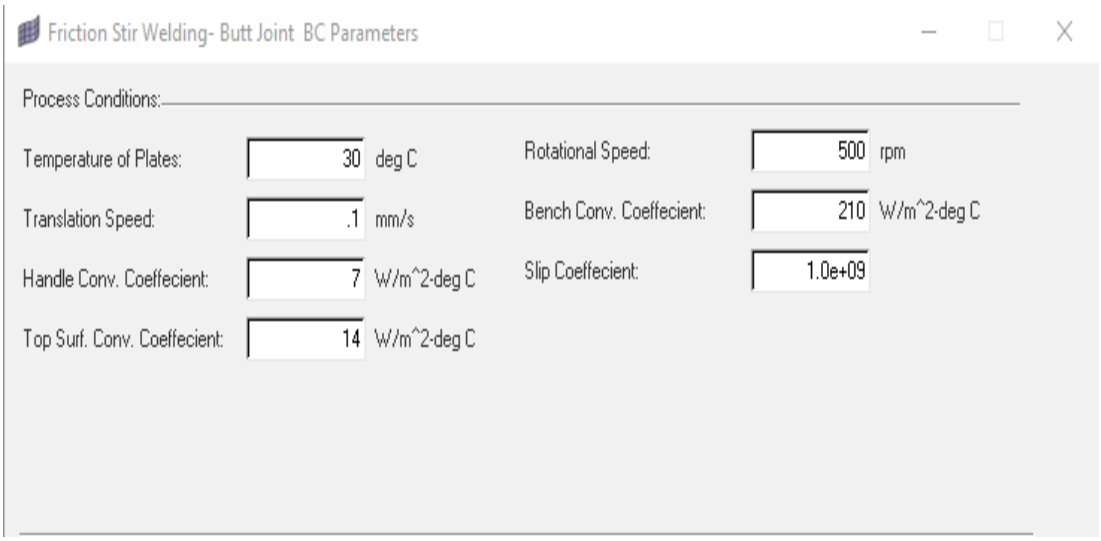

Figure 5.28: Process Parameter Information

The study's comprehensive approach allowed for a detailed analysis of how different welding parameters affect the joint's properties. The findings provide valuable insights for optimizing FSW conditions to achieve desired mechanical properties and minimal residual stresses in welded joints of dissimilar aluminum alloys and copper. This research contributes to advancing welding techniques in automotive and aerospace, where these materials are extensively used.

In the current study, simulations were conducted to weld AA2024 and AA7075 with copper using three different levels of input parameters. The objective was to estimate the effects of these parameters on maximum temperature and residual stresses during the welding process. The results of these simulations provide critical insights into optimizing the welding process for these dissimilar materials. Table 5.10 presents the simulated maximum temperatures and residual stresses observed during the welding of AA2024 and copper, with AA2024 positioned on the left side and the copper plate on the right side. These simulations were crucial in understanding the thermal and mechanical behavior of the welded joints.

Table 5.10: L9 orthogonal array with S/N ratio at Cu on the right side and AA2024 on the left side

S.N	TTA (°)	TS (mm/s)	TRS (rpm)	Stress (MPa)	Temperature ($°C$)	S/N ratio (w.r.t stress)	S/N ration (w.r.t temp.)
1	1	0.1	500	29.8	533.7	-29.4872	54.5459
2	2	0.2	500	29.71	535.9	-29.4581	54.5817
3	3	0.3	500	21.69	537.5	-29.9827	54.6076
4	2	0.1	1000	17.45	722.8	-24.8359	57.1816
5	3	0.2	1000	18.54	722.9	-25.3622	57.1828
6	1	0.3	1000	19.11	696.6	-25.6252	56.8597
7	3	0.1	1500	14.22	852.7	-23.0580	58.6169
8	1	0.2	1500	14.48	824.8	-23.2094	58.3291
9	2	0.3	1500	14.27	826.8	-23.0885	58.3480

Furthermore, the signal-to-noise ratio (SNR) was designed concerning both stress and temperature for all parameter sets. The SNR analysis helps identify the robustness of the welding process under varying conditions and is instrumental in optimizing the

welding parameters for better joint performance and reliability [295]. The simulations revealed that the selected parameters significantly influence the thermal profile and residual stress distribution within the welded joints. By analyzing these results, it becomes possible to fine-tune the welding process to achieve the desired balance between mechanical strength and thermal stability. This approach ensures that the welded joints exhibit minimal residual stresses and optimal mechanical properties, which are critical for applications in industries such as aerospace and automotive [296, 297].

Table 5.11: Signal to Noise Ratios for Larger is better

Level	TRS (rpm)	Traverse speed (mm/min)	Tilt angle (°)
1	54.58	56.78	56.58
2	57.07	56.70	56.70
3	58.43	56.61	56.80
Delta	3.85	0.18	0.22
Rank	1	3	2

Table 5.12: Signal to Noise Ratios for Smaller is better

Level	TRS (rpm)	Traverse speed (mm/min)	Tilt angle (°)
1	-29.64	-25.79	-26.11
2	-25.27	-26.01	-25.79
3	-23.12	-26.23	-26.13
Delta	6.52	0.44	0.34
Rank	1	2	3

Table 5.10 shows that the highest temperature of 852.7°C and the minimum residual stress of 14.22 MPa were achieved in Experiment 7, where the TRS rpm was set at 1500, the TS at 0.1 mm/s, and the TTA at 3°. Conversely, the minimum temperature of 533.7°C and the maximum residual stress of 29.8 MPa were recorded in Experiment 1, which had a TRS of 500 rpm, a TS of 0.1 mm/s, and a TTA of 1°. These findings underscore the significant impact of the selected process parameters on the thermal and mechanical outcomes of the friction stir welding process. The higher TRS in Experiment 7 leads to increased frictional heating, resulting in a higher maximum temperature. This elevated temperature likely facilitates better plastic

deformation and material flow [298], which in turn reduces residual stress. The optimal TTA of 3° further enhances the stirring action, promoting a more homogeneous weld and contributing to the reduction in residual stress. On the other hand, the lower TRS in Experiment 1 results in less frictional heating, yielding a lower maximum temperature. The insufficient heat generation at this setting is likely insufficient to fully soften the material, leading to increased residual stress. Additionally, the minimal TTA of 1° may not provide adequate stirring, resulting in a less uniform weld and higher residual stresses.

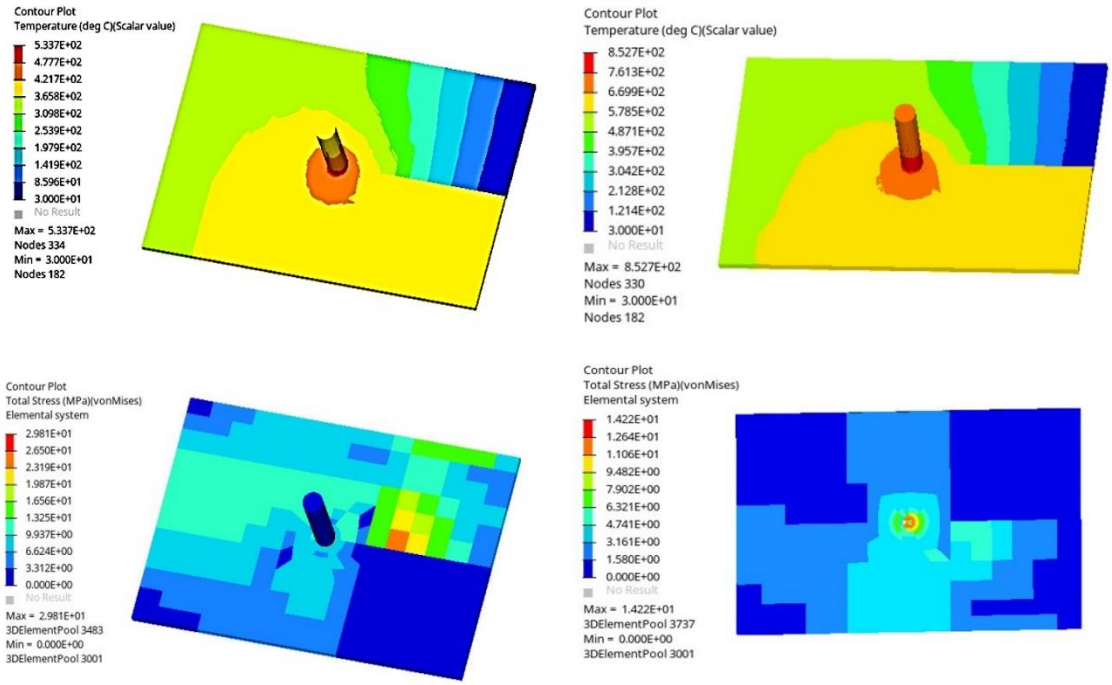

Figure 5.29: Temperature and stress distribution of FSW joints of AA2024 and Copper

Table 5.11 and 5.12 demonstrate that the TRS significantly influences the maximum temperature during the FSW. The delta value, which measures the change in response between the highest and lowest levels of each parameter, is considerably larger for rpm compared to TS and TTA. This indicates that changes in TRS have a more pronounced effect on the temperature than the other parameters. The high delta value for rpm suggests that increasing the TRS substantially raises the temperature generated during welding. This is because higher TRS enhance the friction between the workpiece and the rotating tool, leading to greater heat generation. The elevated temperature facilitates the flow and the plastic deformation of the materials being

welded, promoting better mixing and bonding at the weld interface. Consequently, the quality and strength of the welded joint improve with optimal temperature control [299]. The delta values for TS and TTA are comparatively smaller, indicating a lesser impact on temperature. While these parameters do influence the welding process, their effects are more subtle. TS affects the input heat/ unit length of the weld, with slower speeds allowing more time for heat to accumulate and higher temperatures to be reached. However, its impact is not as substantial as that of rotational speed. The TTA primarily affects the stirring action and material flow but does not significantly alter the overall heat generation. These findings underscore the importance of carefully selecting the TRS to control the temperature during FSW. By optimizing this parameter, it is possible to achieve the desired thermal conditions that facilitate effective welding and minimize defects. However, it is also essential to consider the interplay between all process parameters to ensure a balanced approach that yields high-quality welds with minimal residual stresses and enhanced mechanical properties.

Fig. 5.29 depicts the simulated maximum residual stress and maximum temperature during the FSW of AA2024 and copper, with AA2024 positioned on the left side and the copper plate on the right side. The analysis focuses on understanding the thermal and mechanical behavior of the welded joint under varying process parameters.

The simulation results highlight significant differences in temperature dissemination and residual stress levels across the joint. The maximum temperature reached during the welding process in determining the quality of the weld. Higher temperatures facilitate better plastic deformation and material flow, which are essential for achieving a sound weld with good mechanical properties. The temperature distribution also affects the formation of IMCs, which can influence the joint's strength and durability. Residual stresses, on the other hand, are critical indicators of the internal stresses remaining in the material after welding. These stresses can affect the structural integrity and performance of the welded joint. High residual stresses may lead to issues such as warping, cracking, or reduced fatigue life. Therefore, understanding the residual stress distribution is vital for optimizing the welding process and ensuring the long-term reliability of the joint.

The simulations reveal that TRS significantly impacts both the maximum temperature and residual stresses. As observed, higher TRS lead to increased temperatures, which can enhance the weld quality by promoting better material mixing and reducing

defects. However, excessive temperatures can also increase the risk of undesirable microstructural changes or excessive residual stresses. Thus, finding the optimal TRS is essential for balancing these effects.

Additionally, the TS and TTA also influence the temperature and residual stress distribution, albeit to a lesser extent compared to rotational speed. Lower TS allow more time for heat generation and accumulation, resulting in higher temperatures and potentially higher residual stresses. The TTA affects the material flow and stirring action, impacting the heat input and stress distribution.

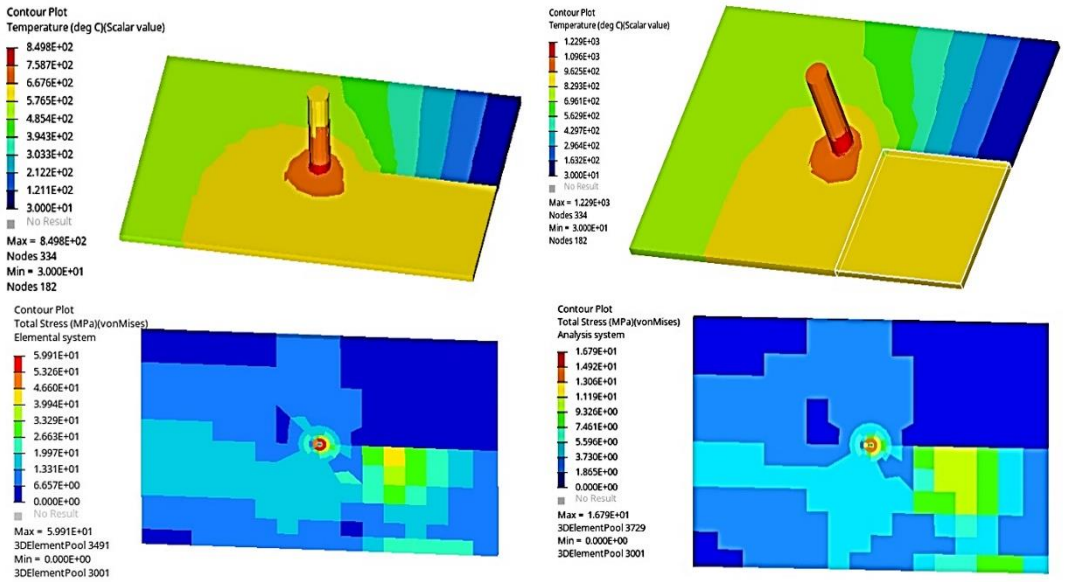

Figure 5.30: Stress and temperature distribution of FSWed joints of Cu and AA7075

Table 5.13: L9 orthogonal array with S/N ratio when Cu on the left side and AA2024 on the right side.

S.N	TTA (°)	TS (mm/s)	TRS (rpm)	Stress (MPa)	Temperature (°C)	S/N ratio (w.r.t stress)	S/N ration (w.r.t temp.)
1	1	0.1	500	159.91	849.8	-35.55	58.5863
2	2	0.2	500	16.74	1219	-24.475	61.7201
3	3	0.3	500	16.09	1229	-24.131	61.791
4	2	0.1	1000	110	924.4	-40.828	59.3172
5	3	0.2	1000	121.9	916.8	-41.72	59.2455
6	1	0.3	1000	114.2	903.4	-41.153	59.1176
7	3	0.1	1500	63.05	1132	-35.994	61.0769
8	1	0.2	1500	58.02	1126	-35.272	61.0308
9	2	0.3	1500	65.53	1101	-36.329	60.8357

Table 5.13 reveals that the maximum temperature of 1229°C and minimum residual stress of 16.09 MPa were achieved in experiment number 3. Conversely, the minimum temperature of 849.8°C and maximum residual stress of 159.91 MPa were observed in experiment number 1.

Table 5.14: L9 orthogonal array with S/N ratio when Cu on the left side and AA7075 on the right side

S.N	TRS (rpm)	TS (mm/s)	TTA (°)	Temperature ($°C$)	S/N ration (w.r.t temp.)	Stress (MPa)	S/N ratio (w.r.t stress)
1	500	0.1	1	793.4	57.9898	41.37	-32.3337
2	500	0.2	2	794.6	58.0030	41.43	-32.3463
3	500	0.3	3	794.7	58.0041	44.03	-32.8750
4	1000	0.1	2	1061	60.5143	27.99	-28.9401
5	1000	0.2	3	1052	60.4403	30.60	-29.7144
6	1000	0.3	1	1029	60.2483	29.55	-29.4111
7	1500	0.1	3	1262	62.0212	24.70	-27.3247
8	1500	0.2	1	1247	61.9173	23.24	-27.8539
9	1500	0.3	2	1227	61.7769	23.85	-27.5498

These results highlight the significant influence of process parameters on the thermal and mechanical outcomes of the welding process. Experiment 3's optimal combination of parameters yielded the best results in terms of minimizing residual stress while maintaining a high temperature for effective welding. In contrast, experiment 1 showed the least favorable conditions with high residual stress and lower temperature. Fig. 5.30 illustrates the maximum residual stress and temperature during the welding of Cu and AA7075. The results show that placing the copper plate on the left side consistently produced higher temperatures compared to other configurations. This trend indicates that the positioning of the copper plate significantly affects the thermal distribution during the welding process, leading to variations in the generated temperature.

CHAPTER 6

6. Conclusions and Future Work

The FSW of dissimilar alloys AZ91D and AA2024 was successfully fabricated by three distinct tool pin profile (Circular, triangular, and square), and observed the following conclusions.

1. The square pin profile demonstrated strong intermixing at the AA2024 and AZ91D interface compared to other pin profiles. Acoustic assistance during welding enhanced mixing and disrupted oxide layers, facilitating a strong metal-to-metal bond between AZ91D and AA2024 in square pin profile weldments.
2. UTS varied with the tool pin profile used, with the square pin profile achieving the highest UTS of 153.7 MPa and the triangular pin profile yielding the lowest UTS of 123.84 MPa, possibly due to the formation of a brittle β phase layer.
3. The triangular pin profile exhibited the maximum average hardness value (92.42 HV) at the SZ, while the square pin profile showed the minimum average hardness (85.26 HV). This variation in hardness within the welded region can be attributed to intercalated microstructures such as lamellae and complex vortexes.
4. Fractography indicated brittle fracture behavior predominantly associated with IMC layers for triangular and threaded pin profiles, influencing crack propagation within the SZ.
5. The highest UTS of 147.26 MPa was achieved with an TRS of 700 rev/min and a TS of 35 mm/min, whereas the lowest UTS of 113.47 MPa occurred at an TRS of 500 rev/min and a TS of 35 mm/min.
6. Using a TRS of 700 rev/min resulted in a maximum joint efficiency of 68.09%, indicating highly effective bonding between AZ91D and AA2024 alloys, whereas a TRS of 500 rev/min led to a minimum joint efficiency of 52.46%.
7. TRS significantly influences the quality and strength of friction stir welded (FSWed) joints, impacting microstructure development, IMC (IMC) formation, and the occurrence of voids or fractures, all affecting UTS and overall joint efficiency.
8. Thick layers of IMCs such as Al12Mg17 and Mg+ Al12Mg17 were observed in the SZ of FSWed joints processed with lower TRS and TS settings. Improper

FSW parameters leading to reduced TRS contributed to the formation of these IMC layers, which can markedly reduce the UTS of the joints.

9. The SZ exhibited a maximum hardness of 92 HV at an TRS of 500 rev/min and a TS of 35 mm/min. This hardness was higher than that of AZ91D but lower than that of AA2024, owing to intercalated microstructures like lamellae and complex vortexes within the welded region.
10. Fractography analysis revealed brittle failure characterized by cleavage facets on large fracture surfaces, indicating propagation through pre-existing cracks due to high micro hardness in the welded region, which reduced plasticity.
11. The incorporation of SiC and TiO_2 nanoparticles into FSWed joints significantly improves mechanical properties. With SiC and TiO_2 nanoparticles, the average hardness in the stir zone increased to 172 HV and 164 HV, respectively, compared to 147 HV without nanoparticles. Additionally, the joint efficiency improved markedly, with SiC and TiO_2 showing efficiencies of 40.66% and 42.09% relative to AA7075, and 49.39% and 51.14% relative to AA2024. This enhancement is attributed to the more uniform stress distribution, which reduces crack initiation and propagation, and the refinement of dimple size, which enhances ductility.
12. The presence of nanoparticles results in a fine recrystallized grain structure within the stir zone and a well-distributed reinforcement in the aluminum matrix. The mechanical stirring during FSW ensures that the reinforced particles are evenly distributed, contributing to improved hardness and joint efficiency.
13. During friction stir welding (FSW) of AA2024 and copper, the highest observed temperature and lowest residual stress were 852.7°C and 14.22 MPa, respectively, when AA2024 was placed on the left side in experiment number 7. In contrast, the maximum temperature reached 1229°C with a residual stress of 16.04 MPa when AA2024 was placed on the right side, using process parameters TRS of 500 rpm, TS of 0.3 mm/s, and a TTA of 3°.
14. For AA7075 and copper, the highest temperature and lowest residual stress were 1262°C and 24.70 MPa, respectively, with AA7075 on the right side, using TRS of 1500 rpm, TTA of 3°, and TS of 0.1 mm/s. Overall, the tool's TRS has the most significant impact on temperature rise during FSW, compared to TS and TTA.

6.1 Future work and recommendation

This section outlines potential directions for future work, offering valuable insights for both the research community and industry stakeholders.

- Study the formation mechanisms of intermetallic compounds (IMCs), alloying element distribution, and grain refinement.
- Study the influence of welding parameters on fracture toughness and fatigue resistance to design reliable joints.
- Investigate how varying surface roughness of the tool pin and shoulder affects material flow, heat generation, and weld quality.
- Optimize roughness levels to balance frictional heat generation and material deformation.
- Study the correlation between friction magnitude and heat input to ensure consistent temperature distribution across the weld.
- Develop numerical models to simulate the effects of surface roughness and friction magnitude on weld formation.

References

[1] Barcellona, G. Buffa, L. Fratini, D. Palmeri, On microstructural phenomena occurring in friction stir welding of aluminum alloys, Journal of Materials Processing Technology 177 (2006) 340–343

[2] T. Minton, D.J. Mynors , Utilization of engineering workshop equipment for friction stir welding, Journal of Materials Processing Technology 177 (2006) 336–339.

[3] H.W. Zhang, Z. Zhang, J.T. Chen, 3D modeling of material flow in friction stir welding under different process parameters, Journal of Materials Processing Technology 183 (2007) 62–70.

[4] Olivier Lorrain, Véronique Favier, Hamid Zahrouni, Didier Lawrjaniec, Understanding the material flow path of friction stir welding process using unthreaded tools, Journal of Materials Processing Technology 210 (2010) 603–609.

[5] Cemal Meran, The joint properties of brass plates by friction stir welding, Materials and Design 27 (2006) 719–726.

[6] Hasan Okuyucu, Adem Kurt, Erol Arcaklioglu, Artificial neural network application to the friction stir welding of aluminum plates, Materials and Design 28 (2007) 78–84.

[7] Z. Zhang, H.W. Zhang , Numerical studies on the effect of transverse speed in friction stir welding, Materials and Design 30 (2009) 900–907.

[8] Moataz M. Attallah, Hanadi G. Salem, Friction stir welding parameters: a tool for controlling abnormal grain growth during subsequent heat treatment, Materials Science and Engineering A 391 (2005) 51–59.

[9] Wang Kuai-she, WU Jia-lei, Wang Wen, ZHOU Long-hai, LIN Zhao-xia, KONG Liang, Underwater friction stir welding of ultrafine grained 2017 aluminum alloy, J. Cent. South Univ. (2012) 19: 2081-2085.

[10] A. Pirondi, L. Collini, D. Fersini, Fracture and fatigue crack growth behaviour of PMMC friction stir welded butt joints, Engineering Fracture Mechanics 75 (2008) 4333–4342.

[11] Y.G. Kim, H. Fujii, T. Tsumura, T. Komazaki, K. Nakata, Three defect types in friction stir welding of aluminum die casting alloy, Materials Science and Engineering A 415 (2006) 250–254.

[12] Yingchun Chen, Huijie Liu, Jicai Feng, Friction stir welding characteristics of different heat-treated-state 2219 aluminum alloy plates, Materials Science and Engineering A 420 (2006) 21–25.

[13] Sato YS, Park SHC, Michiuchi M, Kokawa H. Constitutional liquation during dissimilar friction stir welding of Al and Mg alloys. Scripta Materialia. 2004;50:1233-6.

[14] Hirano S, Okamoto K, Doi M, Okamura H, Inagaki M, Aono Y. Microstructure of dissimilar joint interface of magnesium alloy and aluminum alloy by friction stir welding. Yosetsu Gakkai Ronbunshu/Quarterly Journal of the Japan Welding Society. 2003;21:539-45.

[15] Chen YC, Nakata K. Friction stir lap joining aluminum and magnesium alloys. Scripta Materialia. 2008;58:433-6

[16] Rai. R, De A. Bhadeshia HKDH, Debroy T, Friction stir welding tools, science and technology of welding and joining, 16, 325-342, 2011.

[17] C.J. Dawes, P.L. Threadgill, E.J.R. Spurgin, and D.G. Staines, “Development of the New Friction Stir Technique for Welding Aluminum—Phase II,” TWI member report 5651/35/95, Nov 1995.

[18] Christian B. Fuller, Friction Stir Tooling: Tool Materials and Designs , Friction Stir Welding and Processing, pp7-35, 2007. DOI:10.1361/fswp2007p007.

[19] L. Christodoulou, W. Palko, and C. Fuller, Equipment and Processing Variables Affecting Friction Stir Processing of NiAl Bronze, Friction Stir Welding and Processing III, K.V. Jata, M.W. Mahoney, R.S. Mishra, and T.J. Lienert, Ed., TMS, 2005, p 57–66 48.

[20] M.W. Mahoney, C.B. Fuller, W.H. Bingel, and M. Calabrese, “Friction Stir Processing of Cast NiAl Bronze,” THERMEC 2006, July 4–8, 2006 (Vancover, Canada), TMS.

[21] M.W. Mahoney, W.H. Bingel, S.R. Sharma, and R.S. Mishra, Microstructural Modification and Resultant Properties of Friction Stir Processed Cast NiAl Bronze, Mater. Sci. Forum, Vol 426–432, 2003, p 2843–2848.

[22] Fu Zhi-Hong, HE Di-qiu, Wang Hong, friction str welding of aluminum alloys, Journal of Wuhan university of Technology, Material Science edition 19: 61-64.

[23] R.S. Mishra and Zy Ma (2005), Friction stir welding and processing, Materil science and Engineering R 50: 1-78.

[24] Greitmann MJ and Peter Deimel (2005), friciton stir welding- Innovative technology for joining aluminum components, Otto-graf journal 16: 185-192.

[25] Ghosh M, Kumar K, Kailas SV, Ray AK 920100, Optimization of friction stir welding parameters for dissimilar aluminum alloys, Materials and Design 31: 3033-3037.

[26] K. S. Anil Kumar, S. M. Murigendrappa, Hemantha Kumar, and Himanshu Shekhar, Effect of tool rotation speed on microstructure and tensile properties of FSW joints of 2024-T351 and 7075-T651 reinforced with SiC nano particle: The role of FSW single pass, AIP Conference Proceedings 1943, 020056 (2018).

[27] Barenji, R. V. (2016). Effect of tool traverse speed on microstructure and mechanical performance of friction stir welded 7020 aluminum alloy. Proceedings of the Institution of Mechanical Engineers, Part L: Journal of Materials: Design and Applications, 230(2), 663–673.

[28] Narges Dialami , Miguel Cervera and Michele Chiumenti, Effect of the Tool Tilt Angle on the Heat Generation and the Material Flow in Friction Stir Welding, Metals 2019, 9, 28.

[29] Hassan., (2002), The Effect of welding condition on the nugget zone in friction stir welds AA 7010 alloy, In 6th International trends in Welding Research Conference Proceedings, 287–292.

[30] Hassan, K.A.A., Norman, A.F., Price, D.A., and Prangnell, P.B., (2003), Stability of nugget zone grain structures in high strength Al-alloy friction stir welds during solution treatment, Acta Materialia, Vol.51(7), pp.1923–1936.

[31] Huang, C. & Kou, S. Partially melted zone in Aluminum welds-liquation mechanism and directional soldification. Welding Journal, 2000, 79(5), 113s-120s.

[32] L. Commin, M. Dumont, J.-E. Masse, L. Barrallier, Friction stir welding of AZ31 magnesium alloy rolled sheets: Influence of processing parameters, Acta Materialia 57 (2009) 326–334

[33] Z. Zhang, H.W. Zhang, Numerical studies on controlling of process parameters in friction stir welding, journal of materials processing technology 209 (2009) 241–270

[34] D. Jacquin, B. de Meester, A. Simar, D. Deloison, F. Montheillet, C. Desrayaud, A simple Eulerian thermomechanical modeling of friction stir welding, Journal of Materials Processing Technology 211 (2011) 57–65.

[35] Mustafa, B. The influence of stirrer geometry on bonding and mechanical properties in friction stir welding process. Materials and Design 2004, 35, 343–347.

[36] K. Elangovan, V. Balasubramanian, and M. Valliappan, Effect of Tool Pin Profile and Tool Rotational Speed on Mechanical Properties of Friction Stir Welded AA6061 Aluminum Alloy, Materials and Manufacturing Processes, 23: 251–260, 2008.

[37] Vijay, S.J., and Murugan, N., (2010), Influence of tool pin profile on the metallurgical and mechanical properties of friction stir welded Al-10wt.% TiB2 metal matrix composite, Materials and Design, Vol.31(7), pp.3585–3589.

[38] Pothur Hema, Experimental Investigations on AA 6061 Alloy Welded Joints by Friction Stir Welding, Aluminum Alloys and Composites,2020, Chapter (8), https://doi.org/10.5772/intechopen.89797.

[39] Sivaraj, P.,Kanagarajan, D., and Balasubramanian, V., (2014a), Effect of post weld heat treatment on fracture toughness properties of friction stir welded AA7075-T651 aluminum alloy joints, Journal of Manufacturing Engineering, Vol.9(2), pp.110–115.

[40] Krishnaja Devireddy, Venkateswarlu Devuri, Murali Mohan Cheepu, Balina Kranthi Kumar, Analysis of the Influence of Friction Stir Processing on Gas Tungsten Arc Welding of 2024 Auminum Alloy Weld Zone, International Journal of Mechanical and Production Engineering Research and Development 8 (1) 2018 243-252

[41] C. Yeni ,S.Sayer, M. Pakdil , Comparison of mechanical and microstructural behaviour of TIG, MIG and Friction Stir welded 7075 Aluminium Alloy, Kovove Mater. 47 (2009), 341–347.

[42] Peel M, Steuwer A, et al. Microstructure, mechanical properties and residual stresses as a function of welding speed in aluminium AA5083 friction stir

welds. Acta Materialia. 2003;51:4791-4801.Jitender Kundu and Hari Singh 2018 Adv in Mater Proc Technol **4** 183.

[43] Hakan Aydın, Ali Bayram, Agah Uguz , Kemal Sertan Akay, Tensile properties of friction stir welded joints of 2024 aluminum alloys in different heat-treated-state, Materials and Design 30 (2009) 2211–2221.

[44] Yang Xu , Liming Ke , Sheng Ouyang, Yuqing Mao, Pengliang Niu, Precipitation behavior of intermetallic compounds and their effect on mechanical properties of thick plate friction stir welded Al/Mg joint, Journal of Manufacturing Processes Volume 64 , April 2021, Pages 1059-1069.

[45] Liu L, Ren D, Liu F. A Review of Dissimilar Welding Techniques for Magnesium Alloys to Aluminum Alloys. Materials. 2014; 7: 3735-3757.

[46] Venkateswaran P, Reynolds AP. Factors affecting the properties of Friction Stir Welds between aluminum and magnesium alloys. Materials Science and Engineering A. 2012;545:26- 37.

[47] Hirano S, Okamoto K, Doi M, Okamura H, Inagaki M, Aono Y. Microstructure of dissimilar joint interface of magnesium alloy and aluminum alloy by friction stir welding. Yosetsu Gakkai Ronbunshu/Quarterly Journal of the Japan Welding Society. 2003;21:539-45

[48] Firouzdor V, Kou S. Al-to-Mg friction stir welding: Effect of positions of Al and Mg with respect to the welding tool. Welding Journal (Miami, Fla). 2009;88:213S-24S.

[49] Zettler R, Da Silva AAM, Rodrigues S, Blanco A, Dos Santos JF. Dissimilar Al to Mg alloy friction stir welds. Advanced Engineering Materials. 2006;8:415-21.

[50] Abbasi Gharacheh M, Kokabi AH, Daneshi GH, Shalchi B, Sarrafi R. The influence of the ratio of "rotational speed/traverse speed" (ω/v) on mechanical properties of AZ31 friction stir welds. International Journal of Machine Tools and Manufacture. 2006;46:1983-7

[51] Esparza JA, Davis C, Trillo EA, Murr LE. Friction-stir welding of magnesium alloy AZ31B. J Mater Sci Lett 2002;21:917–20.

[52] Vaidya WV, Horstmann M, Seib E, Toksoy K, Kocak M. Assessment of fracture and fatigue crack propagation of laser beam and friction stir welded aluminum and magnesium alloys. Adv Eng Mater 2006;8:399–406.

[53] Sumit Jain, R.S. Mishra, Husain Mehdi, Influence of SiC Microparticles and Multi-Pass FSW on Weld Quality of the AA6082 and AA5083 Dissimilar Joints. Silicon (2023). https://doi.org/10.1007/s12633-023-02455-x

[54] Shaurya Bhatnagar, Gaurav Kumar, Husain Mehdi, Mukesh Kumar, Optimization of FSW parameters for enhancing dissimilar joint strength of AA7050 and AA6061 using Response Surface Methodology (RSM), materials today proceedings, 2023. https://doi.org/10.1016/j.matpr.2023.04.144.

[55] Sipokazi Mabuwa, Velaphi Msomi, Husain Mehdi, Tiyamike Ngonda, A study on the metallurgical characterization of the longitudinally sampled friction stir processed TIG welded dissimilar aluminum joints, Journal of Process Mechanical Engineering, 2023, https://doi.org/10.1177/09544089231169589.

[56] Yamamoto N, Liao J, Watanabe S, Nakata K. Effect of IMC layer on tensile strength of dissimilar friction-stir weld of a high strength Mg alloy and Al alloy. Mater Trans 2009;50(12):2833–8.

[57] Hirano, S., Okamoto, K., Doi, M., Kamura, O., Inagaki, M., Aono, Y., 2004. Microstruc- ture of the interface in magnesium alloy to aluminium alloy dissimilar joints produced byfrictionstirwelding.Weld.Int.18,702–708.

[58] Acerra, F., Buffa, G., Fratini, L. et al. On the FSW of AA2024-T4 and AA7075-T6 T-joints: an industrial case study. Int J Adv Manuf Technol 48, 1149–1157 (2010). https://doi.org/10.1007/s00170-009-2344-9.

[59] X.Q. Lv, C.S. Wu, C.L. Yang, G.K. Padhy, Weld microstructure and mechanical properties in ultrasonic enhanced FSW of Al alloy to Mg alloy, J. Mater. Process. Tech. 254 (2018) 145-157, https://doi.org/10.1016/j.jmatprotec.2017.11.031.

[60] X.Q. Lv, C.S. Wu, G.K. Padhy, Diminishing IMC layer in ultrasonic vibration enhanced FSW of aluminum alloy to magnesium alloy, Mater. Lett. 230 (2017) 81-84, http://dx.doi.org/10.1016/j.matlet.2017.05.090.

[61] Khodir, S.A., Shibayanagi, T., 2007. Dissimilar friction stir welded joints between 2024-T3 aluminum alloy and AZ31 magnesium alloy. Mater. Trans. 48, 2501–2505.

[62] Kostka, A., Coelho, R.S., Dos Santos, J., Pyzalla, A.R., 2009. Microstructure of FSW of aluminium alloy to magnesium alloy. Scripta Mater. 60, 953–956.

[63] Yan, J.C., Xu, Z.W., Li, Z.Y., Li, L., Yang, S.Q., 2005. Microstructure characteristics and performance of dissimilar welds between magnesium alloy and aluminum formed by friction stirring. Scripta. Mater. 53, 585–589.

[64] Long, T. & Reynolds, A. P. (1 March 2006). Parametric Studies of FSW by Commercial Fluid Dynamic Simulation. Science and Technology of Welding and Joining, 11 (2), 200-208. http://dx.doi.org/10.1179/174329306X85985.

[65] Husain Mehdi, Sumit Jain, Msomi, V. et al. Effect of IMCs on Mechanical and Microstructural Properties of Dissimilar Alloys Al-7Si/AZ91D. J. of Materi Eng and Perform (2023). https://doi.org/10.1007/s11665-023-08302-9.

[66] Y.C. Chen and K. Nakata, Friction stir lap joining aluminum and magnesium alloys, Scripta Materialia 58 (2008) 433–436.

[67] Mofid, M.A., Abdollah-zadeh, A. & Gür, C.H. Investigating the formation of IMCs during FSW of magnesium alloy to aluminum alloy in air and under liquid nitrogen. Int J Adv Manuf Technol 71, 1493–1499 (2014). https://doi.org/10.1007/s00170-013-5565-x.

[68] Venkateswaran, P., Xu, ZH., Li, X. et al. Determination of mechanical properties of Al–Mg alloys dissimilar friction stir welded interface by indentation methods. J Mater Sci 44, 4140–4147 (2009). https://doi.org/10.1007/s10853-009-3607-4.

[69] M.Haghshenas, A.P. Gerlich, Joining of automotive sheet materials by friction-based welding methods: A review, Engineering Science and Technology, an International Journal, 21 (1), 2018, 130-148.

[70] C. Liu , D.L. Chen, S. Bhole, X. Cao , M. Jahazi, Polishing-assisted galvanic corrosion in the dissimilar friction stir welded joint of AZ31 magnesium alloy to 2024 aluminum alloy, Materials Characterization 60 (2009), 370-376.

[71] C. B. Jagadeesha, FSW between Al alloy and Mg Alloy: the comparative study, Journal of Mechanical Behaviour of Materials, 26(1–2), 2017, 25–42.

[72] Yang Xu, Liming Ke, Sheng Ouyang, Yuqing Mao, Pengliang Niu, Precipitation behavior of IMCs and their effect on mechanical properties of thick plate friction stir welded Al/Mg joint, Journal of Manufacturing Processes, 64, 2021, 1059-1069.

[73] Singh, V.P., Kumar, D., Mahto, R.P. et al. Microstructural and Mechanical Behavior of Friction-Stir-Welded AA6061-T6 and AZ31 Alloys with

Improved Electrochemical Corrosion. J. of Materi Eng and Perform 32, 4185–4204 (2023). https://doi.org/10.1007/s11665-022-07380-5.

[74] Alireza Masoudian, Arvin Tahaei, Atefeh Shakiba, Fariborz Sharifianjazi, Jamshid Aghazadeh Mohandesi, Microstructure and mechanical properties of friction stir weld of dissimilar AZ31-O magnesium alloy to 6061-T6 aluminum alloy, Transactions of Nonferrous Metals Society of China, 24 (5), 2014, 1317-1322.

[75] A. Abdollahzadeh, A. Shokuhfar, J.M. Cabrera, A.P. Zhilyaev, H. Omidvar, In-situ nanocomposite in FSW of 6061-T6 aluminum alloy to AZ31 magnesium alloy, Journal of Materials Processing Technology, 263, 2019, 296-307.

[76] Sameer MD, Anil Kumar Birru, Mechanical and metallurgical properties of friction stir welded dissimilar joints of AZ91 magnesium alloy and AA 6082-T6 aluminium alloy, Journal of Magnesium and Alloys 7 (2019) 264–271.

[77] Saravanakumar, R., Rajasekaran, T. & Pandey, C. Underwater Friction Stir Welded Armour Grade AA5083 Aluminum Alloys: Experimental Ballistic Performance and Corrosion Investigation. J. of Materi Eng and Perform (2023). https://doi.org/10.1007/s11665-023-07836-2.

[78] R Saravanakumar, T Rajasekaran, C Pandey, Optimisation of underwater FSW parameters of aluminum alloy AA5083 using RSM and GRA, Proceedings of the Institution of Mechanical Engineers, Part E: Journal of Process Mechanical Engineering, 2023, https://doi.org/10.1177/095440892211344.

[79] Saravanakumar, R., Rajasekaran, T., Pandey, C. et al. Influence of Tool Probe Profiles on the Microstructure and Mechanical Properties of Underwater Friction Stir Welded AA5083 Material. J. of Materi Eng and Perform 31, 8433–8450 (2022). https://doi.org/10.1007/s11665-022-06822-4.

[80] Saravanakumar, R., Rajasekaran, T., Pandey, C. et al. Mechanical and Microstructural Characteristics of Underwater Friction Stir Welded AA5083 Armor-Grade Aluminum Alloy Joints. J. of Materi Eng and Perform 31, 8459–8472 (2022). https://doi.org/10.1007/s11665-022-06832-2.

[81] Park, S.H.C., Sato, Y.S. & Kokawa, H. Microstructural evolution and its effect on Hall-Petch relationship in FSW of thixomolded Mg alloy AZ91D. Journal of Materials Science 38, 4379–4383 (2003). https://doi.org/10.1023/A:1026351619636.

[82] Somasekharan, A.C., Murr, L.E. Characterization of complex, solid-state flow and mixing in the friction-stir welding (FSW) of aluminum alloy 6061-T6 to magnesium alloy AZ91D using color metallography. J Mater Sci 41, 5365–5370 (2006). https://doi.org/10.1007/s10853-006-0342-y.

[83] Yazdipour A, Heidarzadeh A. Dissimilar butt FSW of Al 5083-H321 and 316L stainless steel alloys. Int J Adv Manuf Technol. 2016;87(9–12):3105–3112.

[84] Khodaverdizadeh H, Mahmoudi A, Heidarzadeh A, et al. Effect of FSW parameters on strain hardening behavior of pure copper joints. Mater Des.2012;35:330–334.

[85] Buffa G, Campanile G, Fratini L, Prisco A. FSW of lap joints: influence of process parameters on the metallurgical and mechanical properties. Mater Sci EngA 2009; 519(1-2):19–26.

[86] Liu HJ, Fuji H, Maeda M, Nogi K. Mechanical properties offriction stir welded joints of 1050-H 24 aluminium alloy. SciTechnol Weld Join 2003;8(6):450–4.

[87] Elangovan K, Balasubramanian V, Valliappan M. Effect of tool pin profile and TRS on mechanical properties of friction stir welded AA6061 aluminium alloy.Mater Manuf Process 2008;23(3):251–60.

[88] Fujii H, Cui L, Tsuji N, Maeda M, Nakata K, Nogi K. Frictionstir welding of carbon steels. Mater Sci Eng A2006;429(1-2):50–7.

[89] Cavaliere P, De Santis A, Panella F, Squillace A. Effect ofwelding parameters on mechanical and microstructuralproperties of dissimilar AA6082–AA2024 joints produced byFSW. Mater Des 2009;30(3):609–16.

[90] Chen S-T, Lui T-S, Chen L-H. Effect of revolutionary pitch onthe microhardness drop and tensile properties of frictionstir processed 1050 aluminium alloy. Mater Trans2009;50(8):1941–8.

[91] Yang YK, Dong H, Kou S. Liquation tendency and liquid-film formation in friction stir spot welding. Weld J2008;87:202–11.

[92] Champagne VK III, West MK, Rokni MR, Curtis T,Champagne V Jr, McNally B. Joining of cast ZE41A Mg towrought 6061 Al by the cold spray process and friction stirwelding. J Therm Spray Technol 2016;25(1):143–59.

[93] C. Yang, D.R. Ni, P. Xue, B.L. Xiao, W. Wang, K.S. Wang, Z.Y. Ma, A comparative research on bobbin tool and conventional FSW of Al-Mg-Si alloy plates, Materials Characterization 145 (2018) 20–28.

[94] Shuai Tan, Feiyan Zheng, Juan Chen, Jingyu Han, Yujuan Wu, Liming Peng, Effects of process parameters on microstructure and mechanical properties of friction stir lap linear welded 6061 aluminum alloy to NZ30K magnesium alloy, Journal of Magnesium and Alloys, 5 (1), 2017, 56-63.

[95] P. Venkateswaran, A.P. Reynolds, Factors affecting the properties of Friction Stir Welds between aluminum and magnesium alloys, Materials Science and Engineering: A, 472 (1–2), 2008, 179-186.

[96] N. Afrin, D.L. Chen, X. Cao, M. Jahazi, Microstructure and tensile properties of friction stir welded AZ31B magnesium alloy, Materials Science and Engineering: A, 472, (1–2), 2008, 179-186.

[97] Sun YF, Fujii H. The effect of SiC particles on the microstructure and mechanical properties of friction stir welded pure copper joints. Mater Sci Eng 2011;528:5470-5.https://doi.org/10.1016/j.msea.2011.03.077.

[98] Saeidi, M.; Barmouz, M.; Givi, M.K.B. Investigation on AA5083/AA7075+Al2O3 joint fabricated by FSW: Characterizing microstructure, corrosion and toughness behavior. Mater. Res. **2015**, 18, 1156–1162.

[99] Jamalian, H.M.; Ramezani, H.; Ghobadi, H.; Ansari, M.; Yari, S.; Besharati Givi, M.K. Processing-structure-property correlation in nano-SiC-reinforced friction stir welded aluminum joints. J. Manuf. Process. **2016**, 21, 180–189.

[100] Mirjavadi, S.S.; Alipour, M.; Emamian, S.; Kord, S.; Hamouda, A.M.S.; Koppad, P.G.; Keshavamurthy, R. Influence of TiO2 nanoparticles incorporation to friction stir welded 5083 aluminum alloy on the microstructure, mechanical properties and wear resistance. J. Alloys Compd. **2017**, 712, 795–803.

[101] Bahrami M, Dehghani K, Besharati Givi MK. A novel approach to develop aluminum matrix nano-composite employing FSW technique. Mater Des 2014;53:217-25. https://doi.org/10.1016/j.matdes.2013.07.006.

[102] Bahrami M, Helmi N, Dehghani K, Givi MKB. Exploring the effects of SiC reinforcement incorporation on mechanical properties of friction stir welded 7075 aluminum alloy:fatigue life, impact energy, tensile strength. Mater Sci

Eng 2014;595:173-8. https://doi.org/10.1016/j.msea.2013.11.068.

[103] Bahrami M, Farahmand Nikoo M, Besharati Givi MK. Microstructural and mechanical behaviors of nano SiCreinforced AA7075-O FSW joints prepared through two passes. Mater Sci Eng 2015;626:220-8. https://doi.org/10.1016/j.msea.2014.12.009.

[104] Karthikeyan P, Mahadevan K. Investigation on the effects of SiC particle addition in the weld zone during FSW of Al 6351 alloy. Int J Adv Manuf Technol 2015;80:1919-26. https://doi.org/10.1007/s00170-015-7160-9.

[105] Singh R, Kumar V, Feo L, Fraternali F. Experimental investigations for mechanical and metallurgical properties of friction stir welded recycled dissimilar polymer materials with metal powder reinforcement. Compos B Eng2016;103:90-7. https://doi.org/10.1016/j.compositesb.2016.08.005.

[106] Abioye TE, Zuhailawati H, Anasyida AS, Yahaya SA, Dhindaw BK. Investigation of the microstructure, mechanical and wear properties of AA6061-T6 friction stir weldments with different particulate reinforcements addition. J Mater Res Technol 2019;8:3917-28. https://doi.org/10.1016/j.jmrt.2019.06.055.

[107] Nosko M, _Step_anek M, Zif_c_ak P, Orov_cı´k L, Nagy, Dvor_ak T,et al. Solid-state joining of powder metallurgy Al-Al 2 O 3 nanocomposites via friction-stir welding: effects of powder particle size on the weldability, microstructure, and mechanical property. Mater Sci Eng A 2019; 754:190-204.https://doi.org/10.1016/j.msea.2019.03.074.

[108] Tebyani SF, Dehghani K. Effects of SiC nanopowders on the mechanical properties and microstructure of interstitial free steel joined via friction stir spot welding. Mater Des 2016;90:660-8. https://doi.org/10.1016/j.matdes.2015.11.016.

[109] Hirano, S., Okamoto, K., Doi, M., Kamura, O., Inagaki, M., Aono, Y., 2004. Microstruc- ture of the interface in magnesium alloy to aluminium alloy dissimilar joints produced by FSW. Weld. Int. 18, 702–708.

[110] Somasekharan, A.C., Murr, L.E., 2004. Microstructures in friction-stir welded dissimilar magnesium alloys and magnesium alloys to 6061-T6 aluminum alloy. Mater. Character 52, 49–64.

[111] Yan, J.C., Xu, Z.W., Li, Z.Y., Li, L., Yang, S.Q., 2005. Microstructure characteristics and performance of dissimilar welds between magnesium alloy and aluminum formed by friction stirring. Scripta. Mater.53,585–589.

[112] Yamamoto, N., Liao, J., Watanabe, S., Nakata, K., 2009. Effect of IMC layer on tensile strength of dissimilar friction-stir weld of a high strength Mg alloy and Al alloy. Mater. Trans. 50, 2833–2838.

[113] Khodir, S.A., Shibayanagi, T., 2007. Dissimilar friction stir welded joints between 2024-T3 aluminum alloy and AZ31 magnesium alloy. Mater. Trans. 48, 2501–2505.

[114] Firouzdor, V., Kou, S., 2010. Formation of liquid and intermetallics in Al-to-Mg FSW. Metall. Mater. Trans. A 41, 3238–3251

[115] Firouzdor, V., Kou, S., 2010. Al-to-Mg FSW: effect of material position, travel speed, and rotation speed. Metall. Mater. Trans. A 41, 2914–2935.

[116] Rao, H.M., Yuan, W., Badarinarayan, H., 2015. Effect of process parameters on mechanical properties of friction stir spot welded magnesium to aluminum alloys. Mater. Des. 66, 235–245.

[117] Buffa, G., Baffari, D., Di Caro, A., Fratini, L., 2015. FSW of dissimilar aluminium–magnesium joints: sheet mutual position effects. Sci. Technol. Weld. Join. 20, 271–279.

[118] Liang, Z., Chen, K., Wang, X., Yao, J., Yang, Q., Zhang, L., Shan, A., 2013. Effect of tool offset and TRS on enhancing mechanical property of Al/Mg dissimilar FSW joints. Metall. Mater. Trans. A 44, 3721– 3731.

[119] C. Liu , D.L. Chen, S. Bhole, X. Cao , M. Jahazi, Polishing-assisted galvanic corrosion in the dissimilar friction stir welded joint of AZ31 magnesium alloy to 2024 aluminum alloy, Materials Characterization 60 (2009), 370-376.

[120] C. B. Jagadeesha, FSW between Al alloy and Mg Alloy: the comparative study, Journal of Mechanical Behaviour of Materials, 26(1–2), 2017, 25–42.

[121] A.A. McLean, G.L.F. Powell, I.H. Brown, V.M. Linton, FSW of magnesium Alloy AZ31B to aluminum alloy 5083, Sci. Technol. Weld. Join. 8 (2003) 462-464.

[122] Y.S. Sato, H.S.C. Park, M. Michiuchi, H. Kokawa, Constitutional liquation during dissimilar FSW of Al and Mg alloys, Scr. Mater 50 (2004) 1233-1236.

[123] Liu G, Murr L, Niou C, Mcclure J, Vega F. Microstructural aspects of the friction-stir welding of 6061-T6 aluminum [J]. Scripta Materialia, 1997, 37: 355−361.

[124] Gaafer A, Mahmoud T, Mansour E. Microstructural and mechanical characteristics of AA7020-O Al plates joined by FSW [J]. Materials Science and Engineering A, 2010, 527: 7424−7429.

[125] Firouzdor V, Kou S. Al-to-Mg FSW: Effect of material position, travel speed, and rotation speed. Metallurgical and Materials Transactions A: Physical Metallurgy and Materials Science. 2010; 41:2914-35.

[126] Zettler R, Da Silva AAM, Rodrigues S, Blanco A, Dos Santos JF. Dissimilar Al to Mg alloy friction stir welds. Advanced Engineering Materials. 2006; 8:415-21.

[127] PJ Lokesh Kumar, P Sevvel, TG Loganathan and D Prakash, Investigation on the distribution and role of intermetallic aggregates in influencing the mechanical strength of the friction stir welded AZ91C Mg – AA6061 Al alloy joints, Materials Research Express, 10, 026516. https://doi.org/10.1088/2053-1591/acbbbb.

[128] Lokesh Kumar, P. J., Sevvel, P. and Loganathan, T. G., Impact of TRS on the microstructural transitions and tensile properties of the dissimilar AZ80A-Mg – AA6061-Al joints fabricated by FSW" Practical Metallography, 60 (5), 2023, 289-318. https://doi.org/10.1515/pm-2022-1029.

[129] Pai Peng, Wen Wang, Ting Zhang, Qiang Liu, Xiaohu Guan, Ke Qiao, Jun Cai, Kuaishe Wang, Effects of interlayer metal on microstructures and mechanical properties of friction stir lap welded dissimilar joints of magnesium and aluminum alloys, Journal of Materials Processing Technology, 299, 2022, 117362. https://doi.org/10.1016/j.jmatprotec.2021.117362.

[130] S.S. Mirian Mehrian, M. Rahsepar, F. Khodabakhshi, A.P. Gerlich, Effects of friction stir processing on the microstructure, mechanical and corrosion behaviors of an aluminum-magnesium alloy, Surface and Coatings Technology, 405, 2021, 126647. https://doi.org/10.1016/j.surfcoat.2020.126647.

[131] Sameer MD, Anil Kumar Birru, Mechanical and metallurgical properties of friction stir welded dissimilar joints of AZ91 magnesium alloy and AA 6082-

T6 aluminum alloy, Journal of Magnesium and Alloys, 7, (2), 264-271. https://doi.org/10.1016/j.jma.2018.09.004.

[132] K. Elangovan, V. Balasubramanian, and M. Valliappan, Effect of Tool Pin Profile and Tool Rotational Speed on Mechanical Properties of Friction Stir Welded AA6061 Al-alloy, Materials and Manufacturing Processes, 23: 251–260, 2008.

[133] M Krishna, Dr K C Udaiyakumar, D K Mohan Kumar and H Mohammed Ali, Analysis on effect of using different tool pin profile and mechanical properties by friction stir welding on dissimilar Al-alloys Al6061 and Al7075, IOP Conf. Series: Materials Science and Engineering 402 (2018) 012099.

[134] Y.Wang, X.L Shi, R.S Mishra, T.J Watson, "Friction stir welding of devitrified AL-4.0Y-4.0Ni-0.9Co alloy produced by amorphous powder", Scripta Materialia 56 (2007) 971-974.

[135] Dawood HI, Kahtan S. Mohammed, Azmi Rahmat, M. B. Uday, Effect of small tool pin profiles on microstructures and mechanical properties of 6061 Al-alloy by friction stir welding, Trans. Nonferrous Met. Soc. China 25(2015) 2856−2865.

[136] Z.Y.Ma, R.S Mishra, M.W. Mahoney," Superplastic deformation behavior of friction stir processed 7075Al alloy", Acta Materialia 50 (2002), 4419-4430.

[137] T. Srinivasa Rao, G. Madhusudhan Reddy, S. R. Koteswara Rao, Microstructure and mechanical properties of friction stir welded AA7075−T651 Al-alloy thick plates, Trans. Nonferrous Met. Soc. China 25(2015) 1770−1778.

[138] Nilesh Kumar, R.S Mishra, " Ultrafine Grained Al-Mg-Sc Alloy via friction Stir Processing", Metallurgical and Materials Transaction, 44A (2013) 934-945.

[139] Z.Y Ma, S.R Sharma, R.S Mishra, " Effect of Multipass Friction Stir Processing on Microstructure and tensile properties of a Cast Al-Si Alloy", Scripta Materialia, 54 (2006) 1623-1626.

[140] Z.Y.Ma, R.S Mishra, F.C Liu, "Superplastic behaviour of Micro-region in two-pass friction stir processing 7075Al alloy", Materialia Science and Engineering A 505 (2009) 70-78.

[141] Jianqing Su, Jiye Wang, R.S Mishra, Ray Xu, " Microstructure and Mechanical Properties of Friction Stir Processing Ti-6Al-4V Alloy", Material Science and Engineering A 573 (2013) 67-74.

[142] F. Khodabakhshi, A.P. Gerlich, A. Simchi, A.H. Kokabi, Hot deformation behavior ofan aluminum-matrix hybrid nanocomposite fabricated by friction stir processing,Mater. Sci. Eng. A 626 (2015) 458–466,

[143] SunYF, Fujii H. The effect of SiC particles on the microstructure and mechanicalproperties of friction stir welded pure copper joints. Mater Sci Eng A2011;528:5470–5.

[144] Gibson BT, Lammlein DH, Prater TJ, Longhurst WR, Cox CD, Ballun MC,et al. Friction stir welding: process, automation, and control. J Manuf Process, 2014;16:56–73.

[145] Azimzadegan T, Serajzadeh S. An Investigation into microstructures and mechanical properties of AA7075-T6 during friction stir welding at relatively high rotational speeds, J. Mat. Eng. Perf., 2010, **19**, p1256−1263.

[146] H.A. Deore , A. Bhardwaj, A.G. Rao, J. Mishra, V.D. Hiwarkar, Consequence of reinforced SiC particles and post process artificial ageing on microstructure and mechanical properties of friction stir processed AA7075, Defence Technology 16 (2020) 1039-1050.

[147] Rathee S, Maheshwari S, Siddiquee AN, Srivastava M (2017) Effect of tool plunge depth on reinforcement particles distribution in surface composite fabrication via friction stir processing. Defence Technology 13(2):86–91.

[148] Olivier Lorrain, Véronique Favier, Hamid Zahrouni, Didier Lawrjaniec, Understanding the material flow path of friction stir welding process using unthreaded tools, Journal of Materials Processing Technology 210 (2010) 603–609.

[149] Harish Suthar, Anirban Bhattacharya, Surajit Kumar Paul, Local deformation response and failure behavior of AA6061-AA6061 and AA6061-AA7075 friction stir welds, CIRP Journal of Manufacturing Science and Technology 30 (2020) 12–24.

[150] Jerry Wong, Patricia Zambrano, Indira Escamilla, Bernardo Gonzalez, Victor Mucino, Rafael Colás, Friction stir linear welding of an Al-alloy, Advanced Materials Research Vol. 68 (2009) pp 116-121.

[151] Noor Zaman Khan, Arshad Noor Siddiquee, Zahid A. Khan, Ashim K. Mukhopadhyay, Mechanical and microstructural behavior of friction stir

welded similar and dissimilar sheets of AA2219 and AA7475 aluminium alloys, Journal of Alloys and Compounds, 695, 2017, 2902-2908.

[152] Rodriguez, R. I., Jordon, J. B., Allison, P. G., Rushing, T., & Garcia, L. (2015). Microstructure and mechanical properties of dissimilar friction stir welding of 6061-to-7050 aluminum alloys. Materials and Design, 83, 60–65.

[153] Jianqing Su, Jiye Wang, R.S Mishra, Ray Xu, " Microstructure and Mechanical Properties of Friction Stir Processing Ti-6Al-4V Alloy", Material Science and Engineering A 573 (2013) 67-74.

[154] Gibson BT, Lammlein DH, Prater TJ, Longhurst WR, Cox CD, Ballun MC,et al. Friction stir welding: process, automation, and control. J Manuf Process, 2014;16:56–73.

[155] B.B. Verma, J.D. Atkinson, M. Kumar, Study of fatigue behaviour of 7475 aluminium alloy, Bulletin of Materials Science 24 (2001) 231–236.

[156] M. Esmaily, A. Shokuhfar, Numerical simulation of heat transfer in friction stir welding of 7075-T6 aluminum alloy and high carbon steel using Arbitrary Lagrangian-Eulerian technique, Mat.-wiss. u. Werkstofftech. 2010, 41, No. 5, 350-355.

[157] Nilesh Kumar, R.S Mishra, " Ultrafine Grained Al-Mg-Sc Alloy via friction Stir Processing", Metallurgical and Materials Transaction, 44A (2013) 934-945

[158] Kalemba-Rec, I., Kopyściański, M., Miara, D., & Krasnowski, K. (2018). Effect of process parameters on mechanical properties of friction stir welded dissimilar 7075-T651 and 5083-H111 aluminum alloys. International Journal of Advanced Manufacturing Technology, 97(5–8), 2767–2779.

[159] Z.Y.Ma, R.S Mishra, M.W. Mahoney," Superplastic deformation behavior of friction stir processed 7075Al alloy", Acta Materialia 50 (2002), 4419-4430.

[160] Mehta, K. P., & Badheka, V. J. (2016). Effects of tilt angle on the properties of dissimilar friction stir welding copper to aluminum. Materials and Manufacturing Processes, 31(3), 255–263.

[161] Bozkurt, Yahya, and Serdal duman. "The effect of welding parameters on the mechanical and microstructural properties of friction stir welded dissimilar AA 3003H24 and 2124/SiC/25p-T4 alloy joints." Scientific Research and Essays 6, no. 17 (2011): 3702-3716.

[162] Harish Suthar, Anirban Bhattacharya, Surajit Kumar Paul, Local deformation response and failure behavior of AA6061-AA6061 and AA6061-AA7075 friction stir welds, CIRP Journal of Manufacturing Science and Technology 30 (2020) 12–24.

[163] Y.Wang, X.L Shi, R.S Mishra, T.J Watson, "Friction stir welding of devitrified AL-4.0Y-4.0Ni-0.9Co alloy produced by amorphous powder", Scripta Materialia 56 (2007) 971-974.

[164] Pourali, M., Abdollah-zadeh, A., Saeid, T., & Kargar, F. (2017). Influence of welding parameters on intermetallic compounds formation in dissimilar steel/aluminum friction stir welds. Journal Of Alloys And Compounds, 715, 1-8.

[165] Raghu Babu G., Murti K. G. K. and Ranga Janardhana G., An experimental study on the effect of welding parameters on mechanical and microstructural properties of AA6082-T6 friction stir welded butt joints‖, ARPN Journal of Engineering and Applied Sciences, no. 3, (2008):68-74.

[166] Ratnam, C., Sudheer Kumar, B., & Sunil Ratna Kumar, K. (2018). Optimization of friction stir welding parameters to improve the mechanical properties of dissimilar AA2024 and AA5083 aluminium alloys. International Journal of Mechanical and Production Engineering Research and Development, 8(6), 937–944.

[167] Hassan, Kh AA, Prangnell P. B., Norman A. F., Price D. A., and Williams S. W.. "Effect of welding parameters on nugget zone microstructure and properties in high strength aluminium alloy friction stir welds." Science and Technology of Welding and joining 8, no. 4 (2003): 257-268.

[168] Olivier Lorrain, Véronique Favier, Hamid Zahrouni, Didier Lawrjaniec, Understanding the material flow path of friction stir welding process using unthreaded tools, Journal of Materials Processing Technology 210 (2010) 603–609.

[169] Saravanan, V., Banerjee, N., Amuthakkannan, R. et al. Microstructural Evolution and Mechanical Properties of Friction Stir Welded Dissimilar AA2014-T6 and AA7075-T6 Aluminum Alloy Joints. Metallogr. Microstruct. Anal. 4, 178–187 (2015).

[170] Jerry Wong, Patricia Zambrano, Indira Escamilla, Bernardo Gonzalez, Victor Mucino, Rafael Colás, Friction stir linear welding of an aluminum alloy, Advanced Materials Research Vol. 68 (2009) pp 116-121.

[171] Dawood HI, Kahtan S. Mohammed, Azmi Rahmat, M. B. Uday, Effect of small tool pin profiles on microstructures and mechanical properties of 6061 aluminum alloy by friction stir welding, Trans. Nonferrous Met. Soc. China 25(2015) 2856−2865.

[172] Kumar, S., Wu, C. Strengthening Effects of Tool-Mounted Ultrasonic Vibrations during Friction Stir Lap Welding of Al and Mg Alloys. Metall Mater Trans A 52, 2909–2925 (2021). https://doi.org/10.1007/s11661-021-06282-w.

[173] Sachin Kumar, Chuansong Wu, Suppression of intermetallic reaction layer by ultrasonic assistance during FSW of Al and Mg based alloys, Journal of Alloys and Compounds Volume 827, 25 June 2020, 154343. https://doi.org/10.1016/j.jallcom.2020.154343.

[174] Chunliang Yang, ChuanSong Wu, Lei Shi, Modeling the dissimilar material flow and mixing in FSW of aluminum to magnesium alloys, Journal of Alloys and Compounds Volume 843, 30 November 2020, 156021, https://doi.org/10.1016/j.jallcom.2020.156021.

[175] Huachen Liu , Yikun Chen, Zhenhua Yao, Feixiang Luo, Effect of Tool Offset on the Microstructure and Properties of AA6061/AZ31B FSW Joints, Metals 2020, 10(4), 546; https://doi.org/10.3390/met10040546.

[176] Bandi, A., Bakshi, S.R. Effect of Pin Length and Rotation Speed on the Microstructure and Mechanical Properties of Friction Stir Welded Lap Joints of AZ31B-H24 Mg Alloy and AA6061-T6 Al Alloy. Metall Mater Trans A 51, 6269–6282 (2020). https://doi.org/10.1007/s11661-020-06020-8.

[177] Sameer MD , Anil Kumar Birru, Mechanical and metallurgical properties of friction stir welded dissimilar joints of AZ91 magnesium alloy and AA 6082-T6 aluminium alloy, Journal of Magnesium and Alloys 7 (2019) 264–271.

[178] Abdollahzadeh A, Shokuhfar A, Cabrera JM, Zhilyaev AP, Omidvar H, In-situ nanocomposite in FSW of 6061-T6 Aluminum alloy to AZ31 magnesium alloy, Journal of Materials Processing Tech. (2018), https://doi.org/10.1016/j.jmatprotec.2018.08.025

[179] Zhao, Y., Jiang, S., Yang, S. et al. Influence of cooling conditions on joint properties and microstructures of aluminum and magnesium dissimilar alloys by FSW. Int J Adv Manuf Technol 83, 673–679 (2016). https://doi.org/10.1007/s00170-015-7624-y

[180] Banglong Fu, Guoliang Qin , Fei Li, Xiangmeng Meng, Jianzhong Zhang, Chuansong Wu, FSW process of dissimilar metals of 6061-T6 aluminum alloy to BanglongFu ,GuoliangQin AZ31B magnesium alloy, Journal of Materials Processing Technology 218 (2015) 38–47. http://dx.doi.org/10.1016/j.jmatprotec.2014.11.039.

[181] Yong Zhao, Zhengping Lu, Keng Yan, Linzhao Huang, Microstructural characterizations and mechanical properties in underwater FSW of aluminum and magnesium dissimilar alloys, Materials & Design (1980-2015) Volume 65, January 2015, Pages 675-681 https://doi.org/10.1016/j.matdes.2014.09.046.

[182] Kwang-Jin LEE, Eui-Pyo KWON, Microstructure of stir zone in dissimilar friction stir welds of AA6061-T6 and AZ31 alloy sheets, Trans. Nonferrous Met. Soc. China 24(2014) 2374−2379.

[183] Liang, Z., Chen, K., Wang, X. et al. Effect of Tool Offset and TRS on Enhancing Mechanical Property of Al/Mg Dissimilar FSW Joints. Metall Mater Trans A 44, 3721–3731 (2013). https://doi.org/10.1007/s11661-013-1700-4.

[184] P. Venkateswaran, A.P. Reynolds, Factors affecting the properties of Friction Stir Welds between aluminum and magnesium alloys, Materials Science and Engineering A 545 (2012) 26– 37.

[185] Jing Shang, Kehong Wang ⇑ , Qi Zhou, Deku Zhang, Jun Huang, Guangle Li, Microstructure characteristics and mechanical properties of cold metal transfer welding Mg/Al dissimilar metals, Materials and Design 34 (2012) 559–565.

[186] Woong-Seong Chang, S.R. Rajesh, Chang-Keun Chun and Heung-Ju Kim, Microstructure and Mechanical Properties of Hybrid Laser-FSW between AA6061-T6 Al Alloy and AZ31, J. Mater. Sci. Technol., 2011, 27(3), 199-204.

[187] Yan Yong, Zhang Da-Tong, Qiu Cheng, Zhang Wen, Dissimilar FSW between 5052 aluminum alloy and AZ31 magnesium alloy, Transactions of Nonferrous Metals Society of China, 20, 2010, s619-s623.

[188] A.C. Somasekharan, L.E. Murr, Microstructures in friction-stir welded dissimilar magnesium alloys and magnesium alloys to 6061-T6 aluminum alloy, Materials Characterization 52 (2004) 49– 64.

[189] C. Hamilton, A. Sommers, S. Dymek, A thermal model of friction stir welding applied to Sc-modified Al–Zn–Mg–Cu alloy extrusions, International Journal of Machine Tools & Manufacture 49 (2009) 230–238.

[190] C. Hamilton, S. Dymek, A. Sommers, A thermal model of friction stir welding in aluminum alloys, International Journal of Machine Tools & Manufacture 48 (2008) 1120–1130.

[191] Seung Hwan C. Park, Yutaka S. Sato, Hiroyuki Kokawa, Kazutaka Okamoto, Satoshi Hirano, Masahisa Inagaki, Rapid formation of the sigma phase in 304 stainless steel during friction stir welding, Scripta Materialia 49 (2003) 1175–1180.

[192] G. Buffa, A. Ducato, L. Fratini, Numerical procedure for residual stresses prediction in friction stir welding, Finite Elements in Analysis and Design 47 (2011) 470–476.

[193] G.R. Argade, K. Kandasamy, S.K. Panigrahi, R.S. Mishra, Corrosion behavior of a friction stir processed rare-earth added magnesium alloy, Corrosion Science 58 (2012) 321–326.

[194] Y.S. Sato, Y. Kurihara, S.H.C. Park, H. Kokawa, N. Tsuji, Friction stir welding of ultrafine grained Al alloy 1100 produced by accumulative roll-bonding, Scripta Materialia 50 (2004) 57–60.

[195] S. Mironov, Y.S. Sato, H. Kokawa, H. Inoue, S. Tsuge, Structural response of superaustenitic stainless steel to friction stir welding, Acta Materialia 59 (2011) 5472–5481.

[196] L. Fratini, G. Buffa, R. Shivpuri, Mechanical and metallurgical effects of in process cooling during friction stir welding of AA7075-T6 butt joints, Acta Materialia 58 (2010) 2056–2067.

[197] S. Mironov, Y.S. Sato, H. Kokawa, Development of grain structure during friction stir welding of pure titanium, Acta Materialia 57 (2009) 4519–4528.

[198] L. Commin, M. Dumont, J.-E. Masse, L. Barrallier, Friction stir welding of AZ31 magnesium alloy rolled sheets:Influence of processing parameters, Acta Materialia 57 (2009) 326–334.

[199] R. Nandan, G.G. Roy, T.J. Lienert, T. Debroy, Three-dimensional heat and material flow during friction stir welding of mild steel, Acta Materialia 55 (2007) 883–895.

[200] N. Kamp, A. Sullivan, R. Tomasi, J.D. Robson, Modelling of heterogeneous precipitate distribution evolution during friction stir welding process, Acta Materialia 54 (2006) 2003–2014.

[201] S.R. Ren, Z.Y. Ma, L.Q. Chen, Effect of welding parameters on tensile properties and fracture behavior of friction stir welded Al–Mg–Si alloy, Scripta Materialia, 56(2007), 69-72.

[202] Omar S. Salih, Hangan Ou, W.Sun, D.G McCartney, "A review of friction stir welding of aluminum matrix composite", Material and Design 86 (2015) 61-71.

[203] Z.Y.Ma, F.C.Liu, R.S Mishra, " Superplastic deformation mechanism of ultrafined grained aluminum alloy produced friction stir welding", Acta Materialia, 58 (2010) 4693-4704.

[204] Jianqing Su, Jiye Wang, R.S Mishra, Ray Xu, " Microstructure and Mechanical Properties of Friction Stir Processing Ti-6Al-4V Alloy", Material Science and Engineering A 573 (2013) 67-74

[205] Z.Y.Ma, S.R Sharma, R.S Mishra, M.W Mahoney, " Micro structural modification of cast aluminum alloy via friction stir processing", Material Science Forum, vol 426-432 (2003) 2891-2896.

[206] Z.y.Ma, R.S Mishra, F.C Liu, "Super plastic behaviour of Micro-region in two pass friction stir processing 7075Al alloy", Materialia Science and Engineering A 505 (2009) 70-78.

[207] Z.Y. Ma, R.S Mishra, M.W Mahoney, " Superplasticity in Cast A356 induced via friction Stir Processing", Scripta Materialia 50 (2004) 931-935.

[208] Nilesh Kumar, R.S Mishra, " Ultrafined Grained Al-Mg-Sc Alloy via friction Stir Processing", Metallurgical and Materials Transaction, 44A (2013) 934-945.

[209] Jian Qing Su, T.W Nelson, T.R. McNelley, "Development of Nano crystalline structure in Cu during Friction Stir Processing", Material Science and Engineering A, 525 (2011) 5458-5464.

[210] S.R Sharma, R.S Mishra, Z.Y Ma, "Effect of friction stir processing on fatigue behaviour of A356 Alloy", Scripta Materialia 51 (2004) 237-241.

[211] Z.Y Ma, R.S Mishra, “Cavitation in super plastic 7075 Al alloy prepared via friction stir processing, Acta Materialia 51 (2003) 3551-3569.

[212] Z.Y Ma, R.S.Mishra, M.W Mahoney, R. Grimes, “Effect of Friction Stir Processing on the the kinectic of superplastic deformation in an Al-Mg-Zr Alloy”, Metallurgical and Material Transaction, 36A (2005), 1447-1458.

[213] S.Jana, R.S Mishra, J.B Baumann, “ Effect of friction stir processing on fatigue behavior of an investigation cast Al-7Si-0.6Mg alloy, Acta Materialia, 58 (2010) 989-1003.

[214] S. Jana, R.S. Mishra, J.A Baumann, G. Grant, “ Effect of process parameters on abnormal grain growth during FSP of a cast Al-Alloy”, Material Science and Engineering A, 528 (2010) 189-199.

[215] R.S Mishra, Z.Y.Ma, I. Charit, “Friction stir processing: A Novel technique for fabrication of surface composite”, Matrial Science and Engineering A 341 (2003) 307-310.

[216] Z.y. Ma, R.S.Mishra, M.W.Mahoney, R.Grimes,” High strain rate super plasticity in friction stir processed Al-4Mg-1Zr alloy”, Material Science and Engineering A 351 (2003) 148-153.

[217] Z.Y.Ma, R.S Mishra, M.W. Mahoney,” Super plastic deformation behavior of friction stir processed 7075Al alloy”, Acta Materialia 50 (2002), 4419-4430.

[218] Z.Y.Ma, S.R Mishra, R.S Mishra, “Effect of Friction Stir Processing on the microstructure of CastA356 Al”, Material Science and Engineering A 433 (2006), 269-278.

[219] S.Jana, R.S.Mishra, J.B Baumann, G. Grant, “Effect of stress ratio the fatigue behaviour of a friction stir processed cast Al-Si-Mg alloy, Scripta Materialia 61 (2009), 992-995.

[220] J.Q. Su, T.W Nelson, R.S Mishra, M.Mahoney, “Microstructure investigation of friction stir welding 7050-T651 aluminum, acta materialia, 2002.

[221] Jiye wang, Jianqing Su, R.S Mishra, Ray Xu, John A. Baumann, “Tool wear mechanism in friction stir welding of Ti-6Al-4V”, wear 321 (2014), 25-32.

[222] Y.Wang, X.L Shi, R.S mishra, T.J Watson, “Friction stir welding of devitrified AL-4.0Y-4.0Ni-0.9Co alloy produced by amorphose powder”, Scripta Materialia 56 (2007) 971-974.

[223] I. Dinaharan and E. T. Akinlabi, “Low cost metal matrix composites based on aluminum, magnesium and copper reinforced with fly ash prepared using friction stir processing,” *Compos. Commun.*, vol. 9, no. April, pp. 22–26, 2018, doi: 10.1016/j.coco.2018.04.007.

[224] N. Sun, Y. H. Yin, A. Gerlich, and T. H. North, “Tool design and stir zone grain size in AZ31 friction stir spot welds,” *Sci. Technol. Weld. Join.*, vol. 14, pp. 747–752, 2009.

[225] G. Padmaaban and V. Balasubramanian, “Selection of FSW tool pin profile, shoulder diameter and material for joining AZ31B magnesium alloy - An experimental approach,” *Mater. Des.*, vol. 30, no. 7, pp. 2647–2656, 2009, doi: 10.1016/j.matdes.2008.10.021.

[226] D. Bakavos and P. B. Prangnell, “Effect of reduced or zero pin length and anvil insulation on friction stir spot welding thin gauge 6111 automotive sheet,” *Sci. Technol. Weld. Join.*, vol. 14, no. 5, pp. 443–456, 2009, doi: 10.1179/136217109X427494.

[227] Y. HU, Y. qing CHEN, L. LI, H. dong HU, and Z. ang ZHU, “Microstructure and properties of Al/Cu bimetal in liquid–solid compound casting process,” *Trans. Nonferrous Met. Soc. China (English Ed.*, vol. 26, no. 6, pp. 1555–1563, 2016, doi: 10.1016/S1003-6326(16)64261-9.

[228] R. Beygi, M. Kazeminezhad, and A. H. Kokabi, “Microstructural Evolution and Fracture Behavior of Friction-Stir-Welded Al-Cu Laminated Composites,” vol. 45, no. January, pp. 361–370, 2014, doi: 10.1007/s11661-013-1989-z.

[229] R. Beygi, M. Kazeminezhad, and A. H. Kokabi, “Butt joining of Al − Cu bilayer sheet through friction stir welding,” *Trans. Nonferrous Met. Soc. China*, vol. 22, no. 12, pp. 2925–2929, 2012, doi: 10.1016/S1003-6326(11)61555-0.

[230] T. K. Bhattacharya, H. Das, and T. K. Pal, “Influence of welding parameters on material flow, mechanical property and intermetallic characterization of friction stir welded AA6063 to HCP copper dissimilar butt joint without offset,” *Trans. Nonferrous Met. Soc. China (English Ed.*, vol. 25, no. 9, pp. 2833–2846, 2015, doi: 10.1016/S1003-6326(15)63909-7.

[231] A. O. Al-Roubaiy, S. M. Nabat, and A. D. L. Batako, “Experimental and theoretical analysis of friction stir welding of Al–Cu joints,” *Int. J. Adv. Manuf.*

Technol., vol. 71, no. 9–12, pp. 1631–1642, 2014, doi: 10.1007/s00170-013-5563-z.

[232] A. Paoletti, F. Lambiase, and A. Di Ilio, "Analysis of forces and temperatures in friction spot stir welding of thermoplastic polymers," *Int. J. Adv. Manuf. Technol.*, vol. 83, no. 5–8, pp. 1395–1407, 2016, doi: 10.1007/s00170-015-7669-y.

[233] E. T. Akinlabi and S. A. Akinlabi, "Effect of Heat Input on the Properties of Dissimilar Friction Stir Welds of Aluminium and Copper," *Am. J. Mater. Sci.*, vol. 2, no. 5, pp. 147–152, 2012, doi: 10.5923/j.materials.20120205.03.

[234] M. E. Aalami-Aleagha, B. Hadi, and M. A. Shahbazi, "3-Dimensional Numerical Analysis of Friction Stir Welding of Copper and Aluminum," *J. Mech. Sci. Technol.*, vol. 30, no. 8, pp. 3767–3776, 2016, doi: 10.1007/s12206-016-0739-8.

[235] E. Akinlabi and A. Els-Botes, "Effect of Travel speed on Joint properties of Dissimilar Metal Friction Stir Welds.," *News.Mak.Ac.Ug*, no. March, pp. 155–161, 2011.

[236] Liu G, Murr L, Niou C, Mcclure J, Vega F. Microstructural aspects of the friction-stir welding of 6061-T6 aluminum [J]. Scripta Materialia, 1997, 37: 355−361.

[237] I. Charit, R.S. Mishra, High strain rate superplasticity in a commercial 2024 Al alloy via friction stir processing, Materials Science and Engineering: A Volume 359, Issues 1–2 , 25 October 2003, Pages 290-296.

[238] Gaafer A, Mahmoud T, Mansour E. Microstructural and mechanical characteristics of AA7020-O Al plates joined by friction stir welding [J]. Materials Science and Engineering A, 2010, 527: 7424−7429.

[239] Firouzdor V, Kou S. Al-to-Mg friction stir welding: Effect of material position, travel speed, and rotation speed. Metallurgical and Materials Transactions A: Physical Metallurgy and Materials Science. 2010; 41:2914-35.

[240] Preety Rani, R.S. Mishra, Husain Mehdi, Effect of Nano-sized Al2O3 particles on microstructure and mechanical properties of aluminum matrix composite fabricated by multipass FSW, Part C: Journal of Mechanical Engineering Science (SAGE), 2022. https://doi.org/10.1177/09544062221110822.

[241] Morisada Y, Fujii H, Nagaoka T, Nogi K, Fukusumi M. Fullerene/A5083 composites fabricated by material flow during friction stir processing. Composites Part A: Applied Science and Manufacturing. 2007; 38:2097-101.

[242] Somasekharan AC, Murr LE. Characterization of complex, solid-state flow and mixing in the friction-stir welding (FSW) of aluminum alloy 6061-T6 to magnesium alloy AZ91D using color metallography. Journal of Materials Science. 2006; 41:5365-70.

[243] Junjie ZhaoChuanSong WuLei Shi, Effect of ultrasonic field on microstructure evolution in friction stir welding of dissimilar Al/Mg alloys,Journal of Materials Research and Technology, 17, 2022, 1-21.

[244] Abdollahzadeh A, Shokuhfar A, Cabrera JM, Zhilyaev AP, Omidvar H, In-situ nanocomposite in friction stir welding of 6061-T6 Aluminum alloy to AZ31 magnesium alloy, Journal of Materials Processing Tech. (2018), 263, 296-307. https://doi.org/10.1016/j.jmatprotec.2018.08.025

[245] Baghdadi AH, Selamat NFM, Sajuri Z. Effect of tool offsetting on microstructure and mechanical properties dissimilar friction stir welded Mg-Al alloys, IOP Conference series: materials science and engineering, 238. IOP Publishing Ltd.; 2017:012018.

[246] Murr LE, Li Y, Flores RD, Trillo EA, McClure JC. Intercalation vortices and related microstructural features in the friction-stir welding of dissimilar metals. Materials Research Innovations. 1998; 2:150-63.

[247] Murr LE. A review of FSW research on dissimilar metal and alloy systems. Journal of Materials Engineering and Performance. 2010; 19:1071-89.

[248] B. Strass, G. Wagner, C. Conrad, B. Wolter, S. Benfer, W. Fürbeth, Realization of Al/Mghybrid-joints by ultrasound supported friction stir welding - Mechanical properties, microstructure and corrosion behavior, Adv. Mater. Res. 966–967 (2014) 521–535.

[249] S. Kumar, C.S. Wu, Z. Sun, W. Ding, Effect of ultrasonic vibration on welding load, macrostructure, and mechanical properties of Al/Mg alloy joints fabricated by friction stir lap welding, Int. J. Adv. Manuf. Technol. 100 (2019) 1787–1799.

[250] Abdellah Nait Salah, Sipokazi Mabuwa, Husain Mehdi, Velaphi Msomi, Mohammed Kaddami, Prabhujit Mohapatra, Effect of Multipass FSP on Si-rich TIG Welded Joint of Dissimilar Aluminum Alloys AA8011-H14 and AA5083-

H321: EBSD and Microstructural Evolutions. Silicon (2022). https://doi.org/10.1007/s12633-022-01717-4.

[251] T. Dursun, C. Soutis, Recent developments in advanced aircraft aluminium alloys, Mater. Des. **(1980-2015) 56,** 862-871 (2014).

[252] Luca Boccarusso, Antonello Astarita, Pierpaolo Carlone , Fabio Scherillo , Felice Rubino , Antonino Squillace, Dissimilar friction stir lap welding of AA 6082 - Mg AZ31: Force analysis and microstructure evolution, Journal of Manufacturing Processes, 44, 2019, 376-388.

[253] Su-Ta Chen, Truan-Sheng Lui, Li-Hui Chen, Effect of Revolutionary Pitch on the Microhardness Drop and Tensile Properties of Friction Stir Processed 1050 Aluminum Alloy, Materials Transactions, Vol. 50, No. 8 (2009) pp. 1941-1948.

[254] Morishige T, Kawaguchi A, Tsujikawa1 M, Hino M, Hirata T, Higashi K. Dissimilar welding of Al and Mg alloys by FSW [J]. Materials Transactions, 2008, 49(5): 1129−1131.

[255] Mohammadi J, Behnamian Y, Mostafaei A, Izadi H, Saeid T, Kokabi AH, Gerlich AP, Friction stir welding joint of dissimilar materials between AZ31B magnesium and 6061 aluminum alloys: Microstructure studies and mechanical characterizations, Materials Characterization, 101, 2015, 189-207.

[256] Husain Mehdi, R.S. Mishra, Modification of Microstructure and Mechanical Properties of AA6082/ZrB2 Processed by Multipass Friction Stir Processing. Journal of Materials Engineering and Performance, 32, 285–295 (2023). https://doi.org/10.1007/s11665-022-07080-0.

[257] P. Motalleb-nejad, T. Saeid, A. Heidarzadeh, Kh. Darzi, M. Ashjari, Effect of tool pin profile on microstructure and mechanical properties of friction stir welded AZ31B magnesium alloy, Materials and Design 59 (2014) 221–226.

[258] K. Elangovan, V. Balasubramanian, and M. Valliappan, Effect of Tool Pin Profile and Tool Rotational Speed on Mechanical Properties of Friction Stir Welded AA6061 Aluminium Alloy, Materials and Manufacturing Processes, 23, 2008, 251–260.

[259] V. Firouzdor, S. Kou, Al-to-Mg friction stir welding: effect of positions of Al and Mg with respect to the welding tool, Weld. J. 88 (2009) 213-224.

[260] S.H.C. Park, Y.S. Sato, H. Kokawa, Microstructural evolution and its effect on Hall-Petch relationship in friction stir welding of thixomolded Mg alloy AZ91, Mater Sci. 38 (2003) 4379-4383.

[261] Singh R K R, Sharma C, Dwivedi D K, Mehta N K, Kumar P. The microstructure and mechanical properties of friction stir welded Al−Zn−Mg alloy in as welded and heat treated conditions [J]. Materials & Design, 2011, 32(2): 682−687.

[262] Li X W, Zhang D T, Qiu C, Zhang W. Microstructure and mechanical properties of dissimilar pure copper/1350 aluminum alloy butt joints by friction stir welding [J]. Transactions of Nonferrous Metals Society of China, 2012, 22(6): 1298−1306.

[263] Firouzdor, V., Kou, S. Al-to-Mg Friction Stir Welding: Effect of Material Position, Travel Speed, and Rotation Speed. Metall Mater Trans A 41, 2914–2935 (2010). https://doi.org/10.1007/s11661-010-0340-1.

[264] Junjie ZhaoChuanSong WuLei Shi, Effect of ultrasonic field on microstructure evolution in friction stir welding of dissimilar Al/Mg alloys,Journal of Materials Research and Technology, 17, 2022, 1-21.

[265] Abdollahzadeh A, Shokuhfar A, Cabrera JM, Zhilyaev AP, Omidvar H, In-situ nanocomposite in friction stir welding of 6061-T6 Aluminum alloy to AZ31 magnesium alloy, Journal of Materials Processing Tech. (2018), 263, 296-307. https://doi.org/10.1016/j.jmatprotec.2018.08.025

[266] B. Strass, G. Wagner, C. Conrad, B. Wolter, S. Benfer, W. Fürbeth, Realization of Al/Mghybrid-joints by ultrasound supported friction stir welding - Mechanical properties, microstructure and corrosion behavior, Adv. Mater. Res. 966–967 (2014) 521–535.

[267] S. Kumar, C.S. Wu, Z. Sun, W. Ding, Effect of ultrasonic vibration on welding load, macrostructure, and mechanical properties of Al/Mg alloy joints fabricated by friction stir lap welding, Int. J. Adv. Manuf. Technol. 100 (2019) 1787–1799.

[268] J. Fayomi, A.P.I. Popoola, O.M. Popoola, O.P. Oladijo, O.S.I. Fayomi, Tribological and microstructural investigation of hybrid AA8011/ZrB2-Si3N4 nanomaterials for service life improvement, Results in Phys. **14**, 102469 (2019).

[269] X. Chen, Y. Peng, S. Peng, S. Yao, C. Chen, P. Xu, Flow and fracture behavior of aluminum alloy 6082-T6 at different tensile strain rates and triaxialities, PLoS One **12:7**, e0181983 (2017).

[270] Abdellah Nait Salah, Sipokazi Mabuwa, Husain Mehdi, Velaphi Msomi, Mohammed Kaddami, Prabhujit Mohapatra, Effect of Multipass FSP on Si-rich TIG Welded Joint of Dissimilar Aluminum Alloys AA8011-H14 and AA5083-H321: EBSD and Microstructural Evolutions. Silicon (2022). https://doi.org/10.1007/s12633-022-01717-4.

[271] T. Dursun, C. Soutis, Recent developments in advanced aircraft aluminium alloys, Mater. Des. **(1980-2015) 56,** 862-871 (2014).

[272] V. Firouzdor, S. Kou, Al-to-Mg friction stir welding: effect of positions of Al and Mg with respect to the welding tool, Weld. J. 88 (2009) 213-224.

[273] S.H.C. Park, Y.S. Sato, H. Kokawa, Microstructural evolution and its effect on Hall-Petch relationship in friction stir welding of thixomolded Mg alloy AZ91, Mater Sci. 38 (2003) 4379-4383.

[274] Singh R K R, Sharma C, Dwivedi D K, Mehta N K, Kumar P. The microstructure and mechanical properties of friction stir welded Al−Zn−Mg alloy in as welded and heat treated conditions [J]. Materials & Design, 2011, 32(2): 682−687.

[275] Li X W, Zhang D T, Qiu C, Zhang W. Microstructure and mechanical properties of dissimilar pure copper/1350 aluminum alloy butt joints by friction stir welding [J]. Transactions of Nonferrous Metals Society of China, 2012, 22(6): 1298−1306.

[276] Morisada Y, Fujii H, Nagaoka T, Fukusumi M. MWCNTs/AZ31 surface composites fabricated by friction stir processing [J]. Materials Science and Engineering A, 2006, 419(1): 344−348.

[277] Chandan Pandey, Nitin Saini, Manas Mohan Mahapatra, Pradeep Kumar, Study of the fracture surface morphology of impact and tensile tested cast and forged (C&F) Grade 91 steel at room temperature for different heat treatment regimes, Engineering Failure Analysis, 71, 2017, 131-147.

[278] Jitendra Kumar, Gaurav Kumar, Husain Mehdi & Mukesh Kumar, Optimization of FSW parameters on mechanical properties of different aluminum alloys of AA6082 and AA7050 by response surface methodology. Int J Interact Des Manuf (2023). https://doi.org/10.1007/s12008-023-01425-2.

[279] R. E. Śliwa, P. Myśliwiec, R. Ostrowski, and M. Bujny, “Possibilities of joining different metallic parts of structure using friction stir welding methods,”

Procedia Manuf., vol. 27, pp. 158–165, 2019, doi: 10.1016/j.promfg.2018.12.059.

[280] I. Galvão, A. Loureiro, D. Verdera, D. Gesto, and D. M. Rodrigues, “Influence of tool offsetting on the structure and morphology of dissimilar aluminum to copper friction-stir welds,” Metall. Mater. Trans. A Phys. Metall. Mater. Sci., vol. 43, no. 13, pp. 5096–5105, 2012, doi: 10.1007/s11661-012-1351-x.

[281] E. T. Akinlabi, R. M. Mahamood, S. A. Akinlabi, and E. Ogunmuyiwa, “Processing parameters influence on wear resistance behaviour of friction stir processed Al-TiC composites,” Adv. Mater. Sci. Eng., vol. 2014, no. March 2016, 2014, doi: 10.1155/2014/724590.

[282] R. B. Azhiri, R. M. Tekiyeh, E. Zeynali, M. Ahmadnia, and F. Javidpour, “Measurement and evaluation of joint properties in friction stir welding of ABS sheets reinforced by nanosilica addition,” Measurement, 2018, doi: 10.1016/j.measurement.2018.05.005.

[283] Husain Mehdi, Lalit Batra, Abhendra Pratap Singh & Chandrabhanu Malla, Multi-response optimization of FSW process parameters of dissimilar aluminum alloys of AA2014 and AA6061 by response surface methodology (RSM). Int J Interact Des Manuf (2023). https://doi.org/10.1007/s12008-023-01409-2.

[284] A. P. Reynolds, “Factors Affecting the Properties of Friction Stir Welded Aluminum Lap Joints,” pp. 281–287.

[285] R. Sathiskumar, N. Murugan, I. Dinaharan, and S. J. Vijay, “Characterization of boron carbide particulate reinforced in situ copper surface composites synthesized using friction stir processing,” Mater. Charact., vol. 84, pp. 16–27, 2013, doi: 10.1016/j.matchar.2013.07.001.

[286] A. Bhatia and R. Wattal, “Friction stir welding of carbon steel: Effect on microstructure and tensile strength,” Mater. Today Proc., no. xxxx, 2020, doi: 10.1016/j.matpr.2020.02.378.

[287] V. J. Arulmoni, M. S. Ranganath, and R. S. Mishra, “Effect of Single and Multiple-Pass Friction Stir Processing on Microstructure , Effect of Single and Multiple-Pass Friction Stir Processing on Microstructure , Hardness and Tensile Properties of a 99 . 99 % Cu with Carbon Nano Tubes,” no. May, 2015.

[288] R. M. S. Ingari, “analysis of microstructure , microhardness , tensile strength and wear properties of al 6082 / sic composite using multi-pass friction stir processing,” no. 4, pp. 138–149, 2017.

[289] M. M. Moradi, H. J. Aval, and R. Jamaati, “Microstructure and mechanical properties in nano and microscale SiC-included dissimilar friction stir welding of AA6061-AA2024,” vol. 0836, no. November, 2017, doi: 10.1080/02670836.2017.1393976.

[290] Y. Morisada, H. Fujii, T. Nagaoka, and M. Fukusumi, “MWCNTs/AZ31 surface composites fabricated by friction stir processing,” Mater. Sci. Eng. A, vol. 419, no. 1–2, pp. 344–348, 2006, doi: 10.1016/j.msea.2006.01.016.

[291] S. Pradeep Devaneyan, R. Ganesh, and T. Senthilvelan, “On the Mechanical Properties of Hybrid Aluminium 7075 Matrix Composite Material Reinforced with SiC and TiC Produced by Powder Metallurgy Method,” Indian J. Mater. Sci., vol. 2017, pp. 1–6, 2017, doi: 10.1155/2017/3067257.

[292] L. Fratini and G. Buffa, “CDRX modelling in friction stir welding of aluminium alloys,” vol. 45, pp. 1188–1194, 2005, doi: 10.1016/j.ijmachtools.2004.12.001.

[293] R. Beygi, M. Kazeminezhad, and A. H. Kokabi, “Microstructural Evolution and Fracture Behavior of Friction-Stir-Welded Al-Cu Laminated Composites,” vol. 45, no. January, pp. 361–370, 2014, doi: 10.1007/s11661-013-1989-z.

[294] E. T. Akinlabi, “Effect of shoulder size on weld properties of dissimilar metal friction stir welds,” J. Mater. Eng. Perform., vol. 21, no. 7, pp. 1514–1519, 2012, doi: 10.1007/s11665-011-0046-6.

[295] I. Galvão, A. Loureiro, D. Verdera, D. Gesto, and D. M. Rodrigues, “Influence of tool offsetting on the structure and morphology of dissimilar aluminum to copper friction-stir welds,” Metall. Mater. Trans. A Phys. Metall. Mater. Sci., vol. 43, no. 13, pp. 5096–5105, 2012, doi: 10.1007/s11661-012-1351-x.

[296] K. S. Mehra and S. Singh, “Investigation of Friction stir welded joint of AA6061 material using Altair Hyper Weld,” vol. 7, no. 12, pp. 305–309, 2016.

[297] R. Butola, Q. Murtaza, and R. M. Singari, “An experimental and simulation validation of residual stress measurement for manufacturing of friction stir processing tool,” Indian J. Eng. Mater. Sci., vol. 27, no. 4, pp. 826–836, 2020.

[298] R. Butola, N. Choudhary, R. Kumar, P. Kumar, M. Zubair, and R. M. Singari, “Materials Today : Proceedings Measurement of residual stress on H13 tool

steel during machining for fabrication of FSW / FSP tool pins," Mater. Today Proc., no. xxxx, 2020, doi: 10.1016/j.matpr.2020.11.656.

[299] V. J. Arulmoni, R. S. Mishra, and M. S. Ranganath, "Experimental Investigations on Friction Stir Processed Copper and Enhancement of Mechanical Properties of the Composite Material Experimental Investigations on Friction Stir Processed Copper and Enhancement of Mechanical Properties of the Composite Materic" no. September, 2014.

List of Publications

1. **Pradeep Kumar Mouria**, Ranganath M. Singari & Reeta Wattal "**Influence of rotational tool speed on metallurgical characterization of friction stir welded joint of AZ91D and AA2024".** JOURNAL OF ADHESION SCIENCE AND TECHNOLOGY__IMPACT FACTOR 2.431 (SCI) https://doi.org/10.1080/01694243.2023.2245196.
2. **Pradeep Kumar Mouria**, Ranganath M. Singari & Reeta Wattal "**Impact of tool pin profile on mechanical and microstructural properties of friction stir welded joints of AA2024 and AZ91D"** Journal of Materials Engineering and Performance**,** IMPACT FACTOR 2.036 (SCI) https://doi.org/10.1007/s11665-023-08999-8
3. **Pradeep Kumar Mouria**, Ranganath M. Singari & Reeta Wattal "**Microstructural and mechanical response of SiC and TiO_2 particles reinforced friction stir welded AA7075 and AA2024"** International Journal on Interactive Design and Manufacturing (IJIDeM) IMPACT FACTOR 2.1 (SCOPUS) https://doi.org/10.1007/s12008-023-01667-0
4. **Pradeep Kumar Mouria**, Ranganath M. Singari & Reeta Wattal "Prediction of temperatures and residual stresses during FSW of AA2024 and AA7075 with copper using HYPERWELD software" presented at International Conference on Advancement in materials, Manufacturing and industrial applications (ICAMMIA-2023) DOI (Journal): 10.37591/JoPC